Ph.D. thesis on

EXPLORATION OF THE SECOND SOLAR SPECTRUM THROUGH POLARIMETRIC STUDIES

Submitted by

H. D. Supriya

Thesis Supervisor:
Dr. B. Ravindra

Thesis Co-Supervisor:
Prof. K. N. Nagendra

Indian Institute of Astrophysics
Bengaluru

Registered for Ph.D. degree in the

Department of Physics, Pondicherry University

Puducherry

March 2016

Declaration

I hereby declare that the material presented in this thesis, submitted to the Department of Physics, Pondicherry University, for the award of Ph.D. degree, is the result of investigations carried out by me, at Indian Institute of Astrophysics, Bangalore under the joint supervision of Dr. B. Ravindra and Prof. K. N. Nagendra. The results reported in this thesis are new, and original, to the best of my knowledge, and have not been submitted in whole or part for a degree in any University. Whenever the work described is based on the findings of other investigators, due acknowledgment has been given. Any unintentional omission is duly regretted.

H. D. Supriya
(Ph.D. candidate)
Indian Institute of Astrophysics
Bengaluru 560 034
March 2016

Certificate

This is to certify that the work embodied in this thesis entitled “Exploration of the Second Solar Spectrum through polarimetric studies”, has been carried out by Ms. H. D. Supriya, under our supervision and the same has not been submitted in whole or part for Degree, Diploma, Associateship Fellowship or other similar title to any University.

Dr. B. Ravindra
(Thesis supervisor)
Indian Institute of Astrophysics
Bengaluru 560 034
March 2016

Prof. K. N. Nagendra
(Thesis co-supervisor)
Indian Institute of Astrophysics
Bengaluru 560 034
March 2016

Acknowledgments

I am grateful to my guide Dr. B. Ravindra and co-guide Prof. K. N. Nagendra, from the Indian Institute of Astrophysics (IIA) for their kind agreement to guide me jointly which has enabled me to complete my thesis work. Their support enabled me to work on a topic that was of immense interest to me. Both of them have always extended their support and constant guidance throughout my Ph.D. research career.

I am indebted to the Director, IIA, for providing me with the research facilities to work at IIA. I would like to express my gratitude to the Dean and the Board of Graduate Studies for their help and guidance in various official matters during the tenure of my Ph.D.

I am thankful to my doctoral committee members at IIA Prof. K. E. Rangarajan and Dr. Gajendra Pandey for their constructive inputs at every stage of my research. I would also like to extend my sincere gratitude to Prof. G. Chandrasekaran, doctoral committee member at Pondicherry University (PU) for his unconditional support both academically and for various official purposes at PU. I would also like to extend my appreciation to Prof. N. Satyanarayana, Dean, PU; Prof. Ramaswamy Murugan, Head of the Department of physics, PU; Dr. K. V. P. Latha, PU for their cooperation in all the official matters concerned with PU.

This work could not have been completed without the support of Prof. J. O. Stenflo, Dr. M. Sampoorna, Dr. M. Bianda and Dr. H. N. Smitha. I sincerely thank them for all the useful discussions and fruitful collaboration which helped me learn and understand the subject in a better way. I extend my thanks to my other collaborators Dr. R. Ramelli, and Dr. L. S. Anusha for creating a healthy work environment which helped me to progress in my research.

I would like to thank the financial support provided by Istituto Ricerche Solari Locarno (IRSOL), Switzerland and COST ACTION MP1104, which enabled me to visit IRSOL in connection with my research and also attend the meeting, “Theory and modeling of polarization in astrophysics” in Prague. I would like to thank Dr. Han Uitenbroek for providing the realistic atmospheric modeling code used for the modeling of the Ca I 4227 Å line in my thesis. I extend my thanks to the computer center staff at IIA, specially Dr. Baba Varghese, Mr. Anish Parwage and Mr. Ashok for all the support provided by them. I acknowledge the use of the HYDRA cluster

at IIA for most of the computations presented in this thesis.

The list is endless if I start naming my family and friends who have extended their wholehearted support and encouragement all throughout the journey. I thank all of them for making my dream of doing Ph.D. come true. I dedicate this thesis to all my teachers who have always inspired, encouraged and influenced me in various ways.

List of publications

In International refereed journals

1. *Polarized line formation with lower level polarization and partial frequency redistribution*
   Supriya, H. D., Sampoorna, M., Nagendra, K. N., Stenflo, J. O., & Ravindra, B. 2016, **ApJ**, under review.

2. *Center-to-limb observations and modeling of the Ca* I *4227 Å line*
   Supriya, H. D., Smitha, H. N., Nagendra, K. N., Stenflo, J. O., Bianda, M., Ramelli, R., Ravindra, B., & Anusha, L. S. 2014, **ApJ**, 793, 42.

3. *An efficient decomposition technique to solve angle-dependent Hanle scattering problems*
   Supriya, H. D., Sampoorna, M., Nagendra, K. N., Ravindra, B., & Anusha, L. S. 2013, **J. Quant. Spectrosc. Radiat. Transfer**, 119, 67.

4. *Quantum interference with angle-dependent partial frequency redistribution: solution of the polarized line transfer in the non-magnetic case*
   Supriya, H. D., Smitha, H. N., Nagendra, K. N., Ravindra, B., & Sampoorna, M. 2013, **Mon. Not. Roy. Astron. Soc.**, 429, 275.

5. *The effect of electron scattering redistribution on atomic line polarization*
   Supriya, H. D., Nagendra, K. N., Sampoorna, M., & Ravindra, B. 2012, **Mon. Not. Roy. Astron. Soc.**, 425, 527.

In refereed conference proceedings

1. *Modeling the center-to-limb variation of the Ca* I *4227 Å line using FCHHT models*
   Supriya, H. D., Smitha, H. N., Nagendra, K. N., Stenflo, J. O., Bianda, M., Ravindra, B., Ramelli, R., & Anusha, L. S. 2015, in "Polarimetry: From the Sun to Stars and Stellar Environments", November 30 - December 5, 2014, Punta Leona, Costa Rica, Eds. K. N. Nagendra, et al., Proc. IAU Symp. 305, (Cambridge: Cambridge University Press), 381.

2. *Electron scattering redistribution effect on atomic line polarization*
   Supriya, H. D., Nagendra, K. N., Ravindra, B., & Sampoorna, M. 2014, in ASP Conf. Ser., 489, Solar Polarization 7, Eds. K. N. Nagendra, et al. (San Francisco, CA:ASP), 117.

Abstract

The discovery of Zeeman effect opened a new window to observe the Sun. It enabled to understand the magnetic field which is one of the basic features that govern different physical processes on the Sun. These magnetic fields leave their signatures in the splitting and polarization of spectral lines which can be extracted using spectro-polarimetry. With the advent of increasingly powerful telescopes, like with the SOT/SP instrument on-board the Japanese HINODE satellite, which achieved a spatial resolution of 0.3 arcsec (or 200 km on the Sun), the small-scale structure of solar magnetic fields have been explored via the Zeeman effect. It is however now understood that the fundamental building blocks of solar magnetism are present on scales much smaller than those resolved by HINODE. The polarization of line radiation which is caused by resonance scattering on bound atomic levels acts as a tool to measure these small scale magnetic fields. A modification of this process by external magnetic fields is called the Hanle effect. Comparison between the available constraints from the Hanle effect with the magnetic fluxes resolved by the HINODE spacecraft reveals that about two thirds of the total magnetic flux remains invisible at the HINODE 200 km resolution, since this flux is tangled on very small scales, possibly 10-100 m, which is nearly 4 orders of magnitude smaller than the HINODE resolution limit. While Hanle effect constraints on the properties of this "hidden" magnetic flux exist, very little is known about its depth dependence. One of the main objectives of the thesis is to explore the center-to-limb variation (CLV) of the Stokes profiles which is in turn governed by the height variation of the temperature-density structure in the solar atmosphere. Apart from this we study one of the primary physical quantity needed to carry out the analysis of the scattering process i.e., the redistribution matrix. These studies are motivated by the existence of many unexplained signatures in the Second Solar Spectrum (SSS), which is the linearly polarized spectrum of the Sun caused by coherent scattering process.

The thesis is divided into three parts. The first part is dedicated to the observations and modeling of the CLV of the well known Ca I 4227 Å line. Not much progress is done in the literature in the area of modeling the CLV of different lines in the SSS because of the complexity of the problem. The main challenge is to obtain a single model atmosphere which can provide a simultaneous fit to the CLV of the (I,

Q/I) spectra. From the theoretical perspective, the line radiative transfer modeling of the observed data in the magnetically quiet regions using the scattering theory is essential. To this end, we have to solve the polarized line transfer equation that governs the absorption, emission and scattering of radiation in the stellar atmosphere. We use the one-dimensional (1D) modeling approach to study the CLV of the Ca I 4227 Å line, which exhibits largest scattering polarization of all the lines in the visible spectrum of the Sun. For the purpose of our studies we have observed the Ca I 4227 Å line at 14 positions from the center-to-limb on the Sun using Zurich Imaging Polarimeter-3 at Istituto Ricerche Solari Locarno in Switzerland. We have modeled the CLV of this line using different realistic solar atmospheres (Chapter 2). From the studies in Chapter 2 we concluded that no single 1D model attempted by us helps us in providing a simultaneous fit to the CLV of the Stokes profile. The solar atmosphere is too complex to be represented by a 1D model atmosphere. We have to go beyond 1D modeling like multi-dimensional modeling to represent the actual solar atmosphere. However this does not represent an impediment to the use of the Ca I 4227 Å line for solar magnetic field diagnostics. To demonstrate this we have carried out a model independent analysis to determine the turbulent weak magnetic fields in the solar atmosphere.

The second and third part of the thesis is dedicated to the theoretical studies of the fundamental physical quantity called the redistribution matrix which is required to study the physics of scattering processes. The redistribution matrix contains all the information of the scattering process, and hence is an important parameter to be studied in detail. In this regard, there are certain approximations made in different theoretical approaches developed in the literature to enable reduce the complexity of the problem. However, such approximations point towards the existence of spectral features in the SSS which cannot be explained using the available standard theories. Our efforts in the second and third part of the thesis is to relax some of the approximations and study its effects on the emergent Stokes profiles by considering different examples.

In second part of the thesis we study a series of problems concerning the polarized line formation with the angle-dependent partial frequency redistribution (PRD). The liner polarization of the strong resonance lines are sensitive to the type of frequency redistribution used. The PRD matrix is dependent on the incoming and outgoing frequencies and angles. In order to reduce the computational efforts angle-averaged PRD functions are used in most of the studies in the literature. In Chapters 3, 4 and 5 we consider different problems and relax this approximation and study the effects of using angle-dependent PRD on emergent Stokes profiles. In Chapter 3 we study the effect of electron scattering redistribution on atomic line polarization in non-magnetic regime. We use angle-dependent electron scattering and atomic redis-

tribution functions and present efficient numerical technique to solve this problem. In Chapter 4 we study the combined effects of angle-dependent PRD and quantum interference phenomena arising between the fine structure (J) states of a two-term atom or between the hyperfine structure (F) states of a two-level atom by restricting our attention to the case of non-magnetic and collisionless line scattering on atoms. From the studies in Chapters 3 and 4 in the non-magnetic regime we conclude that the effect of angle-dependent PRD are sensitive to the optical thickness of the slab used for the radiative transfer studies. In Chapter 5 we study the effect of using angle-dependent PRD in the presence of weak magnetic field, i.e. the Hanle effect. We present efficient decomposition techniques to solve the problem at hand. We point towards the necessity to use angle-dependent PRD to solve the Hanle transfer problem accurately, especially for the Stokes U parameter by taking the example of vertical magnetic fields and turbulent magnetic fields.

In the third part we have attempted to relax another common assumption made in our previous calculations, i.e. assuming the polarization of the lower-level of the atom involved in the scattering process is zero. In Chapter 6 we formulate a general theory for magnetized media to handle the problem of radiative transfer including the effects of PRD and polarization of the lower-level of the atom involved in the transition, starting from Kramers-Heisenberg scattering formulation. We then obtain the radiative transfer equation starting from the well established quantum field theory approach for the problem at hand. Further we apply this theory to two case studies in the non-magnetic regime which leads us to the conclusion that the effects of lower level polarization are significant only in the line core. Based on our conclusion we also propose a simplified numerical approach to solve the problem of polarized radiative transfer with PRD and lower-level polarization. Finally conclusions and future outlook of the contents presented in this thesis are given in Chapter 7.

Contents

Chapter 1

Introduction

The Sun being the closest star allows us to explore the different processes that governs the physics of the solar atmosphere. Spectral analysis gave birth to the modern astrophysics with the discovery and classification of absorption lines in the Sun's spectrum by Joseph Fraunhofer. In 1897 Pieter Zeeman discovered the famous Zeeman effect which describes the effect of magnetic fields on radiation (Zeeman, 1897). The Sun being a prototype dynamo creates magnetic fields which encodes its signature on the spectral lines. Therefore it is very important to decode this information and understand in detail the properties of the radiation, its formation process and the origin. It is now known that the magnetic fields are responsible for almost all the variability we see on the Sun and the other stars. The information about these magnetic fields are encoded in the polarization of the radiation coming from the Sun in the form of the splitting and polarization of spectral lines which is nothing but the Zeeman effect. The Zeeman effect was first introduced to astrophysics by George Ellery Hale in 1908. He predicted the existence of strong magnetic fields in sunspots (Hale, 1908) using Zeeman's discovery of the effect of magnetic fields on radiation. This discovery opened the window to the study of stellar and solar magnetic fields in particular demonstrating that information from the Sun is not contained only in the intensity measurements, but also in the polarization of the radiation. Further measurements of Sun's magnetic field have lead to the development of magnetohydrodynamics and dynamo theories.

The tool to remotely sense the Sun's magnetic field is "spectro-polarimetry". Spectro-polarimetry adds a new dimension to the observational astrophysics. It was G. G. Stokes who showed how complete information of a light beam can be obtained by measuring both intensity and polarization of light. With the advent of ground and space based telescopes with high spatial and spectral resolution we are able to explore the solar magnetic fields in a greater detail. We know that the magnetic fields on the Sun vary over a range of field strengths - few Gauss to kilo Gauss. Whereas Zeeman effect can be conveniently used to measure the stronger fields, diagnostic

tools like Hanle effect is essential to measure weak fields. Further details regarding the measurement of Stokes profiles and usage of them to diagnose solar magnetic fields are given in the next section.

1.1 Solar polarization

Polarization is produced when the spatial symmetry is broken in the physical process that generates the radiation that we observe. The breaking of the spatial symmetry can be due to the presence of a magnetic field, electric field, by instrumental polarization within the telescope, or by an anisotropic excitation process (radiative or collisional). The atomic energy levels are split in the presence of external magnetic fields and thus it cause the emitted radiation to be polarized. This phenomenon is the well known Zeeman effect. It manifests itself in the circular polarization as longitudinal Zeeman effect, which in turn gives information about the line-of-sight component of the magnetic field. Further the linear polarization is produced by the transverse Zeeman effect and carries information on the field component perpendicular to the line-of-sight. Thus by measuring the full Stokes vector it is possible to obtain the strength and orientation of the magnetic field.

Figure 1.1 shows an example of a spectrograph-based full disk solar magnetogram which are nothing but the smoothed maps of the circular polarization produced by the longitudinal Zeeman effect. Early solar magnetograms showed that the apparent field strengths increased with the angular resolution of the instrument. This raised the question what would be the strength of the magnetic fields if we further increase the angular resolution.

A technique introduced by Stenflo (1973) called the "line-ratio" technique answered this question. From these studies it became clear that more than 90% of the net magnetic flux on the "quiet-Sun" through the resolution elements had its origin in magnetic fields with strengths 1–2 kG (see also Howard & Stenflo, 1972; Stenflo, 1994; Stenflo et al., 1984). Since the apparent field strengths in these line-ratio observations were of order 1–10 G, this finding implied that the kG flux elements were far smaller in area than the existing resolution of the instruments. Further studies revealed that 99% of the non-magnetic photosphere is fully magnetized with weak, mixed-polarity fields far smaller than the angular resolution that we can reach. While Zeeman effect is successfully used as a diagnostic tool to measure strong magnetic fields, it is blind or insensitive to these "hidden" weak magnetic fields. Fortunately there exists another diagnostic tool, the Hanle effect (Stenflo, 1982), which helps us to diagnose weak magnetic fields (also see Faurobert-Scholl, 1993; Faurobert-Scholl et al., 1995; Stenflo et al., 1998). The details regarding Hanle effect are described in the next section.

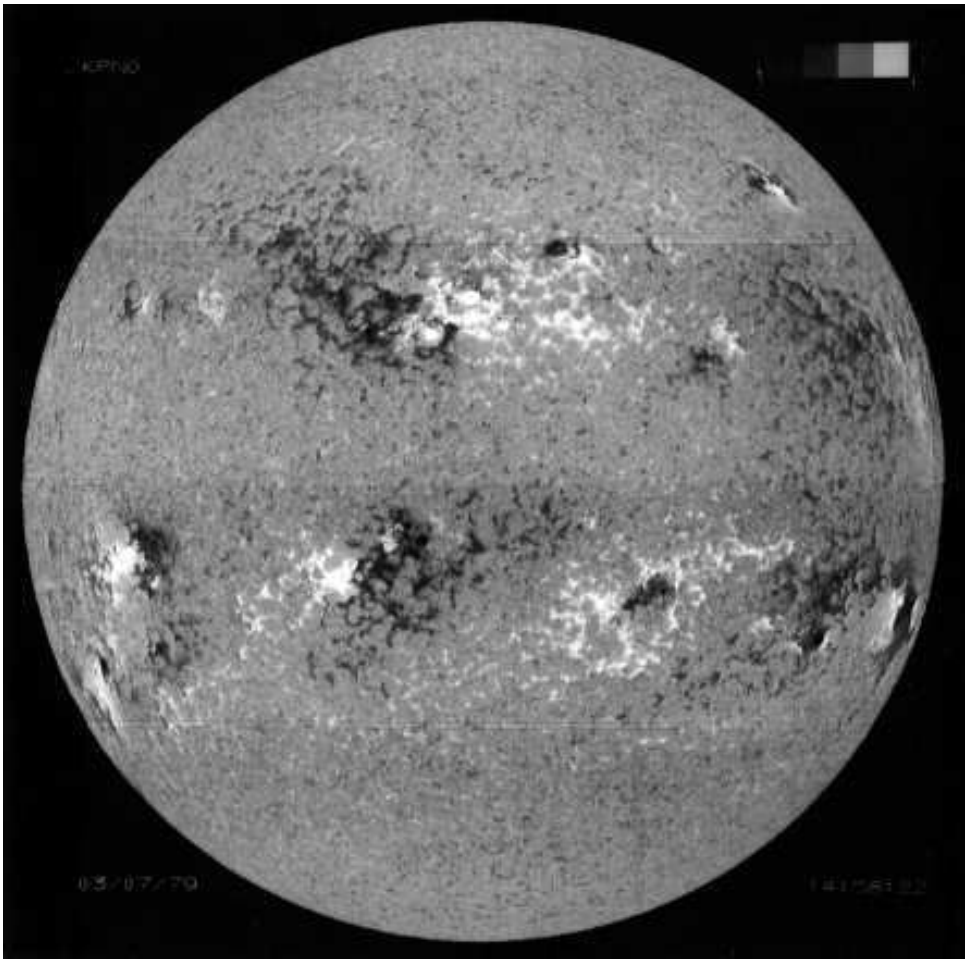

Figure 1.1: Full-disk solar magnetogram taken from Stenflo (1994). It was recorded on 7 March 1979 at the National Solar Observatory at Kitt Peak. Heliographic north is at top, east is to the left. Bright areas represent regions where the magnetic field is directed towards the observer, dark regions where it is directed away from the observer.

1.1.1 Scattering polarization - Second Solar Spectrum and the Hanle effect

As mentioned above, one of the process that leads to the breaking of symmetry and hence generation of polarization signal is scattering. In contrast to the Zeeman effect, the Hanle effect is a coherence phenomenon that only occurs in coherent scattering process, where there is a phase relation between the absorption and emission processes. These scattering processes produce polarization even in the absence of magnetic fields. A well known example for this case is the polarization of the blue sky by Rayleigh scattering on molecules. The Sun's spectrum is polarized by coherent scattering, but the degree of polarization is small due to the small degree of anisotropy of the incident radiation field (Stenflo, 2005) for scattering processes inside the Sun's atmosphere. However the measurement of small polarization signals have become possible with the advent of highly sensitive instruments such as the **Z**urich **Im**aging

Polarimeter (ZIMPOL; cf. Povel 1995, Stenflo 1984, Stenflo 1985, Stenflo & Povel 1985) with a precision of measurement of 10^{-5} in the degree of polarization. Due to the limb darkening of the solar disk we see anisotropic radiative scattering in the Sun. The non-magnetic scattering polarization is zero at the disk center due to symmetry reasons and monotonically increases as we move towards the limb. The entire solar spectrum, both lines and continuum, is polarized by such scattering in the solar atmosphere. The scattering polarization in the Sun was predicted in 1920s by Öhman (1929). It was Brückner (1963) who provided first reliable observation of the scattering polarization in Ca I 4227 Å line close to the limb.

The linearly polarized spectrum of the Sun produced due to the coherent scattering process (Stenflo et al., 1983a,b) is called the Second Solar Spectrum (SSS). It is referred to as the second spectrum of the Sun because of the diversity it shows compared to the well studied intensity spectrum i.e., the first solar spectrum. It was therefore natural to call this new and unfamiliar spectrum the "Second Solar Spectrum" (Ivanov, 1991; Stenflo & Keller, 1997). A spectral atlas of SSS has been produced, which in three volumes covers the wavelength from 3160 to 6995 Å (Gandorfer, 2000, 2002, 2005). Although the SSS exists regardless of whether there are magnetic fields or not, the shapes and amplitudes of the various structures get modified by magnetic fields. This modification goes under the name "Hanle effect". It was discovered by Wilhelm Hanle in Göttingen in 1923 (Hanle, 1924; Moruzzi & Strumia, 1991). The Hanle effect is a coherency phenomenon that only occurs when coherent scattering contributes to the line formation. It represents all magnetic-field induced modifications of the scattering polarization. The first observation of the Hanle effect in an astrophysical context was done in solar prominences by Leroy et al. (1977) at the Pic duMidi Observatory. Since then it is used widely for solar weak magnetic field diagnostic purposes (see for example Sahal-Brechot, 1977; Bommier, 1980; Landi Degl'Innocenti, 1982; Stenflo, 1982; Querfeld et al., 1985; Moruzzi & Strumia, 1991; Faurobert-Scholl, 1993; Stenflo, 1994; Faurobert-Scholl et al., 1995; Faurobert-Scholl, 1996; Stenflo et al., 1998; Bianda et al., 1998; Trujillo Bueno, 1999; Faurobert, 2000; Trujillo Bueno, 2001; Stenflo, 2002; Faurobert, 2003; Landi Degl'Innocenti & Landolfi, 2004; Anusha et al., 2011; Faurobert, 2012).

In a classical description the damped dipole oscillations that are induced by the incident radiation precess in the presence of a magnetic field, as illustrated in Figure 1.2. In the illustrated case it is assumed that vertical oscillations are induced by the excitation process, and that we observe the emitted radiation along the magnetic field direction. The trajectory of the damped oscillator forms a rosette pattern that becomes more isotropic when the field is stronger. The emitted polarization is obtained from the Fourier transform of the rosette pattern. In the absence of magnetic fields the scattered radiation would be linearly polarized in the vertical direction (in

the illustrated case), but as the field strength is increased, the plane of polarization gets rotated, and the amount of polarization is reduced. The Hanle effect leaves its imprints in the linear polarization. Its two main signatures are depolarization and rotation of the plane of polarization when the scattering geometry resembles 90° scattering.

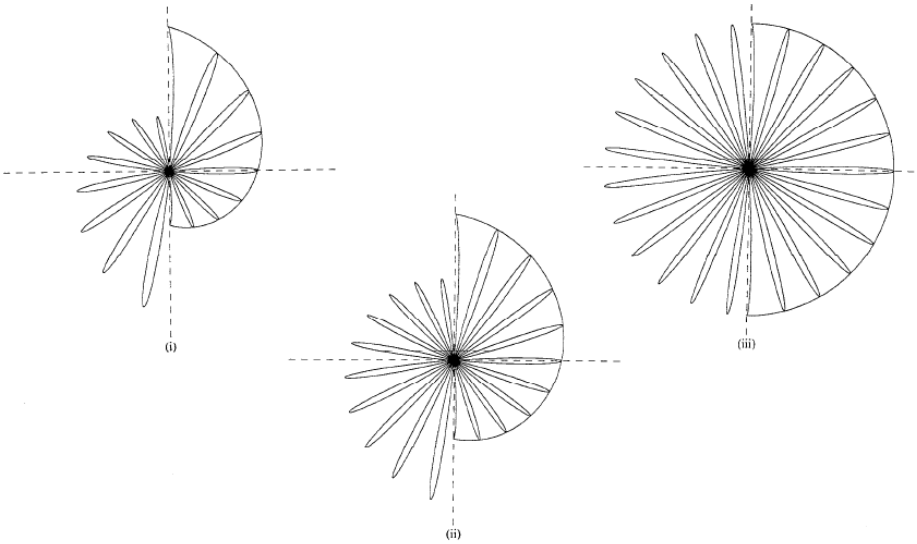

Figure 1.2: Trajectory of a damped classical oscillator, illustrating the Hanle effect depolarization and rotation of the plane of polarization when the magnetic field is oriented along the line of sight. The three diagrams represent different values of the field strength, which increases from left to right. This illustration is taken from Stenflo (1994).

According to the quantum mechanical description of the Hanle effect, magnetic fields remove the degeneracy of the radiatively excited and coherently superposed magnetic substates and thereby cause partial decoherence that leaves a signature in the polarization of the scattered radiation. It is the ratio between the Zeeman splitting and the radiative damping width of the atomic states that determine the Hanle depolarization. If they are comparable then we are in the optimal Hanle regime and if the Zeeman splitting is much larger than the radiative damping width of the atomic state then we are in the saturated Hanle regime (Stenflo, 1994; Trujillo Bueno, 2001; Sampoorna et al., 2007a,b, 2008c). The observations and recording of the SSS opened up the field of the theoretical studies to study the fundamental physical processes that govern the polarized structures. SSS is a source of information to learn more about atomic physics namely the quantum-mechanical interference between atomic states of different total angular momentum quantum numbers (Stenflo, 1980), hyperfine structure, abundances and isotope ratios (Stenflo, 1997), radiative transfer physics, solar magnetic fields, and the thermodynamics of the solar atmosphere. Other interesting problems studied are optical pumping that creates ground-state atomic polarization (Trujillo Bueno & Landi Degl'Innocenti, 1997; Manso Sainz & Trujillo Bueno, 2003b, 2007), and molecular scattering (Stenflo & Keller, 1997; Berdyug-

ina et al., 2002). Figure 1.3 shows an example of SSS indicating the phenomena of quantum interference. The observed profiles in Figure 1.3 are of Ca II K and H lines recorded by Stenflo (1980). The quantum interference resulting because of the coherent superposition of states (as indicated in the upper right diagram) is responsible for the sign reversal of the SSS in Figure 1.3 (Stenflo, 1980).

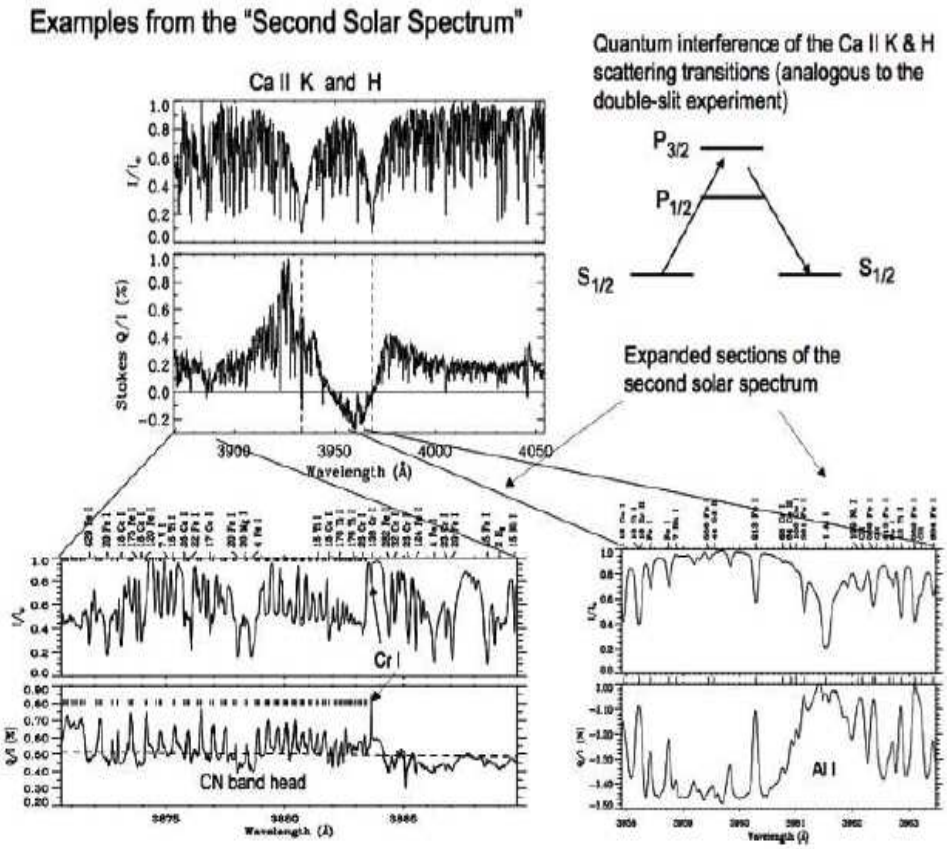

Figure 1.3: The above figure is taken from Stenflo (2015b). The top left panel are the observations of the 200 Å wide Ca II K and H line taken by Stenflo (1980). The zoomed in version of the SSS in the bottom panels indicate the sign reversal resulting from the quantum interference between the atomic states. The top right panel indicates the quantum interference between the upper total angular momentum states of the H and K lines.

1.2 Measurement of Stokes parameters

The measurement of Stokes parameters (I, Q, U, and V), provides a complete description of a partially polarized beam and is the key ingredient to understand solar polarization. The Stokes parameters introduced by G. G. Stokes in 1852 can be defined in a variety of ways, which are all equivalent but in its own way convenient for use in different contexts. Stokes parameters were introduced to astrophysics by Subrahmanyan Chandrasekhar in 1946 (Chandrasekhar, 1950). In the monograph by Jan Stenflo (Stenflo, 1994) a detailed description of the representation of the po-

larized light and different approaches to define the Stokes parameters are given. We recall the equations and description given in Stenflo (1994) in this section (see also Collett, 1993).

One of the simplest ways to represent Stokes vector $\boldsymbol{I}$, which consists of the Stokes parameters I, Q, U, V, or, S_k, k = 0,1,2,3, i.e.,

$$\boldsymbol{I} = \begin{pmatrix} S_0 \\ S_1 \\ S_2 \\ S_3 \end{pmatrix} = \begin{pmatrix} I \\ Q \\ U \\ V \end{pmatrix}, \tag{1.1}$$

is the operational one in terms of four idealized filters F_k in a measurement process which directly relates to the understanding of polarimetric observations. By considering a set of idealized filters as shown in Figure 1.4 the meaning of the four Stokes parameters I, Q, U, and V can be visualized. F_0 represents empty space, F_1 and F_2 transmit linear polarization with the electric vector at position angles 0 and 45°, respectively, while F_3 transmits right-handed circular polarization. If I_k is the observed value behind each filter then

$$I_k = \frac{1}{2}(S_0 + S_k), \tag{1.2}$$

and the inverse relation is given by

$$S_k = 2I_k - I_0. \tag{1.3}$$

S_0 thus represents the ordinary intensity, S_1 and S_2 the amount of linear polarization along position angles 0 and 45°, and S_3 the amount of right-handed circular polarization. If we instead choose the filters F_1 and F_2 to transmit linear polarization at 90° and -45°, and F_3 left-handed circular polarization, then the signs of Q, U, and V would change.

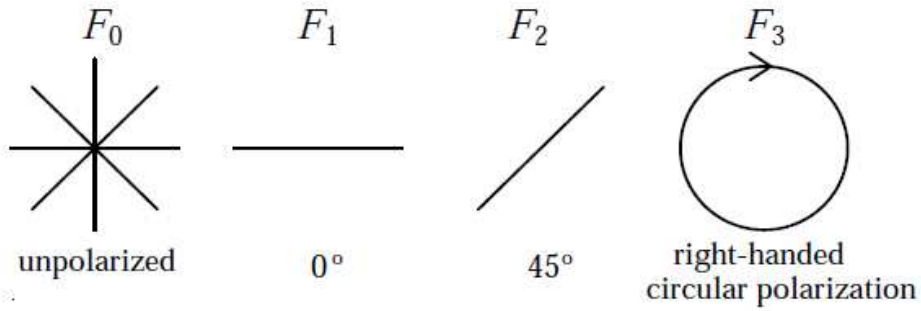

Figure 1.4: Symbolic representation of the four idealized filters F_k. The above figure is taken from Stenflo (1994)

1.2.1 Jones calculus and coherency matrix formalism

If $\boldsymbol{e}_1$ and $\boldsymbol{e}_2$ represent orthogonal basis vectors in a plane perpendicular to the light beam, then electric vector $\boldsymbol{E}$ at any point in space can be written as

$$\boldsymbol{E} = Re(E_1\boldsymbol{e}_1 + E_2\boldsymbol{e}_2), \tag{1.4}$$

where

$$E_k = E_{0k}e^{-i\omega t}, \quad k = 1, 2, \tag{1.5}$$

and E_{0k} are complex amplitudes. The Jones vector $\boldsymbol{J}$ can now be defined as

$$\boldsymbol{J} = \begin{pmatrix} E_1 \\ E_2 \end{pmatrix}. \tag{1.6}$$

Since each of the complex number E_1 and E_2 has a real and an imaginary part, the Jones vector is characterized by a set of four parameters like Stokes vector. However the Stokes vector can represent partially polarized light, but the Jones vector can only represent 100% elliptically polarized light. This is because, as we know each photon is always 100% elliptically polarized. In nature we often deal with an ensemble of photons created by stochastically independent atomic processes because of which they are mutually uncorrelated with different polarization states. Even a linear superposition of Jones vectors represents 100% elliptically polarized light, as the superposition is coherent and phase-preserving. Thus in order to describe partially polarized light we need an "incoherent" superposition of the photons. This can be obtained by the superposition of bilinear products of Jones vectors for each individual wave train because of which the factor $e^{-i\omega t}$ disappears. Following this the 2×2 coherency matrix $\boldsymbol{D}$ of the radiation field is defined as

$$\boldsymbol{D} = \langle \boldsymbol{J}\boldsymbol{J}^\dagger \rangle, \tag{1.7}$$

where $\boldsymbol{J}^\dagger$ is the adjoint of $\boldsymbol{J}$, and the bracket represents averaging over a statistical ensemble of uncorrelated photons.

1.2.2 Mueller calculus

If we consider a wave train that enters a medium as Jones vector $\boldsymbol{J}'$ and exists it as $\boldsymbol{J}$ then the relation between them can be described as

$$\boldsymbol{J} = \boldsymbol{w}\boldsymbol{J}'. \tag{1.8}$$

$\boldsymbol{w}$ is a 2×2 matrix that describes the property of a medium, and does not depend on whether we make a coherent or incoherent superposition of the many wave trains. Further the coherency matrix transforms as

$$\boldsymbol{D} = \boldsymbol{w}\boldsymbol{D}'\boldsymbol{w}^{\dagger}. \tag{1.9}$$

The transformation of the Stokes vector $\boldsymbol{I}'$ by a medium can be described by the 4×4 "Mueller matrix" $\boldsymbol{M}$ as

$$\boldsymbol{I} = \boldsymbol{M}\boldsymbol{I}'. \tag{1.10}$$

The Mueller matrix can be expressed in terms of the Jones matrix $\boldsymbol{w}$ using the relation between the Stokes parameters and the coherency matrix formalism as

$$\boldsymbol{M} = \boldsymbol{T}\boldsymbol{W}\boldsymbol{T}^{-1}, \tag{1.11}$$

where the matrix $\boldsymbol{W}$ contains all the physical properties of the medium and can be written as

$$\boldsymbol{W} = \boldsymbol{w} \otimes \boldsymbol{w}^{*} = \begin{pmatrix} w_{11}w_{11}^{*} & w_{11}w_{12}^{*} & w_{12}w_{11}^{*} & w_{12}w_{12}^{*} \\ w_{11}w_{21}^{*} & w_{11}w_{22}^{*} & w_{12}w_{21}^{*} & w_{12}w_{22}^{*} \\ w_{21}w_{11}^{*} & w_{21}w_{12}^{*} & w_{22}w_{11}^{*} & w_{22}w_{12}^{*} \\ w_{21}w_{21}^{*} & w_{21}w_{22}^{*} & w_{22}w_{21}^{*} & w_{22}w_{22}^{*} \end{pmatrix}. \tag{1.12}$$

The symbols $\otimes$ and $*$ denote tensor product and complex conjugation, respectively. The matrix $\boldsymbol{T}$ is a purely mathematical transformation matrix without physical contents, given by

$$\boldsymbol{T} = \begin{pmatrix} 1 & 0 & 0 & 1 \\ 1 & 0 & 0 & -1 \\ 0 & 1 & 1 & 0 \\ 0 & -i & i & 0 \end{pmatrix}, \tag{1.13}$$

and

$$\boldsymbol{T}^{-1} = \frac{1}{2}\begin{pmatrix} 1 & 1 & 0 & 0 \\ 0 & 0 & 1 & i \\ 0 & 0 & 1 & -i \\ 1 & -1 & 0 & 0 \end{pmatrix}. \tag{1.14}$$

The Mueller matrix is a very flexible tool that can be used in the radiative transfer equation for the Stokes vector, both as the 4×4 absorption matrix that contains the Zeeman effect, and the scattering matrix that can include both coherent and incoherent scattering, frequency redistribution, and the Hanle effect. The characteristics of the medium described by the Mueller matrix can be a telescope system or a stellar atmosphere. If the medium is described as a sequence of consecutive components

$i = 1, 2, ..., n$ like a sequence of retarders, polarizers, or modulators in a telescope system, or a sequence of differential layers in a stellar atmospheres, each with its own Muller matrix $\boldsymbol{M}_i$, then

$$\boldsymbol{M} = \boldsymbol{M}_n \boldsymbol{M}_{n-1} .... \boldsymbol{M}_2 \boldsymbol{M}_1, \tag{1.15}$$

where index i increases in the propagation direction. The evaluation of the Mueller matrix for the problem at hand is the important task when dealing with polarized radiative transfer. We concentrate on this particular task in the Parts II and III of the present thesis. In the next section we describe about one of the important lines in the SSS namely, the Ca I 4227 Å line and the efforts till date towards its modeling.

1.3 The Ca I 4227 Å line and its modeling

In the present thesis we are interested in studying one particular line in the SSS, namely, the Ca I 4227 Å line. This line is of particular interest because of the large scattering polarization that it exhibits of all the lines in the visible part of the SSS. It was one of the lines to be first observed and studied in the SSS. The Ca I 4227 Å line arises due to the transition between the atomic states with total angular momentum $J = 0$ and $J = 1$.

The first observation of the linear polarization of this line is presented in Figure 1.5 which was taken by Redman (1941). He wrote "*For the most part the profiles are indistinguishable, but there is a small difference amounting to about 1.8 percent of the continuous spectra at line intensity 60 percent. Examinations of likely sources of errors suggests that this may be real. The ratio of theoretical to observed effect is of the order of ten.*" Though Redman observed real signals, the previously predicted theoretical values (Zanstra, 1941) made him doubt his observations. More than a decade later in 1954, Jäger observed the scattering polarization in this line (Jäger, 1954). He detected a significant amount of linear polarization in the line core of the Ca I 4227 Å line. He also noticed a large difference at the line core between the signals observed at the north and the east limb positions which he predicted to be due to the solar magnetic fields. Another decade later, Brückner (1963) measured several points across the Ca I 4227 Å line profile using the 45cm Gregory-Coude telescope at Istituto Ricerche Solari Locarno (IRSOL). He established that the linear polarization in the wings of the Ca I 4227 Å line is stronger than in the core.

A major step forward in the measurements of the Ca I 4227 Å line occurred when Stenflo (1974) observed more points across the Ca I 4227 Å line profile. He also established the center-to-limb variation (CLV) of this line which was confirmed later by the polarized line profiles obtained by Wiehr (1975). The Hanle effect in the core

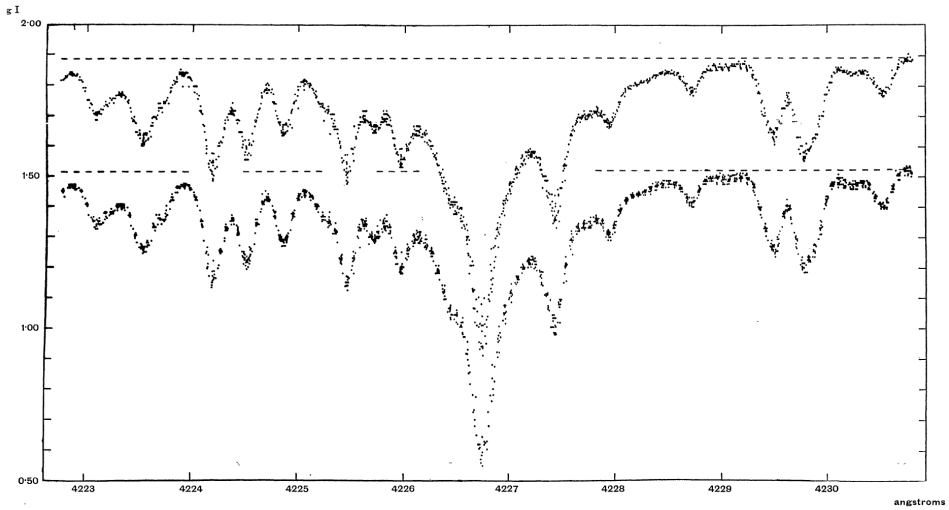

Figure 1.5: First observations (Log I vs wavelength (Å)) of the Ca I 4227 Å line. The top curve represents the observations taken parallel to the solar limb and the bottom curve perpendicular to the solar limb. The figure is taken from Redman (1941).

of the Ca I 4227 Å line was first observed by Stenflo (1982). There are many efforts since 1970s to observe this line with high precision instruments (see, e.g., Stenflo et al., 1980; Stenflo, 1982; Bianda et al., 1998; Gandorfer, 2002). Figure 1.6 shows the observations of the Ca I 4227 Å line by Stenflo et al. (1980). These observations were obtained using the High Altitude Observatory Stokesmeter at the Sacramento Peak Observatory. Modeling of the Ca I 4227 Å line also opened the pathway to test the theory of linear polarization. One of the first attempts to model the non-magnetic observations by Brückner (1963) of this line was by Dumont et al. (1973). Other observations and modeling efforts are briefly accounted below. Another interesting feature exhibited by this line is the the triple peak structure in the linear polarization profile (see bottom panel of Figure 1.6). A theoretical understanding of the wing polarization of the Ca I 4227 Å line was first provided by Dumont et al. (1973). Later Rees & Saliba (1982) showed how the wing polarization peaks could be understood as an effect of partial frequency redistribution (PRD) in polarized radiative transfer for strong lines (also see Saliba, 1985; Frisch, 1996; Holzreuter et al., 2005). Hence these wing peaks of the Ca I 4227 Å line are famously called PRD wing peaks. One of the early attempts to model the polarization profiles of the Ca I 4227 Å line observed in both quiet and active regions was by Faurobert-Scholl (1992) using the observations of Stenflo (1982). Her treatment included the effects of PRD and radiative transfer.

Other interesting aspect of this line is the spatial variation of the wing polarization in $(Q/I, U/I)$ spectra along the spectrograph slit. These variations were noticed by Bianda et al. (2003) in the observations near an active region. Later these spatial variations were also observed in quiet regions by Sampoorna et al. (2009) and were

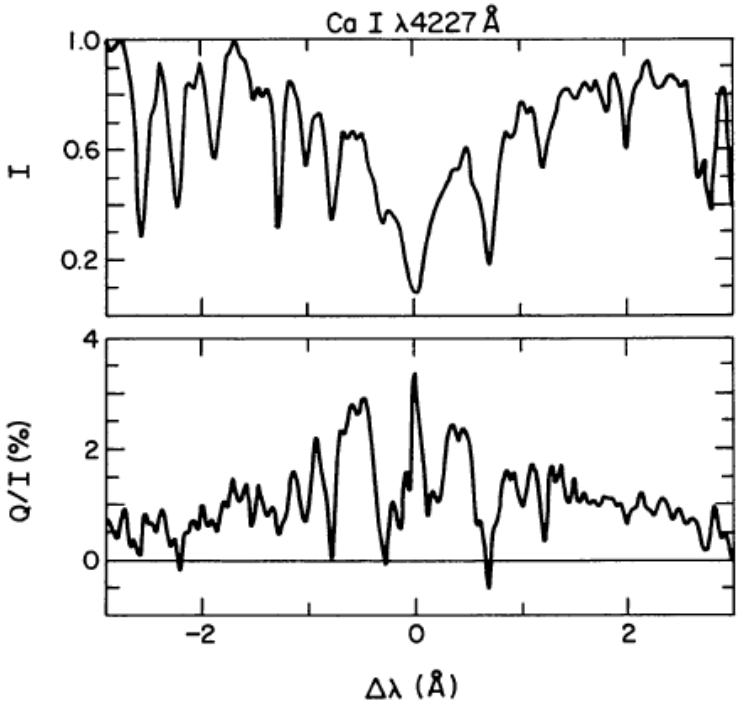

Figure 1.6: Intensity and polarization recording of the Ca I 4227 Å line by Stenflo et al. (1980) obtained at 7″ inside the south polar limb with an effective spectral resolution of about 30 mÅ. The figure is taken from Stenflo et al. (1980).

predicted to arise possibly due to the local inhomogeneities in the atmospheric layers. A detailed modeling of the Ca I 4227 Å line profile observed in a quite region near the solar limb is presented by Anusha et al. (2010). The authors employed last scattering approximation to model them. The idea of using the Hanle effect near the disk center to measure chromospheric magnetic fields was proposed by Trujillo Bueno (2001). This is referred to as 'forward scattering Hanle effect' (a very small angle scattering near the disk center). In an axially symmetric one-dimensional (1D) atmosphere with no oriented magnetic fields, the scattering polarization is zero when the line-of-sight is parallel to the atmospheric normal. The forward scattering Hanle effect is the non-zero scattering polarization produced in the presence of an oriented magnetic field by the Hanle effect. Observations of the forward scattering Hanle effect in the Ca I 4227 Å line near the disk center were performed by Bianda et al. (2011). Subsequently, these observations were modeled by Anusha et al. (2011) to determine the chromospheric weak magnetic fields.

However, most of the above mentioned studies concerned either the limb or the near disk center observations and modeling. To better understand the solar atmosphere it is very important to study the CLV of different lines which maps the height variation of various atmospheric quantities. The first non-magnetic CLV observation of the Ca I 4227 Å line was done by Stenflo et al. (1980) and subsequently analyzed

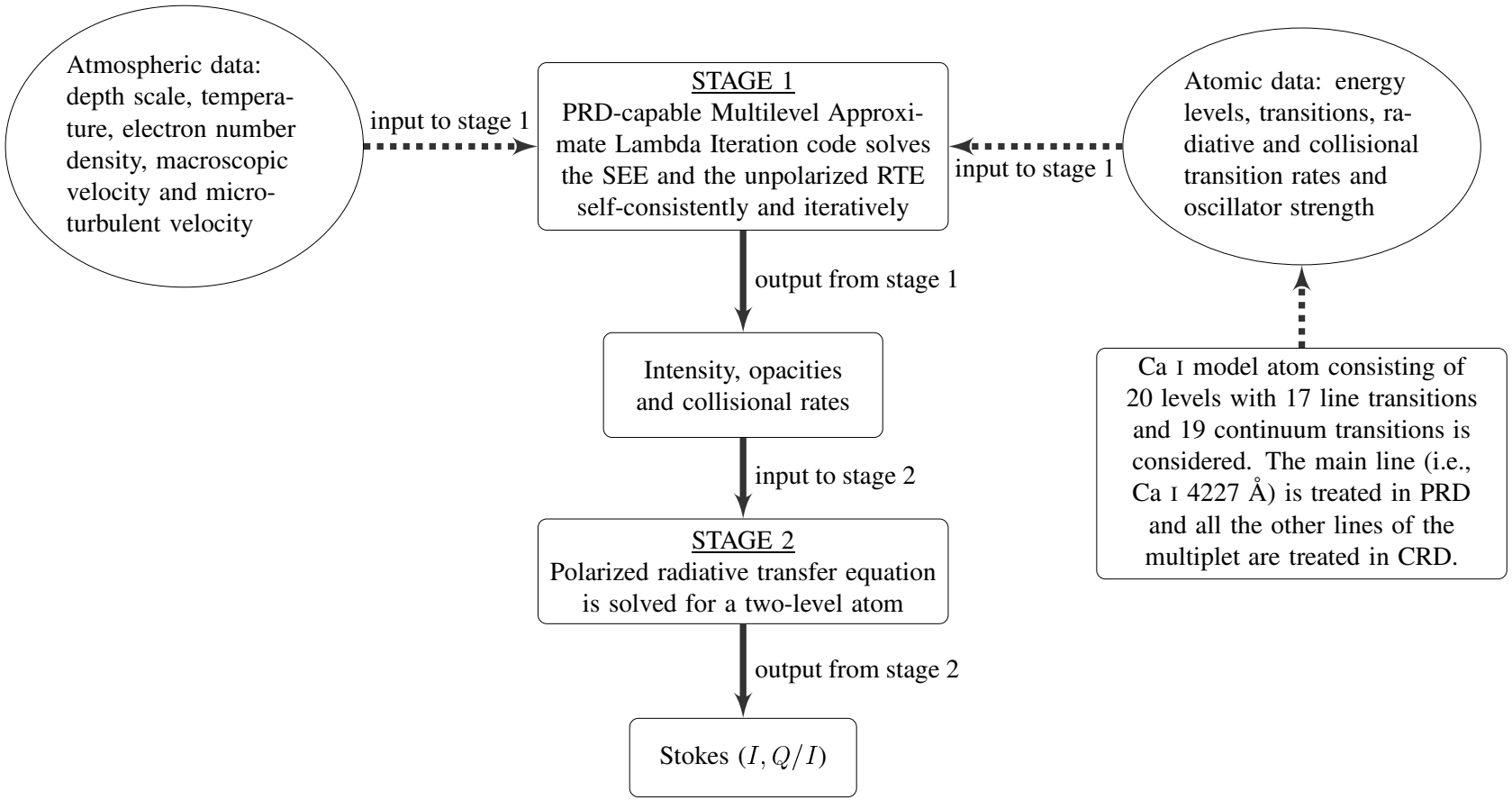

Figure 1.7: Flow-chart of the two-stage modeling procedure to solve the polarized radiative transfer problem. First stage uses the multi-level radiative transfer code developed by Uitenbroek (2001) and the second stage uses POLY code developed by D. M. Fluri to solve the non-magnetic polarized radiative transfer equation with angle-averaged PRD (see Fluri et al., 2003). SEE - statistical equilibrium equation; RTE - radiative transfer equation.

by Auer et al. (1980). Further Faurobert-Scholl (1994) used the CLV of the line center polarization observed by Stenflo et al. (1980, see also Bianda et al. 1998, 1999) to study the Hanle effect due to the magnetic canopies in the chromosphere. Part I of the present thesis concerns the observations and modeling of the CLV of the Ca I 4227 Å line. The CLV modeling is a challenge as it is necessary to find a single solar model atmosphere which provides a simultaneous fit to both the intensity and polarization at all the limb distances. Further details regarding the CLV observations and modeling of the Ca I 4227 Å line are described in Section 2.1 of Chapter 2. Though there are many efforts in the literature to study the Ca I 4227 Å line, it still poses challenge to the theorists, there by helping them to improve the modeling efforts. A detailed radiative transfer modeling of this line would in turn help to map the temperature structure within the solar atmosphere in a better way.

Modeling of different lines in the SSS (in particular the Ca I 4227 Å line which is our line of interest) requires to take account of atomic physics of the atom involved in the transition and depth dependence of various physical parameters of the solar atmosphere. To this end, we need to solve for the statistical equilibrium equations and polarized radiative transfer equation accounting for PRD. This modeling procedure is carried out in a two-stage process which is pictorially represented in Figure 1.7. In the first stage we use the multi-level radiative transfer code by Uitenbroek (2001, from now on referred to as the RH-code) developed to handle 1D, two-dimensional (2D) and three-dimensional (3D) problems. This code solves the statistical equilibrium equations using the multi-level accelerated lambda iteration (MALI) scheme of Rybicki & Hummer (1991) and the unpolarized radiative transfer equation. There are two main input parameters that goes into the first stage modeling procedure namely, the model atom and the model atmosphere. The model atom contains all the information on the atomic levels of the atom involved in the transition such as the energy levels, transitions, radiative and collisional transition rates, and oscillator strength. Apart from the main atom under consideration the details of all the other transitions in the solar spectrum arising from other elements are included in the transfer computations as blend lines. A detailed account of atomic data of different lines of the solar spectrum can be found in Kurucz (1990). The other input parameter is the model atmosphere. For our studies in the present thesis we use 1D solar model atmospheres by Fontenla et al. (1993); Avrett (1995); Fontenla et al. (2009). These model atmospheres contain all the information about the solar atmosphere like depth scale (either as column mass or optical depth), temperature, electron number density, macroscopic velocity, and microturbulent velocity. There are many 1D solar models available in the literature, taking different solar structures into account and each one is updated and made more sophisticated over a period of time. Some of the examples of 1D model atmosphere can be found in Kurucz (1969,

1973, 1979); Vernazza et al. (1973, 1976); Machado et al. (1980); Vernazza et al. (1981); Avrett et al. (1984); Maltby et al. (1986); Fontenla et al. (1990, 1991, 1993); Avrett (1995); Fontenla et al. (2006, 2007, 2009). The output obtained from the first stage like intensity, opacities and collisional rates are used as inputs to the second stage. The second stage is developed by D. M. Fluri and is called the POLY code. The POLY code solves the non-magnetic polarized radiative transfer equation for a two-level atom (Fluri et al., 2003). This two-stage modeling procedure is adopted to model different lines of SSS in the literature by Holzreuter et al. (2005); Holzreuter & Stenflo (2007a,b) and later by Anusha et al. (2010, 2011); Smitha et al. (2012a, 2013b, 2014) after suitable modifications to account for the relevant physics of the problem under consideration. In Part I of this thesis, we appropriately use this code to model the CLV observations of the Ca I 4227 Å line. In the next section we elaborate on the theories developed to understand scattering polarization.

1.4 Theory of scattering polarization

In this section we present two important theoretical approaches developed to study the physics of spectral line polarization. With this we also point out at the advantages and limitations of each of the approaches. Before we describe the theoretical approaches we want to give a brief account of the fundamental quantity in the polarized line transfer theory namely, the redistribution matrix.

1.4.1 Partial frequency redistribution

In a resonance scattering event the photon of frequency ν' is absorbed by the atom and is scattered by emitting a photon of frequency ν. The redistribution function determines the probability of this event occurring in a scattering process. If the frequency of the scattered (emitted) photon is correlated to the frequency of the incident (absorbed) photon then it is classified as partial frequency redistribution (generally referred to as PRD). If there is no correlation between the frequency of the emitted and absorbed photon then it is called as complete frequency redistribution (generally referred to as CRD). Transfer problems with CRD are much easier to solve than transfer problems with PRD. Though CRD mechanism is sufficient in describing subordinate and weak resonance lines, PRD is very essential to account for intensity and polarization profiles of strong resonance lines.

PRD effects are described by the 4×4 redistribution matrix $\boldsymbol{R}(\nu, \boldsymbol{\Omega}, \nu', \boldsymbol{\Omega}')$ which gives the joint probability of absorbing a photon with frequency ν' traveling in the direction $\boldsymbol{\Omega}'$ and reemitting a photon with frequency ν and in the direction $\boldsymbol{\Omega}$. The redistribution matrix also depends on the local properties of the atmosphere, such as

the value and direction of the magnetic field, $\boldsymbol{B}$. This redistribution matrix contains all the information about the physics of a scattering event and forms an important ingredient to the polarized radiative transfer problem.

The scalar frequency-coherent redistribution function, commonly referred to as type-II redistribution function, $r_{II}(\xi, \xi')$ for a two-level atom in the atomic frame was first introduced by Hummer (1962). It describes the absorption of radiation with frequency ξ' followed by a reemission at the same frequency. If we consider an atomic system with infinitely sharp lower level and radiatively broadened upper level then $r_{II}(\xi, \xi')$ for a two-level atom in the atomic frame is given by

$$r_{II}(\xi, \xi') = \mathcal{L}(\xi)\delta(\xi - \xi'), \tag{1.16}$$

where δ is the Dirac distribution and $\mathcal{L}(\xi)$ is the Lorentzian rest frame absorption profile. Further we consider the same atomic system whose upper level is not only broadened radiatively but also by collisions, then the scalar frequency-incoherent scattering function, referred to as type-III redistribution function, r_{III} in the atomic frame for a two-level atom is given by

$$r_{III}(\xi, \xi') = \mathcal{L}(\xi)\mathcal{L}(\xi'). \tag{1.17}$$

A detailed explanation of the scalar redistribution functions is given in Mihalas (1978). Further studies on scalar redistribution function was also done by Oxenius (1965); Heinzel (1981); Hubený et al. (1983); Hubeny & Cooper (1986); Hubeny & Lites (1995). A more detailed and recent account on the theory of PRD is given in Hubeny & Mihalas (2014). Figure 1.8 gives the schematic representation of the frequency-coherent and incoherent scattering described above.

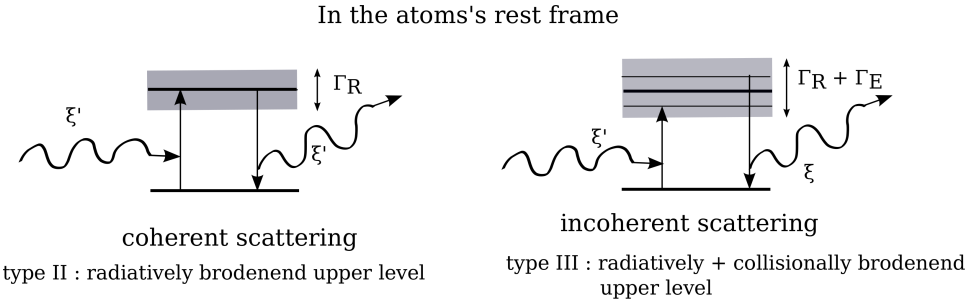

Figure 1.8: Schematic representation of the atomic system considered for coherent and incoherent scattering in the atomic frame. Γ_R and Γ_E represent the radiative and elastic collisional rates of the upper level, respectively.

The expression of r_{II} and r_{III} in the laboratory frame is denoted as R_{II} and R_{III}, respectively and these expressions can be found in Mihalas (1978). The determination of the expression for redistribution function in the laboratory frame involves ac-

counting for thermal motion of the atoms. Two assumptions are made in this process, first that the atomic velocity is unchanged during the scattering process, second that the velocity distribution for the lower level of the transition is a Maxwellian. A more elaborate discussion on these assumptions and the possibility of relaxing them can be found in Hubeny (1985); Landi Degl'Innocenti (1996); Bommier (1999, 2003). The efforts are majorly concentrated on deriving the expression for the redistribution matrix from quantum mechanical calculations, where the scattering occurs between different atomic states. The Rayleigh (or resonance) scattering takes place when the quantum numbers of the initial and final states are the same. The first quantum mechanical derivation of the redistribution matrix taking into account the effects of collisions was given by Omont et al. (1972). Further the effects of magnetic field were included in Omont et al. (1973). Starting from this, Domke & Hubeny (1988) derived a very general expression of the redistribution matrix for scattering of arbitrarily polarized radiation by an atom undergoing collisions. The expression for the redistribution matrix proposed by these authors was extensively used for further studies. Using this expression Faurobert-Scholl (1992) pointed out the sensitivity of the line-wing polarization to the elastic collisional rate. Nagendra (1994) showed how depolarizing collisions affect the line-core polarization. By applying master equation theory, Bommier (1997a) derived a more elegant but equivalent expression of the PRD matrix of Domke & Hubeny (1988) for the non-magnetic case. Further, the explicit form of the laboratory frame PRD matrix in the presence of an arbitrary magnetic field, for the case of a two-level atom without atomic polarization in the lower level was derived in Bommier (1997b).

A classical oscillator theory for frequency-coherent scattering of polarized radiation in the presence of magnetic fields was developed by Stenflo (1994, 1997, 1998). The theory developed by Stenflo (1998) is based on a semi-classical approach using the Kramers-Heisenberg dispersion formula. The Kramers-Heisenberg formula gives differential cross-section for scattering of a photon by an atomic electron. This approach has formed the basis for many studies developed later. More details of the Kramers-Heisenberg approach can also be found in the Part III of the present thesis where we use the same approach to handle the problem of lower-level polarization (LLP) with PRD. Also theory proposed by Stenflo (1998) was further extended for the particular case of a normal Zeeman triplet in the atomic rest frame by Bommier & Stenflo (1999) to handle PRD effects. This theory was developed for the special case of J^* = 0 $\rightarrow$ 1 $\rightarrow$ 0 scattering transition. The corresponding laboratory frame redistribution matrices were derived in Sampoorna et al. (2007a). In Sampoorna et al. (2007b) an equivalence between the quantum electrodynamic approach (Bommier, 1997b) and the classical oscillator theory (based on Bommier & Stenflo,

[*] J being the total angular momentum quantum number

1999) was shown for the particular case of $J = 0 \rightarrow 1 \rightarrow 0$ scattering transition. The theory given in Sampoorna et al. (2007a) for the special case of $J = 0 \rightarrow 1 \rightarrow 0$ transition was extended phenomenologicaly in Sampoorna (2011a) to the general case of $J_a \rightarrow J_b \rightarrow J_a$ scattering transition, where J_a and J_b are the total angular momentum quantum numbers of the lower and upper levels respectively. Also Smitha et al. (2011b, 2013a) used the semi-classical approach to formulate a PRD matrix for the case of two-term atom taking into account the interference between the upper J-states in the linear Zeeman regime (magnetic splitting much smaller than the fine structure splitting). Later Sowmya et al. (2014a) extended this to the arbitrary field strengths (including the Paschen-Back effect regime). The angle-averaged version of this PRD matrix derived in Smitha et al. (2011b) was used in Smitha et al. (2011a) for the non-magnetic polarized radiative transfer. For the case of a two-level atom with hyperfine structure splitting, the non-magnetic PRD matrix was derived by Smitha et al. (2012b) which includes the F-state interference effects. Sowmya et al. (2014b) have derived the PRD matrix for F-state interference in the presence of arbitrary field strengths. Also recently Sowmya et al. (2015) have derived PRD matrix in arbitrary magnetic fields with level-crossings from the combination of hyperfine and fine structure splittings. We refer the reader to review articles on PRD by Hubeny (1985); Frisch (1988, 1996); Frisch et al. (2001); Stenflo (1996b). A detailed review is given in Sampoorna (2008) and more recently by Nagendra (2014, 2015).

We have to note that in all the above mentioned studies a two-level or two-term atomic system with unpolarized lower-level is considered. In Part III of the present thesis we extend the formalism presented in Sampoorna (2011a) to include the effects of the polarization of the lower-level and study its effects on Stokes profiles. To determine the form of the redistribution matrix for scattering polarization both in the presence and absence of magnetic fields is still a subject of research. Further details on the redistribution matrices are given in the next section which describes one of the theoretical approaches developed to handle polarized radiative transfer using the scattering matrix formalism. Redistribution matrix is the fundamental element of this approach.

There were other efforts to handle the complex problem of PRD. The coherent scattering theory based on the concept of metalevels which can account for the polarization of the lower-level was developed by Landi degl'Innocenti et al. (1997). Also a heuristic approach to solve the polarized line transfer equation with PRD in a multi-level atom, without LLP is presented in Sampoorna et al. (2013). More recently a new quantum scattering theory has been proposed by Casini et al. (2014). They derive a generalized redistribution function taking account of polarization of the lower-level.

1.4.2 Redistribution matrix or Scattering matrix formalism

The most natural way to describe PRD effect is by means of a redistribution function and hence the scattering matrix formalism is also referred to as the redistribution matrix formalism. It is a semi-classical approach. The redistribution matrix naturally appears in the scattering approach which can be used to study transfer of line radiation (Stenflo, 1994) basically consisting of polarized differential and integral equations. We describe these equations in this section.

The traditional scattering approach is presented in Mihalas (1978) for the unpolarized case. The extension of this for the polarized case is given in Stenflo (1994); Ivanov et al. (1997). For a detailed list of papers in this field see Nagendra (2003, 2014, 2015) and see also Nagendra & Sampoorna (2009). The polarized radiative transfer equation for a two-level atom with unpolarized lower level in the component form can be written as

$$\mu \frac{\partial I_i}{\partial \tau} = [\varphi(x) + r]\,[I_i(\tau, x, \mathbf{\Omega}) - S_i(\tau, x, \mathbf{\Omega})]\,, \tag{1.18}$$

where $i = 0, 1, 2$ refer to the Stokes parameters (I, Q, U) respectively. The ray direction is given by $\mathbf{\Omega} = (\theta, \chi)$, with $\theta = \cos^{-1}(\mu)$ and χ being the polar angles. x is the frequency in non-dimensional units. The line optical depth is denoted by τ and $\varphi(x)$ is the normalized Voigt function $H(a,\, x)$, where a represents a constant damping parameter. The ratio of continuum to the line absorption coefficient is denoted by r. The positive Q is defined as electric vector parallel to the solar limb. The total source vector is given by

$$S_i(\tau, x, \mathbf{\Omega}) = \frac{\varphi(x)\, S_{l,i}(\tau, x, \mathbf{\Omega}) + r\, S_{c,i}}{\varphi(x) + r}, \tag{1.19}$$

where $S_{c,i}$ are the components of the unpolarized continuum source vector. We assume that $S_{c,0} = B_{\nu_0}$, where B_{ν_0} is the Planck function at the line center, and $S_{c,1} = S_{c,2} = 0$. The line source vector can be written as

$$S_{l,i}(\tau, x, \mathbf{\Omega}) = G_i(\tau) + \int_{-\infty}^{+\infty} \oint \sum_{j=0}^{2} \frac{\hat{R}_{ij}(x, \mathbf{\Omega}, x', \mathbf{\Omega}', \boldsymbol{B})}{\varphi(x)}\, I_j(\tau, x', \mathbf{\Omega}')\, \frac{\mathrm{d}\Omega'}{4\pi}\, \mathrm{d}x', \tag{1.20}$$

where $\mathbf{\Omega}'$ (θ', χ') is the direction of the incoming ray defined with respect to the atmospheric normal. The solid angle element $\mathrm{d}\Omega' = \sin\theta'\, \mathrm{d}\theta'\, \mathrm{d}\chi'$ where $\theta' \in [0, \pi]$ and $\chi' \in [0, 2\pi]$. The primary source is assumed to be unpolarized, so that $G_0(\tau) = \epsilon B_{\nu_0}$ and $G_1(\tau) = G_2(\tau) = 0$. Here, $\hat{R}_{ij}(x, \mathbf{\Omega}, x', \mathbf{\Omega}', \boldsymbol{B})$ is the Hanle redistribution matrix with angle-dependent PRD, and $\boldsymbol{B}$ represents an oriented vector magnetic

field. The thermalization parameter $\epsilon = \Gamma_I/(\Gamma_R + \Gamma_I)$, with Γ_I and Γ_R being the inelastic collisional de-excitation rate and the radiative de-excitation rate, respectively. The Stokes intensity and source vectors can be decomposed using the irreducible spherical tensors $\mathcal{T}^K_Q(i, \mathbf{\Omega})$ (with $K = 0, 1, 2$ being the multipolar index of the radiation, and $-K \leqslant Q \leqslant +K$) introduced by Landi Degl'Innocenti (1984, also see Landi Degl'Innocenti & Landolfi 2004). For the particular case of angle-averaged PRD matrix and 1D planar geometry, this type of decomposition allows the source vector to become independent of the angles (θ, χ) and the specific intensity to become independent of the azimuthal angle χ of the radiation field, leading to simplification of the problem. Such a useful decomposition technique was given by Frisch (2007) based on the decomposition of the polarization phase matrix in terms of the irreducible spherical tensors.

From Equation (1.20) it is clear how the PRD effects can easily be accounted for in the scattering formalism through the $\hat{R}_{ij}(x, \mathbf{\Omega}, x', \mathbf{\Omega}', \boldsymbol{B})$. This is one of the main advantages of the scattering formalism. PRD effects in radiative transfer were first accounted by Dumont et al. (1977) who considered only the case of pure Doppler redistribution in the line core. The computations involving the combined PRD effects at both the line core and wings were done by Rees & Saliba (1982). Also in this paper a very convenient approximation called the 'hybrid approximation' was introduced. According to this approximation, the non-magnetic PRD matrix can be written as

$$\boldsymbol{R}(x, \mathbf{\Omega}, x', \mathbf{\Omega}') = R(x, \mathbf{\Omega}, x', \mathbf{\Omega}')\boldsymbol{P}_R(\mathbf{\Omega}, \mathbf{\Omega}'), \tag{1.21}$$

where full decoupling of the frequency redistribution $R(x, \mathbf{\Omega}, x', \mathbf{\Omega}')$, and the polarization - represented by the angular phase matrix $\boldsymbol{P}_R(\mathbf{\Omega}, \mathbf{\Omega}')$, is assumed. $\boldsymbol{P}_R(\mathbf{\Omega}, \mathbf{\Omega}')$ is nothing but the Rayleigh phase matrix given in Chandrasekhar (1950). Because of the computational complexities involved in the radiative transfer problem, the frequency redistribution function is often angle-averaged independent of the phase matrix. This reduces the computer CPU requirements and the PRD matrix can thus be written as

$$\boldsymbol{R}(x, \mathbf{\Omega}, x', \mathbf{\Omega}') = R(x, x')\boldsymbol{P}_R(\mathbf{\Omega}, \mathbf{\Omega}'), \tag{1.22}$$

This technique was suggested in Rees & Saliba (1982) where they used it to solve the non-magnetic 1D polarized transfer equation. It was also used in other non-magnetic studies by Faurobert (1987, 1988); Nagendra (1988, 1994); Paletou & Faurobert-Scholl (1997); Sampoorna et al. (2010); Sampoorna & Trujillo Bueno (2010); Anusha et al. (2010); Sowmya et al. (2012); Nagendra & Sampoorna (2012). A similar angle-average approximation is also used in the computations of polarized radiative transfer solution in the presence of magnetic fields, by Faurobert-Scholl (1991); Nagendra et al. (1999); Faurobert-Scholl et al. (1999); Fluri et al. (2003);

Nagendra et al. (2002); Sampoorna et al. (2008a); Anusha et al. (2011). Though the angle-average approximation is valid for intensity computations, it is definitely questionable for the computations of the linear polarization profiles. This is because as discussed in the previous sections of this chapter, the linear polarization is directly controlled by the anisotropy of the incident radiation field.

There are many studies in the literature to test the angle-average approximation. Dumont et al. (1977) undertook the preliminary studies of the polarized line transfer using angle-dependent PRD. Following this there were studies by McKenna (1985); Faurobert (1987, 1988) for the case of resonance lines. The case of Hanle effect with angle-dependent PRD was considered by Nagendra et al. (2002). The main challenge involved in the angle-dependent PRD computations is the use of effective numerical techniques. All the above authors used numerical methods which were computationally expensive. Frisch (2009, 2010) proposed decomposition techniques to solve angle-dependent PRD problems which reduce the computational cost needed to handle such PRD problems. Efficient numerical methods were developed using this decomposition technique by Sampoorna et al. (2011); Sampoorna (2011b); Nagendra & Sampoorna (2011) to solve polarized radiative transfer problem both in the presence and absence of magnetic fields. This decomposition technique is also applied in the studies presented in Part II of the present thesis to solve the angle-dependent polarized radiative transfer problems for different cases. We have extended the numerical methods developed in the above mentioned papers for the problem at hand. Also a detailed review of the angle-dependent PRD studies is given in Sampoorna (2014). We want to recall here that all the above mentioned studies are for the case of a two-level atom with unpolarized, infinitely sharp lower atomic level. This is often considered as one of the drawback or limitation of the scattering matrix approach. We address this issue in Part III of the present thesis. As a first attempt we derive the type II redistribution matrix for a magnetic case taking account of PRD and population imbalances in the lower atomic level. However the information about the lower level population imbalances can be obtained only by solving the statistical equilibrium equations (SEEs) of the different atomic levels involved in the transition. SEEs can be effectively handled using another established formalism to solve the polarized radiative transfer problem called the “density matrix formalism". The details of this formalism is described in the next section.

1.4.3 Density matrix formalism

The other important theoretical formulation to study the problem of polarized radiative transfer is the one developed by Landi Degl’Innocenti (1983) within the framework of the density-matrix formalism. It is a self-consistent theoretical approach de-

veloped starting from the basic principles of quantum electrodynamics. A clear and detailed derivation of this theoretical scheme can be found in Landi Degl'Innocenti & Landolfi (2004). We recall briefly a few equations given in Landi Degl'Innocenti & Landolfi (2004) in this section. As described in the previous section the radiative transfer equation plays the central role in the scattering matrix approach. In the density matrix approach it is the SEEs which are coupled to the radiative transfer equation that guide the behavior of the polarized radiation. The main advantage of the quantum theory for scattering polarization is its ability to account for the atomic polarization of all the levels in the model atom considered. The atomic polarization represents the presence of population imbalances and/or quantum interferences (coherences) between pairs of magnetic sublevels. The formulation of the SEEs to determine the atomic polarization in the quantum mechanical framework was proposed by Bommier & Sahal-Brechot (1978) and Bommier (1980) through the density operator. This is a very powerful tool to describe any physical system that is in a statistical mixture of states which is defined as

$$\hat{\rho} = \sum_{\alpha} p_{\alpha} \mid \psi_{\alpha}\rangle\langle\psi_{\alpha} \mid, \tag{1.23}$$

where p_{α} is the probability of finding the system in the pure state $\mid \psi_{\alpha}\rangle$. The density matrix elements contain all the information about the system. Landi Degl'Innocenti (1983) with further advancement of the density matrix formalism described the generation and transfer of polarized radiation self consistently for a multi-level atomic system in the presence of arbitrary field strength. It is shown in Landi Degl'Innocenti & Landolfi (2004) that the diagonal terms of the density matrix represent the populations in the magnetic sublevels, and the off-diagonal terms represent the quantum interferences between different magnetic sublevels.

The derivation of the SEEs and the transfer equation involves the same starting point i.e., the equation describing the time evolution of the expectation value of a given dynamical variable $O(t)$ with the corresponding quantum operator $\hat{O}(t)$. In particular, if we replace $O(t)$ and $\hat{O}(t)$ by the density matrix elements associated to the atomic system, and the corresponding quantum operator (projection operator), then we obtain the SEEs for the density matrix. Instead if we replace $O(t)$ and $\hat{O}(t)$ by individual polarization tensor ($\boldsymbol{J}^{\dagger}\boldsymbol{J}$) describing the radiation field and corresponding quantum operator (number operator) then we obtain the radiative transfer equations. In this way we obtain the self consistent SEEs and the transfer equation in the quantum mechanical framework. However in the simplification of the time evolution equation for SEEs there is an assumption made that the process of emission and absorption are independent. This assumption is also known as Markovian approximation implying that the radiation field illuminating the atom is spectrally

flat (i.e. independent of frequency). Thus we obtain the SEEs in which different rates (transfer and relaxation rates) that appear are dependent on the local properties of the radiation field illuminating the atom. Within the same theoretical framework we also obtain the polarized radiative transfer equation which contains the absorption and emission coefficients which depend on the local values of the density matrix elements. This coupled set of equations has to be solved to obtain the solution of the radiative transfer problem (referred to as the NLTE problem of second kind in Landi Degl'Innocenti & Landolfi, 2004). A schematic representation of the simultaneous solution is shown in Figure 1.9 (taken from Landi Degl'Innocenti & Landolfi, 2004). Efficient numerical methods to handle this problem was developed by Trujillo Bueno & Manso Sainz (1999).

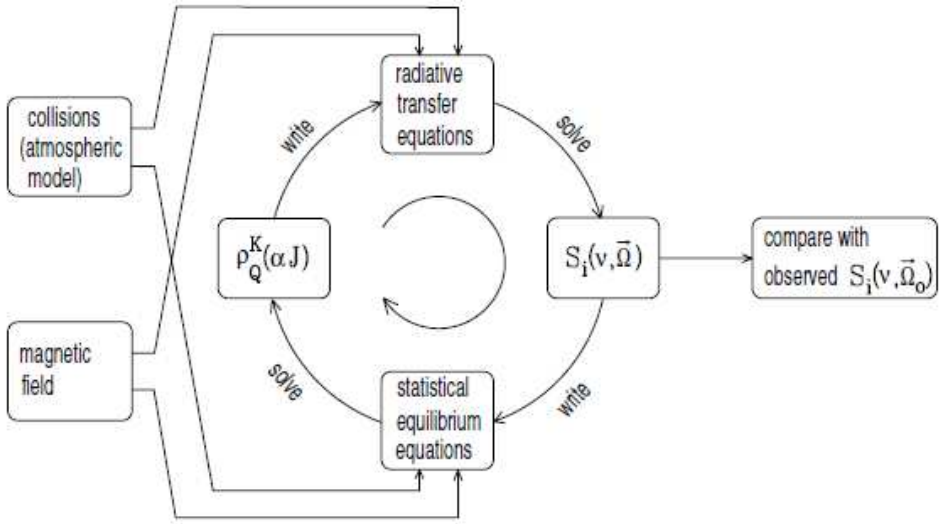

Figure 1.9: Schematic representation of the NLTE problem of the second kind which is solved iteratively. This Figure is taken from Landi Degl'Innocenti & Landolfi (2004).

The main advantage of the self consistent density matrix formalism is that it allows the possibility of taking LLP into account. The general assumption of considering the lower atomic level to be unpolarized is valid when the lower atomic level involved in the scattering transition is 0 or $1/2$ and is definitely questionable otherwise. The importance of LLP was first highlighted in the theoretical studies by Trujillo Bueno & Landi Degl'Innocenti (1997) using the density matrix formalism. They considered the case of transition between $J_a = 1$ and $J_b = 0$. This case is of particular interest because if the polarization of the lower-level is not taken into account then the resulting polarization is zero (since the upper level corresponds to $J_b = 0$). Following this, Landi degl'Innocenti (1998) attempted to explain the linear polarization peaks of the Na I D_1 and D_2 lines using the theory of optical depopulation pumping of the lower level. The theory of density matrix formalism with LLP was applied to the modeling of Mg I b_2 line in Trujillo Bueno (1999). In the same pa-

per the importance of the depolarizing elastic collisions and their role in decreasing the alignment of the atomic levels (see also Trujillo Bueno, 2001; Casini et al., 2002) was shown. The operation of the ground-level Hanle effect and importance of the selective absorption from the ground level to the generation of the polarization in the He I triplet system was demonstarted in Trujillo Bueno et al. (2002). Manso Sainz & Trujillo Bueno (2003b, 2010) presented the importance of atomic polarization of the metastable levels of the Ca II infrared triplet. The challenge of including the LLP also manifests in the radiative transfer computations. This is because the consideration of the lower-level atomic polarization leads to a coupled system of non-linear transfer equations, even for the simplest case of a two-level atom. The details of this can be found in Appendix C of the present thesis.

Though the density matrix formalism is successful, it suffers from the main limitation that it cannot account for the PRD effects. This limitation arises because of the Markovian approximation made in obtaining the SEEs and radiative transfer equation self consistently. There are numerous studies in the literature highlighting the importance of PRD specifically in the wings of the strong resonance lines (Nagendra, 2003, also refer to the previous sections). In this regard there were attempts by Landi degl'Innocenti et al. (1997) to formulate a theory for coherent scattering taking account of LLP based on the concept of metalevels. Recently Belluzzi et al. (2015) derived the type II redistribution matrix for a two term atom with hyperfine structure splitting in the non-magnetic regime by including the polarizability of the lower hyperfine levels (F levels). But in their studies they considered the contribution from LLP as a free parameter. Also a new quantum scattering theory is proposed by Casini et al. (2014) in which they present a generalized redistribution function considering the effects of LLP.

Thus we have two well established theoretical methods to study polarized radiative transfer. The first one is the scattering matrix formalism which can successfully account for the PRD effects but not the effects of LLP and the second one is the density matrix formalism which is self consistent and can account for LLP but not for PRD. This points towards the need to develop an intermediate theory which can exploit the strengths of both the scattering matrix formalism and the density matrix formalism. Our aim is towards this in Part III of the present thesis. We have derived the collisionless redistribution matrix using the scattering matrix formalism and including the contribution from the population imbalances of the lower atomic level. The information about the population imbalances of the lower atomic level is further obtained using the density matrix formalism. In the next section we describe different numerical schemes developed so far to handle the polarized radiative transfer problem.

1.5 Numerical methods to solve polarized radiative transfer problems

One of the earliest attempts to solve the polarized radiative transfer problem with CRD for non-magnetic resonance scattering was by Stenflo & Stenholm (1976). They used Rybicki's core saturation method and treated Stokes Q as a perturbation to the Stokes I. Then the studies involving the comparison of line profiles obtained with CRD and PRD were done by McKenna (1984). The next important step was by Rees & Saliba (1982) who introduced hybrid approximation and also used differential equation based scalar Feautrier method to solve the polarized radiative transfer problem with angle-averaged PRD functions of Hummer (1962). Further Dumont et al. (1977) and Faurobert (1987) used Feautrier method to solve this vector transfer problem with angle-dependent PRD functions of Hummer (1962). While McKenna (1984) used perturbative Feautrier method, Faurobert (1987, also see Faurobert 1988) used non-perturbative Feautrier method. There was another exact method developed around this time called the Discrete Space Method by Nagendra (1988, see also Nagendra 1989, 1994, 1995). The above mentioned exact methods are accurate and general. They can handle PRD problems of any level of complexity. But the main disadvantage of these methods is that they are computationally expensive requiring large computer memory and CPU time.

To overcome this, another method was developed called the Polarized Approximate Lambda Iteration (PALI) method which is based on operator perturbation. The PALI method was developed for both density matrix formalism and scattering matrix formalism. The PALI methods were generalizations of the scalar Approximate Lambda Iteration (ALI) method developed by Olson et al. (1986) to include polarization. A detailed review of unpolarized ALI methods is given in Hubeny (1992) and Hubeny & Mihalas (2014). The development of PALI method for the density matrix formalism is given in Trujillo Bueno & Landi Degl'Innocenti (1996); Trujillo Bueno & Manso Sainz (1999); Manso Sainz & Trujillo-Bueno (1999); Manso Sainz & Trujillo Bueno (2003a). A detailed review of all these methods can be found in Trujillo Bueno (2003). The development of PALI method for the scattering matrix formalism was through a series of papers. The PALI-1 was developed by Faurobert-Scholl et al. (1997) for the case of resonance line scattering with CRD. Then this was extended to include the effects of PRD by Paletou & Faurobert-Scholl (1997) which is nothing but the PALI-2 method. The PALI-3 was developed by Nagendra et al. (1998) for the Hanle effect with CRD. The 1D domain based PRD was included in Nagendra et al. (1999) which is the fourth in the series of PALI method development (PALI-4) and was extended in Nagendra et al. (2000) for solar weak

magnetic field diagnostics (PALI-5). Fluri et al. (2003) extended further to include the 2D frequency domain logic of Bommier (1997a,b) for the weak magnetic field case (PALI-6). In all the PALI methods a Fourier decomposition of the radiation field and of the phase matrix with respect to the azimuth angle are used which in turn reduce the complexity of the problem. A PALI method for non-domain based Hanle PRD problem was presented in Sampoorna et al. (2008b). This may be referred to as PALI-7 method which uses the frequency decomposition technique of Frisch (2007). A detailed review of PALI methods can be found in Nagendra (2003); Nagendra & Sampoorna (2009); Nagendra (2014).

The other important numerical approach developed is the scattering expansion method (SEM). This method is based on the Neumann series expansion of the components of the source vector contributing to the polarization. SEM was first formulated by Frisch et al. (2009) for solving the polarized line transfer with CRD. This method is now extended to solve transfer problem with PRD by Sampoorna et al. (2011); Nagendra & Sampoorna (2011); Sowmya et al. (2012); Smitha et al. (2012b). In all these studies it is shown that the SEM is faster than the PALI method and is very efficient while handling angle-dependent PRD problems. In the present thesis we have used both the PALI and SEM for our studies. A recent review by Nagendra (2014) gives very elaborate explanation of both the PALI and SEM. The development of powerful numerical methods to solve polarized PRD line transfer problems in multi-dimensional atmospheres is reviewed in Anusha & Nagendra (2014, see also Anusha & Nagendra 2013 and references therein).

1.6 Outline of the thesis

The present thesis is concentrated on two important aspects of studies concerning polarized radiative transfer. The first is the studies about observations and modeling of SSS which will help us understand the solar atmosphere in a better way. The second is the studies concerning basic tool required to study the polarized radiation i.e. redistribution matrix. These studies are presented as three parts in the thesis.

The Part I of the thesis (Chapter 2) is dedicated to the CLV observations and modeling of the Ca I 4227 Å line. The observational details concerning CLV of the Ca I 4227 Å line is presented in this chapter. Also the challenges and procedure followed to undertake simultaneous CLV modeling of the intensity and linear polarization spectra are described. At the end we describe a solar model atmosphere independent analysis to obtain an estimate of the depth dependence of the turbulent weak magnetic fields in the solar atmosphere.

The Part II of the thesis is dedicated to a series of studies concerning angle-dependent PRD problems. In this part of the thesis we consider different problems

and study the impact of using angle-dependent PRD on emergent Stokes profiles in each of those cases. In Chapter 3 we consider the problem of studying the effect of electron scattering redistribution on atomic line polarization in the non-magnetic regime. For our studies we have considered angle-dependent atomic redistribution and non-coherent electron scattering. We have proposed new and efficient numerical methods based on PALI and SEM to handle this problem. In this chapter we also present a set of parametric studies to understand the effects of electron scattering in a better way. In Chapter 4 we study the combined effects of angle-dependent PRD and the quantum interference phenomena arising either between the fine structure (J) states of a two-term atom or between the hyperfine structure (F) states of a two-level atom. We consider collisionless line scattering on atoms in the non-magnetic regime for our studies. We propose SEM to solve this problem and finally compare the emergent Stokes profiles obtained when angle-averaged and angle-dependent PRD functions are used. In Chapter 5 our concentration is on the effects of angle-dependent PRD matrix in the presence of weak magnetic fields (Hanle effect). We propose efficient decomposition technique, and the numerical method to solve this problem. We adopt proper methodology to incorporate frequency domain logic of Bommier (1997a,b) to solve angle dependent Hanle transfer problem. We finally consider different examples of micro-turbulent and vertical magnetic fields to establish the efficiency of our proposed method compared to the previous approximate methods.

In the last part of the thesis (Chapter 6) we address another important problem concerning the development of a polarized radiative transfer theory including the effects of LLP and PRD. In this chapter we first derive the collisionless redistribution matrix including the effects of LLP and PRD for a general magnetic case. Then we appropriately obtain the different elements of the radiative transfer equation for the problem at hand starting from the quantum field theory of Stenflo (1994). We finally use the derived collisionless redistribution matrix in the non-magnetic regime (Appendix A) to numerically solve the radiative transfer equation and study the combined effects of LLP and PRD. Based on the results we obtained we also propose a simpler numerical method to solve this problem. Appendix A describes the type II redistribution matrix with LLP for the non-magnetic case. Appendix B describes the validation of the absorption matrix elements obtained from quantum field theory of Stenflo (1994). Finally Appendix C gives the details of the numerical method we have followed to solve the problem of polarized radiative transfer with LLP and PRD. The Summary and future prospects are described in Chapter 7.

Part I

One dimensional modeling of the center-to-limb observations

Chapter 2

Modeling the center-to-limb observations of the Ca I 4227 Å line*

An Overview

The observed center-to-limb variation (CLV) of the scattering polarization in different lines of the Second Solar Spectrum (SSS) can be used to constrain the height variation of various atmospheric parameters, in particular the magnetic fields via the Hanle effect. In this chapter we explain our attempt to model the nonmagnetic CLV observations of the Q/I profiles of the Ca I 4227 Å line recorded with the Zurich Imaging Polarimeter-3 at Istituto Ricerche Solari Locarno (IRSOL). For modeling, we use the polarized radiative transfer (RT) with partial frequency redistribution (PRD) with a number of realistic one-dimensional (1D) model atmospheres. We find that all the standard Fontenla-Avrett-Loeser (FAL) model atmospheres, which we used, fail to simultaneously fit the observed $(I, Q/I)$ at all the limb distances (μ). However, an attempt is made to find a single model which can provide a fit to at least the CLV of the observed Q/I instead of a simultaneous fit to the $(I, Q/I)$ at all μ. To this end we construct a new 1D model by combining two of the standard models after modifying their temperature structures in the appropriate height ranges. This new combined model closely reproduces the observed Q/I at all μ but fails to reproduce the observed rest intensity at different μ. Hence we find that no single 1D model atmosphere succeeds in providing a good representation of the real Sun. This failure of 1D modeling approach can probably be overcome by using multi-dimensional modeling which is computationally expensive. To eliminate an even wider choice of 1D models, we also attempted to simultaneously model the CLV of the $(I, Q/I)$ spectra using the Fontenla-Curdt-Haberreiter-Harder-Tian (FCHHT) solar model atmospheres which are updated and recent versions of the FAL models.

*The contents of this chapter are based on Supriya et al. (2014b, 2015)

However these models also failed to provide a simultaneous fit to the $(I, Q/I)$ at all μ. This failure of 1D models does not however, cause an impediment to the magnetic field diagnostic potential of the Ca I 4227 Å line. To demonstrate this we deduce the field strength at various μ positions without invoking the use of RT.

2.1 Introduction

One of the commonly observed and well-studied lines in the SSS is the strong, chromospheric Ca I 4227 Å line (see, e.g., Stenflo et al., 1980; Stenflo, 1982; Gandorfer, 2002). This is a normal Zeeman triplet line arising due to the transition between the atomic states with total angular momentum $J = 0 \rightarrow 1 \rightarrow 0$. It exhibits the largest scattering polarization among all the lines in the Sun's visible spectrum (Stenflo et al., 1980). The core of the Ca I 4227 Å line is formed around a height of about 1000 km above the photosphere, making it chromospheric in nature. The Hanle effect in the core of the Ca I 4227 Å line was first observed by Stenflo (1982). Further details on the various observational and modeling efforts of this line is described in Section 1.3 of Chapter 1.

To better understand the physics of scattering and to exploit it for various diagnostic purposes, we need to systematically study the CLV of the SSS. This will help us sample the height information of the atmospheric parameters and magnetic fields, as observations made at different lines of sight sample different heights in the solar atmosphere. A few attempts have been made so far in detailed modeling of the CLV observations of $(I, Q/I)$ spectra of atomic and molecular lines in the SSS. The most challenging aspect of such CLV modeling is to find a single model atmosphere which can fit both I and Q/I at all limb distances μ $(= \cos\theta)$ simultaneously. One such attempt was made by Holzreuter & Stenflo (2007a) to model CLV of the Ca II K line. They discuss the possibility of constructing a two-component atmospheric model (using a combination of a hot and a cool atmospheric component) to achieve a fit to the observed CLV profiles. A height-dependent mixing ratio was required in order to simultaneously fit the I and Q/I spectra at all limb distances. The authors also demonstrate that a single atmospheric model with optimized temperature structure can be used to achieve a fit to the Ca II K line CLV data. However, the authors find that different extents of modification in the temperature structure are required for different limb distances. Another paper in which such CLV studies have been done is that of Shapiro et al. (2011) who consider the molecular CN violet system. They discuss the general problems involved in obtaining a simultaneous fit to the I and Q/I profiles using the standard 1D single atmospheric model as well as two-component atmospheric models. They finally construct an anisotropy-modified single 1D atmospheric model to simultaneously fit I and Q/I at all μ.

The CLV of the Ca I 4227 Å line away from the active regions was first observed by Stenflo et al. (1980) and analyzed by Auer et al. (1980). The CLV of the line center polarization observed by Stenflo et al. (1980) was later used by Faurobert-Scholl (1994) to study the Hanle effect due to the magnetic field canopies in the chromosphere. The CLV observations of this line were also done by Bianda et al. (1998, 1999). In this chapter we attempt a detailed simultaneous modeling of the observed CLV of both I and Q/I profiles of the Ca I 4227 Å line. For this purpose we solve the polarized RT equation by taking account of PRD effects in the non-magnetic regime. Standard 1D atmospheric FAL models (Fontenla et al., 1993; Avrett, 1995) are used to obtain a fit to the $(I, Q/I)$ spectra. We find that it is not possible to achieve a simultaneous $(I, Q/I)$ fit to the CLV observations with a single 1D model atmosphere. If we consider the CLV of Q/I alone, then we find it necessary to modify the original temperature structure of the standard FAL atmospheric models to obtain a fit. Such modifications of the original temperature structure were also used in previous works by Holzreuter & Stenflo (2007a); Smitha et al. (2012a, 2013b). In the present chapter, the original temperature structure of the standard FAL-A atmosphere is modified. Later, the modified FAL-A ($\overline{\mathrm{FALA}}$) is combined with FAL-X atmospheric model to construct a single component model. It turns out that this newly constructed combined model can closely reproduce the observed Q/I at different limb distances. The combined model though provides a fit to the observed CLV of the Q/I, it fails to fit the CLV of the rest intensity and of the continuum intensity. This suggests that the next step would be to use the multi-dimensional modeling, which is computationally expensive. Before arriving at this conclusion we also tried simultaneously modeling the CLV of the $(I, Q/I)$ spectra using the FCHHT (Fontenla et al., 2009) solar 1D model atmospheres. We expect that these kind of studies will help us to eliminate or justify the 1D modeling approach before proceeding towards multi-dimensional modeling.

In Section 2.2 we give the details of the CLV observations. Section 2.3 is devoted to the modeling procedure and the results obtained using FAL model atmospheres. Section 2.4 gives the details of the results obtained using FCHHT model atmospheres. Section 2.5 explains why a two-component modeling approach cannot be used in the present case. Section 2.6 describes the observational analysis to determine the depth dependence of magnetic fields. Concluding remarks are given in Section 2.7.

2.2 Observational details

The CLV observations of the Ca I 4227 Å line presented in this chapter were obtained with the Zurich Imaging Polarimeter-3 (Ramelli et al., 2010) at IRSOL in Switzer-

land on 2012 October 16. The observations were taken at 14 different μ positions (0.10, 0.15, 0.20, 0.25, 0.30, 0.35, 0.40, 0.45, 0.50, 0.60, 0.70, 0.80, 0.90 and 1.0), starting from the heliographic north pole at $\mu = 0.1$ up to the disk center at $\mu = 1$. Figure 2.1 shows the CCD images of the Ca I 4227 Å line at five selected positions on the solar disk. The polarization modulation was done with a piezo-elastic modulator. The spectrograph slit was 60 μm wide, corresponding to a spatial extent of 0.5arcsec on the solar disk. The CCD covered 190arcsec along the slit. The CCD images have 140 effective pixel resolution elements in the spatial direction, with each element corresponding to 1.38arcsec, and 1240 pixels in the wavelength direction, with one pixel corresponding to 5.30 mÅ.

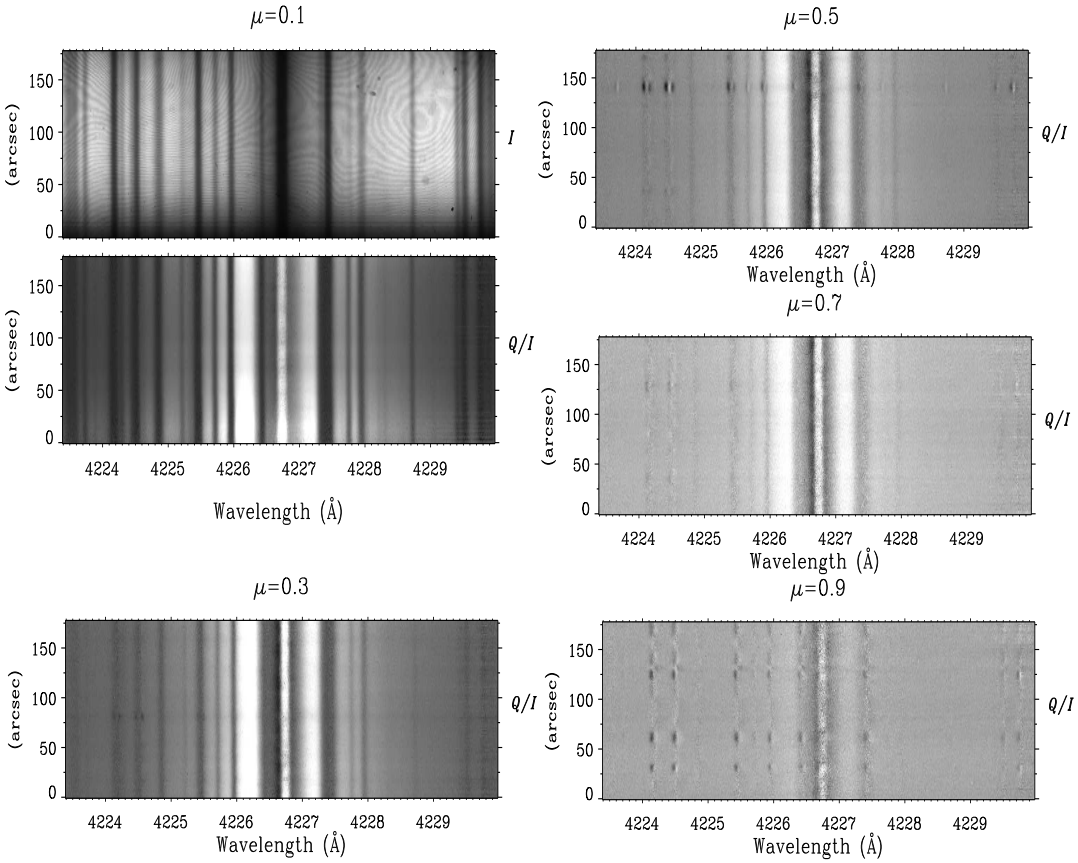

Figure 2.1: CCD images of I (only for $\mu = 0.1$) and Q/I at five selected μ values of the Ca I 4227 Å line. The observations were taken on 2012 October 16 at IRSOL in Switzerland.

To keep the solar image position stable, the primary image guiding system is used (Küveler et al., 2011). In addition, below $\mu = 0.35$ a rotating glass tilt plate is used to keep the distance between the spectrograph slit and the solar limb image under control. The slit jaw image is digitized by a dedicated CCD camera. An algorithm recognizes the solar limb and the spectrograph slit position on the image. This allows the calculated desired distance between the limb and the slit to be set by automatic control of the tilt plate. Note that this plate is set after the polarization analyzer and hence does not introduce spurious polarization signatures. At each μ

position a measurement is obtained by adding 300 single frames, each of which are obtained with an exposure time of 1 sec. Therefore the effective integration time is 8 minutes. The precision of the pointing at a chosen μ position over 8 minutes using the tilt plate is limited to about $1\mathrm{arcsec}$, which is less than the size of 1 pixel.

An improvement of these measurements is related to the absolute precision which we could reach in measuring Q/I. Previously, the zero polarization value needed to be defined manually was based on indirect considerations (e.g., the CLV of the continuum polarization). For the data set described in this chapter we could reach an absolute precision of about 5×10^{-5}. This is mainly due to (1) the precise control of limb distance, allowed by the tilt plate system described above; (2) the improved control of the rotation of the optical devices, including the polarization analyzer in front of the slit (to compensate for the image rotation originated by the Gregory Coudè telescope); and (3) the optical compensation of the instrumental linear polarization, which is a source of variable offset effects, with an oriented glass plate set in front of the polarization analyzer. It was thus possible to subtract the polarization level measured at disk center in a quiet region from every measurement done at a defined μ position. For symmetry reasons the linear polarization in the continuum is expected to be zero at the disk center. In this way all residual instrumental linear polarization signatures are taken into account.

2.2.1 Stray light correction

The observed profiles contain a contribution from the spectrograph stray light which is about 2% of the continuum intensity. Here we correct both the intensity and polarization profiles for stray light. The effect of stray light, including both its intensity and polarization, was treated in Stenflo (1974). Below are the details of the procedure we have followed.

In the absence of stray light but with instrumental polarization (crosstalk from $I(\lambda)$), the $I(\lambda)$ and $Q(\lambda)$ parameters after polarization calibration are $I'(\lambda) = I(\lambda)$ and $Q'(\lambda) = Q(\lambda) + M_{21} I(\lambda)$, if we assume that the Mueller matrix has been normalized ($M_{11} = 1$), there is no telescope depolarization or it has been calibrated away ($M_{22} = 1$), and that polarization crosstalk from U and V can be disregarded. M_{21} is the spectrally flat instrumental polarization, which for convenience will be renamed p_z, since it represents a flat offset of the zero point of the polarization scale.

In the presence of stray light with an intensity that is a fraction s of the continuum intensity I_c and has a polarization p_s, the apparent or observed Stokes parameters are

$$\begin{aligned} I_{obs}(\lambda) &= I(\lambda) + sI_c, \\ Q_{obs}(\lambda) &= Q(\lambda) + p_z(I(\lambda) + sI_c) + p_s sI_c. \end{aligned} \tag{2.1}$$

We now introduce the notation $r(\lambda) = I(\lambda)/I_c$ and $r_{obs}(\lambda) = I_{obs}(\lambda)/I_{obs,c}$ for the rest intensities. For clarity we attach a λ to the quantities that are spectrally structured, in contrast to the three free parameters of our problem, namely, s, p_s, and p_z, which are constant and spectrally flat. Then

$$r(\lambda) = (1+s)r_{obs}(\lambda) - s. \tag{2.2}$$

Similarly, we define the intrinsic polarization $p(\lambda) = Q(\lambda)/I(\lambda)$ and the apparent polarization $p_{obs}(\lambda) = Q_{obs}(\lambda)/I_{obs}(\lambda)$. One can easily show that

$$p(\lambda) = \left(1 + \frac{s}{r(\lambda)}\right)[p_{obs}(\lambda) - p_z] - \frac{s}{r(\lambda)}p_s. \tag{2.3}$$

To calculate $p(\lambda)$ from the observations we need to insert the expression for $r(\lambda)$ from Equation (2.2) into Equation (2.3).

The intrinsic polarization that contributes to the stray light, as averaged over the wide spectral range, is represented by p_s. Grating ghosts that sample discrete wavelengths spread over a large wavelength range are a major source of spectrograph stray light. In the absence of other information, the best estimate of p_s is probably $p_s \approx p_c$, i.e., to set it equal to the continuum polarization.

The determination of p_z is best made for a disk center recording that is done immediately before or after the measurement at the given μ position (so that one can assume that the instrumental polarization has not changed). At disk center the solar-scattering polarization is zero, so the apparent polarization that we see is simply p_z (in contrast to measurements of disk center, where p_z is mixed with intrinsic solar polarization).

It is important to realize that the problem of correcting for the zero point of the polarization scale is entirely decoupled from the stray light issue. It is the first step to be done, and it gives us the spectrum

$$p'(\lambda) = p_{obs}(\lambda) - p_z, \tag{2.4}$$

which would equal to $p(\lambda)$ in the absence of stray light. To correct $p'(\lambda)$ for stray light we do not need to refer to p_z or disk center observations. The way in which the stray light correction enters can be seen by rewriting Equation (2.3) as

$$p(\lambda) = p'(\lambda) + \frac{s}{r(\lambda)}(p'(\lambda) - p_s). \tag{2.5}$$

If the stray light were unpolarized, then the stray light scaling factor $s/r(\lambda)$, which is large where the rest intensity $r(\lambda)$ is low, acts to amplify the polarization amplitudes $p'(\lambda)$. In the presence of stray light polarization, however, the scaling factor

only acts on the amplitude with respect to the p_s level rather than with respect to the zero level. The stray light polarization therefore reduces the effect of the stray light correction. For polarization amplitudes that is equal to p_s (which represents a broadband polarization background that may be approximated with the continuum polarization level p_c), the stray light correction does not have any effect at all. For the Ca I 4227 Å line, however, the core polarization is usually larger than p_c. In this particular case the stray light polarization becomes a second-order effect (since sp_c is a product of two small quantities). The parameter s is determined exclusively by fitting the Fourier Transform Spectrum of Kurucz et al. (1984), in the same context as the spectral broadening is determined. The above considerations give us a rather well-defined procedure to determine (within the framework of our idealized model) unique estimates of the parameters s, p_z, and p_s. Using these estimates we can correct both the $I(\lambda)$ and $Q(\lambda)/I(\lambda)$ spectra for stray light. In other sections we have dropped the λ dependence of I and Q for notational simplicity. While the observed spectra are corrected for stray light, they have not been corrected for spectral broadening, because the instrumental profile is not known with the precision that is needed to allow a deconvolution. The theoretical spectra, on the other hand, which are used for comparison with the observed spectra, need to be spectrally broadened to emulate the observations. However, one should not apply stray light to the theoretical spectra, since one can easily do the correction to the observed spectra itself. In this way we keep the presentation of the theoretical results independent of the particular properties of the instrument used for the observations, with the single exception of spectral broadening.

2.3 Modeling of the center-to-limb variation observations using FAL model atmospheres

In this section we describe the modeling procedure we have followed to model the CLV of the Ca I 4227 Å line. We started with the aim of finding a single 1D atmosphere model that can simultaneously fit (I, Q/I) CLV of the Ca I 4227 Å line. As a first step towards this, we begin the modeling of the observed profiles by solving the polarized RT equation for a two-level atom. The 1D polarized RT equation along with the other necessary equations in the non-magnetic regime used in this chapter are described in detail elsewhere (see Anusha et al., 2010). The elastic collision rates used in this chapter are computed following the theory presented in Barklem & O'Mara (1997). Additionally, the modeling is done using a two-stage process wherein the intensities are computed using a PRD capable MALI (Multi-level Approximate Lambda Iteration) code of Uitenbroek (2001) in the first stage. In the

second stage, the polarization profiles are computed perturbatively by solving the polarized transfer equation. The details of such a two-stage modeling procedure is described in Holzreuter et al. (2005, see also Anusha et al. 2010). The atom model of the Ca I used in the present chapter is the same as the one discussed in Anusha et al. (2010); hence we do not repeat the details here.

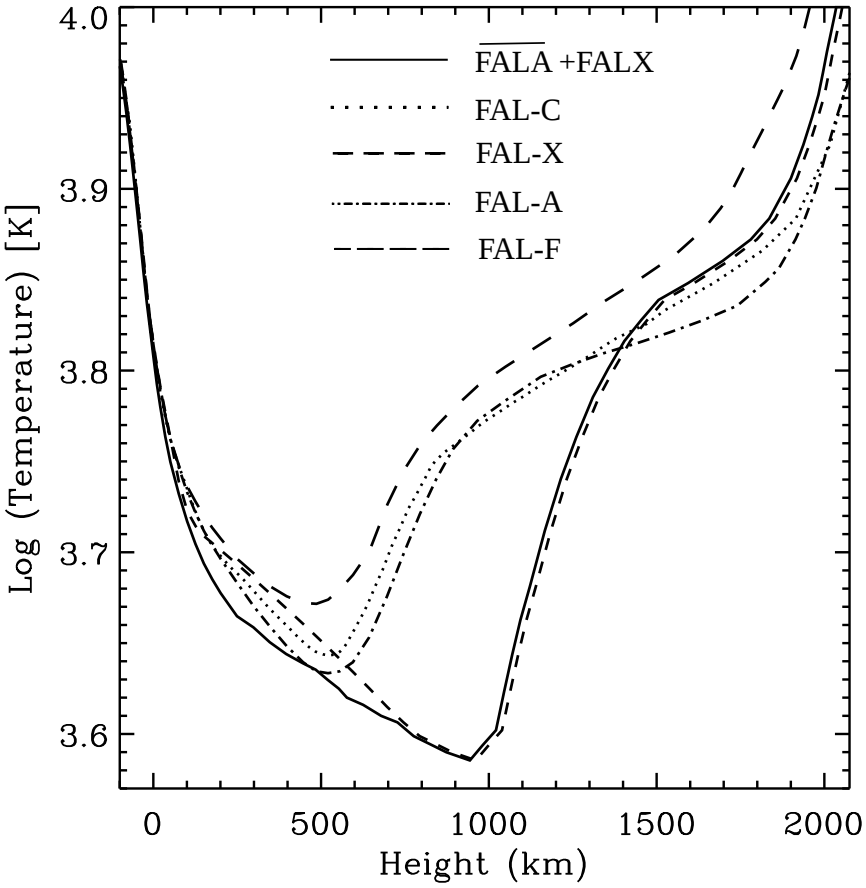

Figure 2.2: Temperature structure of the four standard models, FAL-A, FAL-C, FAL-F, and FAL-X, used in our studies. Along with these standard models the temperature structure of the new model atmosphere $\overline{\mathrm{FALA}} + \mathrm{FALX}$ is also shown.

In our studies we use four standard 1D model atmospheres of the Sun, namely, FAL-A, FAL-C, FAL-F (Fontenla et al., 1993), and FAL-X (Avrett, 1995). The temperature structure of these models are shown in Figure 2.2. Along with the standard models, the temperature structure of our newly constructed model $\overline{\mathrm{FALA}} + \mathrm{FALX}$ is also shown in the figure, details of which will be discussed in Section 2.3.2.

2.3.1 center-to-limb variation behavior at three wavelength positions using FAL model atmospheres

The observed Q/I profiles of the Ca I 4227 Å line show three prominent features: the line center at 4226.7 Å, the blue wing PRD peak at 4226.2 Å and the red wing PRD peak at 4227.1 Å. While the line center of the Ca I 4227 Å line is formed within

a height range of 700–1000 km (covering $0.9 \leqslant \mu \leqslant 0.1$), the blue and red wing PRD peaks are formed at a height of 150–250 km above the level where the vertical continuum optical depth at 5000 Å is unity. To get an idea of the behavior of the polarized spectra as a function of μ, we plot the angular dependence of intensity (only at the line center) and linear polarization at these chosen wavelength positions in Figure 2.3, computed using the standard 1D model atmospheres. As expected, it can be seen from Figure 2.3 that the degree of linear polarization decreases to zero toward the disk center due to symmetry in the scattering geometry.

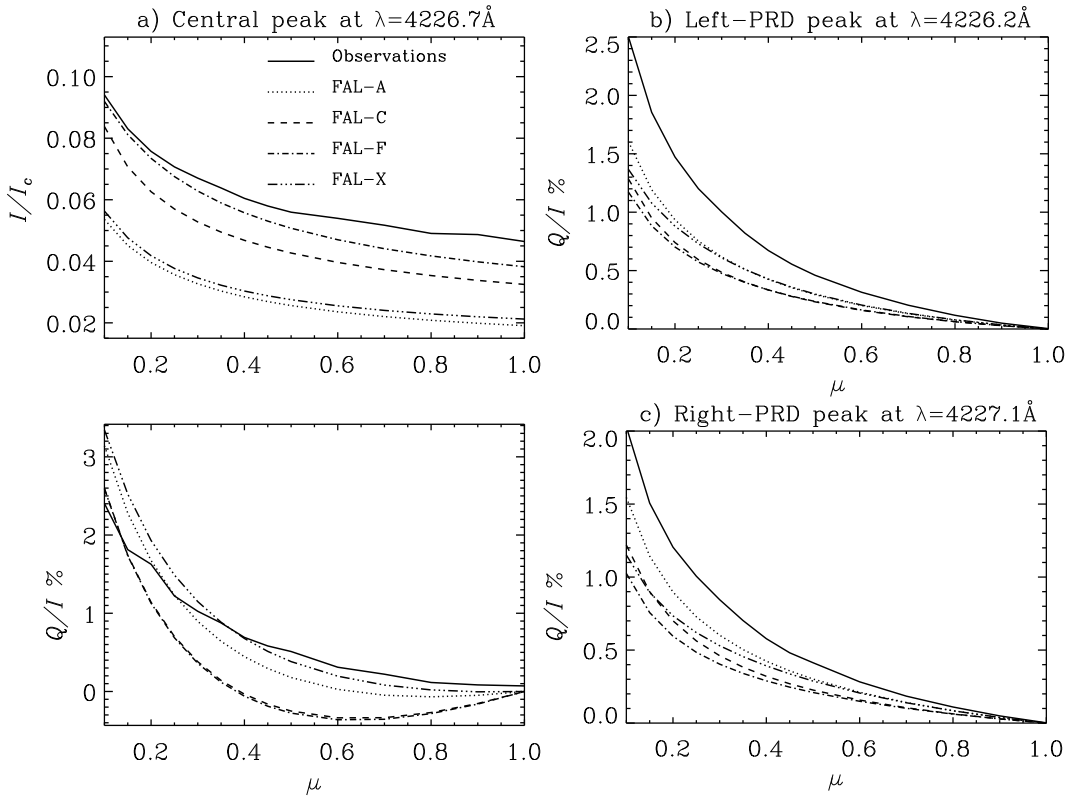

Figure 2.3: Observed (solid line) and calculated intensity and polarization signals as a function of μ (observed at 14 points) at three different wavelength positions in the line profile. The spectra are calculated for the standard models, FAL-X, FAL-C, FAL-A, and FAL-F.

Panels (a) and (b) of Figure 2.3 show a comparison of the observed and theoretical CLV of I and Q/I, respectively, at the line center wavelength. We see that the hottest model FAL-F (dot-dashed line) is more suited for modeling the CLV of the line center intensity. However, the same model is not at all good for Q/I. Instead, it is the coolest model, FAL-X, which provides the closest fit to the observed Q/I. This contrasting behavior seems to point at the fact that we need two different temperatures to simultaneously fit I and Q/I at the line center. From Figure 2.3 (b) we see that the theoretical profile computed using FAL-A also falls close to the observed CLV profile of Q/I. We consider the FAL-X atmosphere rather than FAL-A to provide a better fit to the observed Q/I at the line center for the following reasons: at the

line center and when μ is small, we always expect the non-magnetic Q/I amplitude to be larger as compared with the observed Q/I, because the observed Q/I includes depolarization by magnetic fields. As we go to larger μ, the magnetic fields may enhance the core polarization amplitude. Such behavior was noted by Faurobert-Scholl (1994), who points out that there are enhancement effects due to magnetic fields when $\mu > 0.4$ (this will be discussed in detail in Section 2.3.3). We found the FAL-X model to better satisfy this behavior. Thus we see from Figure 2.3 (b) that the theoretical values of Q/I at the line center when computed with FAL-X are larger than the observed Q/I for $\mu < 0.4$, while FAL-A shows this behavior only for $\mu < 0.25$. Besides this, the theoretical Q/I computed with FAL-A falls much below the observed Q/I as we move toward larger values of μ. For these reasons we consider FAL-X to give a consistent overall fit to the observed CLV of Q/I at the line center, while FAL-A does not.

On the other hand, Figures 2.3 (c) and (d) show the CLV profiles of Q/I at the blue and red wing PRD peak wavelength positions, respectively. We notice that both FAL-F and FAL-X model atmospheres fail to provide a fit to the PRD peaks. It is the theoretical CLV profiles from the FAL-A model that fall closest to the observed CLV of Q/I. Thus we do not find a single 1D atmospheric model which can provide a fit to the entire Stokes (I, Q/I) profiles simultaneously. As a next step we explore the possibility of obtaining a fit to the CLV of the Stokes profiles through a small modification of the temperature structure of the original FAL models at the appropriate heights.

2.3.2 Theoretical fit to the center-to-limb variation of the linear polarization profiles using FAL model atmospheres

From Figures 2.3(c) and (d) we see that although the theoretical profiles from the model FAL-A fall closest to the observed CLV of Q/I, this model fails to provide a satisfactory fit to the Q/I observations. In order to obtain a better fit to the observed CLV of Q/I profiles, we adopt modification of temperature structure at the heights where PRD peaks are formed. We focus our attention only on the fit to the Q/I profiles. Since the FAL-A model atmosphere provides the closest fit to the observed Q/I profiles, we choose this model for further modifications. Accordingly, the temperature of the FAL-A standard model at these heights is reduced by about 200 K. This newly constructed model is denoted as $\overline{\mathrm{FALA}}$. This new model provides a better fit to the wing PRD peaks at all the limb distances.

After achieving a fit to the PRD peaks, we concentrate on obtaining a fit to the linear polarization at the line center. From Figure 2.3(b) we see that it is the FAL-X model atmosphere which fits the observed profiles the closest. Thus, to obtain a satis-

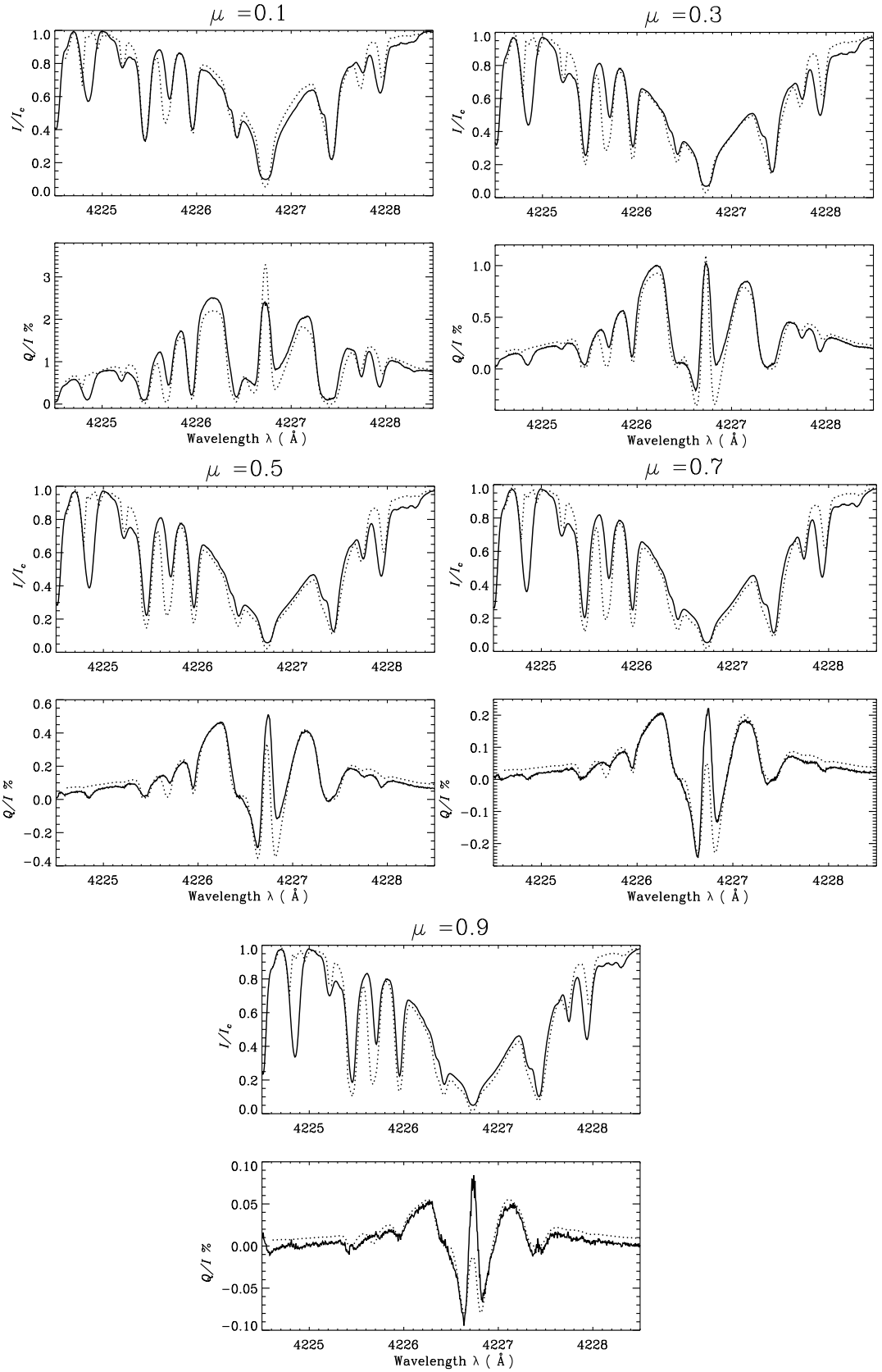

Figure 2.4: Comparison between the observed (solid line) and the theoretical (dotted line) Stokes profiles (I,Q/I) at different limb distances. The combined model atmosphere $\overline{\mathrm{FALA}} + \mathrm{FALX}$ is used to compute the theoretical profiles.

factory fit to the entire Q/I profile we need to combine these two model atmospheres ($\overline{\mathrm{FALA}}$ and FAL-X) at the appropriate heights. The two models are combined such that the new model atmosphere has the temperature structure of $\overline{\mathrm{FALA}}$ up to a height of 400 km and the temperature structure of FAL-X at heights above 400 km. The temperature structure of the new combined model atmosphere ($\overline{\mathrm{FALA}}$ + FALX) is shown as the solid line in Figure 2.2. The results obtained using this combined model atmosphere are discussed below.

2.3.3 Results from the new combined model atmosphere

The theoretical profiles obtained using $\overline{\mathrm{FALA}}+\mathrm{FALX}$ model atmosphere are shown in the Figure 2.4 (dotted line). In addition, a comparison between the observed and theoretical Q/I CLV curves at the blue and red wing PRD peaks and at the line center wavelength using the combined model is shown in Figure 2.5 (dotted line). These theoretical profiles show that we obtain an overall satisfactory fit to the Q/I profiles at all the μ positions using the combined model atmosphere. The theoretical profiles computed using the combined model atmosphere in Figures 2.4 and 2.5 include suitable spectral smearing. This is done by convolving the theoretical spectra with a Gaussian profile having a FWHM of 50 mÅ. The smearing accounts for both the instrumental broadening (40 mÅ) and the broadening by macroturbulent velocity fields (30 mÅ). The macroturbulent smearing corresponds to a velocity of 1.28 km s^{-1}. For deep lines such as the Ca I 4227 Å, the effects of the stray light corrections (the stray light correction procedure is described in Section 2.2.1) are much more important than the smearing. The intensity (I) profiles from the combined model seem to fit the observed data at all the μ positions, with the exception of the line core, where we fail to get a satisfactory fit. At the formation heights of the line center, a rest intensity fit requires a hotter atmospheric model such as the FAL-F, which is not suitable for achieving a good fit to the Q/I profile—which indeed requires cooler models such as the FAL-X. In spite of the carefully determined stray light correction (by s = 2%) to the observed Stokes I profiles, the central line depth still does not come close to reproducing the very deep theoretical I profiles. We have also carried out tests with the use of different microturbulent and macroturbulent velocities, and we found that the choice of turbulent velocity does not significantly affect the rest intensity of the Stokes I profiles.

From Figures 2.4 and 2.5 we notice that for $\mu \leqslant 0.35$ the observed line center Q/I is less than the theoretical value, and for $\mu > 0.35$ it is greater than the Q/I predicted theoretically. Such a discrepancy was also encountered by Faurobert-Scholl (1994) while modeling the CLV of the line center Q/I of the Ca I 4227 Å line. The author found that the ratio of $(Q/I)_{\mathrm{obs}}$ and $(Q/I)_{\mathrm{theory}}$ at the line center was close to

unity for smaller μ values ($\mu < 0.4$) and much greater than one for larger μ values. However, her treatment did not include the stray light corrections. We recall that the observed profiles in Figure 2.5 are corrected for the stray light. In Faurobert-Scholl (1994), although an explanation of the physical mechanism behind this enhancement in polarization for larger μ values was anticipated based on accelerated motions in the chromosphere, it was not completely justified.

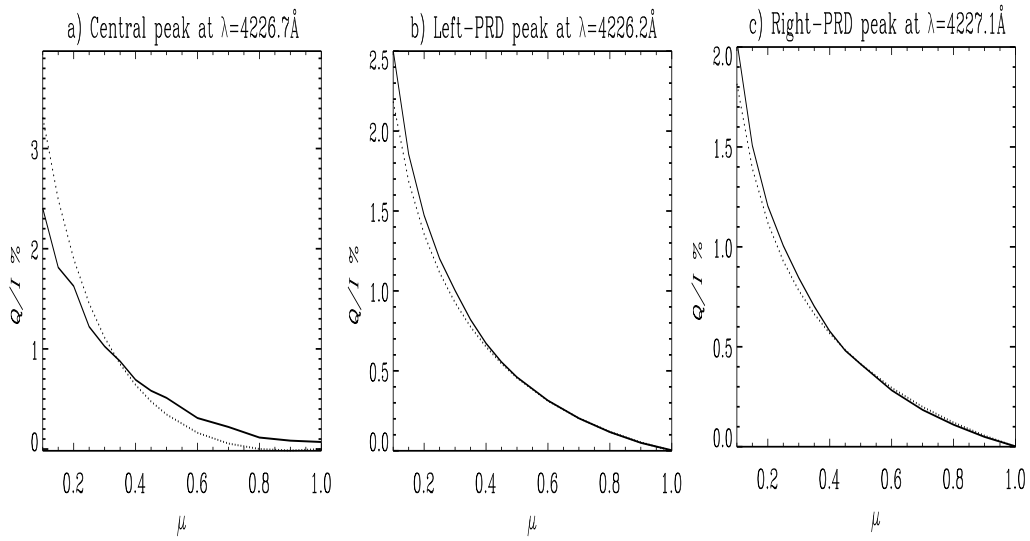

Figure 2.5: CLV of linear polarization at three chosen wavelength positions. The model atmosphere used to obtain the theoretical profiles (dotted line) is the new combined model $\overline{\text{FALA}}$ + FALX.

To examine this discrepancy further, we plot the variation exhibited by Q/I along the spectrograph slit at the line center (solid line) and compare it with the Q/I in the blue wings (dotted line) in Figure 2.6. The observed line center Q/I values are smoothed over a rectangular box corresponding to 5arcsec to reduce contribution from noise. These smoothed values of the observed Q/I at the line center are used for all further computations. From Figure 2.6 we see that the Q/I at the line center shows more variation along the slit than at the blue wing peak. This indicates the presence of varying horizontal magnetic fields and their possible role in modifying the line center Q/I. These varying magnetic fields can in turn be used to understand the observed line center Q/I which are greater than the theoretically predicted values. One possible explanation for this discrepancy could be that observed line center Q/I for $\mu > 0.35$ is enhanced due to the Hanle effect by these varying fields (see also Faurobert-Scholl, 1994). This enhancement is very prominent in case of the near-disk-center observations (see Anusha et al., 2011). However, in our case, it sets in for $\mu > 0.35$ and increases as $\mu \to 1$. This is clear evidence for highly structured, resolved, oriented magnetic fields (predominantly horizontal) in the solar atmosphere. However, the dotted line in Figure 2.6 (for the blue wing) do not exhibit the type of spatial fluctuations that is seen for the line center (solid line). This is be-

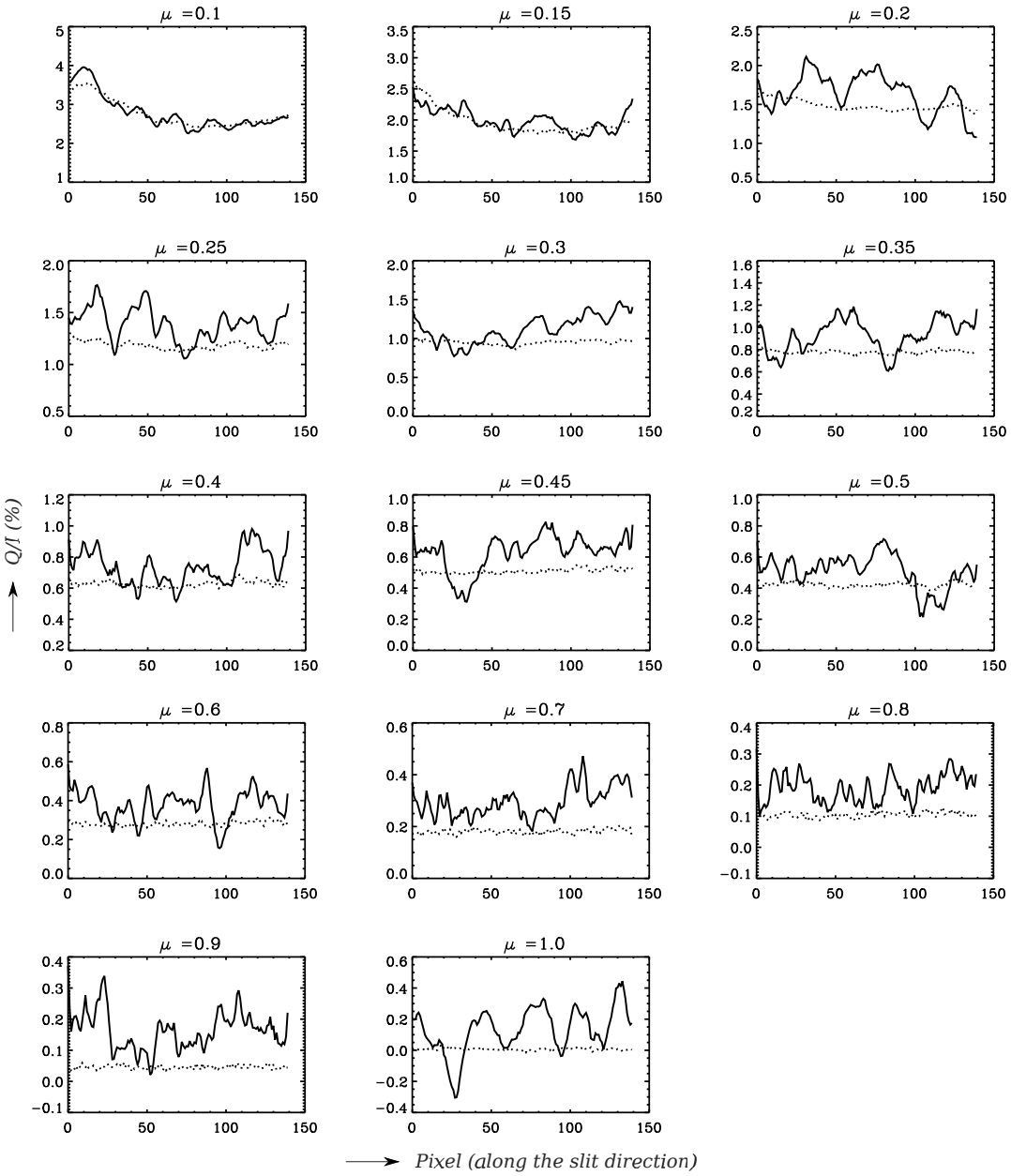

Figure 2.6: Variation of Q/I values along the slit for each μ position (marked over the plots). The solid and the dotted lines correspond to the Q/I value at the line center and at the blue wing peak, respectively.

cause the Hanle effect is absent in the wings. We also note that the spatial variation close to the limb in the blue wing is not really spectrally flat. The details regarding this will be discussed in Section 2.6.

2.3.4 Impact of temperature structure modifications on the standard model atmospheres

In the previous section we described the necessity of constructing a new model in order to obtain a fit to the CLV of the Stokes profiles. To this end, a new model was

constructed by combining two standard models after modifying their temperature structures at the desired heights. The new combined model thus constructed will provide a fit to the CLV of the observed Q/I. The physical consistency of the newly constructed atmospheric model with the modified temperature structure has been checked by verifying that it satisfies the hydrostatic equilibrium at all heights.

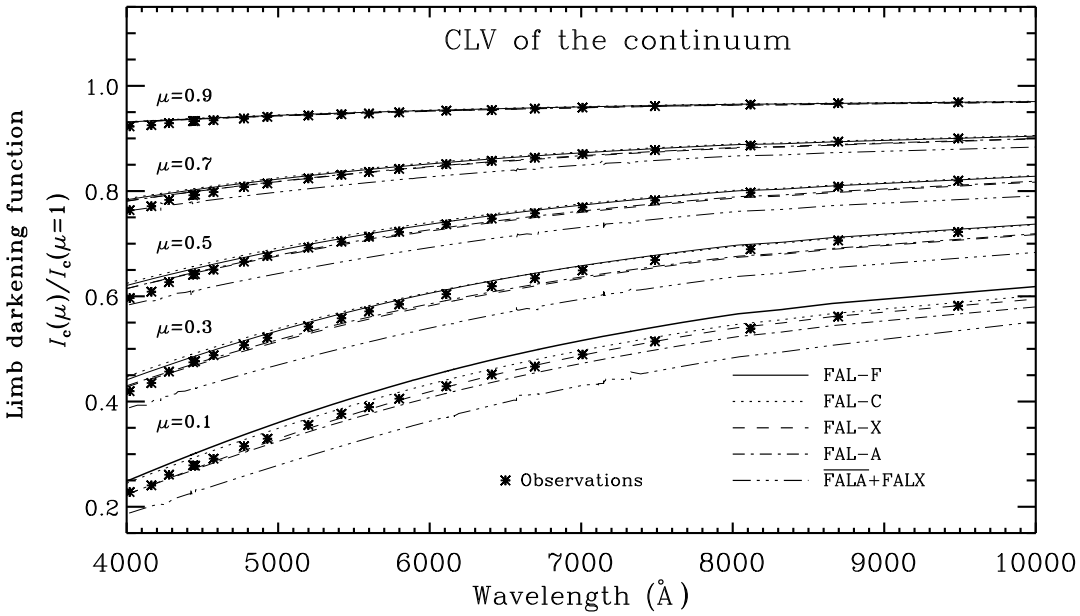

Figure 2.7: Comparison between the observed data for the CLV of continuum intensity from Neckel & Labs (1994) for a range of wavelengths and the theoretical values from different model atmospheres including $\overline{\text{FALA}}$ + FALX.

Next we examine the fit to the CLV of the continuum intensity over a wavelength range spanning from the visible to the infrared. The theoretical continuum intensity obtained using the new model should fit the observed data at all the limb distances and for a range of wavelengths. Figure 2.7 shows the limb-darkening function computed using the standard models and our new model atmosphere $\overline{\text{FALA}}$ + FALX for a range of wavelengths and μ values. The theoretical values from different models are compared with the observed data from Neckel & Labs (1994). The dash-triple-dotted line represents the theoretical values from the new model $\overline{\text{FALA}}$ + FALX. We see that the best fit to the observations is provided by the FAL-C model. Although the combined model is successful in providing a CLV fit to the observed Q/I and satisfies the equilibrium conditions, it does not provide the best fit to the observed CLV of the limb-darkening function and to the observed CLV intensity.

This leads us to the conclusion that it is indeed not possible to obtain a simultaneous fit to all the various types of data with a single 1D model atmosphere; a different atmosphere is needed for each observable. To eliminate an even wider choice of 1D models, in the next section we describe our efforts in modeling the CLV of the Ca I 4227 Å line using FCHHT models.

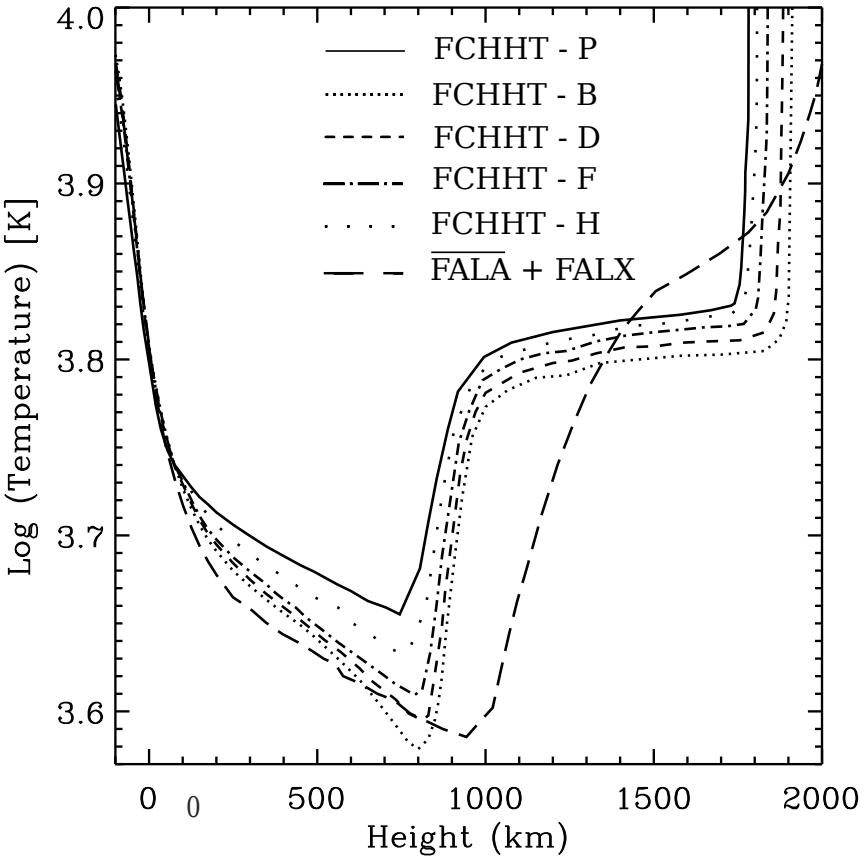

Figure 2.8: Temperature structure of the standard models FCHHT-B, FCHHT-D, FCHHT-F, FCHHT-H, and FCHHT-P used in our studies. Along with these models the temperature structure of the combined model atmosphere $\overline{\mathrm{FALA}} + \mathrm{FALX}$ is also shown.

2.4 Modeling of the center-to-limb variation observations using FCHHT model atmospheres

The temperature structures of the FCHHT models (Fontenla et al., 2009) used are shown in Figure 2.8. These models are more recent and updated versions of the FAL models. Along with the standard FCHHT models, the temperature structure of the combined model $\overline{\mathrm{FALA}}+\mathrm{FALX}$ is also shown. It was the $\overline{\mathrm{FALA}}+\mathrm{FALX}$ model that provided a fit to the observed Q/I profiles at all the limb distances as described in the previous section (Supriya et al., 2014b). We follow a similar modeling procedure as described in the previous section but now using the FCHHT model atmospheres.

Figure 2.9 shows the angular dependence of the intensity (only at the line center) and the linear polarization at three chosen wavelength positions. The theoretical CLV profiles are computed using the standard FCHHT model atmospheres. Panel (a) of Figure 2.9 shows a comparison between the observed and the theoretical CLV in I and Q/I at the line center wavelength. We see that the model FCHHT-P (long dashed line) is more suited for modeling the CLV of the line center intensity. But

the same model is not suitable to reproduce the CLV of the observed Q/I at the line center. Instead it is the model FCHHT-B that provides the closest fit to the CLV of the observed Q/I at the line center. The model FCHHT-B also closely fits the CLV profiles of the Q/I at the blue and red wing PRD peaks as seen from Figures 2.9 (b) and (c), respectively. Thus we do not find a single FCHHT atmospheric model which can provide a fit to the CLV of the Stokes (I, Q/I) spectra simultaneously throughout the line profile.

2.4.1 Comparison of the theoretical Stokes profiles from FCHHT-B and combined model atmospheres

In Figure 2.10 we compare the observations with the theoretical profiles computed using the FCHHT-B model (which provides the closest fit among the FCHHT models) and also the $\overline{\mathrm{FALA}}$+FALX combined model. We see that the theoretical profiles computed using the $\overline{\mathrm{FALA}}$+FALX model indeed provides a better fit to the Q/I profiles at different limb distances as compared to those computed using the FCHHT-B model atmosphere. It was pointed out in the previous section (see also Supriya et al., 2014b) that the $\overline{\mathrm{FALA}}$ + FALX model is successful in providing a good fit to the Q/I profiles at all limb distances, but it fails to fit the rest intensity. However, from Figure 2.10 we see that the FCHHT-B model provides a good fit for the rest intensity at μ = 0.1, but it does not match the rest intensity for $\mu \geqslant 0.3$. Also the FCHHT-B model only reproduces the shape of the observed Q/I but does not provide a good fit to the CLV of the observed Q/I. From Figure 2.10 we see that the theoretical profiles computed using the FCHHT-B model atmosphere (dotted line) has a double peak structure in the Q/I at the line center for $\mu > 0.1$. We would like to note that this double peak cannot be smoothened even after appropriately smearing the theoretical profiles obtained using the FCHHT-B model, unlike in the case of the theoretical profiles obtained using the $\overline{\mathrm{FALA}}$ + FALX model atmosphere. Next we examine the fit to the CLV of the continuum intensity over a wavelength range spanning from the visible to the infrared. Figure 2.11 shows the limb darkening function computed using the FCHHT model atmospheres for a range of wavelengths and μ values. The theoretical values from different models are compared with the observed data from Neckel & Labs (1994). We see that the best fit to the observations is provided by the FCHHT-F model. The FCHHT-B model which provides closest fit to the CLV of the observed Q/I does not provide the best fit to the observed CLV of the limb-darkening function. This leads us to the same conclusion as in the studies from FAL models that it is indeed not possible to obtain a simultaneous fit to all the various observational constraints using single 1D model atmosphere. In search of a single model which satisfies all the observational constraints, the next obvious step

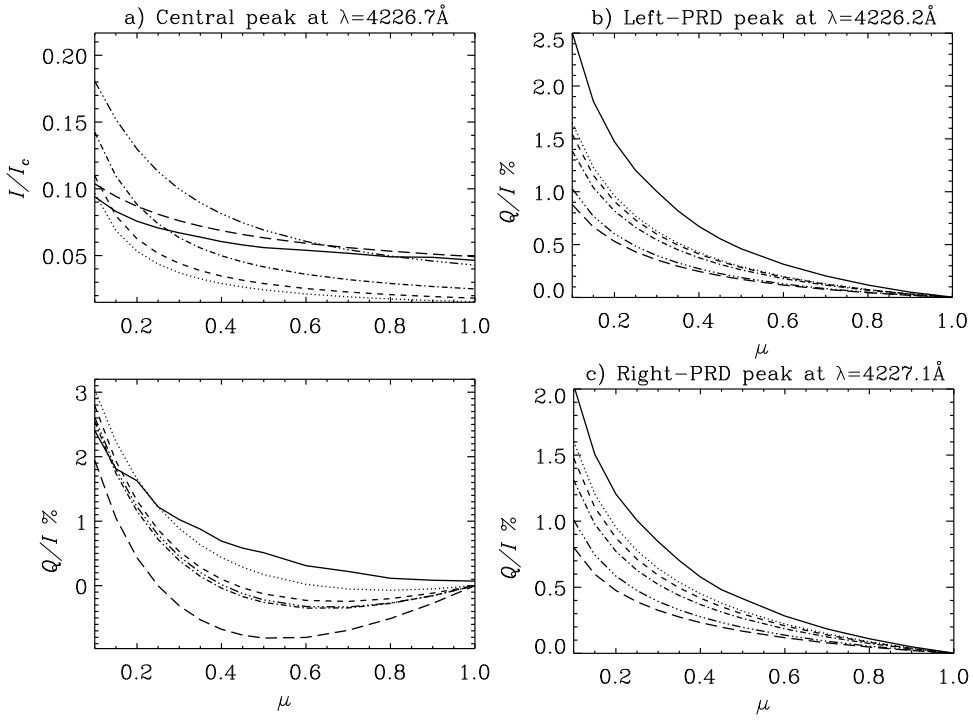

Figure 2.9: Observed (solid line) and calculated intensity and polarization signals as function of μ (observed at 14 points) at three different wavelength positions in the line profile. The theoretical spectra are calculated using standard models FCHHT-B (dotted line), FCHHT-D (dashed line), FCHHT-F (dot-dashed line), FCHHT-H (dash-triple-dotted line), and FCHHT-P (long dashed line).

would be to use the two-component modeling approach with appropriate mixing ratios, as done in Holzreuter & Stenflo (2007a). In the section below we discuss why we cannot adopt such a procedure in modeling the CLV of the Ca I 4227 Å line.

2.5 Two-component modeling approach

In modeling the CLV observations of the Ca II K line, Holzreuter & Stenflo (2007a) explored the possibility of constructing a two-component model atmosphere. This was constructed by mixing the results obtained from two standard model atmospheres in appropriate ratios. Such a method was adopted by making CLV plots of the Ca II K line as shown in their Figure 1. As seen from their figure, the original models FAL-X and FAL-C produce theoretical CLV curves which fall above and below the observed CLV curve of Q/I, respectively. Hence the authors combine results from these two standard models with appropriate mixing ratios to achieve the required fit. In Figures 2.3 and 2.9 of the present chapter we make similar plots of the CLV for the Ca I 4227 Å line. As seen from these figures, none of the standard model atmospheres produce a theoretical CLV curve in Q/I which falls above the observed CLV curve. This does not allow us to apply the same kind of two-

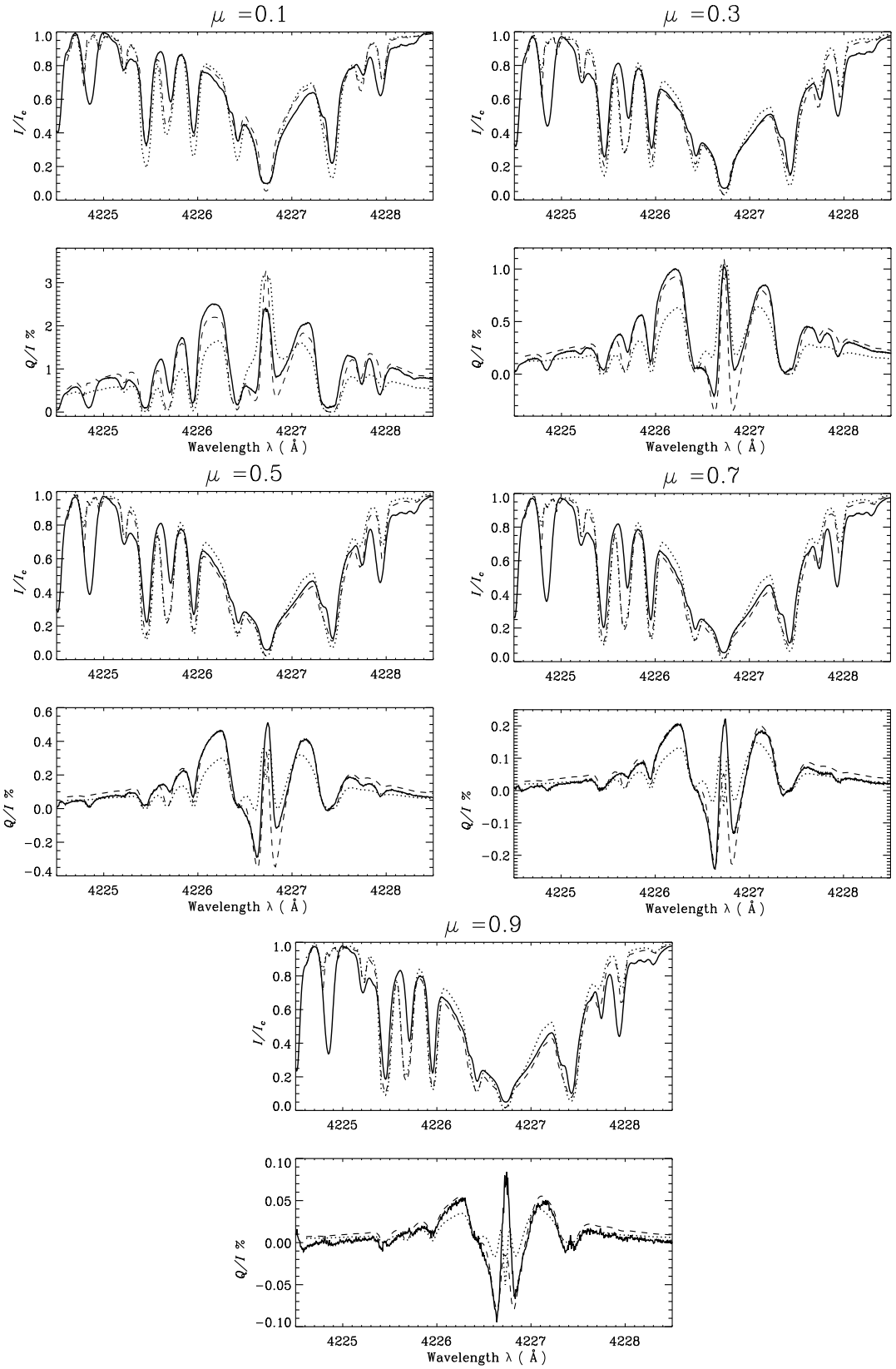

Figure 2.10: Comparison between the observed (solid line) and the theoretical Stokes profiles $(I, Q/I)$ at different limb distances. The theoretical profiles are computed using combined model $\overline{\mathrm{FALA}} + \mathrm{FALX}$ (dashed line) and FCHHT-B (dotted line).

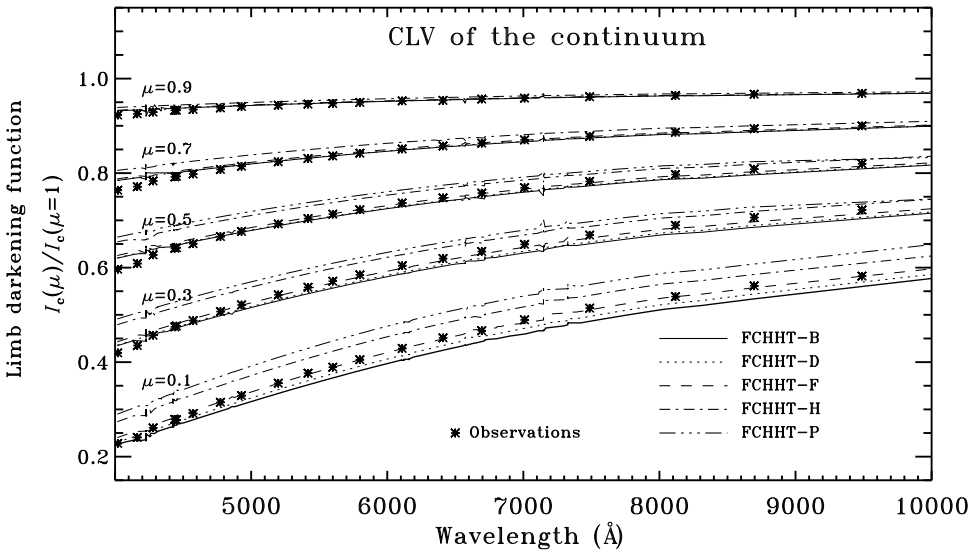

Figure 2.11: Comparison between the observed data for the CLV of continuum intensity from Neckel & Labs (1994) for a range of wavelengths and the theoretical values from different FCHHT model atmospheres.

component modeling procedure as described by Holzreuter & Stenflo (2007a). This suggests that we need to go beyond 1D modeling in the direction of two-dimensional or three-dimensional modeling to obtain a simultaneous fit to the $(I, Q/I)$ at all the limb distances. Such efforts are beyond the scope of our present studies. However, 1D models with modified temperature structures serve as a good initial step to such elaborate computations. The failure of 1D modeling approach does not preclude the use of a given line profile for purposes like magnetic field determination. To demonstrate this fact, in the next section we perform observational analysis of the Ca I 4227 Å line to determine the field strengths for smaller μ.

2.6 Determination of the field strength

In the present section we use an approach similar to that of Bianda et al. (1998, 1999) to determine the field strength at different limb distances. Since the observed Q/I is influenced by so many factors besides the magnetic field, it is imperative to apply *differential* techniques to isolate the Hanle effect from the multitude of other effects. This can be done by using the wing polarization as a reference, since it has been well established that the Hanle effect only operates in the line core but is absent in the wings.

If in Figure 2.6 we compare Q/I in the line core (solid lines) and in the blue wing (dotted lines), we notice that the line core exhibits large spatial variations along the slit, in contrast to the blue wing. Nevertheless, the blue wing polarization exhibits large-scale slow drifts along the slit, which increase significantly as we approach the

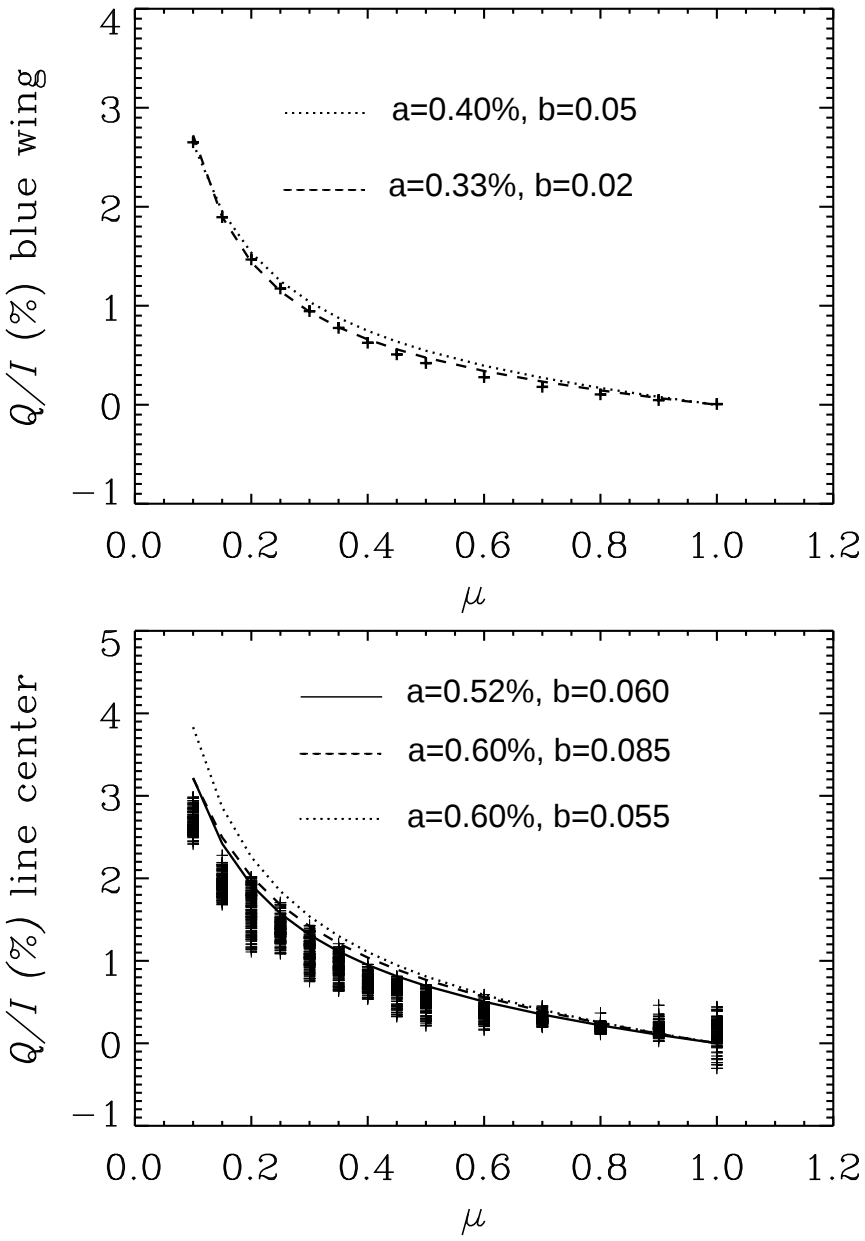

Figure 2.12: CLV of Q/I at the blue wing PRD peak (top panel) and at the line center (bottom panel). Plus sign represents the Q/I value at each pixel along the slit in the bottom panel and spatially averaged value of Q/I in the top panel. The solid, dotted, and dashed curves are obtained using the empirical relation given in Equation (2.7). The corresponding value of the free parameters a and b are indicated in the figure.

limb. Much of this can be explained in terms of a geometric effect due to the limb curvature. Since the solar limb is curved, while the slit is straight, the limb distance (or μ) will vary along the slit. This effect will increase in significance as we get closer to the limb. It is an effect that is nearly identical for the line core and wing (since the core and wing have nearly the same relative CLVs) and therefore can be eliminated when forming the core-to-wing ratio. Similarly, any other unidentified instrumental effect would ratio out. In principle, there may also be non-magnetic effects of solar origin, such as spatial variations of the radiation-field anisotropy, which

may be different between core and wings and therefore would not fully ratio out (although they should be suppressed when forming the ratio, since the non-magnetic fluctuations in the core and wings are not uncorrelated). However, with our rather low spatial resolution and long integration times, these solar effects are expected to be miniscule.

We therefore have strong reasons to believe that practically all the spatial fluctuations that we see in the Q/I core-to-wing ratio are exclusively due to magnetic fields via the Hanle effect. Instead of directly using this ratio as our differential measure, we can scale it with the slit average of the wing polarization to express it in polarization units. This scaling is equivalent to the assumption that the wing polarization should be spatially flat after all effects of limb curvature, unidentified instrumental effects, and solar non-magnetic effects have been corrected for. We thus correct the line core polarization amplitude with the following relation:

$$(Q/I)^{line\ center}_{corrected} = \frac{(Q/I)^{line\ center}_{uncorrected}}{P_b} < P_b >, \tag{2.6}$$

where $P_b = (Q/I)^{blue\ wing\ peak}$ for each pixel and $< P_b >$ is the spatial average of P_b along the slit. With this correction we plot in Figure 2.12 the CLV of the spatially averaged Q/I at the blue wing and the corrected Q/I at the line center. Each "plus" symbol in the bottom panel of Figure 2.12 represents the value of Q/I at each pixel corresponding to the line center. We notice large spatial variations along the slit in the corrected Q/I line center data. This effect is exclusively due to the magnetic fields via the Hanle effect. In order to find the field strengths that contribute to such spatial variation, we follow the method used in Bianda et al. (1998, 1999). We would like to note that in both these papers, the authors use observations taken at different periods for the data analysis. However, in our analysis we consider only one single set of observations and the variation of Q/I along the slit in these observations. To this end we construct the envelopes (continuous lines in Figure 2.12) to our data set, using the analytical relation

$$\frac{Q}{I} = \frac{a(1-\mu^2)}{\mu + b}. \tag{2.7}$$

This relation was first introduced by Stenflo et al. (1997) where a and b are the best-fit free parameters. For our studies we have chosen the same set of free parameters as given in Bianda et al. (1998, 1999). From top panel of Figure 2.12 we see that the dashed line (a = 0.33%, b = 0.02) gives a good fit to the spatially averaged observed CLV profile in the blue wing. In the bottom panel of Figure 2.12 we use three different set of free parameters a and b to construct envelopes for the line center data. The envelopes constructed using the analytical relation given in Equation (2.7) represent the "non-magnetic value", and all the values lying below this envelope are consid-

ered as the depolarized Q/I values due to the Hanle effect. From our modeling efforts we know that the magnetic fields cause an enhancement in the polarization value for $\mu > 0.35$ (see also Faurobert-Scholl, 1994). Hence this envelope-fitting method is good for $\mu \leqslant 0.35$ and becomes questionable for μ larger than about 0.35. However, the transition between the large-angle scattering and small-angle scattering is gradual and smooth. For large μ we gradually enter into the regime of the forward-scattering Hanle effect, for which the kind of techniques developed by Anusha et al. (2011) have to be adopted to derive the field strengths. Full RT modeling is naturally needed for intermediate μ values. Only for smaller μ values it is possible to use a method that avoids the need for RT. In this approach, we first extract an observed depolarization factor via the envelope method and then convert this depolarization into field strength.

Thus we first determine the ratio between the line center Q/I and the corresponding envelope value. This ratio represents the depolarization factor caused by the Hanle effect for each pixel. The conversion of this factor into field strength is dependent on the choice of the envelope, since it represents a single observable, while the magnetic field vector is characterized by three parameters (its spatial components). The magnetic field is therefore underdetermined, so a conversion cannot be unique, but it is still meaningful in a statistical sense, as explained in the following.

For photospheric spectral lines an interpretational model with a spatially averaged microturbulent field distribution could be used to convert Hanle depolarization into field strength (Stenflo, 1982, 1994), because the absence of U/I polarization in combination with insignificant spatial variations (at resolved scales) in Q/I made such a microturbulent interpretational model unavoidable (see also Stenflo, 2013). The situation is, however, entirely different for strong chromospheric lines, such as the Ca I 4227 Å line, which always exhibit large spatial line core variations in both Q/I and U/I, such as those in Figure 2.6. As we have spatially resolved these variations, they should ideally be interpreted in terms of resolved, oriented fields rather than angular distributions. However, since the field vector is underdetermined by the single depolarization factor, we need to eliminate the ambiguity by using the statistical approach, dealing with each depolarization factor as if it were obtained through averaging over an ensemble of field elements. This approach will give field strength values that are meaningful as averages in a statistical sense.

Vertical fields are immune to the Hanle effect; depolarization can only occur if the field has a substantial inclination with respect to the vertical direction. Horizontal fields give the largest depolarization. If we assume the fields to be horizontal, but with orientations that are random in azimuth angle, and let the Hanle depolarization be determined by an ensemble average over such a field distribution, then the field strengths that we extract from this model can be considered to represent *lower limits*

to the true average field strength (since there may exist less inclined fields that are less "visible" to the Hanle effect).

Chromospheric fields are expected to be largely horizontal, forming a "canopy" over the underlying photosphere. The Hanle depolarization factor k_H for a horizontal field distribution with random azimuths can be written as (Stenflo, 1982, 1994)

$$k_H = 1 - 0.75 \sin^2 \alpha_2, \tag{2.8}$$

where the Hanle mixing angle α_K is given by

$$\tan \alpha_K = \frac{KB}{B_0 / k_c^{(K)}}. \tag{2.9}$$

B is the field strength to be determined, K = 1 or 2, $k_c^{(K)}$ is the collisional branching ratio for the $2K$-multipole and B_0 is the characteristic field strength for the Hanle effect.

Figure 2.13 shows the histograms of the field strengths obtained when using Equations (2.8) and (2.9) for all pixels along the spatial direction. By definition, a depolarization factor should be less than or equal to unity; otherwise, it is unphysical. However, some points give an unphysical depolarization factor, both because there is scatter of the Q/I values due to measurement noise and because the chosen envelope may be too low. In such cases the field strength used for the histograms in Figure 2.13 is set to zero. The number of such zero field points depends on the choice of envelope and increases as we move away from the limb because of the increasing contribution from the forward scattering Hanle effect.

Figure 2.13 shows how the field strength fluctuations along the slit vary with different limb distance. For the derivation of the CLV of the average field strength, which is shown in Figure 2.14, we do not average the field strength histograms of Figure 2.13, because they are affected by measurement noise in a nonlinear way (including the truncation used for the unphysical values); instead we average the measured Q/I along the slit (causing the Gaussian instrumental noise to get greatly suppressed) and then convert the average Q/I to field strength. Since the height of line formation increases with decreasing μ, the μ variation displayed by Figure 2.14 may be interpreted in terms of a height variation of the field. In view of the limited statistical sample and the crudeness of the interpretational model, the minor variations with μ in Figure 2.14, which are similar to the ones obtained by Bianda et al. (1998, 1999), are not significant but are compatible with approximate constancy of the average field strength over the height range covered by our μ range.

Note that we have limited the μ range in Figure 2.14 to 0.1–0.35, because as previously mentioned the envelope method is not applicable for larger μ values. Note

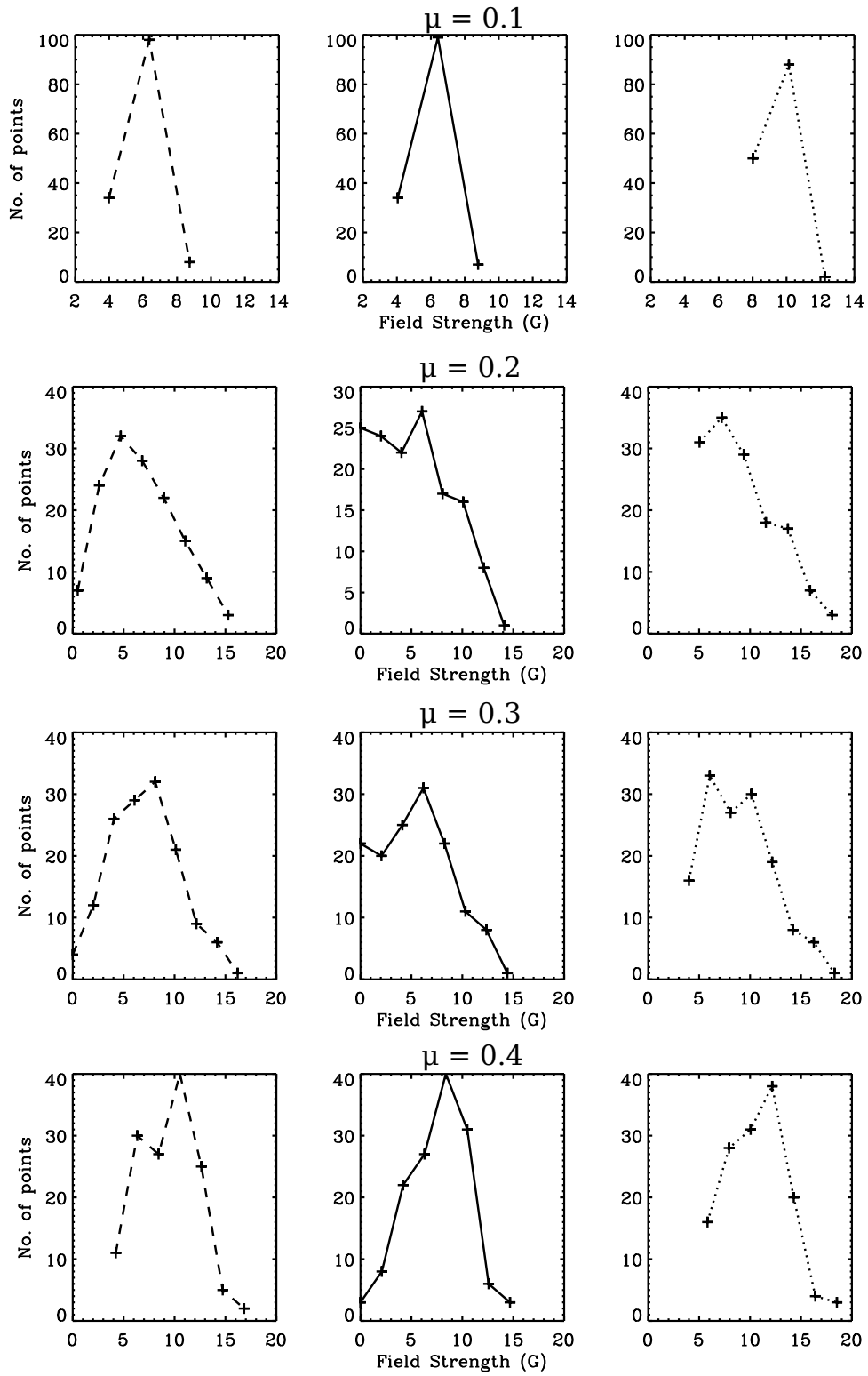

Figure 2.13: Histogram of the field strength at different μ positions. Field strengths are computed for each depolarization value in the spatial direction. Different panels along the row for each μ correspond to field strengths obtained using different envelopes. The solid, dotted, and dashed lines correspond to the solid, dotted, and dashed envelopes in Figure 2.12, respectively.

also how the derived mean field strength depends on the choice of envelope. In spite of these uncertainties, the values are generally limited to the range 6–10 G. We cannot choose envelopes significantly lower than the one represented by the solid line (in the bottom panel of Figure 2.6), because one would then get an excessive number of unphysical depolarization factors. Therefore the 6 G value can be seen as representing a kind of lower limit for the average field strength.

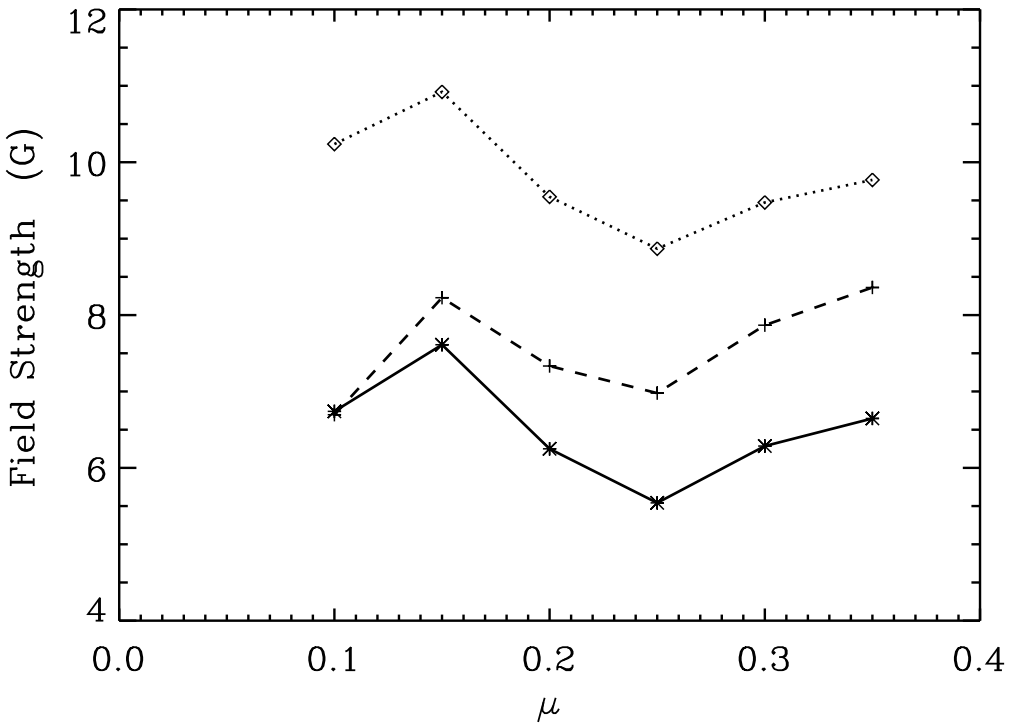

Figure 2.14: Mean value of field strength (G) derived from averaged Q/I value along the slit. The solid, dotted, and dashed lines correspond to the mean field strength derived from the corresponding envelopes indicated in Figure 2.12.

2.7 Conclusions

To understand the depth dependence of various physical quantities in the Sun, such as the magnetic fields, it is important to model the CLV observations of suitable atomic and molecular lines. In this chapter we have attempted to model such CLV observations of the well-known Ca I 4227 Å line. In our approach we take into account the effects of PRD and RT. The observations of this line were carried out in quiet regions on the Sun at 14 positions starting from the limb up to the disk center on 2012 October 16 at IRSOL in Switzerland. This line has the largest degree of linear polarization in the visible region of the SSS and can be modeled by considering a simple two-level atom picture. When trying to model this CLV data we find that none of the standard atmospheric models, we first attempted, such as the FAL-F, FAL-A,

FAL-C, and FAL-X models, could simultaneously fit the observed $(I, Q/I)$ profiles at all the limb distances. To model the CLV of the line center intensity we need FAL-F model, which is the hottest, and to model the CLV of the linear polarization at the line center we need the coolest model, FAL-X. In order to obtain a fit to the observed Stokes profiles, modifications in the temperature structure of the standard models become necessary. With suitable modifications in the desired height range, we constructed $\overline{\mathrm{FALA}}$ and later combined it with FAL-X. While the $\overline{\mathrm{FALA}}$ model gives a good fit to the PRD peaks, the FAL-X gives a good fit to the line center. The combined model has the temperature structure of $\overline{\mathrm{FALA}}$ up to 400 km and that of FAL-X in the upper layers. This new combined model atmosphere gives a good fit to the entire Q/I at all values of μ. In modeling efforts we also found that the Hanle effect not only depolarizes the line core of Q/I (which is true for smaller μ) but also enhances the line core Q/I for larger μ values. This might be due to the highly structured horizontal magnetic fields in the solar atmosphere.

Although the new combined model provides a fit to the CLV of the observed Q/I, it fails to reproduce the observed CLV of the continuum limb-darkening function and the CLV of the observed line core intensity. Further in our studies to eliminate an even wider choice of 1D model atmospheres, we attempted the use of recent and updated FCHHT model atmospheres to obtain a simultaneous fit for the CLV of the $(I, Q/I)$ profiles of the Ca I 4227 Å line. We find that the FCHHT models also fail to provide a simultaneous fit to the $(I, Q/I)$ profiles of the Ca I 4227 Å line. This failure of the 1D models in order to simultaneously fit the observed $(I, Q/I)$ CLV profiles does not restrain the use of the Ca I 4227 Å as a tool to map the magnetic fields. To support this claim, we carried out observational analysis to determine field strength using the Ca I 4227 Å for smaller μ values.

To conclude, it appears that no single 1D atmosphere can completely provide a good representation of the actual solar atmosphere. This shows that the solar atmosphere has a far more complex structure. To simultaneously satisfy the various observational constraints it is therefore unavoidable to go beyond such 1D models—a difficult problem that needs to be approached step by step. This conclusion is not at all a technical failure, meaning that our inability to obtain a simultaneous perfect fit to the CLV of the (I, Q/I) has nothing to do with the weakness of our approach or the method followed in using 1D solar atmosphere models. Instead it is a "profound failure" indicating that the atmosphere of the Sun has such a complexity that it is not possible to represent it in terms of a single 1D atmosphere model. It could mean that the use of 1D models for interpretations of the SSS may give results that are physically incorrect (since they do not represent solar conditions), although the results may formally be mathematically correct. However, 1D modeling efforts may still provide a guideline to the more systematic and sophisticated modeling efforts.

The Ca I 4227 Å line is one of the many lines in the SSS that we have considered for our detailed study. However with the dramatic development in the polarimetric instrumentation we are often confronted with a variety of new features in SSS that demands sophistication in the existing theoretical approaches. The theoretical concentration has always been on studying one of the key parameters that contains the physics of scattering namely the redistribution matrix. In the next two parts of the present thesis our aim is to conduct a few studies by relaxing some of the approximations made in establishing the redistribution matrix and further see its implications on the emergent Stokes profiles.

Part II

Polarized line formation with angle-dependent partial frequency redistribution

Chapter 3

The effect of electron scattering redistribution on atomic line polarization*

An Overview

The polarization of spectral lines is generated by the scattering of angularly anisotropic incident radiation field on the atoms in the stellar atmosphere. This atomic scattering polarization is modified by frequency non-coherent scattering of line photons on free electrons. With modern spectro-polarimeters of high sensitivity, it is possible to detect such changes in the spectral line polarization caused by scattering on electrons. We present new and efficient numerical techniques to solve the problem of line radiative transfer with atomic and electron scattering frequency redistribution in planar media. The evaluation and use of angle-dependent partial frequency redistribution (PRD) functions (both atomic as well as electron scattering type) in the transfer equation require a lot of computing effort. In this chapter, we apply a decomposition technique to handle this numerically difficult problem. This recently developed technique is applied for the first time to the electron scattering partial redistribution. This decomposition technique allows us to devise fast iterative methods of solving the polarized line transfer equation. An approximate lambda iteration (ALI) method and a method based on Neumann series expansion of the polarized source vector are proposed. We show that these numerical methods can be used to obtain a solution of the problem, when both atomic and electron scattering PRD are considered together. This is in contrast with the classical numerical methods which require a great amount of computing time. We show the importance of electron scattering redistribution in the far wing line polarization, which has practical implications in the

*The contents of this chapter are based on Supriya et al. (2012, 2014a)

analysis of polarized stellar or solar spectra, where non-coherent electron scattering (NCES) controls the line wing transfer.

3.1 Introduction

The importance of electron scattering in stellar line formation problems has been recognized for a long time. Dirac (1925) derived the angle-dependent redistribution function for the scattering of low-energy photons ($h\nu < m_e c^2$) on thermal electrons. He arrived at the conclusion that the shift of the lines cannot be produced by such a scattering mechanism, but the broadening may be possible. In early type stars where electron density is high, the scattering of radiation by electrons play an important role. Electron scattering effects on spectral lines was investigated by Münch (1948) for semi-infinite atmosphere in which an absorption line is formed, surrounded by a finite layer of electrons. Since in this case, the photons are scattered from the continuum into the line core, he obtained line profiles with shallower core and broader wings. Hummer & Mihalas (1967) emphasized the importance of treating electron scattering as a redistribution process and its effects on line formation in O and B stars. They show the dependence of angle-averaged electron scattering redistribution function on the frequency difference between outgoing and incoming photons, and that the effect of NCES is to smoothen out the frequency dependence of the radiation field at each depth. They show that near the boundary of the atmosphere, where the mean intensity in the continuum is lower than in the line, this mechanism will be effective in removing photons from the line, thereby leading to a wider and deeper line than would be obtained if the electrons were completely ignored. The broad emission-line wings observed in many Be stars were attributed to electron scattering of line photons (Marlborough, 1969). It was concluded by Bernat & Lambert (1978) that the very broad $H\alpha$ emission wings in P Cyg were caused by electron scattering. The $\lambda 3483$ line of $N_{\rm IV}$ in the WN 6 star HD 192163 was observed to have P cygni type of profile with large emission wings which was accounted for as the non-coherent scattering on free electrons by Castor et al. (1970). Auer & van Blerkom (1972) studied the influence of electron scattering in an expanding medium and they obtained asymmetric line profiles extending preferentially in the red wing. The influence of electron scattering on emission line profiles arising from stellar winds in early-type stars was studied in detail by Hillier (1991). He noticed that the use of electron scattering redistribution will noticeably affect the strength of line wings. Chugai (2001) shows that large line width of broad narrow-topped emission line by early-time spectra of SN 1998S originate as a result of multiple scattering of the photons of the narrow line by the thermal electrons of the opaque circumstellar shell gas. Reference to earlier work in this field can also be found in Rangarajan

et al. (1991).

Studies on the combined effect of angle-averaged PRD and NCES on the polarized resonance line transfer were done by Nagendra et al. (1993). The effects of including angle-dependent PRD functions for the scattering by atoms and electrons were studied by Rangarajan (1999). In the above two references, a discrete ordinate method was used to solve the radiative transfer equation in the Stokes vector basis. In this chapter, the polarized radiative transfer equation including angle-dependent PRD and NCES are discussed. In resonance scattering in lines, there exist correlations between the directions and the frequencies of the incident and scattered photons, which is referred to as PRD. The line polarization is very sensitive to the nature of the frequency redistribution mechanism. The scattering of line photons by electrons can also make significant contribution in the far line wings.

The problem of angle-dependent PRD is characterized by the coupling between the angle and frequency variables. This makes the evaluation of scattering integrals, and the solution of polarized transfer equation a challenging problem. A decomposition technique to reduce the non-axisymmetric Stokes vector transfer equation to cylindrically symmetric one was developed by Frisch (2007). This technique was extended by Frisch (2009) to handle angle-dependent PRD in the presence of a magnetic field. In the absence of magnetic fields, the angle-dependent PRD problem simplifies as shown by Frisch (2010). In this case, the polarized radiation field represented by the Stokes vector (I, Q) can be decomposed into four irreducible components. In this chapter, we use a similar decomposition technique to handle angle-dependent NCES.

Sampoorna et al. (2011) have presented three iterative techniques to solve the polarized line transfer equation in the irreducible basis. These techniques were developed for the purpose of solving angle-dependent atomic redistribution problem. Here we extend these techniques to study the combined effects of PRD by atoms and non-coherent scattering by electrons, on polarized line formation. We present two numerical methods to solve these problems. First one is the ALI type method and the other is based on Neumann series expansion of the polarized source vector component. In recent decades, the ALI methods introduced for scalar radiative transfer problems have been generalized to solve Rayleigh scattering and the weak-field Hanle effect transfer problem (see the reviews by Nagendra, 2003; Trujillo Bueno, 2003; Nagendra & Sampoorna, 2009). These methods have the advantage of being much faster while remaining as accurate as the traditional exact or perturbative methods (see Nagendra et al., 1999).

The outline of the present chapter is as follows. In Section 3.2, we present the relevant transfer equations. Here we extend the Fourier decomposition used for atomic line scattering to treat the process of frequency redistribution by electrons.

In Section 3.3 we present two different numerical methods, namely a polarized ALI method, and the "scattering expansion method" (SEM) based on Neumann series expansion. In Section 3.4, we present a detailed study of angle-dependent electron scattering redistribution function and the corresponding azimuth-averaged redistribution function. Results are presented in Section 3.5, where we discuss in detail the angle-dependent PRD and electron scattering effects on the Stokes I and Q/I profiles. Concluding remarks are presented in Section 3.6.

3.2 Governing equations

3.2.1 The transfer equation in the Stokes vector basis

We consider a one-dimensional isothermal planar atmosphere. The slab is assumed to be self-emitting or irradiated on the lower boundary by an axisymmetric-radiation field. Magnetic fields, when present are assumed to be micro-turbulent. Under these assumptions, the radiation field is axisymmetric and can be described by two Stokes parameters I and Q. The reference direction for negative Q is defined by electric vector parallel to the surface of the atmosphere. For a concise presentation, we denote I by I_0 and Q by I_1 in all the equations appearing in this chapter. However in the figures we use the standard notation of (I, Q) to mean the Stokes parameters.

The polarized transfer equation for the Stokes parameters I and Q can be written in component form as

$$\mu \frac{\partial I_i}{\partial \tau} = \left[\varphi(x) + \beta_c + \beta_e\right]\left[I_i(\tau, x, \mu) - S_i(\tau, x, \mu)\right], \quad i = 0, 1, \tag{3.1}$$

where $\mu = \cos\theta$, with θ being the co-latitude with respect to the atmospheric normal, τ the line optical depth defined by $\mathrm{d}\tau = -k_l \mathrm{d}z$, with k_l the frequency-integrated line absorption coefficient and $\varphi(x)$ the normalized Voigt function. The frequency x is measured in the units of Doppler width. The ratio of continuum to line absorption coefficient is denoted by β_c and the ratio of electron scattering coefficient to line absorption coefficient is denoted by β_e. The above transfer equation 3.1 is the same as Equation 1.18 except that the contribution from electron scattering is now included in Equation 3.1 through β_e and the total source vector. The total source vector is now given by

$$S_i(\tau, x, \mu) = \frac{\varphi(x) S_{l,i}(\tau, x, \mu) + \beta_c S_{c,i} + \beta_e S_{e,i}}{\varphi(x) + \beta_c + \beta_e}, \tag{3.2}$$

where $S_{c,i}$ are the components of the unpolarized continuum source vector. We assume that $S_{c,0} = B$, where B is the Planck function at the line center and $S_{c,1} = 0$.

The line source vector can be written as

$$S_{l,i}(\tau, x, \mu) = G_i(\tau) + \int \oint \sum_{j=0,1} \frac{R_{ij,a}(x, \mathbf{\Omega}, x', \mathbf{\Omega}')}{\varphi(x)} I_j(\tau, x', \mu') \frac{\mathrm{d}\Omega'}{4\pi} \mathrm{d}x', \quad (3.3)$$

where $\mathrm{d}\Omega' = \sin\theta' \, \mathrm{d}\theta' \, \mathrm{d}\chi'$. The outgoing and incoming ray directions $\mathbf{\Omega}$ and $\mathbf{\Omega}'$ are defined, respectively, by their polar angles (θ, χ) and (θ', χ'). For simplicity, we assume that the primary source is unpolarized, namely that $G_0(\tau) = \epsilon B$, where ϵ is the standard two-level atom thermalization parameter. The term $R_{ij,a}(x, \mathbf{\Omega}, x', \mathbf{\Omega}')$ denotes the elements of the redistribution matrix for Rayleigh scattering on atomic bound states (Domke & Hubeny, 1988; Bommier, 1997a). A two-level atom model with unpolarized lower level is assumed.

The electron scattering source vector can be written as

$$S_{e,i}(\tau, x, \mu) = \int \oint \sum_{j=0,1} R_{ij,e}(x, \mathbf{\Omega}, x', \mathbf{\Omega}') I_j(\tau, x', \mu') \, \frac{\mathrm{d}\Omega'}{4\pi} \, \mathrm{d}x', \quad (3.4)$$

where $R_{ij,e}(x, \mathbf{\Omega}, x', \mathbf{\Omega}')$ denotes the elements of the electron scattering redistribution matrix. The angle-dependent electron redistribution matrix is written as

$$\boldsymbol{R}_e(x, \mathbf{\Omega}, x', \mathbf{\Omega}') = \boldsymbol{P}^R(\mathbf{\Omega}, \mathbf{\Omega}') \, r_e(x, \mu, x', \mu', \Delta), \quad (3.5)$$

where $\boldsymbol{P}^R(\mathbf{\Omega}, \mathbf{\Omega}')$ is the angular phase matrix for Rayleigh (resonance) scattering of line photons on free electrons—which scatter according to the dipole scattering law. The angle-dependent electron scattering redistribution function is given by

$$r_e(x, \mu, x', \mu', \Delta) = \frac{1}{2\sqrt{\pi} w \sin(\Theta/2)} \exp\left[\frac{-(x - x')^2}{4w^2 \sin^2(\Theta/2)} \right], \quad (3.6)$$

where $\cos\Theta = \cos\theta \cos\theta' + \sin\theta \sin\theta' \cos\Delta$, with $\Delta = \chi - \chi'$. The quantity w denotes the ratio of electron to atomic Doppler widths. Further details and behavior of $r_e(x, \mu, x', \mu', \Delta)$ are discussed in Section 3.4.

In this chapter we present also the results for angle-averaged electron redistribution problem. The relevant redistribution matrix is written as

$$\boldsymbol{R}_e(x, \mathbf{\Omega}, x', \mathbf{\Omega}') = \boldsymbol{P}^R(\mathbf{\Omega}, \mathbf{\Omega}') \, r_e(x, x'), \quad (3.7)$$

where a factorization of the polarized phase matrix and the redistribution function is assumed (hybrid approximation). The expression for the angle-averaged electron redistribution function is given in Equations (19)–(21) of Nagendra et al. (1993, see also, Rangarajan et al. 1991; Auer & Mihalas 1968).

3.2.2 The transfer equation in the irreducible spherical tensor basis

According to the decomposition technique described in Frisch (2010), we can write $S_{l,i}$ and $I_i(\tau, x, \mu)$ as

$$S_{l,i}(\tau, x, \mu) = \sum_{K,Q\geq 0} \tilde{\mathcal{T}}^K_Q(i,\mu)\mathcal{S}^K_{Q,l}(\tau, x, \mu), \tag{3.8}$$

$$I_i(\tau, x, \mu) = \sum_{K,Q\geq 0} \tilde{\mathcal{T}}^K_Q(i,\mu)\,\mathcal{I}^K_Q(\tau, x, \mu), \tag{3.9}$$

where $i = 0, 1$. The irreducible tensors $\tilde{\mathcal{T}}^K_Q(i,\mu)$ are defined in Frisch (2010) and they are related to the spherical tensors for polarimetry introduced by Landi Degl'Innocenti (1984, see also Landi Degl'Innocenti & Landolfi 2004). We have four terms in the summation over K and Q corresponding to $K = Q = 0$, $K = 2$ with $Q = 0, 1, 2$. We remark that the index Q should not be confused with the Stokes Q parameter. The irreducible line source vector components $\mathcal{S}^K_{Q,l}(\tau, x, \mu)$ may be written as

$$\begin{aligned}\mathcal{S}^K_{Q,l}(\tau, x, \mu) = \delta_{K0}\delta_{Q0}G_0(\tau) + \int_{-\infty}^{+\infty} \mathrm{d}x' \int_{-1}^{+1} \frac{\mathrm{d}\mu'}{2} \frac{\tilde{\mathcal{R}}^K_{Q,a}(x,\mu,x',\mu')}{\varphi(x)} \\ \times \sum_{K',Q'\geq 0} \tilde{\Gamma}^{KK'}_{QQ'}(\mu')\,\mathcal{I}^{K'}_{Q'}(\tau, x', \mu'),\end{aligned} \tag{3.10}$$

where

$$\tilde{\Gamma}^{KK'}_{QQ'}(\mu') = \sum_{j=0,1} \tilde{\mathcal{T}}^K_Q(j,\mu')\,\tilde{\mathcal{T}}^{K'}_{Q'}(j,\mu'). \tag{3.11}$$

The coefficients $\tilde{\Gamma}^{KK'}_{QQ'}(\mu)$ are given in the appendix of Frisch (2010). The functions $\tilde{\mathcal{R}}^K_{Q,a}$ in Equation (3.10) take the form

$$\tilde{\mathcal{R}}^0_{0,a} = \alpha\tilde{r}^{(0)}_{\mathrm{II}} + \left[\beta^{(0)} - \alpha\right]\tilde{r}^{(0)}_{\mathrm{III}}, \tag{3.12}$$

$$\tilde{\mathcal{R}}^2_{Q,a} = W_2\,\mu_2\left\{\alpha\tilde{r}^{(Q)}_{\mathrm{II}} + \left[\beta^{(2)} - \alpha\right]\tilde{r}^{(Q)}_{\mathrm{III}}\right\}, \tag{3.13}$$

where $Q = 0, 1, 2$ and $W_2(J_l, J_u)$ is the atomic polarizability factor depending on the angular momentum of the lower and upper levels of the transition. The coefficients α and $\beta^{(K)}$ (Bommier, 1997b) are the branching ratios:

$$\alpha = \frac{\Gamma_R}{\Gamma_R + \Gamma_I + \Gamma_E} \tag{3.14}$$

and

$$\beta^{(K)} = \frac{\Gamma_R}{\Gamma_R + \Gamma_I + D^{(K)}}, \tag{3.15}$$

where Γ_R is the radiative rate, Γ_I and Γ_E are the inelastic and elastic collisional rates, respectively, and $D^{(K)}$ is the collisional depolarization rate such that $D^{(0)} = 0$. The coefficient μ_2 takes into account the effects of a microturbulent magnetic field. It depends on the magnetic field probability density function (see e.g., Landi Degl'Innocenti & Landolfi, 2004, p.215) and is unity in the absence of magnetic fields. The $\tilde{r}_{\rm X}^{(Q)}$ (with X = II or III) are the Qth-order azimuthal Fourier coefficients of the PRD functions $r_{\rm II}$ and $r_{\rm III}$ of Hummer (1962). They are defined by

$$\tilde{r}_{\rm X}^{(Q)}(x,\mu,x',\mu') = \frac{2-\delta_{0Q}}{2\pi} \times \int_0^{2\pi} r_{\rm X}(x,\mu,x',\mu',\Delta)\cos\left(Q\,\Delta\right)\mathrm{d}\Delta. \tag{3.16}$$

A decomposition technique similar to that of line source vector can be applied also to the electron scattering source vector. It can be written as

$$S_{e,i}(\tau,x,\mu) = \sum_{K,Q\geq 0} \tilde{\mathcal{T}}_Q^K(i,\mu)\,\mathcal{S}_{Q,e}^K(\tau,x,\mu), \tag{3.17}$$

with $i = 0, 1$. The irreducible components of the electron scattering source vector are given by

$$\begin{aligned}\mathcal{S}_{Q,e}^K(\tau,x,\mu) = &\int_{-\infty}^{+\infty}\mathrm{d}x' \int_{-1}^{+1}\frac{\mathrm{d}\mu'}{2}\,\tilde{r}_e^{(Q)}(x,\mu,x',\mu') \\ &\times \sum_{K',Q'\geq 0}\tilde{\Gamma}_{QQ'}^{KK'}(\mu')\,\mathcal{I}_{Q'}^{K'}(\tau,x',\mu').\end{aligned} \tag{3.18}$$

In the case of electron scattering the profile function is unity, and there is no thermal emission unlike the scattering on atoms. The azimuthal Fourier coefficients have the same form as Equation (3.16), but with X replaced by e.

For computational purposes, we define a new quantity $\mathcal{S}_{Q,L}^K$ which is a weighted sum of atomic and electron scattering irreducible source vectors. It is written as

$$\mathcal{S}_{Q,L}^K(\tau,x,\mu) = \frac{\varphi(x)\mathcal{S}_{Q,l}^K(\tau,x,\mu) + \beta_e\mathcal{S}_{Q,e}^K(\tau,x,\mu)}{\varphi(x)}. \tag{3.19}$$

Substituting Equations (3.10) and (3.18) in the above equation, we can write $\mathcal{S}_{Q,L}^K$ as

$$\begin{aligned}\mathcal{S}_{Q,L}^K(\tau,x,\mu) = \delta_{K0}\delta_{Q0}G_0(\tau) + &\int_{-\infty}^{+\infty}\mathrm{d}x' \int_{-1}^{+1}\frac{\mathrm{d}\mu'}{2}\left[\tilde{\mathcal{R}}_Q^K(x,\mu,x',\mu')\right]/\varphi(x) \\ &\times \sum_{K',Q'\geq 0}\tilde{\Gamma}_{QQ'}^{KK'}(\mu')\,\mathcal{I}_{Q'}^{K'}(\tau,x',\mu'),\end{aligned} \tag{3.20}$$

where

$$\tilde{\mathcal{R}}^K_Q(x,\mu,x',\mu') = [\tilde{\mathcal{R}}^K_{Q,a}(x,\mu,x',\mu') + \beta_e \tilde{r}_e^{(Q)}(x,\mu,x',\mu')]. \tag{3.21}$$

Now the total source vector in the irreducible basis is given by

$$\mathcal{S}^K_Q(\tau,x,\mu) = \frac{\varphi(x)\mathcal{S}^K_{Q,L}(\tau,x,\mu) + \beta_c \mathcal{S}^K_{Q,c}(\tau)}{\varphi(x)+\beta_c+\beta_e}, \tag{3.22}$$

with the continuum source vector $\mathcal{S}^K_{Q,c} = \delta_{K0}\delta_{Q0}B$. The components $\mathcal{I}^K_Q$ corresponding to $\mathcal{S}^K_Q$ satisfy a transfer equation similar to Equation (3.1). We introduce the four-component vectors $\boldsymbol{\mathcal{S}}(\tau,x,\mu) = \{\mathcal{S}^0_0, \mathcal{S}^2_0, \mathcal{S}^2_1, \mathcal{S}^2_2\}^{\mathrm{T}}$ and $\boldsymbol{\mathcal{I}}(\tau,x,\mu) = \{\mathcal{I}^0_0, \mathcal{I}^2_0, \mathcal{I}^2_1, \mathcal{I}^2_2\}^{\mathrm{T}}$. Then we can re-write Equation (3.20) in vector form as

$$\boldsymbol{\mathcal{S}}_L(\tau,x,\mu) = \boldsymbol{\mathcal{G}}(\tau) + \int_{-\infty}^{+\infty}\int_{-1}^{+1} \frac{\tilde{\boldsymbol{\mathcal{R}}}(x,\mu,x',\mu')}{\varphi(x)} \boldsymbol{\Gamma}(\mu')\boldsymbol{\mathcal{I}}(\tau,x',\mu')\frac{\mathrm{d}\mu'}{2}\,\mathrm{d}x'. \tag{3.23}$$

The primary source vector $\boldsymbol{\mathcal{G}}(\tau) = \{G_0(\tau),0,0,0\}^{\mathrm{T}}$, where $G_0(\tau) = \epsilon B$ with $\epsilon = \Gamma_I/(\Gamma_I+\Gamma_R)$. The 4×4 matrix $\tilde{\boldsymbol{\mathcal{R}}}$ is diagonal, namely

$$\tilde{\boldsymbol{\mathcal{R}}} = \mathrm{diag}\,[\tilde{\mathcal{R}}^0_{0,a} + \beta_e\tilde{r}_e^{(0)}, \tilde{\mathcal{R}}^2_{0,a} + \beta_e\tilde{r}_e^{(0)}, \tilde{\mathcal{R}}^2_{1,a} + \beta_e\tilde{r}_e^{(1)}, \tilde{\mathcal{R}}^2_{2,a} + \beta_e\tilde{r}_e^{(2)}]. \tag{3.24}$$

The 4×4 matrix $\boldsymbol{\Gamma}$ is a full matrix with elements $\tilde{\Gamma}^{KK'}_{QQ'}$. Owing to its symmetry, it has only ten independent elements (see Equation (3.11) and also Frisch, 2010). When $\tilde{\boldsymbol{\mathcal{R}}}$ is independent of μ and μ' (complete frequency redistribution or angle-averaged PRD), only the two components of the source vector corresponding to the index $Q=0$ are non-zero.

3.3 Numerical methods of solution

We present two iterative methods to solve the problem of angle-dependent PRD and angle-dependent NCES. First one is an ALI-type method and the second one is SEM. These methods for the particular case of scattering on atoms are presented in Sampoorna et al. (2011). Here we generalize these methods to include NCES.

3.3.1 The polarized approximate lambda iteration approach

The formal solution of the transfer equation for the four-component irreducible vector $\boldsymbol{\mathcal{I}}$ can be written as

$$\boldsymbol{\mathcal{I}}_{x\mu} = \boldsymbol{\Lambda}_{x\mu}\left[\boldsymbol{\mathcal{S}}_{x\mu}\right] + \boldsymbol{T}_{x\mu}. \tag{3.25}$$

The explicit dependence of $\boldsymbol{\mathcal{I}}$ and $\boldsymbol{\mathcal{S}}$ on τ is neglected and their dependence on x and μ appear as subscripts. $\boldsymbol{T}_{x\mu}$ is the directly transmitted part of the intensity vector and $\boldsymbol{\Lambda}_{x\mu}$ is the frequency- and angle-dependent 4×4 integral operator. The operator $\boldsymbol{\Lambda}_{x\mu}$ can be written as

$$\boldsymbol{\Lambda}_{x\mu} = \boldsymbol{\Lambda}^*_{x\mu} + \left(\boldsymbol{\Lambda}_{x\mu} - \boldsymbol{\Lambda}^*_{x\mu}\right), \tag{3.26}$$

where $\boldsymbol{\Lambda}^*_{x\mu}$ is the diagonal approximate operator (see Olson et al., 1986). We can setup an iterative scheme by writing

$$\boldsymbol{\mathcal{S}}^{n+1}_{x\mu} = \boldsymbol{\mathcal{S}}^{n}_{x\mu} + \delta\boldsymbol{\mathcal{S}}^{n}_{x\mu}; \qquad \boldsymbol{\mathcal{S}}^{n+1}_{L,x\mu} = \boldsymbol{\mathcal{S}}^{n}_{L,x\mu} + \delta\boldsymbol{\mathcal{S}}^{n}_{L,x\mu}, \tag{3.27}$$

where n is the iteration index. Combining Equations (3.26) and (3.27) with Equation (3.23), we derive an equation for the total line source vector corrections

$$\delta\boldsymbol{\mathcal{S}}^{n}_{L,x\mu} - \int_{-\infty}^{+\infty}\int_{-1}^{+1} \frac{\tilde{\boldsymbol{\mathcal{R}}}_{x\mu,x'\mu'}}{\varphi_x}\boldsymbol{\Gamma}_{\mu'}\, p_{x'}\boldsymbol{\Lambda}^*_{x'\mu'}\left[\delta\boldsymbol{\mathcal{S}}^{n}_{L,x'\mu'}\right]\frac{\mathrm{d}\mu'}{2}\,\mathrm{d}x' = \boldsymbol{r}^{n}_{x\mu}, \tag{3.28}$$

where $p_x = \varphi_x/(\varphi_x + \beta_c + \beta_e)$ and $\boldsymbol{r}^{n}_{x\mu} = \boldsymbol{\mathcal{G}}(\tau) + \overline{\boldsymbol{\mathcal{J}}}^{\,n}_{x\mu} - \boldsymbol{\mathcal{S}}^{n}_{L,x\mu}$, which is the residual vector. The mean intensity is given by

$$\overline{\boldsymbol{\mathcal{J}}}^{\,n}_{x\mu} = \int_{-\infty}^{+\infty}\int_{-1}^{+1} \frac{\tilde{\boldsymbol{\mathcal{R}}}_{x\mu,x'\mu'}}{\varphi_x}\boldsymbol{\Gamma}_{\mu'}\boldsymbol{\Lambda}_{x'\mu'}\left[\boldsymbol{\mathcal{S}}^{n}_{x'\mu'}\right]\frac{\mathrm{d}\mu'}{2}\,\mathrm{d}x'. \tag{3.29}$$

To compute the source vector corrections, we use a frequency-angle by frequency-angle (FABFA) method discussed in Sampoorna et al. (2011). It is extended in this chapter by including angle-dependent electron scattering redistribution function along with the angle-dependent PRD functions. Equation (3.28) can be written formally as

$$\mathbf{A}\,\delta\boldsymbol{\mathcal{S}}^{n}_{L} = \boldsymbol{r}^{n}. \tag{3.30}$$

At each depth point, $\boldsymbol{r}^n$ and $\delta\boldsymbol{\mathcal{S}}^n_L$ are vectors of length $4N_x\,2N_\mu$, where N_x is the number of frequency points in the range $[0, x_{\max}]$ and N_μ is the number of angle points in the range $[0 < \mu \leq 1]$. The matrix $\mathbf{A}$ thus has dimensions $4N_x\,2N_\mu \times 4N_x\,2N_\mu$. For a given x, x', μ, and μ', the matrix $\mathbf{A}$ can be decomposed into $N_x\,2N_\mu \times N_x\,2N_\mu$ of 4×4 blocks. In each block, denoted by $\boldsymbol{\mathcal{A}}$, the elements may be written as

$$\boldsymbol{\mathcal{A}} = \delta_{mn}\delta_{\alpha\beta}\mathbf{E} - w_\beta p_n \mathbf{g}_{m\alpha,n\beta}\boldsymbol{\Gamma}_\beta\boldsymbol{\Lambda}^*_{n\beta}, \tag{3.31}$$

where $m = 1, \ldots, N_x$, $n = 1, \ldots, N_{x'}$, $\alpha = 1, \ldots, 2N_\mu$, and $\beta = 1, \ldots, 2N_{\mu'}$, and $\mathbf{E}$ is the identity operator. The coefficients w_β denote the μ' integration weights and $\mathbf{g}_{m\alpha,n\beta}$ are defined by

$$\mathbf{g}_{m\alpha,n\beta} = \frac{\tilde{\boldsymbol{\mathcal{R}}}_{m\alpha,n\beta}}{\varphi_m}\,\bar{w}_n, \tag{3.32}$$

where $\bar{w}_n$ are the frequency integration weights. This method requires computation of the matrix $\mathbf{A}^{-1}$ before the iteration cycle.

3.3.2 Scattering expansion method

This method is based on Neumann series expansion of the components of the source vector contributing to the polarization. This series amounts to an expansion in the mean number of scattering events (see Frisch et al., 2009). Its first term yields the so-called single scattering solution. Here, following Frisch et al. (2009), we include higher order terms. The computation using SEM involves following steps.

(i) Neglecting polarization, first calculate Stokes I which is given by the component $\mathcal{I}_0^0$. This is the solution of the non-local thermodynamic equilibrium unpolarized radiative transfer equation, which is calculated using scalar version of the ALI described in Section 3.3.1. The redistribution function to be used is $[\tilde{\mathcal{R}}^0_{0,a} + \beta_e \tilde{r}_e^{(0)}]$.

(ii) Using $\mathcal{I}_0^0$, calculate the single scattered source term for each component $\mathcal{S}^2_{Q,L}$ ($Q = 0, 1, 2$). It may be written as

$$\left[\tilde{\mathcal{S}}^2_{Q,L}\right]^{(1)}(\tau, x, \mu) \simeq \int_{-\infty}^{+\infty}\int_{-1}^{+1} \frac{\tilde{R}^2_Q(x, \mu, x', \mu')}{\varphi(x)} \tilde{\Gamma}^{20}_{Q0}(\mu')\, \mathcal{I}^0_0(\tau, x', \mu') \frac{\mathrm{d}\mu'}{2}\, \mathrm{d}x'. \tag{3.33}$$

The superscript 1 stands for single scattering.

(iii) The radiation field $\left[\tilde{\mathcal{I}}^2_Q\right]^{(1)}$ corresponding to each $\left[\tilde{\mathcal{S}}^2_{Q,L}\right]^{(1)}$ is calculated by calling a formal solver.

(iv) $\left[\tilde{\mathcal{I}}^2_Q\right]^{(1)}$ serves as a starting point for calculating the higher order terms. For order (n),

$$\left[\tilde{\mathcal{S}}^2_{Q,L}\right]^{(n)} \simeq \left[\tilde{\mathcal{S}}^2_{Q,L}\right]^{(1)} + \int_{-\infty}^{+\infty} \mathrm{d}x' \int_{-1}^{+1} \frac{\mathrm{d}\mu'}{2} \frac{\tilde{\mathcal{R}}^2_Q(x, \mu, x', \mu')}{\varphi(x)} \times \sum_{Q' \geq 0} \tilde{\Gamma}^{22}_{QQ'}(\mu') \left[\tilde{\mathcal{I}}^2_{Q'}\right]^{(n-1)}(\tau, x', \mu'). \tag{3.34}$$

The iteration is continued until a convergence criteria is satisfied. The component $\mathcal{I}_0^0$ is calculated only once in step (i).

Figure 3.1 shows the variation in maximum relative change of the Stokes I source vector component $(c_0^0)^n$ and of the surface polarization c_p^n as a function of iteration number. The quantities $(c_0^0)^n$ and c_p^n are defined as (see Sampoorna et al., 2011)

$$(c_0^0)^n = \max_{\tau_d, x, \mu} \left\{ \frac{|(\mathcal{S}^0_0)^{n+1}_{x\mu}(\tau_d) - (\mathcal{S}^0_0)^n_{x\mu}(\tau_d)|}{(\overline{\mathcal{S}}^0_0)^{n+1}_{x\mu}(\tau_d)} \right\}, \tag{3.35}$$

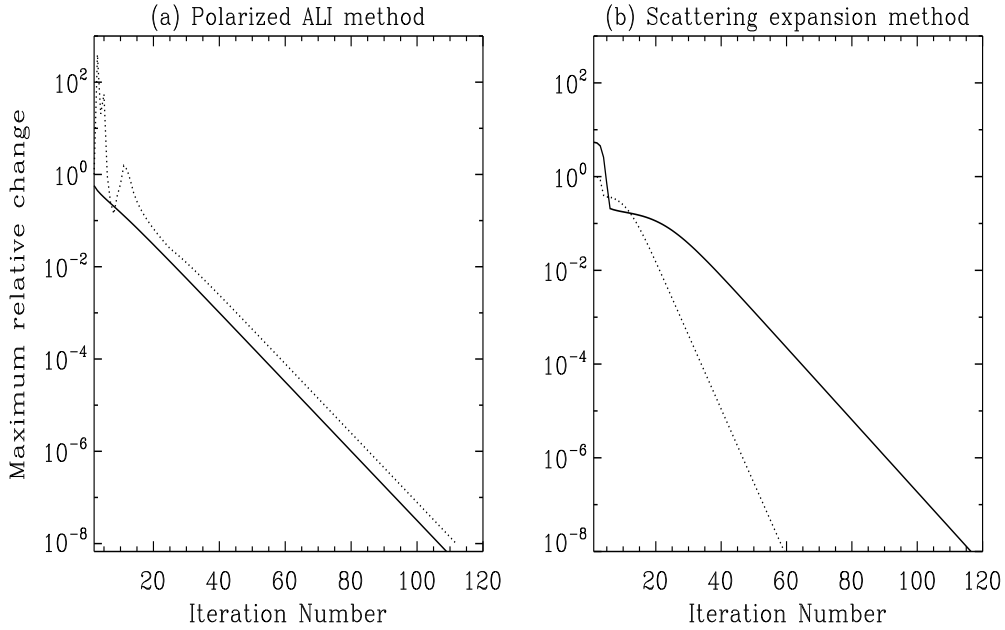

Figure 3.1: Maximum relative change of the Stokes I source vector component $(c_0^0)^n$ (solid line) and of the surface polarization c_p^n (dotted line) as a function of the iteration number. Model parameters are (T, a, ϵ, β_c, β_e, Γ_E/Γ_R) = (10^4, 10^{-3}, 10^{-4}, 0, 10^{-4}, 0). The panels (a) and (b) correspond to the polarized ALI method and the SEM, respectively.

with n the iteration index, τ_d a depth-grid point and

$$c_p^n = \max_{x,\mu} \left\{ \frac{|P_{x\mu}^{n+1} - P_{x\mu}^n|}{|P_{x\mu}^{n+1}|} \right\}, \tag{3.36}$$

where $P = Q/I$ is the degree of linear polarization at the surface. The convergence behavior of the polarized ALI and SEM is not much affected by the electron scattering redistribution. It remains somewhat similar to the corresponding pure atomic redistribution.

3.4 Electron Scattering Redistribution

Electron scattering is known to affect the shapes of the intensity profiles formed in early-type stars. The inclusion of the electron scattering as a redistribution mechanism would be necessary particularly when the polarization of lines is considered. In this section, we discuss the nature of the electron scattering redistribution and its rapid numerical evaluation.

3.4.1 Angle dependent electron scattering redistribution function

Dirac (1925) derived the angle-dependent redistribution function for scattering of low-energy photons ($h\nu < m_e c^2$) on electrons. Chandrasekhar (1950) drew at-

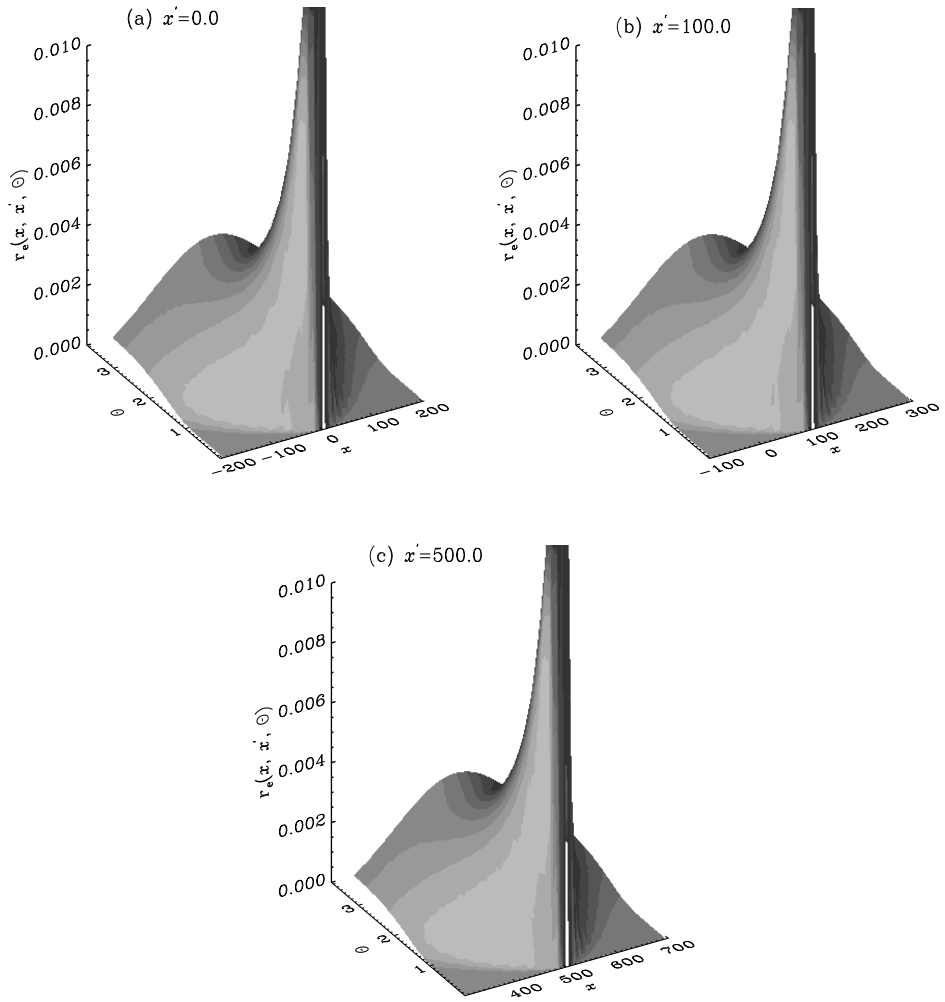

Figure 3.2: Surface plots of angle-dependent electron scattering redistribution functions for different incoming frequencies x'. The X-axis represents the outgoing frequency x, and the Y-axis the scattering angle Θ. Notice that the X-range in panels (a), (b) and (c) are different. These panels correspond, respectively, to incoming frequencies $x' = 0$, 100, and 500.

tention to the possibility of line-broadening by electron scattering and he assumed the anisotropy of the scattered radiation according to Rayleigh's phase function and arrived at the following expression (see Chandrasekhar, 1950, p.336) for angle-dependent electron scattering redistribution function

$$r_e(\nu, \nu', \Theta) = \sqrt{\frac{m_e c^2}{4\pi k T \nu^2 (1 - \cos\Theta)}} \exp\left[\frac{-m_e c^2 (\nu - \nu')^2}{4kT\nu^2(1 - \cos\Theta)}\right], \quad (3.37)$$

where ν' and ν are the frequencies of incident and scattered radiation, respectively, Θ is the scattering angle, k is the Boltzmann constant, c the velocity of light, and m_e and T are the electron mass and temperature, respectively. We provide below the laboratory-frame expression for the angle-dependent electron redistribution

function in atomic Doppler width units. Substituting the electron Doppler width $W = (\nu_0/c)\sqrt{2kT/m_e}$, and $\Delta\nu = \nu - \nu'$, with $\nu = \nu_0$ (Chandrasekhar, 1950), in Equation (3.37), we obtain

$$r_e(\nu, \nu', \Theta) = \frac{1}{2\sqrt{\pi}W \sin(\Theta/2)} \exp\left[\frac{-(\Delta\nu)^2}{4W^2 \sin^2(\Theta/2)}\right]. \tag{3.38}$$

Let $x = (\nu - \nu_0)/\Delta\nu_D$, where $\Delta\nu_D = (\nu_0/c)\sqrt{2kT/m_A}$, is the atomic Doppler width in standard notation. The electron redistribution function in these units can now be written as

$$\begin{aligned} r_e(x, x', \Theta) &= (\Delta\nu_D)^2 r_e(\nu, \nu', \Theta) \\ &= \frac{\Delta\nu_D}{2\sqrt{\pi}w \sin(\Theta/2)} \exp\left[\frac{-(x - x')^2}{4w^2 \sin^2(\Theta/2)}\right], \end{aligned} \tag{3.39}$$

where w is the ratio of electron to atomic Doppler widths and is given by $w \simeq 43\sqrt{A}$, with A being the atomic weight of the atom under consideration. For a helium atom, w is nearly equal to 80. The redistribution function obtained in Equation (3.39) should be normalized to profile function, which in the case of electron scattering is unity. Thus, the normalized angle-dependent redistribution function for electron scattering is simply the expression given in Equation (3.6). In Figure 3.2, we show surface plots of $r_e(x, x', \Theta)$ as a function of the scattered frequency x and the scattering angle Θ for incoming frequencies $x' = 0$, 100 and 500. The surface plots show double peak (forward and backward scattering) type of behavior for all chosen x' values. We see a sharp peak at $x = x'$ and $\Theta = 0$. From Equation (3.39), it can be seen that $r_e(x, x', \Theta)$ becomes a delta function for this choice of parameters. The forward-scattering peak has a value larger than the backward-scattering peak. The reason for this is that when $\Theta = \pi$, the function takes finite values, unlike the forward-scattering case. For Θ other than 0, the function $r_e(x, x', \Theta)$ behaves like a Gaussian function centered at $x = x'$, with a full width at half-maximum of $4w \sin(\Theta/2)\sqrt{\ln 2}$.

3.4.2 The Fourier azimuthal averages and coefficients of electron redistribution functions

The numerical methods described in Section 3.3 involve the azimuthal Fourier coefficients $\tilde{r}_e^{(Q)}$ for $Q = 0, 1, 2$. The moments of order $Q = 0$ are normalized to unity when integrated over all the incoming frequencies and angles, while the moments of orders $Q = 1$ and 2 are normalized to zero. In order to ensure an accurate normalization of $\tilde{r}_e^{(Q)}$ functions, we subdivide each frequency interval of a typical

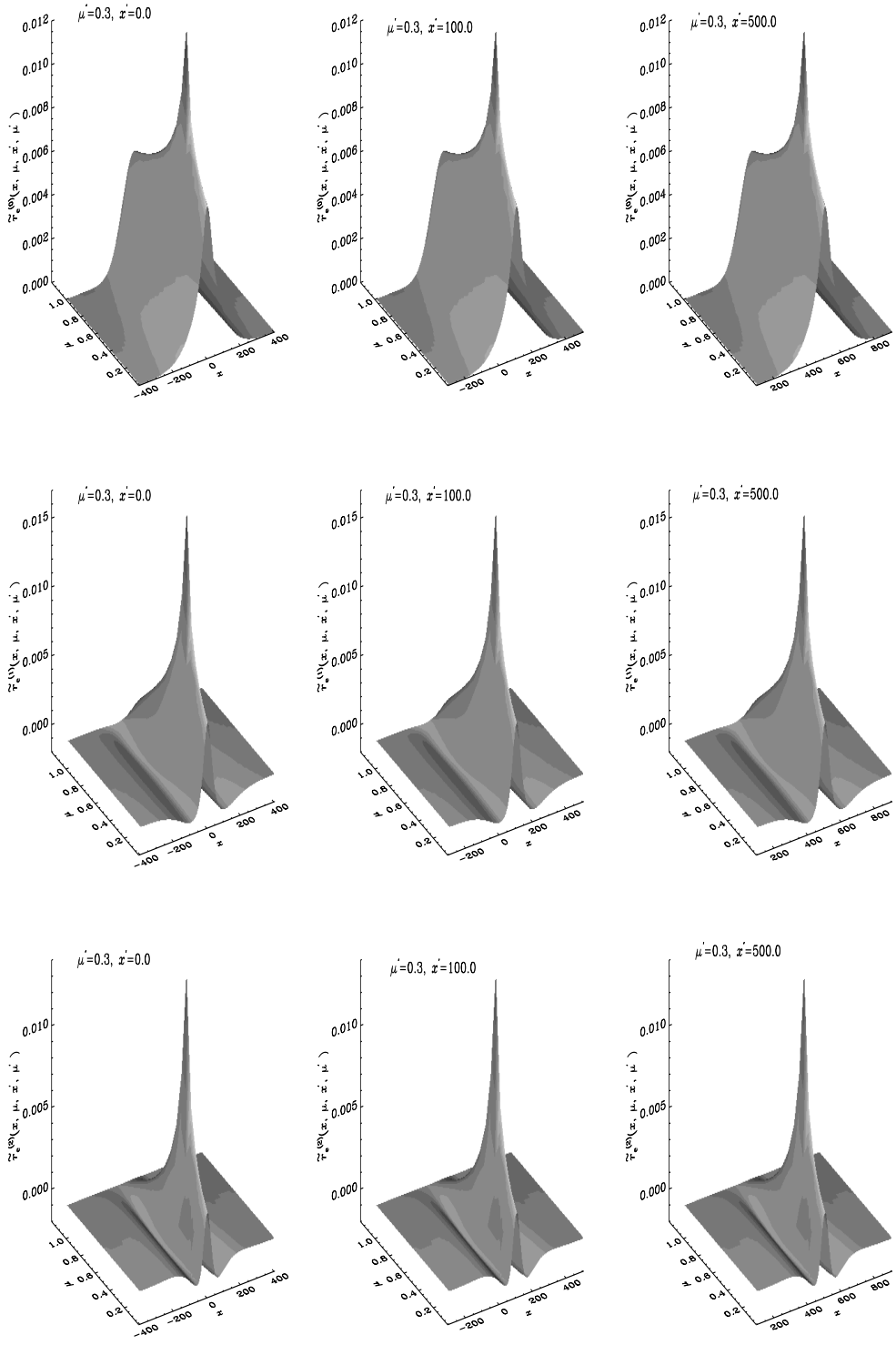

Figure 3.3: Surface plots of azimuth averaged electron redistribution functions with $Q = 0, 1, 2$. The X-axis represents the outgoing frequency x, and the Y-axis the outgoing direction μ. The incoming direction $\mu' = 0.3$. The left-hand column corresponds to the incoming frequency $x' = 0$, the middle column to $x' = 100$, and the right-hand column to $x' = 500$. Notice that $Q = 1, 2$ components can take negative values.

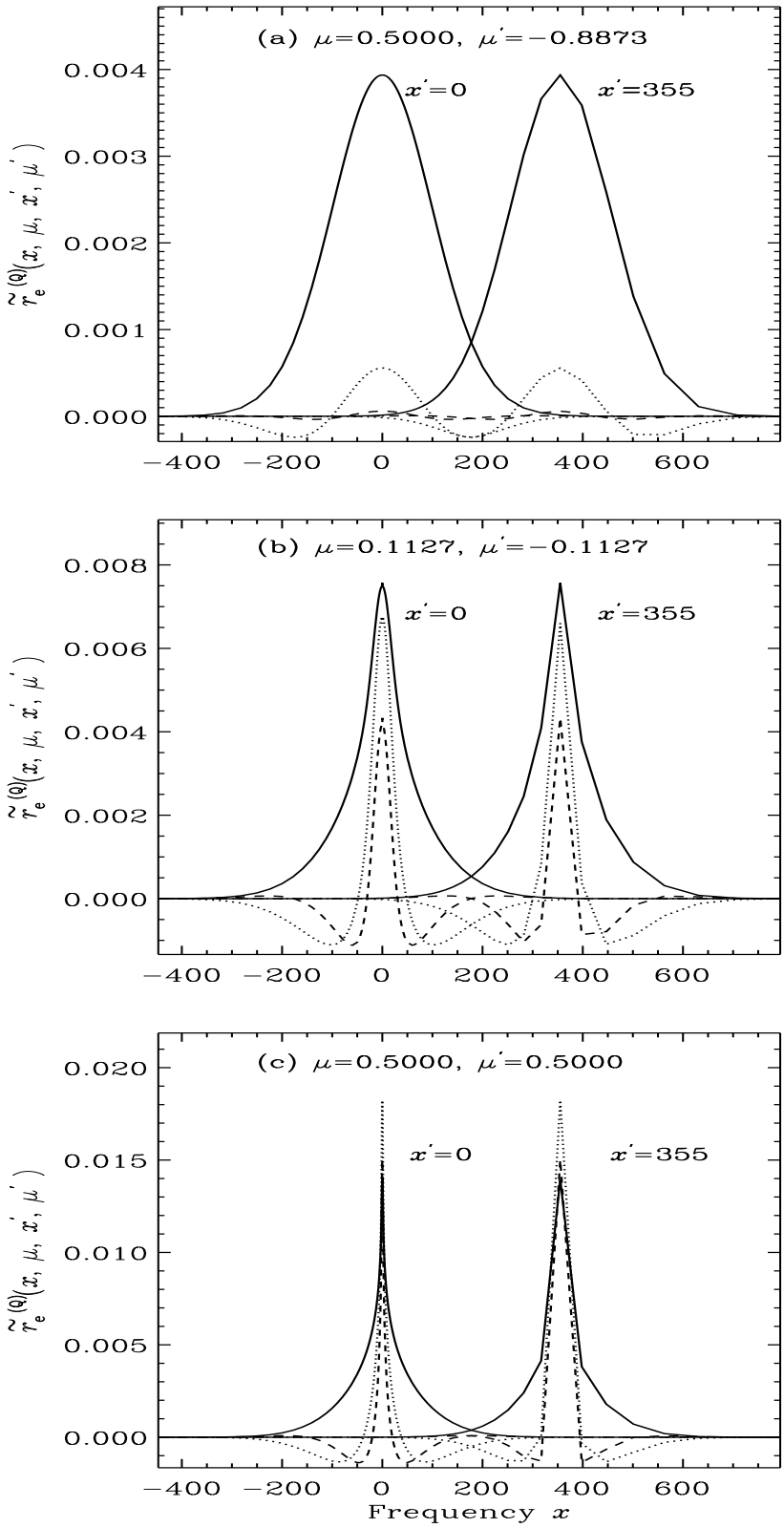

Figure 3.4: Azimuth averaged electron scattering redistribution function, plotted as a function of the outgoing frequency x, for different choices of μ, μ' and x'. Solid, dotted, and dashed curves correspond, respectively, to $Q = 0, 1$, and 2.

line radiative transfer frequency grid into a fine mesh of Simpson quadrature points. A seven-point Gaussian quadrature formula is used for the angular grid. In order to handle the peaks that occur in the forward-scattering situations (see Figures 3.3 and 3.4) we proceed in the following way. We consider a cut-off scattering angle $\Theta_{\rm cut-off} = 10^{-6}$ radians and assume that the NCES redistribution function keeps a constant value, given by its value at the cut-off, when $\Theta < \Theta_{\rm cut-off}$. We have verified that using a solid angle of 10^{-6} radians (or even 10^{-3} radians) the cut-off domain very insignificantly affects the normalization properties. The same property holds also for the emergent Stokes parameters. Therefore, the choice of this cut-off angle is not critical to the correctness of the results presented in this chapter. The tests performed with the cut-off angle show that 10^{-6} radians is a resonable choice.

In Figure 3.3, we show the surface plot of $\tilde{r}_{\rm e}^{(Q)}$ as a function of the outgoing frequency x and the outgoing direction μ for the incoming frequencies $x' = 0$, 100 and 500, when the incoming direction $\mu' = 0.3$. The functions $\tilde{r}_{\rm e}^{(0)}$ show frequency coherent peaks at $x = x'$ for all μ values. The widths of these peaks remain nearly constant for all values of x' and a given choice of μ and μ'. Further the $\tilde{r}_{\rm e}^{(0)}$ function has narrow peak at $\mu = \mu'$. The first and second moments $(Q = 1, 2)$ also exhibit similar behavior, except that they can take negative values. Figure 3.4 shows $\tilde{r}_{\rm e}^{(Q)}$ for all the three values $Q = 0, 1, 2$ as a function of the outgoing frequency x for different choices of (μ, μ') and for different incoming frequencies x'. The frequency $x' = 0$ and 355 are representative of the line center and wing behaviors, respectively. Figure 3.4 clearly shows the sharp peaks that appear in Figure 3.3 for all values of Q. From Figures 3.4(a) and 3.4(b), we observe that the coefficients $\tilde{r}_{\rm e}^{(Q)}$ decrease in magnitude with increasing Q. However, for the special case of backward-scattering (Figure 3.4(c)), the Fourier coefficients for $Q = 1$ and 2 can become larger than the corresponding $Q = 0$ coefficient.

3.5 Results and discussion

In this section, we present the results of computation using parametrized models. We consider isothermal self emitting constant property planar slabs characterized by (T, a, ϵ, β_c, β_e, Γ_E/Γ_R) in the standard notion. T and a give optical thickness and damping parameter, respectively. Each subsection pertains to the effect of an important parameter on the line formation. We illustrate our results through emergent intensity and polarization profiles. Also we relate them to important macroscopic quantities that are representative of a given model, namely the optical depth dependence of the intensity source function S_I and polarized source function S_Q. The ratio S_Q/S_I is a measure of the local anisotropy prevailing at different optical depths within the atmosphere.

For thick slab case by employing the Eddington-Barbier relation (see Faurobert, 1988; Nagendra et al., 1993), the emergent Stokes parameters can be obtained as

$$I(\tau = 0,\, x,\, \mu) = S_I(\tau = \mu/\varphi(x),\, x,\, \mu), \tag{3.40}$$

and

$$Q(\tau = 0,\, x,\, \mu) = S_Q(\tau = \mu/\varphi(x),\, x,\, \mu), \tag{3.41}$$

where S_I and S_Q are the Stokes source components S_0 and S_1 which are defined in Equation (3.2). The percentage of polarization is given (approximately) by

$$p(\tau = 0,\, x,\, \mu) = \frac{S_Q(\tau = \mu/\varphi(x),\, x,\, \mu)}{S_I(\tau = \mu/\varphi(x),\, x,\, \mu)} \times 100. \tag{3.42}$$

Since $S_I(\tau = \mu/\varphi(x),\, x,\, \mu)$ in Equation (3.42) is always positive, the sign of polarization depends on the sign of $S_Q(\tau = \mu/\varphi(x),\, x,\, \mu)$ only. Thus, the limb-darkened radiation field gives negative polarization and the limb-brightened radiation field gives positive polarization.

On the other hand, in the thin-slab case when the monochromatic optical depth of the medium is very small ($T\,\varphi(x)/\mu \ll 1$), the main contribution to the intensity and polarization at the surface comes from the center of the slab (Faurobert, 1987). In other words

$$I(\tau = 0,\, x,\, \mu) = S_I(\tau = T/2,\, x,\, \mu)\,\frac{T\,\varphi(x)}{\mu}, \quad \mu > 0 \tag{3.43}$$

and

$$Q(\tau = 0,\, x,\, \mu) = S_Q(\tau = T/2,\, x,\, \mu)\,\frac{T\,\varphi(x)}{\mu}, \quad \mu < 0, \tag{3.44}$$

for those frequencies that satisfy $T\,\varphi(x)/\mu \ll 1$. The percentage of polarization is given(approximately) by

$$p(\tau = 0,\, x,\, \mu) \simeq \frac{S_Q(\tau = T/2,\, x,\, \mu)}{S_I(\tau = T/2,\, x,\, \mu)} \times 100. \tag{3.45}$$

The ϵ parameter affects the line formation physically through inelastic collisional de-exitation of atoms. On the other hand, β_c affects spectral lines through absorption and emission of line radiation in overlapping continuum. Addition of β_e (electron scattering) introduces redistribution of line photons and hence quantitative difference in the wing polarization.

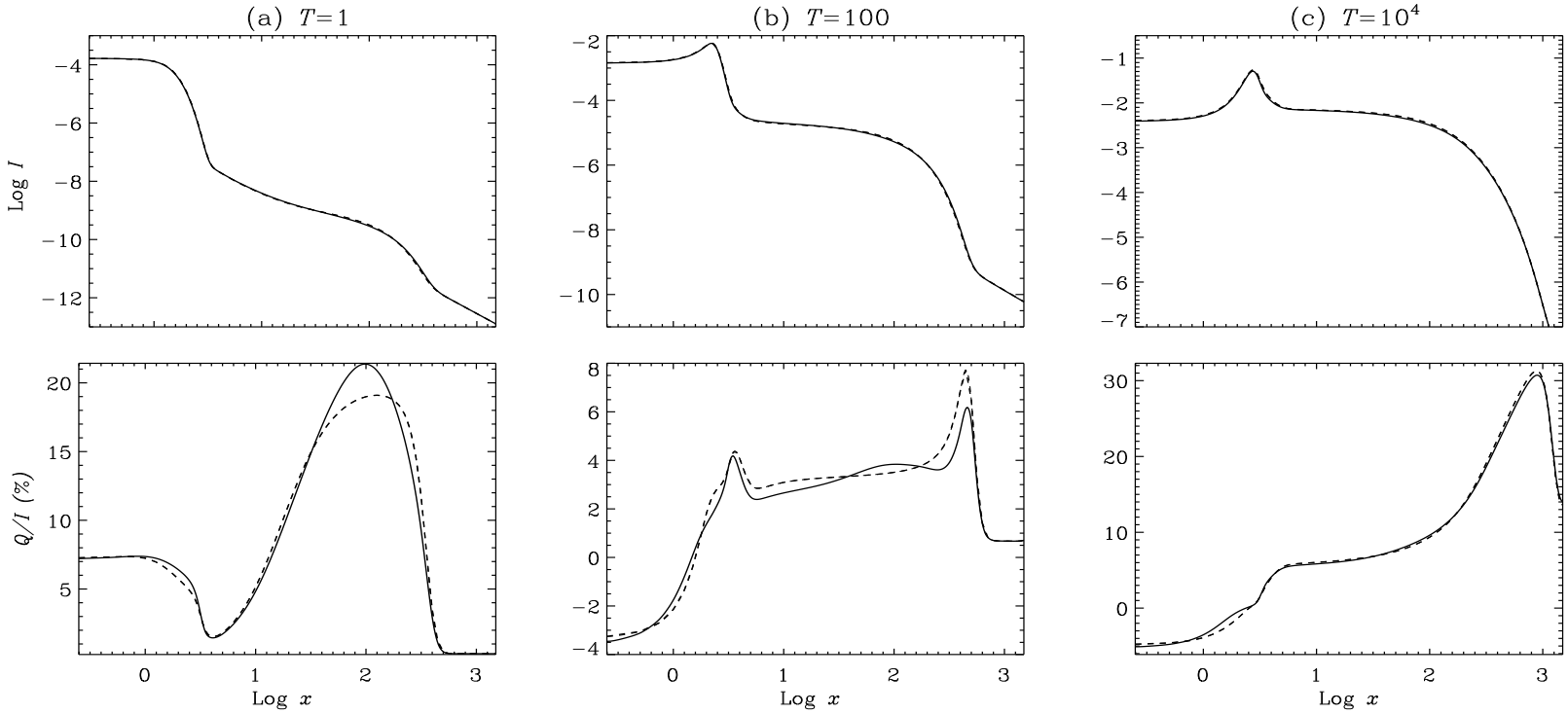

Figure 3.5: A comparison of emergent Stokes profiles at $\mu = 0.11$ for angle-dependent (solid line) and angle-averaged (dashed line) atomic PRD and NCES redistribution functions. The model parameters used are (a, ϵ, β_c, β_e, Γ_E/Γ_R) = (10^{-3}, 10^{-4}, 0, 10^{-4}, 0.05). Panels (a), (b) and (c) show the results for T = 1, 100, and 10^4, respectively.

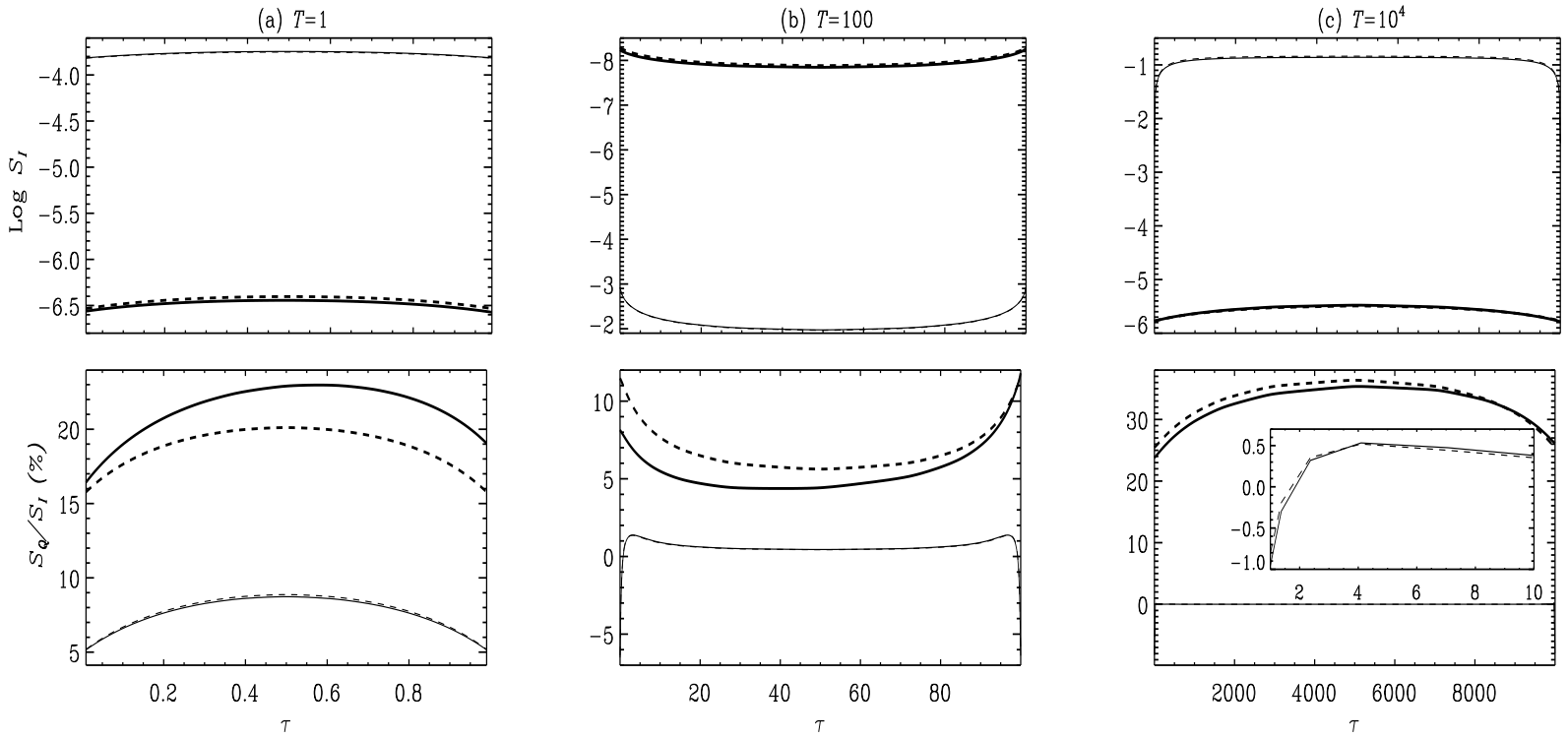

Figure 3.6: Plots of S_I and S_Q/S_I for $T = 1, 100$, and 10^4. Solid and dashed lines represent angle-dependent and angle-averaged cases. The thin lines correspond to $x = 0$, and the thick lines to the frequency of far wing secondary maxima in Q/I shown in Figure 3.5. The secondary peak occurs approximately at $x = 100, 500$, and 800 for $T = 1, 100$, and 10^4, respectively. The other model parameters are the same as in Figure 3.5. The inset in panel (c) shows the variation in S_Q/S_I near the surface layers (not visible in the scale adopted for the main figure).

3.5.1 Stokes profiles with angle-averaged and angle-dependent partial frequency redistribution and electron scattering

In Figure 3.5, we compare the emergent I and Q/I profiles at $\mu = 0.11$ for angle-dependent and angle-averaged atomic PRD and NCES functions. Both the solutions are calculated using the SEM discussed in Section. 3.3.2. The PRD used is a mixture of atomic $r_{\rm II}$ and $r_{\rm III}$ with Γ_E/Γ_R=0.05. The depolarizing elastic collision rate $D^{(2)}$ = 0.5 Γ_E. Figures 3.5(a) and (b) clearly show that the angle-averaged and angle-dependent solutions differ considerably, and in a potentially measurable way. Further the angle-averaged emergent polarization is smaller or larger than the corresponding angle-dependent cases, depending on the value of the optical thickness T of the slab. This difference is seen in pure atomic case also, and the reasons for the differences are discussed in Sampoorna et al. (2011). As in the pure atomic case, the angle-averaged and angle-dependent solutions differ only in the thin-slab case. For thick slabs, the differences are small (see Figure 3.5c). Hence, in practical applications one can work with angle-averaged functions.

The differences between the results for angle-averaged, and angle-dependent NCES was pointed out by Rangarajan (1999). Our computations confirm his conclusions. However, we consider the effects of collisions in atomic redistribution through a combination of $r_{\rm II}$ and $r_{\rm III}$ using an exact treatment of collisional frequency redistribution (according to the formulation of Domke & Hubeny, 1988; Bommier, 1997a). Further we consider large frequency bandwidths ($x_{\rm max} \simeq 1500$ atomic Doppler widths), so that the far wing behavior of NCES is clearly seen. The inner parts of the line ($x < 10$) seem to be controlled by atomic redistribution, whereas the wings of the ($I, Q/I$) profiles ($x > 10$) are controlled by NCES. The I profiles have a characteristic behavior of double slopes—in the wings—one due to atomic and the other due to electron scattering. The appearance of the line center peak and the near wing PRD peak in Q/I depend on the optical thickness of the medium.

In our computations with angle-averaged and angle-dependent NCES, we have obtained a secondary maxima with higher polarization, occurring in the very far wings ($x \gtrsim 100$). The amplitude and the width of these peaks in Q/I depend sensitively on β_e and T. Such peaks are noticable in the pure line case without a background continuum, and no radiation incident on the boundaries. Incidentally, such peaks were not noticed in the very far wings in the earlier works by Nagendra et al. (1993) and Rangarajan (1999) on NCES, possibly because of short frequency bandwidths, small β_e and imposition of unpolarized radiation as the boundary condition, which they used in their calculations. In order to understand quantitatively the appearance of these peaks in Q/I, we have made plots of S_I and the anisotropy factor S_Q/S_I in Figure 3.6. A comparison of angle-averaged and angle-dependent

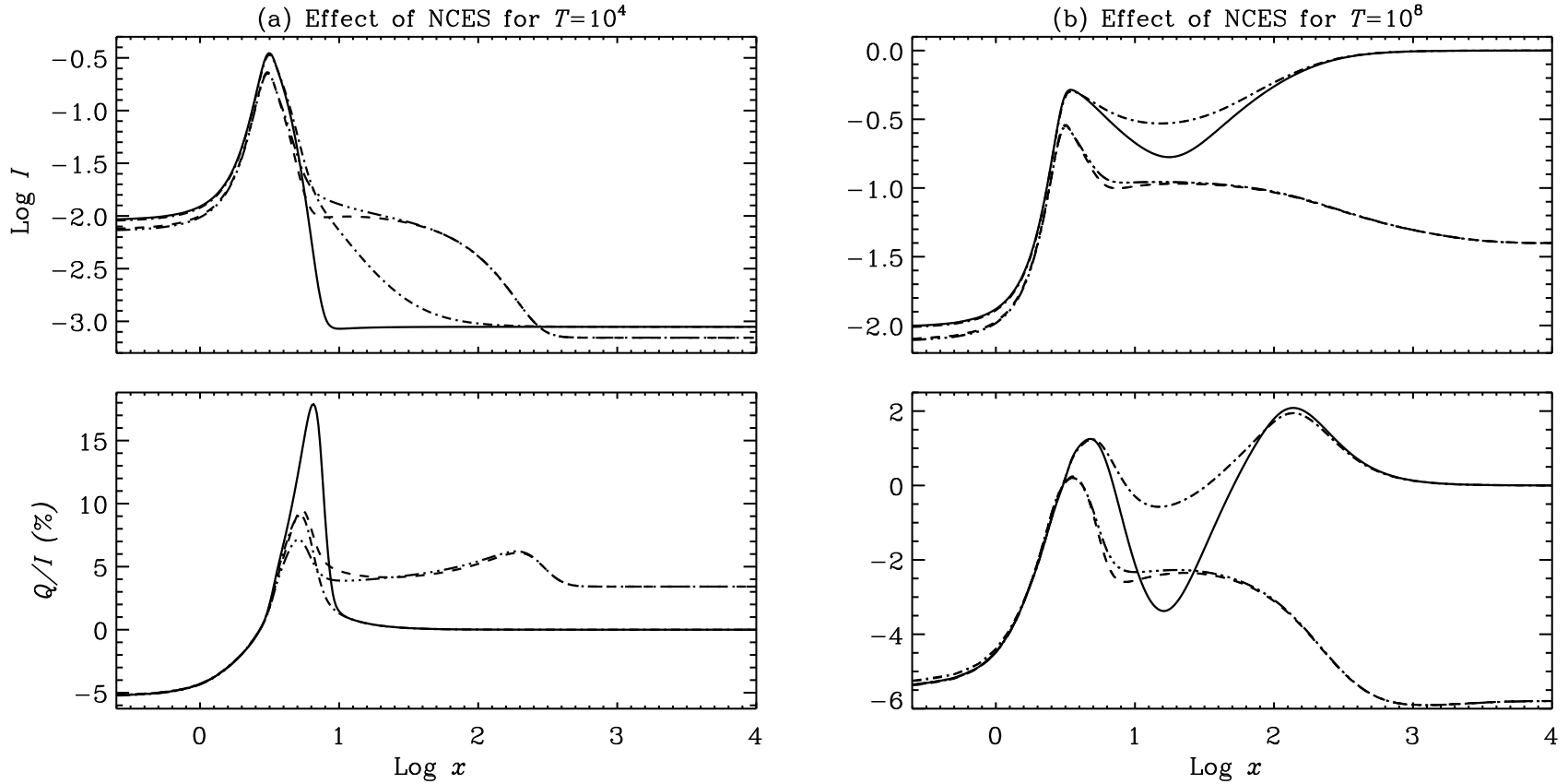

Figure 3.7: The effect of including the electron scattering parameter β_e on line polarization. Panel (a) is for a slab of optical thickness $T = 10^4$ and panel (b) is for $T = 10^8$. The other model parameters are (a, ϵ, β_c, β_e) = (10^{-3}, 10^{-4}, 10^{-8} , 10^{-5}). Different line types are as follows: solid line–pure $r_{\rm II}$ case, dashed line –$r_{\rm II}$ PRD function and NCES, dot-dashed line –a combination of $r_{\rm II}$ and $r_{\rm III}$ with Γ_E/Γ_R = 0.05, and dash-triple-dotted –PRD with ($r_{\rm II}$, $r_{\rm III}$) and NCES.

results is shown for the line center frequency and also for the frequency at which the secondary maximum of polarization occurs due to NCES. Angle-dependent S_Q/S_I shows a slight asymmetry about the slab center at the frequency positions of far wing peaks.

It is unlike the pure atomic redistribution where S_Q/S_I remains symmetric in a self-emitting constant property media. The symmetry is also maintained in the angle-averaged case, with and without NCES. From Figure 3.6 we can see that the value of Q/I at secondary maxima satisfies the relation given in Equation (3.45), to a good approximation, whenever the condition $T\,\varphi(x)/\mu \ll 1$ holds good.

3.5.2 Effect of non-coherent electron scattering

Figure 3.7 shows the effect of including NCES and its influence on atomic line polarization for slabs of different thickness. From Figure 3.7(a), we see that electron scattering has similar effects as that of $r_{\rm III}$ function (i.e. collisional redistribution) in the near wing region, $x \sim 5-6$. Electron scattering behaves like a depolarizing mechanism, as in the case of $r_{\rm III}$ function. However, $r_{\rm III}$ does not produce a far wing peak, electron scattering produces a peak in the frequency range $190 < x < 320$. In the thick-slab case, the appearance of the secondary peak is related to the electron scattering optical depth ($T^e = \beta_e\,T$) satisfying the condition $0.1 \lesssim T^e \lesssim 1$. However, the appearance of secondary peaks in thin-slab cases need not satisfy this condition (see e.g. Figures 3.5a, b).

From Figure 3.7(b), we can see that the shape of the Q/I profiles is completely controlled by the electron scattering for all frequencies $x \gtrsim 8$. The solid and dot-dashed curves in Figure 3.7 show that in the pure atomic case $r_{\rm III}$ controls the shapes of $(I, Q/I)$ wing profiles in a collision-dominated plasma. On the other hand, the electron scattering, when it becomes significant, completely controls the shapes of the $(I, Q/I)$ wing profiles, irrespective of the atomic redistribution mechanism, or the presence of collisions (see dashed and dash-triple-dotted curves in Figure 3.7). In the very far wings, the electron optical depth dominates over the monochromatic line optical depth resulting in the complete dominance of NCES in the line formation process, producing characteristic changes in the $(I, Q/I)$ profiles as described above. The frequency coherence of PRD localizes photons in these far wing frequencies, which are in turn scattered by free electrons. The electron scattering process Doppler-redistributes these line photons during successive scattering events. Each electron scattering imparts a large frequency shift to the scattered photon and helps a line core photon to escape through a wing frequency.

In Figure 3.8, we show the intensity and polarization profiles for angle-averaged atomic PRD ($r_{\rm II}$) and NCES when the parameter β_e is varied. It clearly shows the

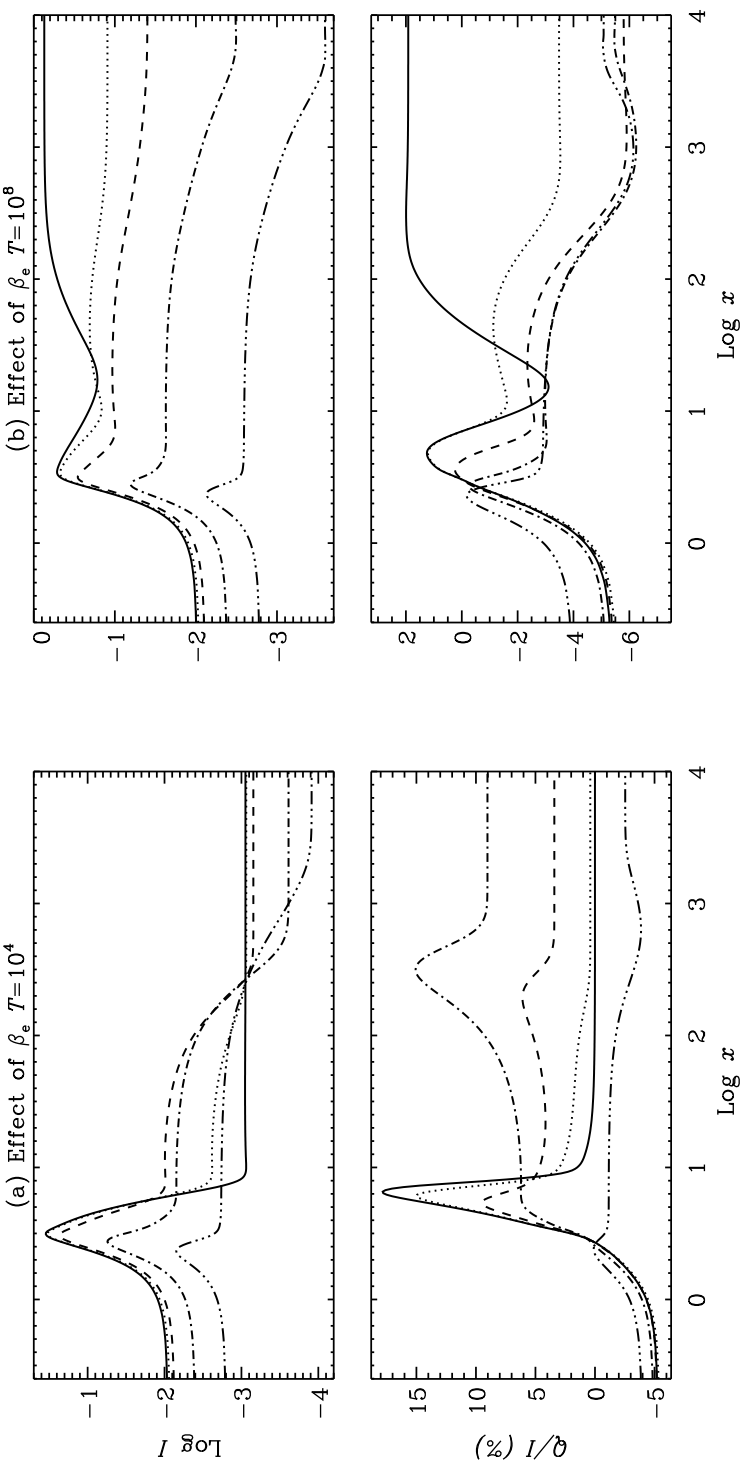

Figure 3.8: The effect of varying the parameter β_e. Panel (a) is for optical thickness $T = 10^4$ and panel (b) is for $T = 10^8$. The other model parameters are (a, ϵ, β_c, Γ_E/Γ_R) = (10^{-3}, 10^{-4}, 10^{-8}, 0). Different line types are solid line ($\beta_e = 10^{-8}$), dotted line ($\beta_e = 10^{-6}$), dashed line ($\beta_e = 10^{-5}$), dot-dashed line ($\beta_e = 10^{-4}$), dash-triple-dotted line ($\beta_e = 10^{-3}$).

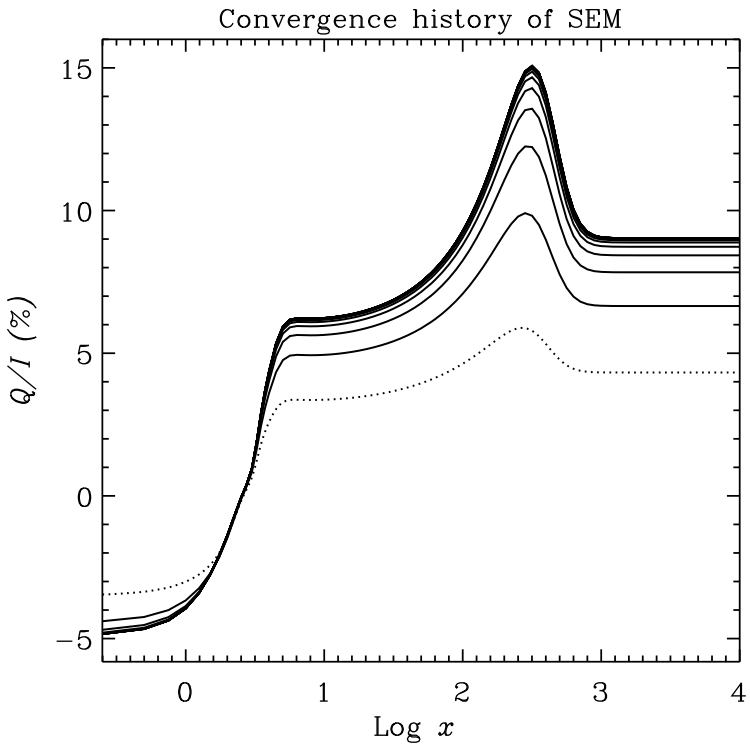

Figure 3.9: The convergence history of the polarization Q/I in the SEM. The dotted line represent the single scattered solution. The model parameters used are the same as those for the dot-dashed line in Figure 3.8(a).

effects of NCES in the wing region. The panel (a) is for optical thickness $T = 10^4$ and the panel (b) is for $T = 10^8$. As β_e is increased, i.e. when the electron scattering is made more dominant, with respect to atomic scattering we see a gradual decrease in the polarization of the near wing PRD peak, and a shift of the peak towards the line center. In Figure 3.8(a), we see the secondary peak in the range $190 < x < 320$ when the condition $0.1 \lesssim T^e \lesssim 1$ is satisfied. An analogous behavior is observed, when β_e is kept fixed and T is varied. In Figure 3.8(b), for the semi-infinite case, we see a prominent and nearly constant value of polarization of around $\sim 2\%$ in the far wing region ($x > 300$) when $\beta_e = 10^{-8}$ namely for which $\beta_e T \sim 1$. Also for this case, the background continuum opacity β_c is the same as that of β_e. Hence instead of a peak structure, we see a constant value of polarization in the far wings. However, in both cases (see, Figures 3.8a and b) as β_e is increased from 10^{-8} to 10^{-3}, the intensity profiles become more deeper. When electron scattering is a dominant scattering mechanism (as for example in the atmospheres of early-type stars or supernova ejecta), β_e can take values like 10^{-3}. In such cases electron scattering affects not only the wings, but also the entire line profile (see e.g. the dash-triple-dotted curve in Figure 3.8).

The secondary peak arising due to NCES is seen for all optical thickness satisfying the condition $0.1 \lesssim T^e \lesssim 1$. Our numerical experiments with a range of values

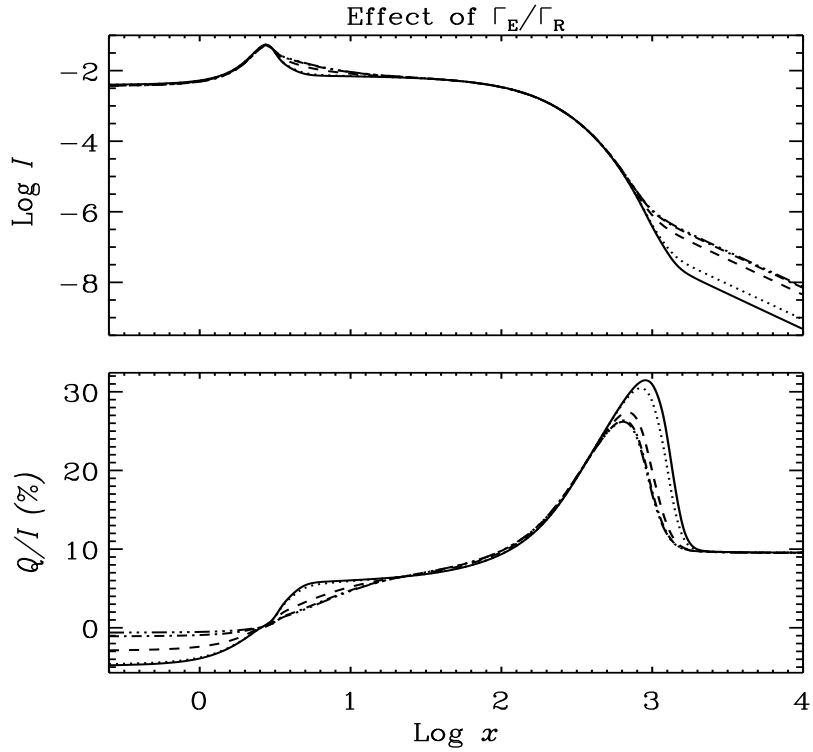

Figure 3.10: Effect of Γ_E/Γ_R. The emergent I and Q/I profiles at $\mu = 0.11$ are computed for the angle-averaged PRD and NCES. Different line types are solid line ($\Gamma_E/\Gamma_R = 0.05$), dotted line ($\Gamma_E/\Gamma_R = 0.1$), dashed line ($\Gamma_E/\Gamma_R = 1$), dot-dashed line ($\Gamma_E/\Gamma_R = 5$) and dash-triple-dotted line ($\Gamma_E/\Gamma_R = 10$). Other model parameters are (T, a, ϵ, β_e, β_c) = (10^4, 10^{-3}, 10^{-4}, 10^{-5}, 0).

of β_e and T, which satisfy the above said condition, show that the amplitude of the secondary peak in the Q/I profile decreases with an increase in optical thickness. However, the width of the peak increases as we go to higher optical thicknesses. In order to explore the presence of a strong secondary Q/I peak in the very far wings, we show in Figure 3.9 the convergence history of the ratio Q/I obtained using SEM. It also illustrates the convergence properties of the SEM. The single scattered solution is close to the converged solution except for very large frequencies and a few iterations are needed to reach the converged solution. The amplitude of the secondary peak that arises due to NCES is fairly weak in the single scattered solution (dotted line in Figure 3.9). Thus, the secondary peak is mainly due to transfer effect (multiple scattering).

3.5.3 Effect of elastic collisions

As the value of Γ_E is changed, the relative contributions of r_{II} and r_{III} also changes. Nagendra (1994) and Nagendra et al. (2002) have shown that the wings of intensity I and the linear polarization profiles are quite sensitive to the depolarizing collisions. Figure 3.10 shows the Stokes parameter I and the ratio Q/I calculated with

the SEM using the angle-averaged redistribution functions and NCES. The factor Γ_E/Γ_R is varied from 0.05 to 10. For $D^{(2)}$ we assume the relation $D^{(2)} = 0.5 \times \Gamma_E$. The polarization amplitude at the line center and the PRD peak in the near wing region decreases with increase in Γ_E/Γ_R which is also seen in the pure atomic case (Nagendra et al., 2002). However, the polarization of the secondary peak arising due to NCES also shows a similar behavior. Further we see a shift in the position of the secondary Q/I peak towards lower frequencies as the ratio Γ_E/Γ_R increases. The intensity profiles are sensitive to the collisions only in the far wing frequency regions near and beyond the secondary peak position in Q/I. This is in contrast to the pure atomic case, where the effects of Γ_E/Γ_R are felt right from the near wing frequencies onwards (see Figure 7 of Nagendra et al., 2002).

3.5.4 Effect of non-coherent electron scattering on intrinsically unpolarized atomic lines

Figure 3.11 shows the emergent I and Q/I profiles at $\mu = 0.11$ computed with angle-dependent atomic PRD and NCES functions. The PRD used is a mixture of atomic $r_{\rm II}$ and $r_{\rm III}$ with Γ_E/Γ_R=0.05. The depolarizing elastic collision rate $D^{(2)}$ = 0.5 Γ_E. In Figure 3.11 we consider atmospheric slab of different optical thickness and the corresponding electron scattering parameter β_e is chosen such that electron scattering optical depth $T^e = \beta_e T = 1$. Further we study three different cases namely, a) polarized atomic line with NCES (solid line), b) intrinsically unpolarized atomic line with NCES (dotted line), and c) polarized atomic line without NCES (dashed line). From Figures 3.11(a), (b) and (c) we see that the secondary peak in Q/I arises purely as an effect of NCES irrespective of whether the atomic line is polarized or not. In the thin slab case (optical thickness $T \leqslant 100$) the inclusion of NCES affects not only the wings but also the line center. In Figures 3.11(a) and (b) when the intrinsic polarization of the atomic line is zero and the effects of NCES are included (the dotted lines) then we see that the emergent polarization is zero for frequencies $x \lesssim 3$ and is non-zero for other frequencies. Further, for the thick slab case Figure 3.11(c) though the electron scattering parameter is very small ($\beta_e = 10^{-8}$) its effects are seen at frequencies $x \gtrsim 200$.

3.5.5 Effect of non-coherent electron scattering and continuum absorption

Figure 3.12 shows the effect of NCES and continuum absorption coefficient (β_c) on line polarization. We consider unpolarized atomic line for this study so that the effects of NCES and continuum can be clearly seen. In Figure 3.12 we fix the value

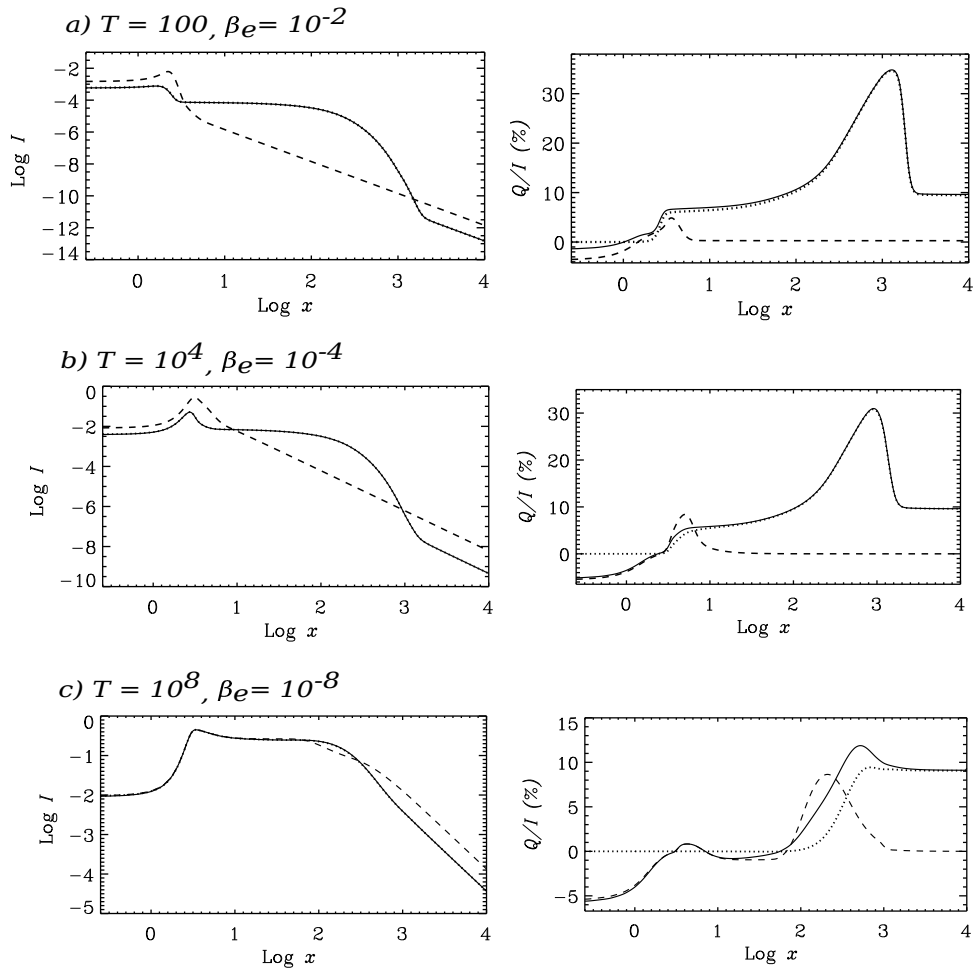

Figure 3.11: A comparison of emergent Stokes profiles at $\mu = 0.11$ for different optical thicknesses. The angle-dependent atomic PRD and NCES redistribution functions are used. The model parameters used are (a, ϵ, β_c, Γ_E/Γ_R, B) = (10^{-3}, 10^{-4}, 0, 0.05, 1). Panels (a), (b) and (c) show the results for different optical thickness T and β_e. See Section 3.5.4 for line types and details.

of β_e ($= 10^{-4}$) and vary β_c. We notice that the shapes of the Stokes profiles are controlled by the relative values of β_e and β_c whichever is dominant. Rangarajan (1999) showed that even the value of Q/I at the line center of the polarized atomic line is sensitive to β_c. However, in our case, as the atomic line is intrinsically unpolarized, β_c does not affect the line core region. From Figure 3.12 we see that when β_c is dominant it depolarizes the wing polarization originally created by NCES. However, when β_e is dominant it polarizes the atomic line in the far wing region.

3.6 Conclusions

The effects of electron scattering on atomic line polarization are studied. The decomposition technique developed by Frisch (2010) has been extended to the case of

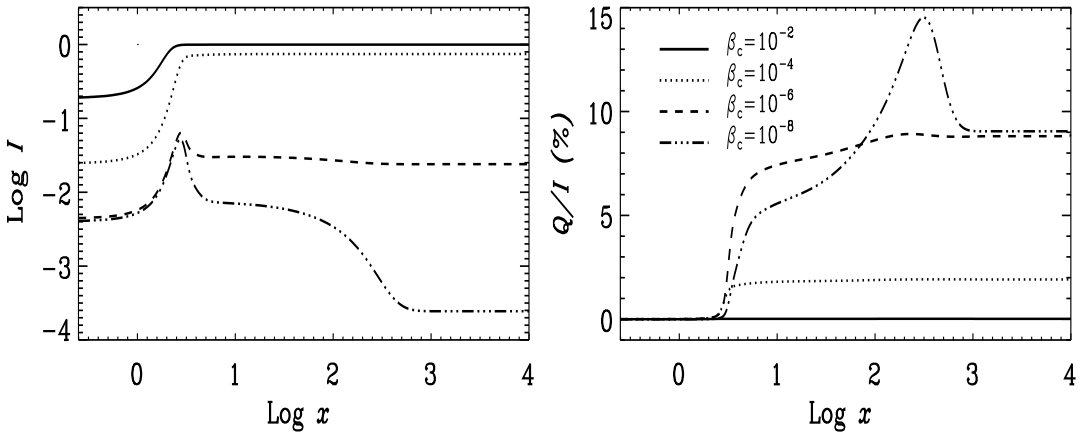

Figure 3.12: Effect of variation of the parameter β_c. The other model parameters are (T, a, ϵ, β_e, Γ_E/Γ_R, B) = (10^4, 10^{-3}, 10^{-4}, 10^{-4}, 0.05, 1). Different line types correspond to: solid line ($\beta_c = 10^{-2}$), dotted line ($\beta_c = 10^{-4}$), dashed line ($\beta_c = 10^{-6}$), and dash-triple-dotted line ($\beta_c = 10^{-8}$).

electron scattering. Two numerical methods, namely an ALI-type method and the other one based on Neumann series expansion, have been developed to solve the transfer equation including electron scattering. The SEM is of great use particularly in problems of large dimensionality (very large number of frequency, angle, and depth grid points). The NCES problem is one such example, which requires a large number of frequency and angle points. The problem becomes particularly difficult when angle-dependent PRD and electron scattering are considered. The SEM takes less computing time and memory as compared to the conventional ALI-type methods. Both these new methods are far superior (in terms of memory and computing time) to the traditional solution methods used so far for solving the same problem. A systematic study of the polarized line formation in a standard two-level picture, but including an exact treatment of electron scattering mechanism is undertaken. When electron scattering becomes important, it drastically affects the line profile, in particular, the line wings. An interesting feature of electron scattering is the generation of a strong secondary maxima in the Q/I profile (several hundred Doppler widths away), which can be interpreted in terms of radiative transfer effects. For $T \gg 1$ this peak appears when the electron optical depth lies between 0.1 and 1. Our study clearly shows that a correct treatment of electron scattering redistribution becomes necessary (either through the use of angle-averaged or angle-dependent functions), when modeling stellar spectral line polarization, where electron scattering forms an important source of opacity.

For the studies in this chapter we considered a simple two-level atomic system. In the next chapter we undertake studies with two-term atomic system and two-level system with interference between hyperfine levels. We study the impact of using

angle-dependent redistribution functions in these cases by comparing the emergent Stokes profiles obtained when angle-averaged functions are used.

Chapter 4

Quantum interference with angle-dependent partial frequency redistribution*

An Overview

Angle-dependent partial frequency redistribution (PRD) matrices represent the physical redistribution in the process of light scattering on atoms. For the purpose of numerical simplicity, it is a common practice in astrophysical literature to use the angle-averaged versions of these matrices, in the line transfer computations. The aim in this chapter is to study the combined effects of angle-dependent PRD and the quantum interference phenomena arising either between the fine structure (J) states of a two-term atom or between the hyperfine structure (F) states of a two-level atom. We restrict our attention to the case of non-magnetic and collisionless line scattering on atoms. A rapid method of solution based on Neumann series expansion is developed to solve the angle-dependent PRD problem including quantum interference in an atomic system. We discuss the differences that occur in the Stokes profiles when angle-dependent PRD mechanism is taken into account.

4.1 Introduction

The Second Solar Spectrum (Stenflo, 1996a; Stenflo & Keller, 1997; Gandorfer, 2000, 2002, 2005) shows several lines which are polarized due to scattering of anisotropic radiation on atoms. Some of the strong lines such as Ca II H and K, Mg II h and k and the Ca I 4227 Å serve as probes of the scattering processes taking place in the solar atmosphere. We know that the physics of light scattering on

*The contents of this chapter are based on Supriya et al. (2013b)

atoms is fully contained in a quantity called PRD matrix. It describes the correlations between the frequency, angle, and polarization of the incoming and outgoing radiation. The PRD effects are considerably strong in the wings of the lines. For the sake of numerical simplicity, angle-averaged versions of the PRD functions are often used in line transfer computations. However, a correct treatment of line scattering requires the use of angle-dependent PRD functions which retain the angle-frequency correlations intact.

The use of angle-dependent PRD functions in the line transfer equation dates back to Dumont et al. (1977) and Faurobert (1987), who considered the non-magnetic resonance scattering on atoms. The angle-dependent PRD functions in the case of magnetic scattering (Hanle effect) were considered by Nagendra et al. (2002, 2003). These authors solved the transfer problem in the Stokes vector basis. The treatment of angle-averaged PRD allows certain level of simplification. Basically, the concerned redistribution matrix (RM) that describes line scattering can be written as a product of a phase matrix (which describes the full polarization and the angular correlations), and the angle-averaged redistribution function (which contains the frequency correlations). Such a factorized form for the RM (called hybrid approximation) allowed considerable numerical simplification. Nevertheless, the use of Stokes vector basis kept the inextricable coupling in polarization between the incoming and outgoing rays, making the solution of the concerned transfer problem a time-consuming process. Frisch (2007) introduced an efficient decomposition method based on the expansion of the phase matrix in terms of the so-called irreducible spherical tensors for polarimetry introduced by Landi Degl'Innocenti (1984). This decomposition technique is similar to the earlier methods proposed by Faurobert-Scholl (1991) and Nagendra et al. (1998) based on the Fourier azimuthal expansion of the phase matrix. However, the decomposition technique of Frisch (2007) is mathematically more elegant and algebraically less tedious. Such a decomposition technique allowed the application of the polarized approximate lambda iteration method to obtain rapid solution of the concerned transfer problem in the irreducible basis (see e.g. Nagendra et al., 1998).

Frisch (2009) presented a decomposition technique for the Hanle scattering problem with angle-dependent PRD. This technique makes use of both the irreducible spherical tensor expansion of the Hanle phase matrix and the Fourier azimuthal expansion of the angle-dependent PRD function. The corresponding non-magnetic case was discussed in Frisch (2010). Recently these powerful techniques were used by Sampoorna et al. (2011), Sampoorna (2011b), Nagendra & Sampoorna (2011), and Supriya et al. (2012) to solve different problems of polarized line formation with angle-dependent PRD. These techniques, in a modified form (suitable to handle scattering in multi-D media, as well as explicitly angle-dependent PRD), are presented

in Anusha & Nagendra (2011b, 2012). They are subsequently used in Supriya et al. (2013a) to solve the Hanle transfer problem in 1D media.

All the papers mentioned above considered the case of a two-level atom model. In this chapter, we extend the above-mentioned techniques to the case of two types of atomic systems. One of them is a two-term atom arising due to fine structure splitting of atomic states, which result in a multiplet. The other atomic system is a two-level atom with hyperfine structure splitting (HFS) of both the upper and lower J-levels taken into account. The scattering in a two-term atom is affected by the interference between the fine structure states - known as J-state interference. The relevant RM that takes into account J-state interference in the upper term was derived by Smitha et al. (2011b) which is essentially an angle-dependent PRD matrix. However, an angle-averaged version of this matrix was used by Smitha et al. (2011a) in line transfer computations in the absence of a magnetic field. The scattering in a two-level atom with HFS is affected by the interference between the F-states. In Smitha et al. (2012b), the relevant RM was derived taking into account the interference between the F-states of the upper J-level, but an angle-averaged version of this matrix was used in Smitha et al. (2012b) in the line transfer computations. The purpose in this chapter is to solve the transfer problem using angle-dependent RM derived for the processes of the J-state interference as well as F-state interference.

In Smitha et al. (2011a), an operator perturbation method was used to solve the transfer problem. In recent years, a faster method of solving the polarized transfer equation is developed based on Neumann series expansion (see Frisch et al., 2009). It is known as scattering expansion method (SEM). Sampoorna et al. (2011); Nagendra & Sampoorna (2011); Sowmya et al. (2012); Supriya et al. (2012) have applied this method to a variety of theoretical problems. In Smitha et al. (2012b) an, angle-averaged version of the SEM was used to solve the transfer equation. In the present chapter, we propose to apply the SEM to solve the radiative transfer equation with angle-dependent RM derived for the J-state interference as well as the RM derived for the case of F-state interference.

In Section 4.2, we present the governing equations of the problem. In Section 4.3, we present the SEM applied to the problem at hand. Section 4.4 is devoted to a description of the results. In Section 4.5, we present the conclusions.

4.2 Governing Equations

In this section, we describe basic equations necessary to compute Stokes profiles for the scattering on an atomic system with an unpolarized lower level. The relevant

transfer equation for the non-magnetic case in the vector form is given by

$$\mu \frac{\partial \boldsymbol{I}(\tau, x, \mu)}{\partial \tau} = [\phi(x) + r][\boldsymbol{I}(\tau, x, \mu) - \boldsymbol{S}(\tau, x, \mu)], \tag{4.1}$$

where $\mu = \cos\theta$ with θ being the colatitude measured with respect to the normal in a slab atmosphere. $\boldsymbol{I} = (I, Q)^{\mathrm{T}}$ and $\boldsymbol{S} = (S_I, S_Q)^{\mathrm{T}}$ are the Stokes vector and the total source vector respectively. The Stokes Q is positive when electric vector vibrations are perpendicular to the solar limb. r is the ratio of continuum to the frequency-integrated line absorption co-efficient. $\phi(x)$ is the combined profile function for the atomic system under investigation. For the case of a two-term atom, it is given by Equation (10) of Smitha et al. (2011a). For the case of a two-level atom with HFS, $\phi(x)$ is given by Equation (7) of Smitha et al. (2012b). τ is the line optical depth scale defined by $d\tau = -k_M dz$, where k_M is the frequency-integrated line absorption coefficient for the multiplet. k_M is given by Equation (8) of Smitha et al. (2011a) in the case of a two-term atom and by Equation (6) of Smitha et al. (2012b) in the case of a two-level atom with HFS. x is the reduced frequency expressed in Doppler width units. The total source vector $\boldsymbol{S}$ can be expressed as

$$\boldsymbol{S}(\tau, x, \mu) = \frac{\phi(x)\boldsymbol{S}_l(\tau, x, \mu) + r\boldsymbol{S}_c}{\phi(x) + r}, \tag{4.2}$$

where $\boldsymbol{S}_c$ is the unpolarized continuum source vector represented by $\boldsymbol{S}_c = B\boldsymbol{U}$, with B the Planck function and $\boldsymbol{U} = (1, 0)^{\mathrm{T}}$. $\boldsymbol{S}_l$ is the line source vector given by

$$\boldsymbol{S}_l(\tau, x, \mu) = \epsilon B\boldsymbol{U} + \frac{1}{\phi(x)} \int_{-\infty}^{+\infty} \mathrm{d}x' \oint \frac{\mathrm{d}\Omega'}{4\pi} \mathbf{R}(x, \boldsymbol{\Omega}, x', \boldsymbol{\Omega}')\boldsymbol{I}(\tau, x', \mu'), \tag{4.3}$$

where $\epsilon = \Gamma_I/(\Gamma_I + \Gamma_R)$ is the probability per scattering that a photon is destroyed by collisional de-excitation. Γ_R and Γ_I are, respectively, the radiative and inelastic collisional de-excitation rates from the upper J-states or the upper F-states to the corresponding lower states. To a first approximation, we assume these rates to be the same for all the fine structure and HFS states of the upper term. The lower terms are assumed to be infinitely sharp. $\boldsymbol{\Omega}(\theta, \varphi)$ and $\boldsymbol{\Omega}'(\theta', \varphi')$ represent the directions of the outgoing and incoming rays, respectively, in the atmospheric co-ordinate system. φ represents the radiation field azimuth and $\mathrm{d}\Omega = \sin\theta\, \mathrm{d}\theta\, \mathrm{d}\varphi$. The RM for an atomic system in the collisionless regime and in the absence of a magnetic field is denoted by $\mathbf{R}(x, \boldsymbol{\Omega}, x', \boldsymbol{\Omega}')$. The elements of this RM can be expressed as

$$\mathbf{R}_{ij}(x, \boldsymbol{\Omega}, x', \boldsymbol{\Omega}') = \sum_{KQ} \mathcal{R}^K(x, \boldsymbol{\Omega}, x', \boldsymbol{\Omega}')(-1)^Q \mathcal{T}^K_Q(i, \boldsymbol{\Omega}) \mathcal{T}^K_{-Q}(j, \boldsymbol{\Omega}'), \tag{4.4}$$

where $i, j = 0, 1$ are the Stokes parameter indices. $\mathcal{T}^K_Q(i, \mathbf{\Omega})$ are the irreducible spherical tensors for polarimetry with $K = 0, 2$ and $-K \leqslant Q \leqslant +K$. Following Frisch (2007), we can write

$$\mathcal{T}^K_Q(i, \mathbf{\Omega}) = \widetilde{\mathcal{T}}^K_Q(i, \mu)\mathrm{e}^{\mathrm{i}Q\varphi}. \tag{4.5}$$

Substituting Equation (4.5) in Equation (4.4) we obtain

$$\mathbf{R}_{ij}(x, \mathbf{\Omega}, x', \mathbf{\Omega}') = \sum_{KQ} \mathrm{e}^{\mathrm{i}Q(\varphi-\varphi')}\mathcal{R}^K(x, \mathbf{\Omega}, x', \mathbf{\Omega}')(-1)^Q\widetilde{\mathcal{T}}^K_Q(i, \mu)\widetilde{\mathcal{T}}^K_{-Q}(j, \mu'). \tag{4.6}$$

The $\mathcal{R}^K(x, \mathbf{\Omega}, x', \mathbf{\Omega}')$ for the case of J-state interference is given by

$$\begin{aligned}
\mathcal{R}^K(x, \mathbf{\Omega}, x', \mathbf{\Omega}') &= \frac{3(2L_b+1)}{2S+1} \sum_{J_a J_f J_b J_{b'}} (-1)^{J_f - J_a} \cos\beta_{J_{b'}J_b} \\
&\times [\cos\beta_{J_{b'}J_b}(h^{\mathrm{II}}_{J_b,J_{b'}})_{J_aJ_f} - \sin\beta_{J_{b'}J_b}(f^{\mathrm{II}}_{J_b,J_{b'}})_{J_aJ_f}](2J_a+1)(2J_f+1) \\
&\times (2J_b+1)(2J_{b'}+1) \begin{Bmatrix} L_a & L_b & 1 \\ J_b & J_f & S \end{Bmatrix} \begin{Bmatrix} L_a & L_b & 1 \\ J_b & J_a & S \end{Bmatrix} \begin{Bmatrix} L_a & L_b & 1 \\ J_{b'} & J_f & S \end{Bmatrix} \\
&\times \begin{Bmatrix} L_a & L_b & 1 \\ J_{b'} & J_a & S \end{Bmatrix} \begin{Bmatrix} 1 & 1 & K \\ J_{b'} & J_b & J_a \end{Bmatrix} \begin{Bmatrix} 1 & 1 & K \\ J_{b'} & J_b & J_f \end{Bmatrix}.
\end{aligned} \tag{4.7}$$

$L_{a,b}$ are the orbital angular momentum quantum numbers of the lower and upper terms, respectively, and S is the spin. $J_{a,f}$ and $J_{b,b'}$ are, respectively, the total angular momentum quantum numbers of the lower and upper term fine structure states. The $(h^{\mathrm{II}}_{J_b,J_{b'}})_{J_aJ_f}$ and $(f^{\mathrm{II}}_{J_b,J_{b'}})_{J_aJ_f}$ are auxiliary functions defined in Equations (14) and (15) of Smitha et al. (2011b). The angle $\beta_{J_{b'}J_b}$ is defined in Equation (10) of Smitha et al. (2011b). The $\mathcal{R}^K(x, \mathbf{\Omega}, x', \mathbf{\Omega}')$ corresponding to the case of F-state interference can be obtained by making the following replacements in Equation (7) above (see Smitha et al., 2012b, for more details)

$$L \to J; \quad J \to F; \quad S \to I_s, \tag{4.8}$$

where F is the total angular momentum quantum number resulting from the angular momentum addition of J and I_s, with I_s being the nuclear spin of the atom under consideration. In Smitha et al. (2011a) as well as in Smitha et al. (2012b), the angle-averaged versions of $\mathcal{R}^K$ was used. However, in the present chapter we consider full angle-dependence of these $\mathcal{R}^K$ components. Substituting Equation (4.6) in Equation (4.3), we obtain for the line source vector components

$$S_{l,i}(\tau, x, \mu) = G_i(\tau) + \frac{1}{\phi(x)} \int_{-\infty}^{+\infty} \mathrm{d}x' \int_{-1}^{+1} \frac{\mathrm{d}\mu'}{2} \sum_{KQ} \widetilde{\mathcal{R}}^K_Q(x, \mu, x', \mu')$$

$$\times(-1)^Q \widetilde{\mathcal{T}}_Q^K(i,\mu) \sum_{j=0,1} \widetilde{\mathcal{T}}_{-Q}^K(j,\mu') I_j(\tau,x',\mu'), \tag{4.9}$$

where $S_{l,i} = (S_{l,I}\,,\, S_{l,Q})$ and $G_i(\tau) = \epsilon B(1,0)$ for $i = 0, 1$. The $\widetilde{\mathcal{R}}_Q^K(x,\mu,x',\mu')$ are the Fourier azimuthal components of $\mathcal{R}^K(x,\boldsymbol{\Omega},x',\boldsymbol{\Omega}')$ and defined as

$$\widetilde{\mathcal{R}}_Q^K(x,\mu,x',\mu') = \frac{1}{2\pi}\int_0^{2\pi} \mathcal{R}^K(x,\boldsymbol{\Omega},x',\boldsymbol{\Omega}')\mathrm{e}^{\mathrm{i}Q(\varphi-\varphi')}\,\mathrm{d}(\varphi-\varphi'). \tag{4.10}$$

Regrouping terms with the same value of $|Q|$, we get

$$\widetilde{\mathcal{R}}_Q^K(x,\mu,x',\mu') = C_Q\int_0^{2\pi} \mathcal{R}^K(x,\boldsymbol{\Omega},x',\boldsymbol{\Omega}')\cos\left[Q(\varphi-\varphi')\right]\mathrm{d}(\varphi-\varphi'), \tag{4.11}$$

where $C_Q = (2-\delta_{Q0})/2\pi$. Following Frisch (2010) we can decompose the Stokes source vector $\boldsymbol{S}$ and Stokes vector $\boldsymbol{I}$ in terms of the irreducible spherical tensors. Such a decomposition provides numerical advantage because the decomposed vectors (called the reduced vectors) are easier to compute. Using the decomposition

$$I_i(\tau,x,\mu) = \sum_{KQ\geqslant 0} \widetilde{\mathcal{T}}_Q^K(i,\mu)\mathcal{I}_Q^K(\tau,x,\mu), \tag{4.12}$$

for the Stokes vector $I_i = (I, Q)$ and a similar decomposition for the primary Stokes vector $\boldsymbol{G}(\tau)$

$$G_i(\tau) = \sum_{KQ\geqslant 0} \delta_{K0}\delta_{Q0}\widetilde{\mathcal{T}}_Q^K(i,\mu)\mathcal{G}_Q^K(\tau), \tag{4.13}$$

and substituting in Equation (4.9), the line source vector components can be expressed as

$$S_{l,i}(\tau,x,\mu) = \sum_{KQ\geqslant 0} \widetilde{\mathcal{T}}_Q^K(i,\mu)\mathcal{S}_{l,Q}^K(\tau,x,\mu), \tag{4.14}$$

where the irreducible line source vector components take the form

$$\mathcal{S}_{l,Q}^K(\tau,x,\mu) = \delta_{K0}\delta_{Q0}\mathcal{G}_Q^K(\tau) + \int_{-\infty}^{+\infty}\mathrm{d}x'\int_{-1}^{+1}\frac{\mathrm{d}\mu'}{2}$$
$$\times\frac{\widetilde{\mathcal{R}}_Q^K(x,\mu,x',\mu')}{\phi(x)}\sum_{K'Q'\geqslant 0}\Gamma_{QQ'}^{KK'}(\mu')\mathcal{I}_{Q'}^{K'}(\tau,x',\mu'). \tag{4.15}$$

The $\Gamma_{QQ'}^{KK'}(\mu')$ which appears in the above expression has the form

$$\Gamma_{QQ'}^{KK'}(\mu') = \sum_{j=0,1}\widetilde{\mathcal{T}}_Q^K(j,\mu')\widetilde{\mathcal{T}}_{Q'}^{K'}(j,\mu'). \tag{4.16}$$

The explicit forms of $\Gamma_{QQ'}^{KK'}(\mu')$ are given in Frisch (2010).

4.3 Numerical method of solution

In this section we present an iterative method called SEM to solve the problem of angle-dependent PRD including quantum interference. SEM is based on Neumann series expansion of the components of the source vector contributing to the polarization. This Neumann series leads to an expansion in terms of the mean number of scattering events (see Frisch et al., 2009) and the first term yields the single scattered solution. The computation using SEM, in the first step, involves the calculation of Stokes I which is allowed to be given by the dominant component $\mathcal{I}_0^0$. This is the solution of the non-local thermodynamic equilibrium unpolarized radiative transfer equation, which is solved using an approximate lambda iteration (ALI) method. The corresponding source function is given by

$$\mathcal{S}_{l,0}^0(\tau,x,\mu) = \epsilon B + \int_{-\infty}^{+\infty} \mathrm{d}x' \int_{-1}^{+1} \frac{\mathrm{d}\mu'}{2} \frac{\widetilde{\mathcal{R}}_0^0(x,\mu,x',\mu')}{\phi(x)} \mathcal{I}_0^0(\tau,x',\mu'). \quad (4.17)$$

Then the single scattered source term for each component $\mathcal{S}_{l,Q}^2$ ($Q = 0,1,2$) is calculated using $\mathcal{I}_0^0$. It may be written as

$$\left[\mathcal{S}_{l,Q}^2\right]^{(1)}(\tau,x,\mu) \simeq \int_{-\infty}^{+\infty} \mathrm{d}x' \int_{-1}^{+1} \frac{\mathrm{d}\mu'}{2} \frac{\widetilde{\mathcal{R}}_Q^2(x,\mu,x',\mu')}{\phi(x)} \Gamma_{Q0}^{20}(\mu') \mathcal{I}_0^0(\tau,x',\mu'). \quad (4.18)$$

The superscript '1' stands for single scattering. The radiation field $\left[\mathcal{I}_Q^2\right]^{(1)}$ corresponding to each $\left[\mathcal{S}_{l,Q}^2\right]^{(1)}$ is calculated by calling a formal solver. $\left[\mathcal{I}_Q^2\right]^{(1)}$ serves as a starting point for calculating the higher order terms. For order (n),

$$\left[\mathcal{S}_{l,Q}^2\right]^{(n)} \simeq \left[\mathcal{S}_{l,Q}^2\right]^{(1)} + \int_{-\infty}^{+\infty} \mathrm{d}x' \int_{-1}^{+1} \frac{\mathrm{d}\mu'}{2} \times \frac{\widetilde{\mathcal{R}}_Q^2(x,\mu,x',\mu')}{\phi(x)} \sum_{Q' \geq 0} \Gamma_{QQ'}^{22}(\mu') \left[\mathcal{I}_{Q'}^2\right]^{(n-1)}(\tau,x',\mu'). \quad (4.19)$$

The iteration is continued until a convergence criterium is satisfied. We note that the component $\mathcal{I}_0^0$ is calculated only once, which in turn simplifies the computation.

4.4 Results and Discussion

In this section we present the emergent Stokes profiles computed using the angle-dependent RM for the cases of J-state interference and F-state interference phenomena individually. We consider an isothermal, self-emitting constant property medium characterized by (T, a, ϵ, r, B). T is the optical thickness of the slab and a is the damping parameter. The Planck function is set to unity. The grid used for com-

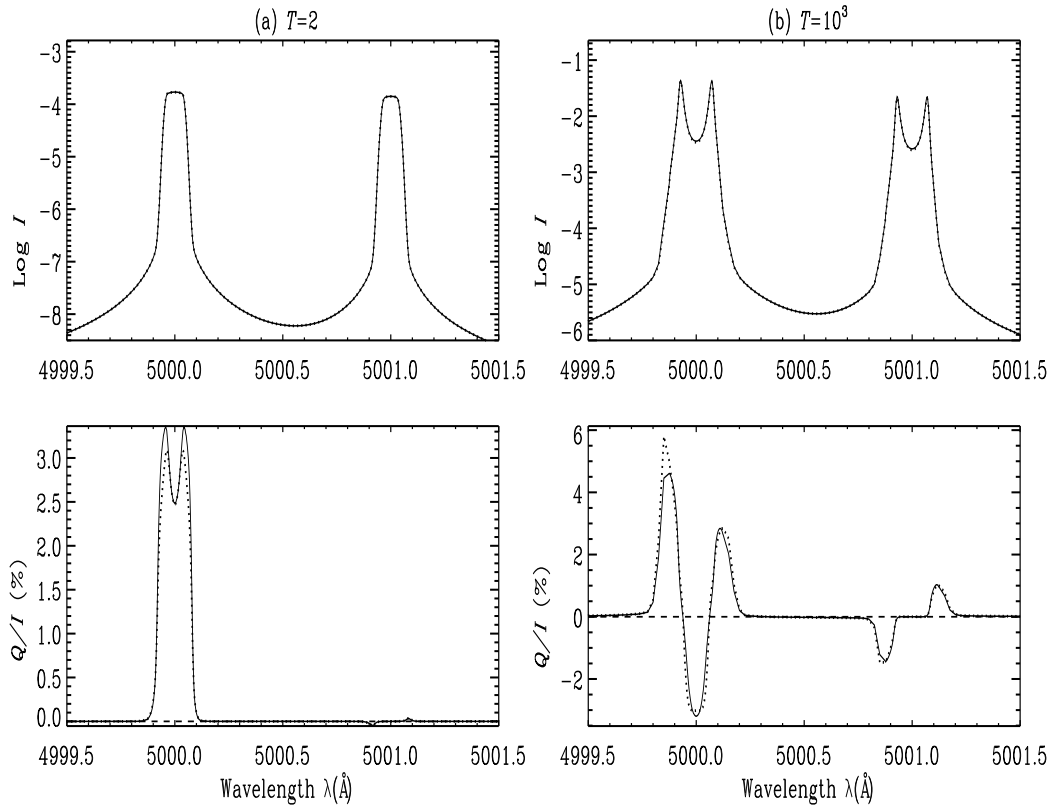

Figure 4.1: A comparison of emergent Stokes profiles for angle-dependent (solid lines) and angle-averaged (dotted lines) PRD including J-state interference at μ = 0.0254. A planar slab model with parameters (a, ϵ, r, B) = (10^{-3}, 10^{-4}, 0, 1) are used. Panels (a) and (b) correspond to optical thickness $T = 2$ and $T = 10^3$ respectively.

putations is specified by (N_d, N_x, N_μ, N_φ). N_d denotes the number of depth points per decade in a logarithmically spaced τ-grid with the first depth point at $\tau_1 = 10^{-2}$. N_x gives the number of frequency grid points which are very closely and equally spaced in the line cores and in between the lines, and are sparsely but equally spaced in the wings of the lines. N_μ, and N_φ specify the number of colatitudes $\theta(\mu)$ and azimuth angles φ, respectively, for both of which we use Gauss-Legendre quadratures.

4.4.1 Fine structure state interference with angle-dependent partial frequency redistribution

A two-term atom with an $L = 0 \rightarrow 1 \rightarrow 0$ scattering transition and spin $S = 1/2$ is considered. The lower and upper terms split into fine-structure levels with J-quantum numbers $J_a = J_f = 1/2$ and $J_b = 1/2, 3/2$ respectively. The allowed transition between the J-states give rise to a doublet at 5000 Å and 5001 Å. It is assumed that Doppler widths of both these lines are the same and equal to 0.025 Å. The grid

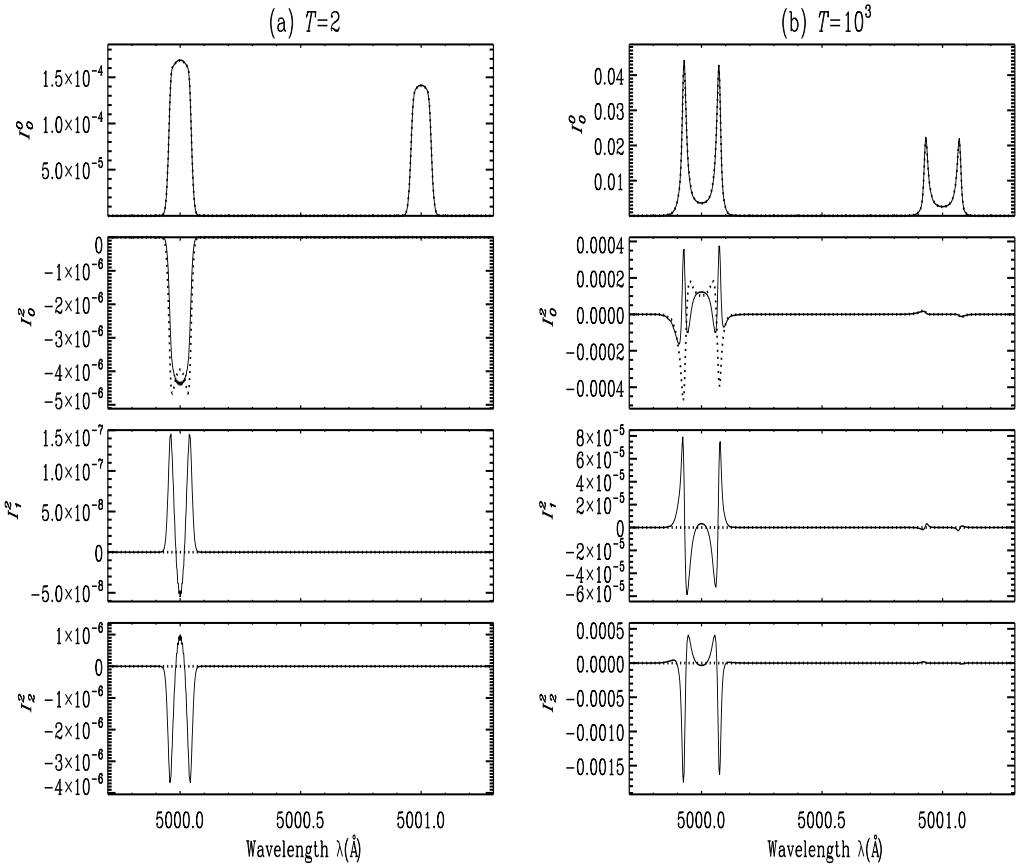

Figure 4.2: A comparison of emergent $\mathcal{I}_Q^K$ for angle-dependent (solid lines) and angle-averaged (dotted lines) PRD including J-state interference at $\mu = 0.0254$. Slab model parameters for the panels (a) and (b) are the same as those of Figure 4.1.

used for computation is given by $(N_d, N_x, N_\mu, N_\varphi) = (5, 308, 7, 15)$. In Figure 4.1 we compare the Stokes I profile and the ratio Q/I computed using angle-averaged and angle-dependent PRD functions including J-state interference effects for different values of optical thickness T. The difference in Q/I obtained using angle-averaged and angle-dependent PRD is quite sensitive to T and nearly vanish for very thick slabs (like $T > 10^4$). For the cases presented in Figure 4.1, the angle-dependent effects are largest in the PRD wing peaks of 5000 Å line. The antisymmetric PRD peaks about the 5001 Å line and the wavelength region in between the two lines are insensitive to angle-dependent effects and are purely controlled by J-state interference effects. In the case of $T = 10^3$, the angle-dependent effects seem to reduce the asymmetry between the wing PRD peaks of 5000 Å line (brought about by the J-state interference effects), when compared to the corresponding angle-averaged case.

The differences between angle-averaged and angle-dependent solutions can be analyzed using irreducible components I_Q^K of the Stokes vector as done for a standard two-level atom case in Sampoorna et al. (2011). Same arguments hold good in the present case also. The Stokes vectors I and Q in terms of the components $\mathcal{I}_Q^K$ which

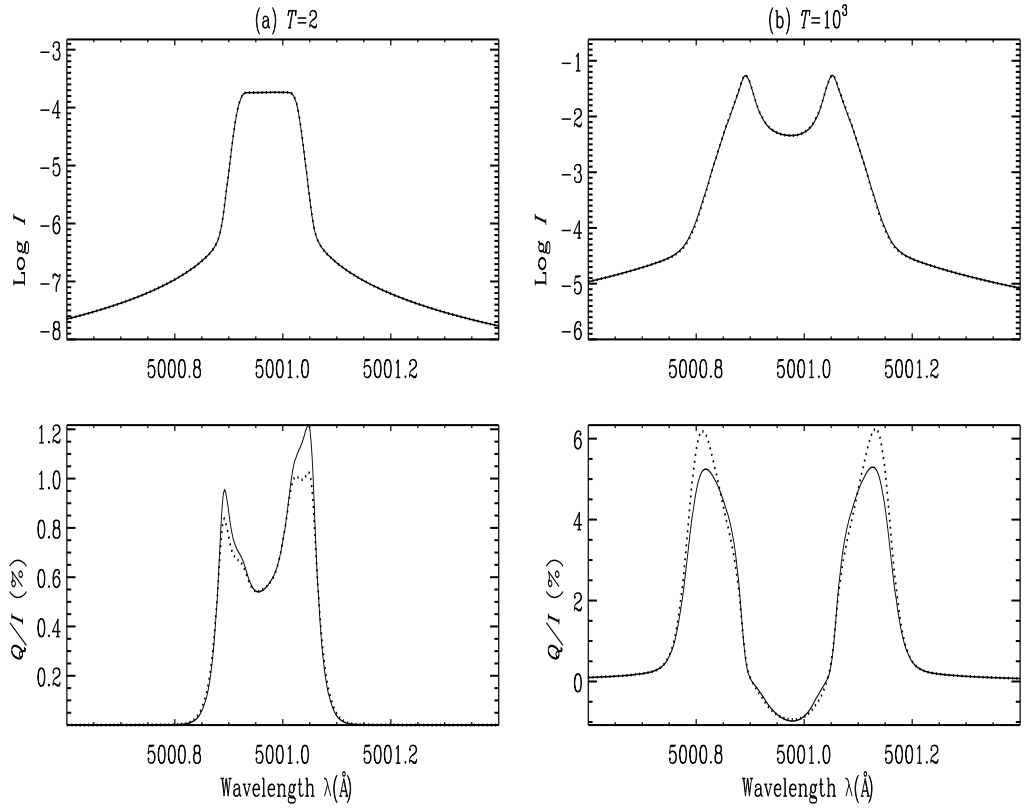

Figure 4.3: A comparison of emergent Stokes profiles for angle-dependent (solid lines) and angle-averaged (dotted lines) PRD including F-state interference at μ = 0.0254. A planar slab model with parameters (a, ϵ, r, B) = (2×10^{-3}, 10^{-4}, 0, 1) are used. Panels (a) and (b) correspond to optical thickness $T = 2$ and $T = 10^3$ respectively.

depend on τ, x, and μ, can be written as

$$I(\tau, x, \mu) = \mathcal{I}_0^0 + \frac{1}{2\sqrt{2}}(3\mu^2 - 1)\mathcal{I}_0^2 - \frac{\sqrt{3}}{2}\mu\sqrt{1-\mu^2}\mathcal{I}_1^2 + \frac{\sqrt{3}}{4}(1-\mu^2)\mathcal{I}_2^2,$$
$$Q(\tau, x, \mu) = -\frac{3}{2\sqrt{2}}(1-\mu^2)\mathcal{I}_0^2 - \frac{\sqrt{3}}{2}\mu\sqrt{1-\mu^2}\mathcal{I}_1^2 - \frac{\sqrt{3}}{4}(1+\mu^2)\mathcal{I}_2^2. \quad (4.20)$$

In Figure 4.2, we show a plot of the components $\mathcal{I}_Q^K$ corresponding to the atmospheric models used in Figure 4.1. We see that for angle-averaged PRD functions the components $Q \neq 0$ are zero. The component $\mathcal{I}_0^0$ is the dominant component contributing to the Stokes I, which is insensitive to the type of PRD function used, namely angle-averaged or angle-dependent (see the top panels of Figure 4.1). From Figure 4.2, we see that the component $\mathcal{I}_0^0$ is insensitive to the choice of the PRD function, while the components $\mathcal{I}_Q^2$ are quite sensitive and hence the sensitivity of Q/I to angle-dependent PRD. We have verified that at the disk center the angle-dependent functions become azimuthally symmetric and hence the angle-dependent polarization profiles closely match with the corresponding angle-averaged profiles.

4.4.2 Hyperfine structure state interference with angle-dependent partial frequency redistribution

We consider a two-level atom with $J = 1/2 \rightarrow 3/2 \rightarrow 1/2$ scattering transition and nuclear spin $I_s = 3/2$. Due to HFS, the upper J-state with $J_b = 3/2$ splits into four F-states with $F_b = 0, 1, 2, 3$ and the lower J-state with $J_a = 1/2$ splits into two F-state with $F_a = 0, 1$. There are six allowed radiative transitions between these F-states which satisfy selection rule $\Delta F = 0, \pm 1$ and are given in Table 1 of Smitha et al. (2012b). Doppler widths of all the lines are again taken to be 0.025 Å. The grid used for the computations is given by (N_d, N_x, N_μ, N_φ) = (5, 417, 7, 15). In this section, we present the studies analogous to those performed in the case

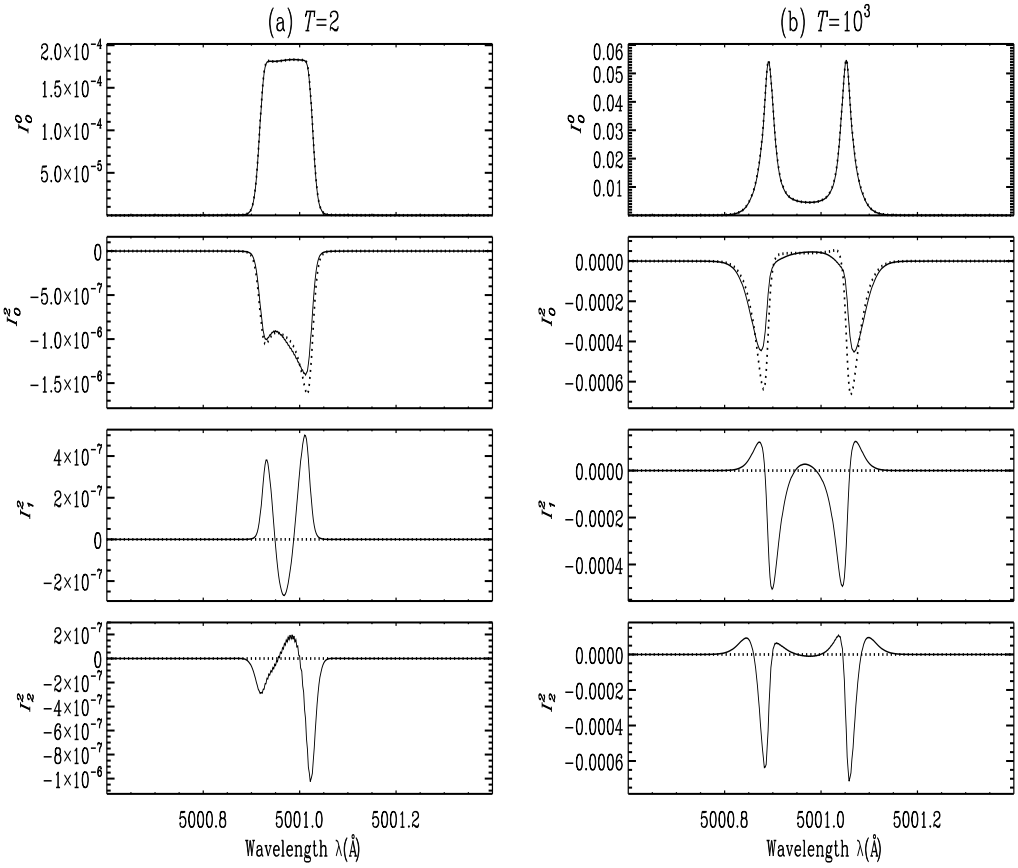

Figure 4.4: A comparison of emergent $\mathcal{I}_Q^K$ for angle-dependent (solid lines) and angle-averaged (dotted lines) PRD including F-state interference at μ = 0.0254. Slab model parameters for the panels (a) and (b) are the same as those of Figure 4.3.

of J-state interference. Therefore, Figures 4.3 and 4.4 are analogous to Figures 4.1 and 4.2, but for the case of F-state interference. Like in the case of two-term atom with J-state interference and two-level atom with zero nuclear spin, in the present case of F-state interference the difference in Q/I computed with angle-averaged and angle-dependent PRD are mainly seen in the wing PRD peaks (see Figure 4.3) for slabs with $T \leqslant 10^3$. For slabs with still larger thickness, angle-dependent effects are

negligible and therefore angle-averaged PRD functions can safely be used. Again, these differences can be analyzed by studying the irreducible spherical components $\mathcal{I}_Q^K$ shown in Figure 4.4. Further, we have verified that the behavior of center-to-limb variation of I and Q/I profiles for F-state interference case is similar to the corresponding J-state interference case.

4.5 Conclusions

We solve the non-magnetic line transfer problem taking into account both the angle-dependent PRD and the effects of quantum interference (J-state and F-state interferences individually), and test the validity of using the angle-averaged approximation of the PRD (as done in Smitha et al. 2011a, 2012b) to solve this problem. The studies have been carried out for two types of atomic system (namely a two-term atom with zero nuclear spin and a two-level atom with non-zero nuclear spin) in a collisionless regime and with unpolarized lower level. The decomposition technique developed by Frisch (2010) to solve line transfer problem with angle-dependent PRD for the case of standard two-level atom with zero nuclear spin is now extended to the case when quantum interference effects are included. This technique helps us to decompose the polarized radiation field into four components that are cylindrically symmetric and satisfy the standard transfer equation. Further, this decomposition technique allows us to solve the transfer equation with angle-dependent PRD including quantum interference phenomena using an efficient numerical technique called SEM.

Numerical results for polarized line transfer problem including J-state interference as well as F-state interference are presented. The differences between angle-averaged and angle-dependent solutions in both the cases are noticed particularly in the near wing PRD peaks. The quantum interference signatures in Q/I are not affected by the angle-dependent effects because these effects arise more from atomic physics than from radiative transfer. In both the J-state and F-state interference cases, the differences between angle-averaged and angle-dependent solutions remain sensitive to the optical thickness T of the slab. The differences are particularly large for slabs of smaller optical thickness (like $T \leqslant 10^3$), but vanish for very thick slabs. However, over the whole optical depth range the differences never get large enough to be of practical importance for the theoretical modeling of observational data. There is therefore generally no need to invoke the much more computer-intensive angle-dependent PRD, since the angle-averaged version is accurate enough for all practical purposes.

The studies done in Chapters 3 and 4 were concerned with the effects of using angle-dependent redistribution function in two-different problems in the non-magnetic regime. In the next chapter we study the effects of angle-dependent PRD

functions in the presence of weak magnetic fields i.e., the Hanle effect. The problem of using the angle-dependent PRD functions in presence of magnetic fields is numerically expensive and in the next chapter we discuss about the efficient numerical techniques to handle this complex problem.

Chapter 5

An efficient decomposition technique to solve angle-dependent Hanle scattering problems*

An Overview

Hanle scattering is an important diagnostic tool to study weak solar magnetic fields. Partial frequency redistribution (PRD) is necessary to interpret the linear polarization observed in strong resonance lines. Usually angle-averaged PRD functions are used to analyze linear polarization. However, it is established that angle-dependent PRD functions are often necessary to interpret polarization profiles formed in the presence of weak magnetic fields. Our aim is to present an efficient decomposition technique, and the numerical method to solve the concerned angle-dependent line transfer problem. Together with the standard Stokes decomposition technique, we employ Fourier expansion over the outgoing azimuth angle to express in a more convenient form, the angle-dependent PRD function for the Hanle effect. It allows the use of angle-dependent frequency domains of Bommier to solve the Hanle transfer problem. Such an approach is self-consistent and accurate compared to a recent approach where angle-averaged frequency domains were used to solve the same problem. We show that it is necessary to incorporate angle-dependent frequency domains instead of angle-averaged frequency domains to solve the Hanle transfer problem accurately, especially for the Stokes U parameter. The importance of using angle-dependent domains has been highlighted by taking the example of Hanle effect in the case of line transfer with vertical magnetic fields in a slab atmosphere. We have also studied the case of polarized line formation when micro-turbulent magnetic fields are present. The difference between angle-averaged and angle-dependent solutions

*The contents of this chapter are based on Supriya et al. (2013a)

is enhanced by the presence of micro-turbulent fields.

5.1 Introduction

We know that the polarization of line radiation is caused by resonance scattering on bound atomic levels and a modification of this process by external magnetic fields is called the Hanle effect. The linear polarization of strong resonance lines is particularly sensitive to the type of the frequency redistribution mechanism used in their evaluation especially in the presence of magnetic fields. The differences of the diffuse radiation field between the linear polarization (Q/I) profiles computed using angle-averaged and angle-dependent PRD functions are illustrated in Faurobert (1988) and Sampoorna et al. (2011) in the non-magnetic (Rayleigh) case. Nagendra et al. (2002) showed that Stokes U profiles computed in planar slabs, for the case of Hanle effect, using the angle-averaged PRD functions differ significantly from those computed using angle-dependent PRD functions.

In the case of angle-dependent PRD functions, the strong coupling that exist between the incoming and scattered radiation makes their evaluation and subsequent use in transfer equation numerically expensive. The use of decomposition technique, developed by Frisch (2009) for the Hanle effect and Frisch (2010) for the Rayleigh case, simplifies this numerically expensive problem. In the non-magnetic case, Sampoorna et al. (2011) used this decomposition technique and developed numerical methods to solve the polarized transfer problem with angle-dependent PRD functions . They also present a detailed historical account of the works on angle-dependent PRD in spectral line polarization. In Sampoorna (2011b) Hanle transfer problem with angle-dependent PRD was solved using single scattering approximation. Further in Nagendra & Sampoorna (2011, hereafter, NS11) the full Hanle transfer problem with angle-dependent PRD functions was solved by including multiple scattering terms and using scattering expansion method (SEM). It may be noted that SEM was first formulated by Frisch et al. (2009) for solving the polarized line transfer equation with complete frequency redistribution (CRD).

In all the above mentioned papers, a Fourier-expansion of the angle-dependent PRD function over azimuth angle difference ($\chi - \chi'$) is employed, where χ and χ' are the azimuth angles of the outgoing and incoming rays. This technique was first introduced by Domke & Hubeny (1988) and was further developed by Frisch (2009) for the Hanle transfer problem. The decomposition technique of Frisch (2009) allowed the Hanle transfer problem to be solved in an azimuth independent Fourier basis. In NS11 this decomposition technique was used together with the angle-averaged frequency domains (approximation III of Bommier, 1997b) to solve the Hanle transfer problem with angle-dependent PRD functions. As one has to use in principle,

angle-dependent domains themselves for angle-dependent PRD transfer problems, the approach taken in NS11 is inconsistent. Such an approximate approach was taken, because it allowed to work in an azimuth independent Fourier basis. Clearly in an axisymmetric Fourier basis, one cannot apply angle-dependent frequency domains as they explicitly depend on azimuth difference $(\chi - \chi')$. This inconsistency is at the base of the slight differences in the angle-dependent Hanle solutions presented in NS11 (see Figure 4 in that paper), and those presented in Nagendra et al. (2002). Indeed, Anusha & Nagendra (2012) pointed out that the use of angle-averaged frequency domains for the angle-dependent Hanle transfer problem (as done in NS11) results in a loss of information.

To overcome this inconsistency, we adopt the technique of the Fourier expansion of angle-dependent Hanle PRD matrix over only the outgoing azimuth angle χ as suggested in Anusha & Nagendra (2012, see also Anusha & Nagendra 2011b). Such an expansion was proposed to solve polarized transfer problems in multi-dimensional media, where the radiation field is non-axisymmetric even in the absence of a magnetic field. In this chapter we apply the decomposition proposed by them to the simpler case of polarized transfer in one-dimensional media, and in the presence of a magnetic field. We show that an expansion only over χ allows to incorporate angle-dependent frequency domains for angle-dependent PRD functions 'self consistently' to solve the transfer problem in the magnetic case.

In Section 5.2, we describe the decomposition technique employed for the Hanle effect with angle-dependent PRD. In Section 5.3, we discuss the behavior of azimuthal Fourier components of redistribution matrix elements. In Section 5.4, we give the equations of the SEM to solve the Hanle transfer problem. In Section 5.5, we discuss the results obtained by considering our new method of azimuth expansion. A comparison with the results obtained from the perturbation method described in Nagendra et al. (2002) and those obtained by using angle-averaged domains (in NS11) is done. In the same section we also revisit the well known problem of vertical field Hanle effect which arises only due to the angle-dependent PRD in line scattering. Further, we discuss in detail the role of micro-turbulent magnetic fields on line transfer using angle-averaged and angle-dependent versions of the redistribution matrix. Conclusions are presented in Section 5.6.

5.2 The decomposition technique

The polarized transfer equation for the Stokes vector can be written in the component form as

$$\mu \frac{\partial I_i}{\partial \tau} = [\varphi(x) + r] \left[I_i(\tau, x, \mathbf{\Omega}) - S_i(\tau, x, \mathbf{\Omega}) \right], \tag{5.1}$$

where $i = 0, 1, 2$ refer to the Stokes parameters (I, Q, U) respectively. The ray direction is given by $\mathbf{\Omega} = (\theta, \chi)$, with $\theta = \cos^{-1}(\mu)$ and χ being the polar angles. x is the frequency in non-dimensional units. The line optical depth is denoted by τ and $\varphi(x)$ is the normalized Voigt function $H(a,\, x)$, where a represents a constant damping parameter. The ratio of continuum to the line absorption coefficient is denoted by r. The total source vector is given by

$$S_i(\tau, x, \mathbf{\Omega}) = \frac{\varphi(x)\, S_{l,i}(\tau, x, \mathbf{\Omega}) + r\, S_{c,i}}{\varphi(x) + r}, \tag{5.2}$$

where $S_{c,i}$ are the components of the unpolarized continuum source vector. We assume that $S_{c,0} = B_{\nu_0}$, where B_{ν_0} is the Planck function at the line center, and $S_{c,1} = S_{c,2} = 0$. The line source vector can be written as

$$S_{l,i}(\tau, x, \mathbf{\Omega}) = G_i(\tau) + \int_{-\infty}^{+\infty} \oint \sum_{j=0}^{2} \frac{\hat{R}_{ij}(x, \mathbf{\Omega}, x', \mathbf{\Omega}', \boldsymbol{B})}{\varphi(x)}\, I_j(\tau, x', \mathbf{\Omega}')\, \frac{\mathrm{d}\Omega'}{4\pi}\, \mathrm{d}x', \tag{5.3}$$

where $\mathbf{\Omega}'$ (θ', χ') is the direction of the incoming ray defined with respect to the atmospheric normal. The solid angle element $\mathrm{d}\Omega' = \sin\theta'\, \mathrm{d}\theta'\, \mathrm{d}\chi'$ where $\theta' \in [0, \pi]$ and $\chi' \in [0, 2\pi]$. The primary source is assumed to be unpolarized, so that $G_0(\tau) = \epsilon B_{\nu_0}$ and $G_1(\tau) = G_2(\tau) = 0$. Here, $\hat{R}_{ij}(x, \mathbf{\Omega}, x', \mathbf{\Omega}', \boldsymbol{B})$ is the Hanle redistribution matrix with angle-dependent PRD, and $\boldsymbol{B}$ represents an oriented vector magnetic field. The thermalization parameter $\epsilon = \Gamma_I/(\Gamma_R + \Gamma_I)$, with Γ_I and Γ_R being the inelastic collisional de-excitation rate and the radiative de-excitation rate, respectively. The Equations 5.1 - 5.3 is the same as Equations 1.18 - 1.20. They are repeated here for clarity.

In the decomposition method used in this chapter, the Stokes vector (I, Q, U) is first decomposed into a set of six irreducible components I^K_Q, using which we can construct an infinite set of integral equations for their Fourier coefficients. Following Frisch (2009) we can decompose the Stokes source vector into six irreducible components S^K_Q as

$$S_i(\tau, x, \mathbf{\Omega}) = \sum_{K=0,2} \sum_{Q=-K}^{Q=+K} \mathcal{T}^K_Q(i, \mathbf{\Omega})\, S^K_Q(\tau, x, \mathbf{\Omega}), \tag{5.4}$$

with a similar decomposition for the Stokes vector I_i in terms of I^K_Q. The $\mathcal{T}^K_Q(i, \mathbf{\Omega})$ are irreducible spherical tensors for polarimetry introduced by Landi Degl'Innocenti

(1984). The irreducible line source vector components are then given by

$$S^K_{l,Q}(\tau,x,\mathbf{\Omega}) = G^K_Q(\tau) + \int_{-\infty}^{+\infty} \mathrm{d}x' \oint \frac{\mathrm{d}\Omega'}{4\pi} \times \frac{1}{\varphi(x)} \sum_{K'=0,2} \sum_{Q''=-K'}^{Q''=+K'} \mathcal{R}^{KK'}_{QQ''}(m,x,x',\Theta,\boldsymbol{B})\, I^{K'}_{Q''}(\tau,x',\mathbf{\Omega}'), \tag{5.5}$$

where $\Theta\ [= \cos^{-1}(\mathbf{\Omega}.\mathbf{\Omega}')]$ is the scattering angle, $G^K_Q(\tau) = (\epsilon B_{\nu_0}, 0, 0, 0, 0, 0)^{\mathrm{T}}$, and $\mathcal{R}^{KK'}_{QQ''}$ are the elements of angle-dependent Hanle redistribution matrix given by

$$\mathcal{R}^{KK'}_{QQ''}(m,x,x',\Theta,\boldsymbol{B}) = \sum_{Q'=-K}^{Q'=+K} [\mathcal{N}^K_{QQ'}(m,\boldsymbol{B})\, R_{\mathrm{II}}(x,x',\Theta) + \mathcal{N}^K_{QQ'}(m,\boldsymbol{B})\, R_{\mathrm{III}}(x,x',\Theta)]\, \Gamma_{KQ',K'Q''}(\mathbf{\Omega}'). \tag{5.6}$$

In this chapter we use approximation II of Bommier (1997b) according to which the redistribution matrix is written as a product of magnetic kernel $\mathcal{N}^K_{QQ'}(m,\boldsymbol{B})$ and the angle-dependent redistribution functions $R_{\mathrm{II,III}}(x,x',\Theta)$ of Hummer (1962). Here the index m (= 1, 2, 3, 4, 5) stands for different frequency domains which depend on (x, x', Θ). The coefficients $\Gamma_{KQ',K'Q''}(\mathbf{\Omega}')$ are defined by

$$\Gamma_{KQ',K'Q''}(\mathbf{\Omega}') = \sum_{i=0}^{3} (-1)^{Q'}\, \mathcal{T}^K_{-Q'}(i,\mathbf{\Omega}')\, \mathcal{T}^{K'}_{Q''}(i,\mathbf{\Omega}'). \tag{5.7}$$

The irreducible components I^K_Q and S^K_Q and the coefficients $\Gamma_{KQ',K'Q''}$ are complex quantities. For practical computations, we prefer working with the real quantities. In order to transfer complex quantities into the real space, we follow the procedure given in Frisch (2007). First we define

$$I^{K,\mathrm{x}}_Q(\tau,x,\mathbf{\Omega}) = Re\,\{I^K_Q(\tau,x,\mathbf{\Omega})\},$$
$$I^{K,\mathrm{y}}_Q(\tau,x,\mathbf{\Omega}) = Im\,\{I^K_Q(\tau,x,\mathbf{\Omega})\}. \tag{5.8}$$

Using these real components, it can be shown that $\boldsymbol{\mathcal{S}}^{\mathrm{r}} = (S^0_0, S^2_0, S^{2,\mathrm{x}}_1, S^{2,\mathrm{y}}_1, S^{2,\mathrm{x}}_2, S^{2,\mathrm{y}}_2)^{\mathrm{T}}$ and the corresponding intensity vector $\boldsymbol{\mathcal{I}}^{\mathrm{r}}$ satisfy the transfer equation given in Equation (5.1) with S_i and I_i replaced by $\boldsymbol{\mathcal{S}}^{\mathrm{r}}$ and $\boldsymbol{\mathcal{I}}^{\mathrm{r}}$, respectively. Now using the $\hat{\boldsymbol{T}}$ matrix given in Section 5.3 of Frisch (2007) the irreducible line source vector in terms of the real quantities can be written as

$$S^{\mathrm{r},K}_{l,Q}(\tau,x,\mathbf{\Omega}) = G^K_Q(\tau) + \int_{-\infty}^{+\infty} \mathrm{d}x' \oint \frac{\mathrm{d}\Omega'}{4\pi}$$

$$\times \frac{1}{\varphi(x)} \sum_{K'=0,2} \sum_{Q''=0}^{Q''=+K'} \mathcal{R}^{\mathrm{r},KK'}_{QQ''}(m,x,x',\Theta,\boldsymbol{B})\, I^{\mathrm{r},K'}_{Q''}(\tau,x',\boldsymbol{\Omega}'). \tag{5.9}$$

Here $\mathcal{R}^{\mathrm{r},KK'}_{QQ''}$ has the same form as Equation (5.6) with $\mathcal{N}^{K}_{QQ'}$ and $\Gamma_{KQ',K'Q''}$ replaced by $\mathcal{N}^{\mathrm{r},K}_{QQ'}$ and $\Gamma^{\mathrm{r}}_{KQ',K'Q''}$. The Q indices take values $[0,+K]$. The elements of matrix $\Gamma^{\mathrm{r}}_{KQ',K'Q''}(\boldsymbol{\Omega}')$ are listed in Appendix D of Anusha & Nagendra (2011a). The explicit form of $\mathcal{N}^{\mathrm{r},K}_{QQ'}(m,\boldsymbol{B})$ can be found in Appendix A of Anusha et al. (2011) where they are denoted by $\boldsymbol{M}^{(i)}(\boldsymbol{B})$ with i playing the role of m in our notation. The formal solution of the transfer equation can now be written as

$$\begin{aligned} I^{\mathrm{r},K}_{Q}(\tau,x,\boldsymbol{\Omega}) &= \int_{\tau}^{+\infty} e^{-(\tau'-\tau)\varphi(x)/\mu}\, S^{\mathrm{r},K}_{Q}(\tau,x,\boldsymbol{\Omega}) \frac{\varphi(x)}{\mu}\,\mathrm{d}\tau', \quad \text{for } \mu>0, \\ I^{\mathrm{r},K}_{Q}(\tau,x,\boldsymbol{\Omega}) &= -\int_{0}^{\tau} e^{-(\tau'-\tau)\varphi(x)/\mu}\, S^{\mathrm{r},K}_{Q}(\tau,x,\boldsymbol{\Omega}) \frac{\varphi(x)}{\mu}\,\mathrm{d}\tau', \quad \text{for } \mu<0. \end{aligned} \tag{5.10}$$

The irreducible components of the line source vector in Equation (5.9) continue to be non-axisymmetric, because of the presence of angle-dependent redistribution function. It is computationally advantageous to express $S^{\mathrm{r},K}_{l,Q}$ in terms of axisymmetric irreducible components. This can be achieved through the introduction of Fourier azimuthal expansion of the angle-dependent PRD functions. In this chapter we use approximation II of Bommier (1997b), the expressions of which for the frequency domains depend on the scattering angle Θ, and hence on $\boldsymbol{\Omega}$ and $\boldsymbol{\Omega}'$. Therefore, to be consistent, we apply Fourier decomposition to the redistribution matrix which contains the angle-dependent frequency domain information (see Anusha & Nagendra, 2012). This can be done as follows:

$$\mathcal{R}^{\mathrm{r},KK'}_{QQ''}(m,x,x',\Theta,\boldsymbol{B}) = \sum_{k=-\infty}^{k=+\infty} \mathrm{e}^{\mathrm{i}k\chi}\, \widetilde{\mathcal{R}}^{(k)KK'}_{QQ''}(m,x,x',\theta,\boldsymbol{\Omega}',\boldsymbol{B}), \tag{5.11}$$

where the Fourier coefficients are given by

$$\widetilde{\mathcal{R}}^{(k)KK'}_{QQ''}(m,x,x',\theta,\boldsymbol{\Omega}',\boldsymbol{B}) = \int_{0}^{2\pi} \frac{\mathrm{d}\chi}{2\pi}\, \mathrm{e}^{-\mathrm{i}k\chi}\, \mathcal{R}^{\mathrm{r},KK'}_{QQ''}(m,x,x',\Theta,\boldsymbol{B}). \tag{5.12}$$

The angle-dependent PRD functions $R_{\mathrm{II,III}}(x,x',\Theta)$ are periodic functions of χ with a period 2π because of which each element of the redistribution matrix $\widetilde{\mathcal{R}}^{(k)KK'}_{QQ''}$ is 2π-periodic. We remark that in the previous attempts on Fourier decomposition, the expansion of angle-dependent functions $R_{\mathrm{II,III}}(x,x',\Theta)$ over $(\chi-\chi')$ was traditionally used (see Domke & Hubeny, 1988; Frisch, 2009, 2010). We show below that an expansion over χ of the angle-dependent redistribution matrix (as done in Anusha & Nagendra, 2012), provides a consistent way of including 'angle-dependent fre-

quency domains' when performing angle-dependent PRD computations. The matrix elements $\widetilde{\mathcal{R}}_{QQ''}^{(k)KK'}$ are studied in detail in Section 5.3. Similar azimuthal Fourier expansions for the primary source term $G_Q^K(\tau)$ can be written as

$$G_Q^K(\tau) = \sum_{k=-\infty}^{k=+\infty} \mathrm{e}^{\mathrm{i}k\chi}\ \tilde{G}_Q^{(k)K}(\tau), \tag{5.13}$$

with

$$\tilde{G}_Q^{(k)K}(\tau) = \begin{cases} G_0(\tau) & if\ \ k=0, \\ 0 & if\ \ k\neq 0. \end{cases} \tag{5.14}$$

Inserting the Fourier azimuthal expansions of $\mathcal{R}_{QQ''}^{\mathrm{r},KK'}(m,x,x',\Theta,\boldsymbol{B})$ and G_Q^K in Equation (5.9), we obtain an expansion for $S_{l,Q}^{\mathrm{r},K}$ which can be expressed as

$$S_{l,Q}^{\mathrm{r},K}(\tau,x,\boldsymbol{\Omega}) = \sum_{k=-\infty}^{k=+\infty} \mathrm{e}^{\mathrm{i}k\chi}\ \tilde{S}_{l,Q}^{(k)K}(\tau,x,\theta), \tag{5.15}$$

with

$$\begin{aligned}\tilde{S}_{l,Q}^{(k)K}(\tau,x,\theta) = \tilde{G}_Q^{(k)K}(\tau) + \int_{-\infty}^{+\infty} \mathrm{d}x' \oint \frac{\mathrm{d}\Omega'}{4\pi}\frac{1}{\varphi(x)} \\ \times \sum_{K'=0,2}\ \sum_{Q''=0}^{Q''=+K'} \widetilde{\mathcal{R}}_{QQ''}^{(k)KK'}(m,x,x',\theta,\boldsymbol{\Omega}',\boldsymbol{B})\, I_{Q''}^{\mathrm{r},K'}(\tau,x',\boldsymbol{\Omega}').\end{aligned} \tag{5.16}$$

Substituting from Equation (5.15) for $S_{l,Q}^{\mathrm{r},K}$ in formal solution we get

$$I_Q^{\mathrm{r},K}(\tau,x,\boldsymbol{\Omega}) = \sum_{k=-\infty}^{k=+\infty} \mathrm{e}^{\mathrm{i}k\chi}\ \tilde{I}_Q^{(k)K}(\tau,x,\theta), \tag{5.17}$$

where

$$\begin{aligned}\tilde{I}_Q^{(k)K}(\tau,x,\theta) &= \int_{\tau}^{+\infty} e^{-(\tau'-\tau)\varphi(x)/\mu}\ \tilde{S}_Q^{(k)K}(\tau,x,\theta)\,\frac{\varphi(x)}{\mu}\,\mathrm{d}\tau', \quad \text{for } \mu>0, \\ \tilde{I}_Q^{(k)K}(\tau,x,\theta) &= -\int_{0}^{\tau} e^{-(\tau'-\tau)\varphi(x)/\mu}\ \tilde{S}_Q^{(k)K}(\tau,x,\theta)\,\frac{\varphi(x)}{\mu}\,\mathrm{d}\tau', \quad \text{for } \mu<0.\end{aligned} \tag{5.18}$$

Thus from Equations (5.16) and (5.17) we get an expression for azimuthal Fourier source vector components as

$$\tilde{S}_{l,Q}^{(k)K}(\tau,x,\theta) = \tilde{G}_Q^{(k)K}(\tau) + \int_{-\infty}^{+\infty} \mathrm{d}x' \oint \frac{\mathrm{d}\Omega'}{4\pi}\frac{1}{\varphi(x)}$$

$$\times \sum_{K'=0,2} \sum_{Q''=0}^{Q''=+K'} \widetilde{\mathcal{R}}^{(k)KK'}_{QQ''}(m,x,x',\theta,\boldsymbol{\Omega}',\boldsymbol{B}) \sum_{k'=-\infty}^{k'=+\infty} \mathrm{e}^{\mathrm{i}k'\chi'}\, \tilde{I}^{(k')K'}_{Q''}(\tau,x',\theta'). \quad (5.19)$$

Notice that the Fourier indices k and k' are not coupled to Q and Q'' unlike in the case of decomposition over $(\chi-\chi')$ (see Frisch, 2009, NS11).

The advantage of working in real irreducible basis is that we can reduce the computational time by restricting the values of azimuthal Fourier index k to positive space using conjugate symmetry relations as shown below. This simplification is analytically complicated in complex basis. From Equation (5.12) we can see that the components $\widetilde{\mathcal{R}}^{(k)KK'}_{QQ''}$ satisfy the symmetry relation

$$\widetilde{\mathcal{R}}^{(k)KK'}_{QQ''} = \left[\widetilde{\mathcal{R}}^{(-k)KK'}_{QQ''}\right]^{*}. \quad (5.20)$$

Using the above relation in Equation (5.11), we get

$$\mathcal{R}^{\mathrm{r},KK'}_{QQ''}(m,x,x',\Theta,\boldsymbol{B}) = Re\left[\sum_{k=0}^{k=+\infty}(2-\delta_{k0})\,\mathrm{e}^{\mathrm{i}k\chi}\,\widetilde{\mathcal{R}}^{(k)KK'}_{QQ''}(m,x,x',\theta,\boldsymbol{\Omega}',\boldsymbol{B})\right]. \quad (5.21)$$

Notice that the Fourier series constitutes only the terms with $k \geqslant 0$ which is useful in practical computations. With this simplification and following as in Equations (5.15)-(5.19), we get

$$S^{\mathrm{r},K}_{l,Q}(\tau,x,\boldsymbol{\Omega}) = Re\left[\sum_{k=0}^{k=+\infty}(2-\delta_{k0})\,\mathrm{e}^{\mathrm{i}k\chi}\,\tilde{S}^{(k)K}_{l,Q}(\tau,x,\theta)\right] \quad (5.22)$$

and

$$I^{\mathrm{r},K}_{l,Q}(\tau,x,\boldsymbol{\Omega}) = Re\left[\sum_{k=0}^{k=+\infty}(2-\delta_{k0})\,\mathrm{e}^{\mathrm{i}k\chi}\,\tilde{I}^{(k)K}_{l,Q}(\tau,x,\theta)\right]. \quad (5.23)$$

The $\tilde{S}^{(k)K}_{l,Q}(\tau,x,\boldsymbol{\Omega})$ now takes the form

$$\tilde{S}^{(k)K}_{l,Q}(\tau,x,\theta) = \tilde{G}^{(k)K}_{Q}(\tau) + \int_{-\infty}^{+\infty}\mathrm{d}x' \oint \frac{\mathrm{d}\Omega'}{4\pi}\frac{1}{\varphi(x)} \sum_{K'=0,2}\sum_{Q''=0}^{Q''=+K'}$$
$$\times\widetilde{\mathcal{R}}^{(k)KK'}_{QQ''}(m,x,x',\theta,\boldsymbol{\Omega}',\boldsymbol{B})Re\left[\sum_{k'=0}^{k'=+\infty}(2-\delta_{k'0})\mathrm{e}^{\mathrm{i}k'\chi'}\,\tilde{I}^{(k')K'}_{Q''}(\tau,x',\theta')\right]. \quad (5.24)$$

5.3 Azimuthal Fourier components of the redistribution matrix elements

In this section, we present the azimuth angle dependence of the Fourier decomposed matrix elements of the redistribution matrix, namely $\widetilde{\mathcal{R}}^{(k)KK'}_{QQ''}(m, x, x', \theta, \mathbf{\Omega}', \boldsymbol{B})$. From Equation (5.21), it is clear that the value of k extends from 0 to $+\infty$. For numerical evaluation it is necessary to truncate this infinite series. Our studies show that the series can be truncated at $k = 4$. We compute Fourier components $\widetilde{\mathcal{R}}^{(k)KK'}_{QQ''}$ numerically. This we do by numerical integration of $\mathcal{R}^{KK'}_{QQ''}$ over the azimuth angle χ using a Gauss-Legendre quadrature with 32 grid points between $[0, 2\pi]$.

Figure 5.1 shows the $\widetilde{\mathcal{R}}^{(k)20}_{00}$ element of the redistribution matrix as a function of x' and χ' for a given set of x, θ, θ' and the magnetic field parameters. The main feature is that the $k = 0$ component is the dominant term. Even though $k \neq 0$ terms depend sensitively on χ', their magnitudes are several orders smaller than the $k = 0$ component. For this reason, we can truncate the Fourier azimuthal expansion of the redistribution matrix elements to the fifth term itself without causing significant errors. In fact for practical computation one can truncate the series at $k = 2$ itself. This would help in rapid computation of the angle-dependent PRD problems in practical applications. However, in the theoretical studies presented in the chapter we use $k = 4$. From Figure 5.1 it follows that the higher order components show several harmonics as χ' varies from 0 to 2π. This behavior is confined to $x' \lesssim 3$ when $x = 0$. For larger values of x', the components approach the value zero. We have verified that the above conclusions remain valid for arbitrary choice of x, θ, θ' and the magnetic field parameters and for other combinations of K, K', Q, Q''.

5.4 Scattering expansion method for Hanle effect with angle-dependent partial frequency redistribution

In Section 5.3, we showed that the azimuthal Fourier expansion of the redistribution matrix (see Equation 5.21) can be truncated to the fifth term. Thus, for $k = 0, 1, 2, 3, 4$, we obtain a finite set of 54 coupled integral equations. The dimensionality of the problem increases to 54 complex quantities from 54 real quantities when we work in full space (i.e. $-4 \leqslant k \leqslant +4$). Thus working in positive half space is computationally advantageous. In this section we present an iterative method to solve this set of coupled equations. This method is based on Neumann series expansion of the components of the source vector contributing to the polarization. Sampoorna et al. (2011) applied this method to solve the transfer problem with angle-dependent PRD in the non-magnetic case and named it as SEM. These

authors also show the efficiency of SEM over the core-wing-based polarized approximate lambda iteration (ALI) method. NS11 employed SEM to solve Hanle transfer problem with angle-dependent PRD. The results obtained by them showed slight inconsistency as compared to the results obtained from perturbation method (Nagen-

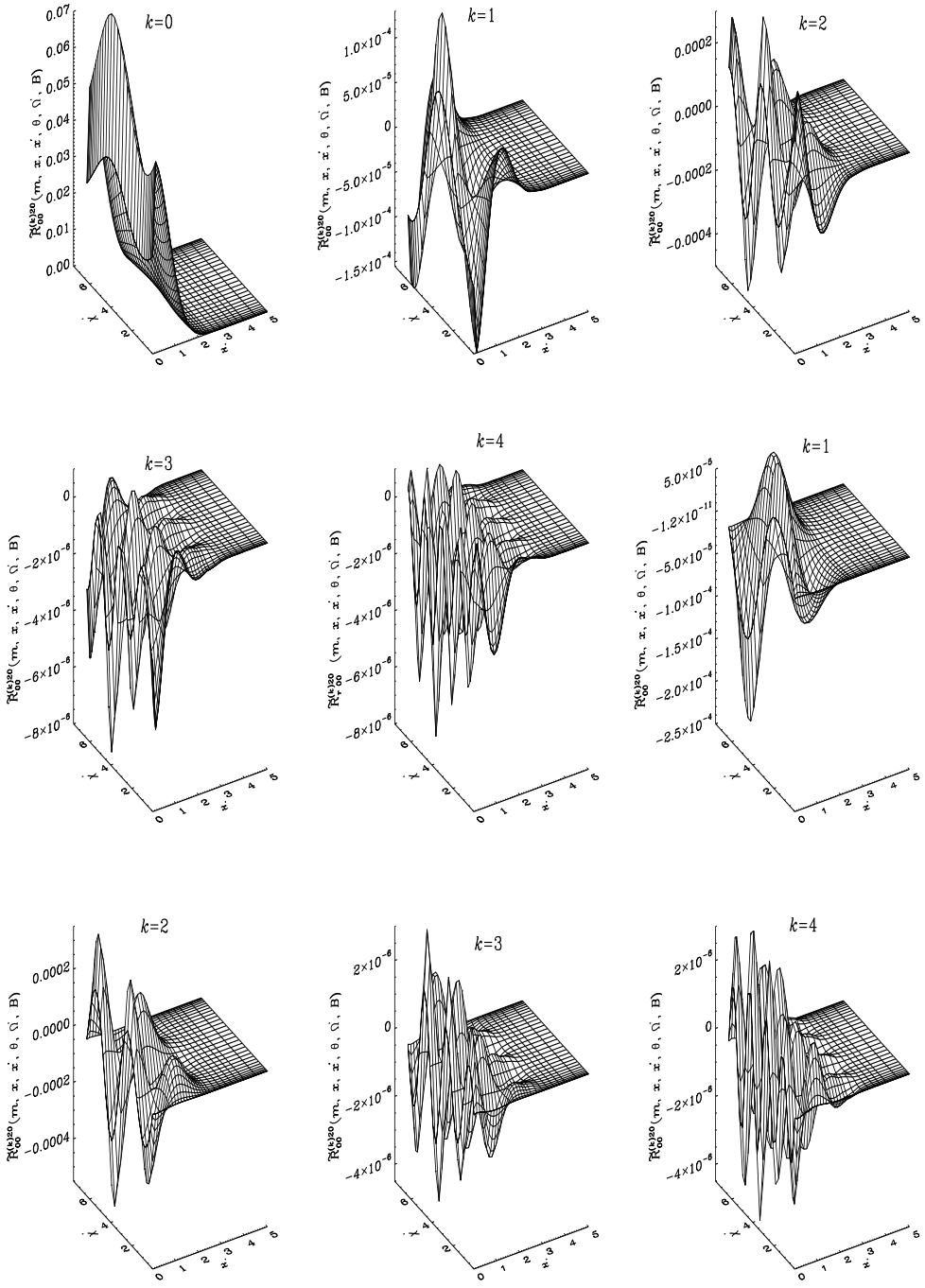

Figure 5.1: Fourier azimuthal components of the type II redistribution matrix elements are shown as a function of x' and χ' for $x = 0$, $\theta = \pi/2$, $\theta' = \pi$ and $(\Gamma, \theta_B, \chi_B) = (1, 30°, 0°)$. The first five panels from left to right correspond to the real part of $\widetilde{\mathcal{R}}_{00}^{(k)20}$ and the remaining panels refer to the imaginary part of $\widetilde{\mathcal{R}}_{00}^{(k)20}$.

dra et al., 2002). This might be due to the use of angle-averaged frequency domains (approximation III) to solve the Hanle transfer problem with angle-dependent PRD functions. Consistency in the results can be obtained by actually using the angle-dependent frequency domains (approximation II).

In SEM, first neglecting polarization we calculate Stokes I. We assume that Stokes I is cylindrically symmetric and is given by the component $\tilde{I}_0^{(0)0}$ itself to an excellent approximation. This approximation yields $k' = K' = Q'' = 0$ in Equation (5.24). The resulting component is the solution of a non-local thermodynamic equilibrium unpolarized radiative transfer equation with the line source function given by

$$\tilde{S}_{l,0}^{(0)0}(\tau, x, \theta) = \epsilon B_{\nu_0} + \int_{-\infty}^{+\infty} \mathrm{d}x' \oint \frac{\mathrm{d}\Omega'}{4\pi} \frac{1}{\varphi(x)} \times \widetilde{\mathcal{R}}_{00}^{(0)00}(m, x, x', \theta, \boldsymbol{\Omega}', \boldsymbol{B})\, \tilde{I}_0^{(0)0}(\tau, x', \theta'). \tag{5.25}$$

Equation (5.25) can be solved using a scalar ALI method based on a core-wing approach. Keeping only the contribution of $\tilde{I}_0^{(0)0}$ on the RHS of Equation (5.24) to the $K = 2$ coefficients and $k = 0,\ 1,\ 2,\ 3,\ 4$, each component $\tilde{S}_{l,Q}^{(k)2}$ can be written as

$$\left[\tilde{S}_{l,Q}^{(k)2}(\tau, x, \theta)\right]^{(1)} \simeq \int_{-\infty}^{+\infty} \mathrm{d}x' \oint \frac{\mathrm{d}\Omega'}{4\pi} \frac{1}{\varphi(x)} \times \widetilde{\mathcal{R}}_{Q0}^{(k)20}(m, x, x', \theta, \boldsymbol{\Omega}', \boldsymbol{B})\, \tilde{I}_0^{(0)0}(\tau, x', \theta'). \tag{5.26}$$

The superscript 1 stands for the single scattering approximation to the polarized component of the source vector. The corresponding radiation field $\left[\tilde{I}_Q^{(k)2}\right]^{(1)}$ for $k = 0,\ 1,\ 2,\ 3,\ 4$ is calculated with a formal solver and it serves as a starting solution for calculating the higher-order terms. The higher-order terms can be obtained by substituting for $\tilde{I}_{Q''}^{(k')2}$ appearing in the RHS of Equation (5.24), from $\left[\tilde{I}_Q^{(k)2}\right]^{(1)}$. We see that indices k, k', Q and Q' are now decoupled whereas they were coupled in the case of Fourier decomposition over $(\chi - \chi')$. Correspondingly the number of non-zero $\left[\tilde{I}_Q^{(k)2}\right]^{(1)}$ has increased from 25 to 54 when changing from Fourier expansion over $(\chi - \chi')$ to that over χ. As a result the dimensionality of the problem has increased in the single-scattered solution computation.

In the computation of higher order scattering terms, apart from keeping the coupling of $(K = 2, Q)$ components with other polarization components $(K' = 2, Q'')$, we also keep the coupling of k with all other k' terms. We recall that in NS11 coupling of k with $k' = 0$ terms were only retained. Thus $\tilde{S}_{l,Q}^{(k)2}$ at order *n* are now given

by

$$\left[\tilde{S}^{(k)2}_{l,Q}(\tau,x,\theta)\right]^{(n)} \simeq \left[\tilde{S}^{(k)2}_{l,Q}(\tau,x,\theta)\right]^{(1)} + \int_{-\infty}^{+\infty} \mathrm{d}x' \oint \frac{\mathrm{d}\Omega'}{4\pi} \frac{1}{\varphi(x)} \sum_{Q''=0}^{Q''=2} \times \widetilde{\mathcal{R}}^{(k)22}_{QQ''}(m,x,x',\theta,\mathbf{\Omega}',\boldsymbol{B})\, Re\left\{ \sum_{k'=0}^{k'=+\infty} (2-\delta_{k'0})\, \mathrm{e}^{\mathrm{i}k'\chi'} \left[\tilde{I}^{(k')2}_{Q''}(\tau,x',\theta')\right]^{(n-1)} \right\}. \tag{5.27}$$

From Figure 5.1 it can be seen that $k = 0$ component of the redistribution matrix elements dominate over the higher order terms ($k \neq 0$). For this reason, despite a strong dependence of $\widetilde{\mathcal{R}}^{(k)KK'}_{QQ''}$ on χ', it is sufficient in the summation over k' to retain the leading term (namely $k' = 0$) in practical computations. The inclusion of higher order terms $k' > 0$ do not affect the solutions significantly. Using only $k' = 0$ term also saves great amount of computing effort.

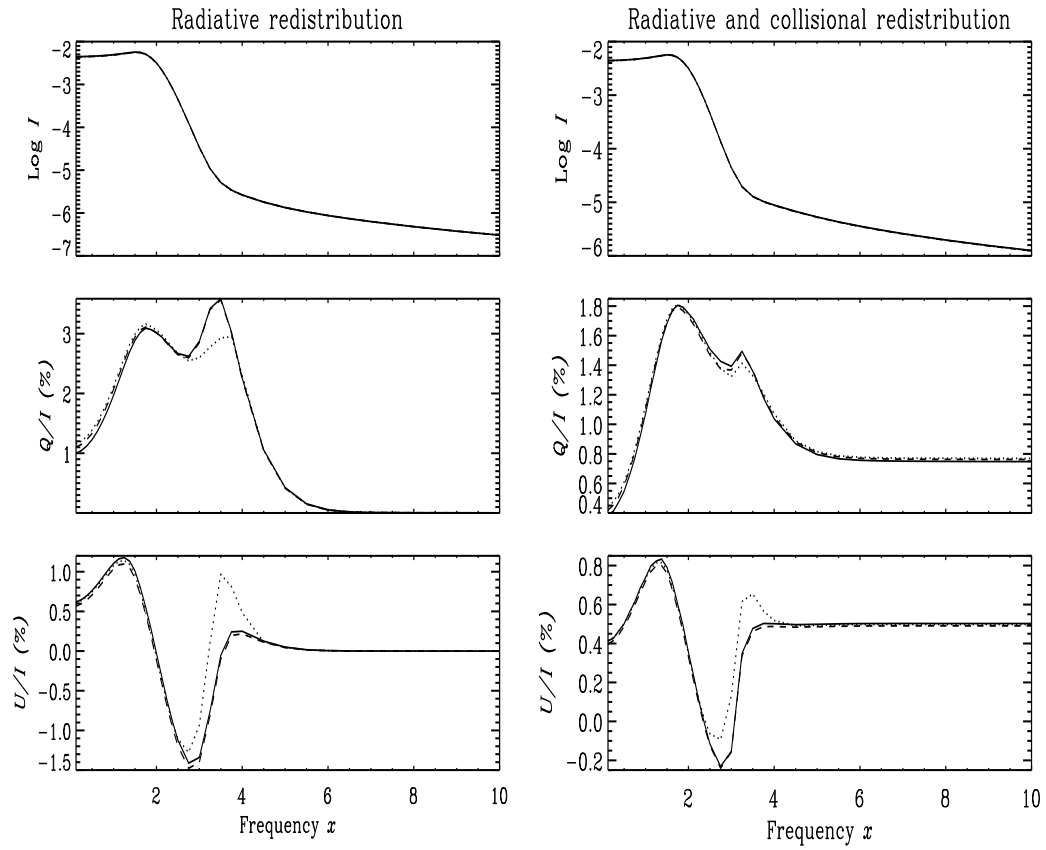

Figure 5.2: Stokes profiles at $\mu = 0.112$ computed using three numerical methods, namely the perturbation method (solid line), the NS11 approach (dotted line), and the self consistent approach used in this chapter (dashed line). Model parameters are (T, a, ϵ, r, B_{ν_0}) = (10, 10^{-3}, 10^{-3}, 0, 1). The magnetic field parameters are taken as (Γ, θ_B, χ_B) = (1, 30°, 0°). The left panel shows the results computed using pure R_{II} function and the right panel is for a combination of R_{II} and R_{III} functions with Γ_E/Γ_R = 1.

5.5 Results and discussions

We compare the Stokes parameter I and the ratios Q/I and U/I computed from our present approach with the perturbation method of Nagendra et al. (2002) and NS11 approach. The perturbation method treats linear polarization as a perturbation to the scalar intensity, and computes the polarization in a two-step process, wherein an accurately computed Stokes I is used as an input in the evaluation of the polarized scattering integral. In successive perturbations, the Stokes Q and U are computed more and more accurately until convergence is reached. The NS11 approach is discussed in Sections 5.1 and 5.5.1. We consider self-emitting plane-parallel, isothermal atmospheres with no incident radiation at the boundaries. The slab models are characterized by (T, a, ϵ, r, B_{ν_0}, Γ_E/Γ_R), where T is the optical thickness of the slab, and Γ_E is the elastic collision rate. The depolarizing collision rate $D^{(2)}$ is set to $\Gamma_E/2$. The plank function B_{ν_0} is taken as unity at the line center. The polarizability factor W_2 is taken as unity (i.e. we consider a $J = 0 \rightarrow 1 \rightarrow 0$ scattering transition with J being the total angular momentum quantum number). The vector magnetic field in the Hanle scattering problem is defined through the field strength parameter $\Gamma = g\omega_L/\Gamma_R$, with g being the Landé factor of the upper level and ω_L the Larmor frequency; the field inclination (θ_B, χ_B) defined with respect to the atmospheric normal. For angle and frequency discretization, we have used quadratures of the same order as those used by NS11. Therefore, we do not elaborate here on the computational aspects.

5.5.1 A comparison with previous approaches to solve the angle-dependent Hanle transfer problem

In this section we present the Stokes profiles of the lines formed in a magnetized slab scattering according to Hanle PRD matrix formulated by Bommier (1997b). In the so called approximation II and III of Bommier (1997b), the switch over from the Hanle phase matrices (in the core) to the Rayleigh phase matrix (in the wings) is achieved through the use of angle-dependent and angle-averaged frequency domains, respectively. It is shown by Bommier (1997b) that the use of frequency domains simplifies the numerical evaluation of the redistribution matrices.

It is natural that in angle-dependent radiative transfer computations involving angle-dependent functions, one should use approximation II involving angle-dependent functions. However, as already discussed in Sections 5.1 and 5.4, in NS11 angle-averaged domains were used in computing the angle-dependent redistribution matrix. Although such an approach is inconsistent, it provides a rapid means of solving the Hanle angle-dependent PRD problems. In the present chapter we test their

approach by actually using angle-dependent frequency domains while computing angle-dependent redistribution matrix (which is fully consistent). In Figure 5.2, we show a comparison of results obtained by the NS11 and the present approach, along with those obtained from the simple perturbation method of Nagendra et al. (2002), which is also consistent, like the present approach. The left panels in Figure 5.2 show the Stokes profiles computed using pure $R_{\rm II}$ function. One can clearly see that the NS11 approach differs from the present approach particularly in the frequency range $3 \lesssim x \lesssim 5$. The present approach and perturbation method give same results. The impact of the approximation used in the NS11 is more severe on the Stokes U parameter. The right panels in Figure 5.2 show the results computed using the same model as in the left panels, but for the introduction of elastic collisions (a combination of $R_{\rm II}$ and $R_{\rm III}$). One can clearly see that the differences between NS11 and the present approach still exist, although the collisions decrease these differences. The present approach, unlike the approximate treatment followed in NS11, thus provides a self-consistent approach to compute the redistribution matrix (i.e. the use of angle-dependent domains to compute angle-dependent redistribution matrices), at the same time requiring manageable computing resources . This has practical implications in realistic modeling of the observed Stokes profiles.

Table 5.1 shows a comparison of computing resources required by three numerical

Table 5.1: Comparison of CPU time taken by different methods for radiative transfer computations. The model parameters used for the computation are (T, a, ϵ, r, B_{ν_0}, Γ_E/Γ_R) = (2×10^6, 10^{-3}, 10^{-3}, 0, 1, 1)

Method	Time (minutes)	Memory
Present approach	28	13GB
Perturbation method	112	7.6GB
NS11 approach	33	226MB

methods. Compared to the perturbation method that requires large computing time (112 minutes to obtain a solution), the approximate method of NS11, and the present method are less expensive. In spite of being inconsistent, the approximate method of NS11 requires far less computing memory compared to the other two methods. This is because in NS11 the polarized transfer equation is solved in a azimuth independent Fourier basis, which thereby avoids introducing azimuth angle grids. The present approach requires larger memory because we now need to discretize the azimuth angle χ' and store the huge matrix $\widetilde{\mathcal{R}}^{(k)KK'}_{QQ''}(m, x, x', \theta, \mathbf{\Omega}', \boldsymbol{B})$. The memory requirement of the present approach is even larger than that of perturbation method because the former involves solving 54 coupled integral equations in Fourier basis, while the later involves solving 3 coupled integral equations in Stokes basis. However, unlike the present approach the convergence is not always guaranteed in the

perturbation method, as angle-frequency coupling is more intricate in Stokes basis than in Fourier basis.

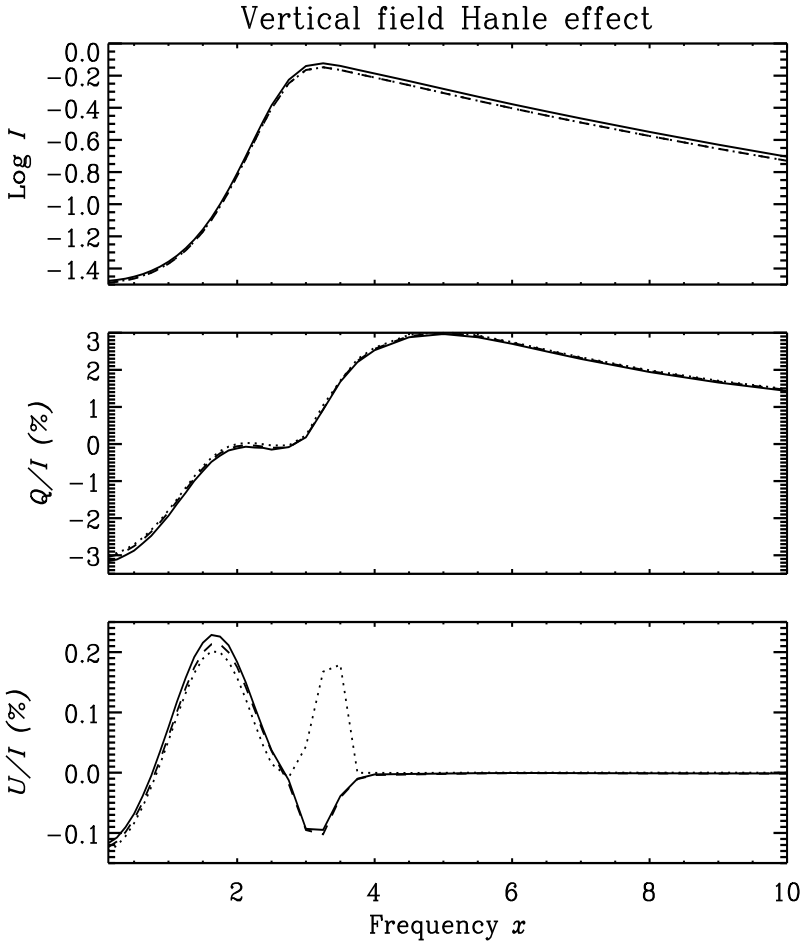

Figure 5.3: A comparison of emergent Stokes profiles computed by three numerical methods discussed in the text. The profiles are presented for $\mu = 0.112$ and for a vertical magnetic field (Γ, θ_B, χ_B) = (1, 0°, 0°). Different line types represent same cases as in Figure 5.2. The slab model parameters are (T, a, ϵ, r, B_{ν_0}, Γ_E/Γ_R) = (2×10^4, 10^{-3}, 10^{-3}, 0, 1, 1).

5.5.2 The vertical field Hanle effect

It is expected that when the magnetic field is parallel to the symmetry axis of the slab (the atmospheric normal), the Hanle effect should vanish. In other words the Stokes U parameter should be zero in this case. This characteristic behavior is satisfied when we work with angle-averaged redistribution functions. When angle-dependent redistribution function is used this behavior is not satisfied. In other words, Stokes U does not vanish, in spite of the field being vertical, as long as the angle-dependent redistribution function is used. The non-zero emergent Stokes U is due to coupling of Stokes U to Stokes I through the components $\widetilde{\mathcal{R}}^{(k)KK'}_{QQ'}$ for $k \neq 0$. The reason for this unexpected behavior is also discussed by Frisch et al. (2001) and numerically

demonstrated in Nagendra et al. (2002). We revisit this interesting problem in Figures 5.3 and 5.4. In Figure 5.3 we show the Stokes profiles computed using NS11 and the present approach, and compare it with the results from the perturbation method. The differences between the NS11 and the present approach are drastic in Stokes U parameter. The Stokes U in the frequency range $3 \lesssim x \lesssim 5$ has opposite signs. The present approach produces Stokes U consistent with the perturbation method. The NS11 approach for approximation II seems to be inadequate in computing U in this particular problem. Such a large difference between the results obtained from NS11 approach and the perturbation method prompts us to conclude that it is safer to use angle-dependent frequency domains to solve angle-dependent Hanle transfer problems.

Figure 5.4 shows the center-to-limb variation of linear polarization for a vertical magnetic field. The intensity exhibits the characteristic limb darkening in the line core and limb brightening in the wings. The Q/I shows limb brightening throughout the line profile. The dependence on μ is non-monotonic in the core region in U/I. Since the angle-dependent functions become azimuthally symmetric at the disk center the U/I approaches zero as the line of sight approaches the disk center. In the line wings, U/I tend to zero for all μ's which is due to the Rayleigh scattering in the line wings, that produces $U/I = 0$ by axisymmetry.

5.5.3 The Hanle effect with micro-turbulent magnetic fields

It is known that the presence of a weak turbulent magnetic field in the solar atmosphere can be detected using Hanle effect. In the case of CRD, Frisch et al. (2009) showed that the polarization obtained using Hanle effect is quite sensitive to the choice of field strength distribution and in general, micro-turbulence is a safe approximation to represent weak turbulent magnetic fields. For a micro-turbulent magnetic field, the scale of variation of the field is small compared to the mean free path of the photons, and this allows to replace all the field dependent physical parameters by their averages over the magnetic field vector probability density function (PDF). In our problem this condition leads to the averaging of the magnetic kernel $\mathcal{N}^{rK}_{QQ'}(m, \boldsymbol{B})$ over the magnetic field vector PDF. In the present chapter we use a PDF corresponding to the isotropic distribution of field orientation (θ_B, χ_B) and a single value of the field strength. As shown in Stenflo (1982, 1994) the Hanle problem with this choice of PDF reduces then to a resonance polarization problem, with a modified value of Q/I. In other words, the micro-turbulent averaged magnetic kernel namely $\left\langle \mathcal{N}^{rK}_{QQ'}(m, \boldsymbol{B}) \right\rangle$ becomes diagonal, and only $\left\langle \mathcal{N}^{r2}_{00}(m, \boldsymbol{B}) \right\rangle$ element is of relevance. The explicit form of $\left\langle \mathcal{N}^{r2}_{00}(m, \boldsymbol{B}) \right\rangle$ is given by (see Appendix B of

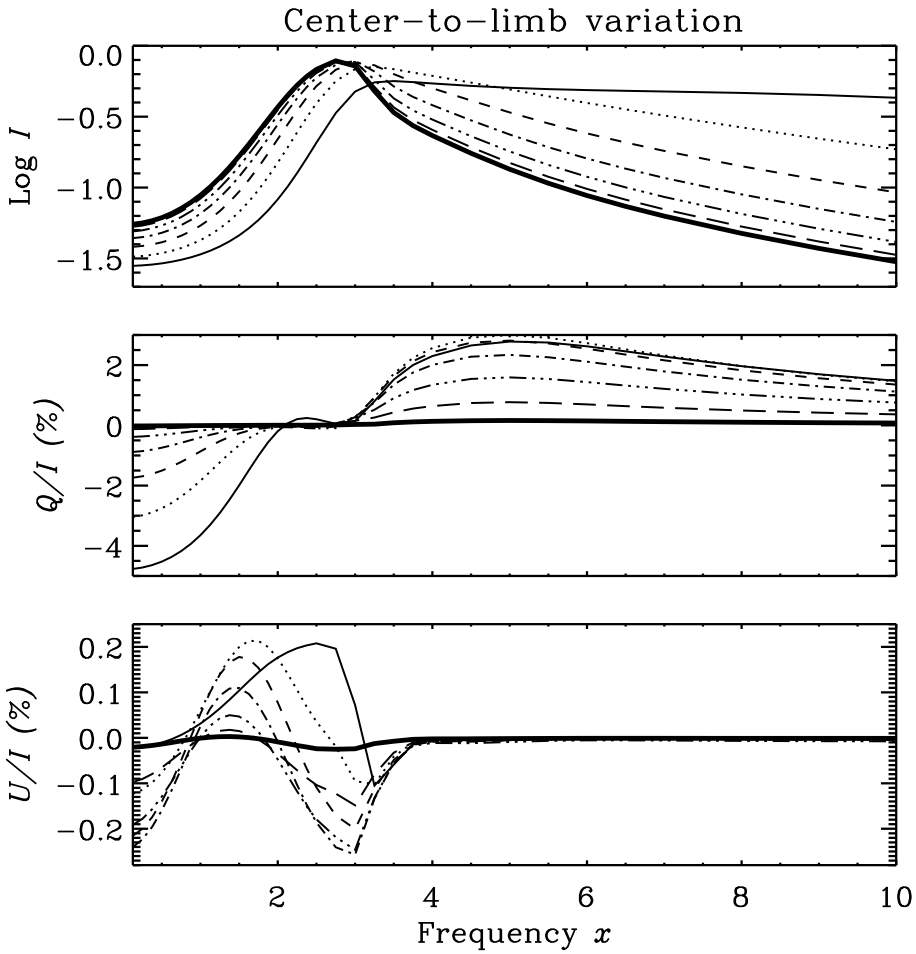

Figure 5.4: Stokes I and ratios Q/I and U/I for different emergent angles ($\theta = \cos^{-1}\mu$) computed for a vertical magnetic field. The atmospheric model is same as in Figure 5.3. Different line types are: solid line, $\mu = 0.025$; dotted line, $\mu = 0.129$; dashed line, $\mu = 0.297$; dot-dashed line, $\mu = 0.50$; dash-triple-dotted line, μ =0.702; long-dashed line, $\mu = 0.871$; and thick solid line, $\mu = 0.974$.

Frisch et al., 2009)

$$\left\langle \mathcal{N}_{00}^{r2}(m, \boldsymbol{B}) \right\rangle = 1 - \frac{2}{5}\frac{\Gamma^2(m)}{1+\Gamma^2(m)} - \frac{2}{5}\frac{4\Gamma^2(m)}{1+4\Gamma^2(m)}, \tag{5.28}$$

where $\Gamma(m)$ denotes the Hanle Γ-parameter in different frequency domains. We refer the reader to Equations (89) of Bommier (1997b) for the explicit form of $\Gamma(m)$ in different frequency domains where the Hanle effect is operative. In frequency domains where the Rayleigh scattering is present, $\Gamma(m) = 0$. Figure 5.5(a) shows the ratio Q/I obtained using the present approach and the NS11 approach in the presence of micro-turbulent magnetic field. The difference between the results obtained using these different methods mainly exists in the transition region $3 \lesssim x \lesssim 5$. Figure 5.5(b) shows the comparison of Q/I profiles computed using angle-averaged and angle-dependent redistribution matrices. For angle-averaged computations, we use

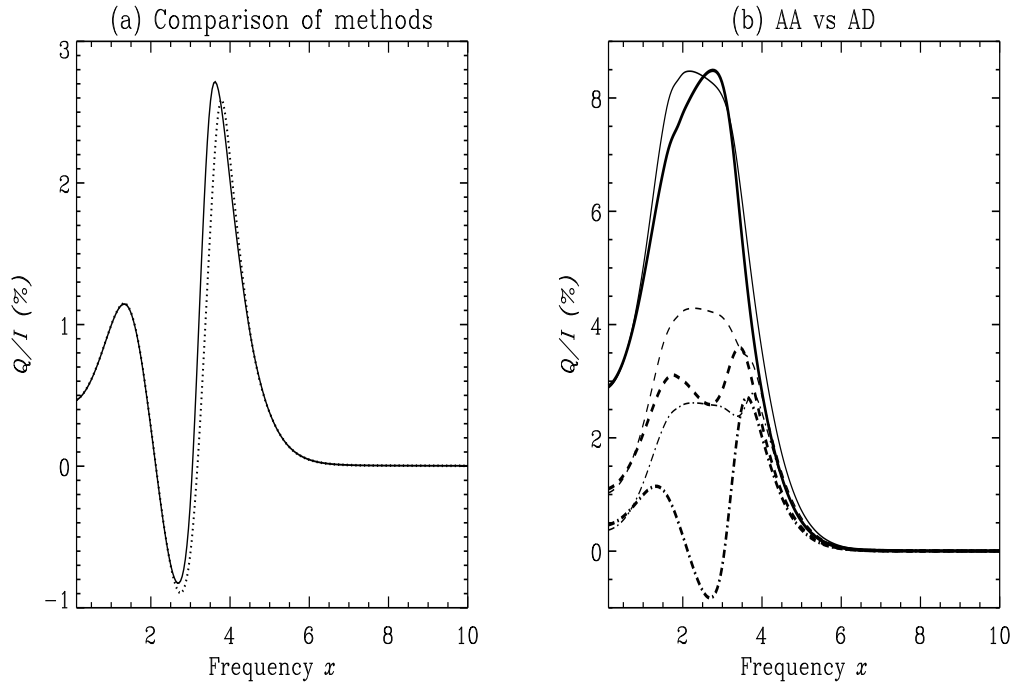

Figure 5.5: Stokes Q/I for emergent angle $\mu = 0.112$ computed for the case of micro-turbulent magnetic field. The atmospheric model is (T, a, ϵ, r, B_{ν_0}, Γ_E/Γ_R) = (10, 10^{-3}, 10^{-3}, 0, 1, 0). Panel (a) shows the comparison of the present approach (solid line) and NS11 approach (dotted line). Panel (b) shows the comparison of angle-averaged and angle-dependent cases. Different line types are : non-magnetic case, solid lines; deterministic magnetic field, dashed lines; and micro-turbulent magnetic field, dot-dashed lines. The thick and thin lines represent angle-averaged and angle-dependent cases respectively. For the micro-turbulent magnetic field case, $\Gamma = 1$ and for the deterministic magnetic field case, (Γ, θ_B, χ_B) = (1, 30°, 0°).

redistribution matrices computed in angle-averaged domains (approximation III of Bommier, 1997b), and for angle-dependent computations the corresponding angle-dependent redistribution matrices are computed in angle-dependent domains (approximation II of Bommier, 1997b). Three different sets of results are presented in Figure 5.5(b), namely non-magnetic, deterministic field, and micro-turbulent field results. We see that in the case of the Hanle effect with micro-turbulent magnetic field, there is depolarization in the line core and in the near wing frequencies as compared to the other two cases. Our studies show that in the case of the Hanle effect with micro-turbulent magnetic field, the differences between angle-averaged and angle-dependent results are prominent in thin slab cases and reduce considerably in thick slab cases. These differences between angle-averaged and angle-dependent results, especially in the $3 \lesssim x \lesssim 5$ region (apart from the line core), were already noticed by Nagendra et al. (2002), for the deterministic magnetic field case. It is interesting to note that such differences get enhanced in the presence of a micro-turbulent magnetic field. This is probably because of the localization of line photons within the micro-turbulent scattering eddies, resulting in a relatively larger number

of scattering. These differences can be clearly seen from Figure 5.5(b).

5.6 Conclusions

In this chapter we have solved the angle-dependent Hanle scattering problem using the angle-dependent PRD theory (approximation II of Bommier, 1997b). This computationally expensive problem is solved using an iterative method based on the Neumann series expansion (SEM). Following Anusha & Nagendra (2011a) we decompose the Stokes parameters in terms of azimuthally symmetric Fourier coefficients, by expanding the Hanle redistribution matrix in terms of the radiation azimuth χ. Only such a decomposition allows the use of angle-dependent frequency domains for solving the angle-dependent Hanle scattering problems. In contrast a decomposition, based on the expansion in terms of $(\chi - \chi')$, as done in NS11, does not allow the use of angle-dependent domains to solve the angle-dependent Hanle scattering problem. For this reason a simpler approach was suggested by NS11 which used angle-averaged frequency domains (approximation III of Bommier, 1997b), to solve the angle-dependent Hanle transfer problem. We show that their approach does not always hold good. We have carried out a numerical study to show the differences between the solutions obtained by NS11 approach and the self-consistent approach used now in this chapter. The U/I profiles in particular show significant differences in the core to wing transition region ($3 \lesssim x \lesssim 5$) of the line. The special case of vertical field Hanle effect is considered as a case study, and the differences between the NS11 and the present approach are examined. It is shown that the present method offers a self-consistent and accurate method of solving the difficult problem of angle-dependent partial redistribution with Hanle scattering. The interesting behavior of Q/I profiles in the presence of micro-turbulent magnetic fields is also examined. We show that the differences between angle-averaged and angle-dependent solutions are enhanced by the presence of a micro-turbulent field. The differences are noticed in both the line core and near wing regions ($3 \lesssim x \lesssim 5$).

In the next part of the thesis we relax another important approximation generally made in studying the effects of redistribution function on polarized line formation namely, the effects of the polarization of the lower level. Generally in the standard methods to study the polarized radiative transfer, the lower level is assumed to be unpolarized. In the next part of the thesis we consider the case of a two-level atom with polarized lower level. We derive the appropriate redistribution matrix and study the influence of lower-level polarization on the polarized line profiles formed under PRD.

Part III

Effects of lower-level polarization on the Stokes profiles

Chapter 6

Polarized line formation with lower-level polarization and partial frequency redistribution *

An Overview

In the well-established theories of polarized line formation with partial frequency redistribution (PRD) for a two-level and two-term atom it is generally assumed that the lower level of the scattering transition is unpolarized. However the existence of unexplained spectral features in some lines of the Second Solar Spectrum (SSS) points toward a need to relax this assumption. There exists a density matrix theory that accounts for the polarization of all the atomic levels, but it is based on the flat-spectrum approximation, corresponding to complete frequency redistribution (CRD). In the present chapter we formulate a theory for magnetized media that includes both the effects of PRD and the lower level polarization (LLP) for a two-level atom. First we derive a collisionless redistribution matrix that includes the combined effects of the PRD and the LLP. We then formulate the relevant transfer equation and solve it using a two stage approach. For the purpose of illustration we consider two case studies in the non-magnetic regime, namely, the J_a = 1, J_b = 0 and J_a = J_b =1, where J_a and J_b represent the total angular momentum quantum numbers of the lower and upper states respectively. Our studies show that the effects of LLP are significant only in the line core. This leads us to propose a simplified numerical approach to solve the concerned radiative transfer problem.

*The contents of this chapter are based on Supriya et al. (2016)

6.1 Introduction

We know that the linear polarization of the spectral lines is produced due to the absorption, emission and scattering of radiation in the solar atmosphere. The anisotropic illumination of the atom induces atomic alignment, which in turn gives rise to the polarization of the radiation (scattering polarization). There are two important theoretical approaches developed so far to study the physics of scattering polarization. The first one is the self-consistent approach developed by Landi Degl'Innocenti (1983) using the density matrix formalism, starting from the principles of quantum electrodynamics. One of the main advantages of this "density matrix" approach is that it allows one to take into account the polarization of all the levels of the atomic system under consideration. This naturally allows to take into account the LLP. The density matrix formalism is developed under the flat spectrum approximation and hence its main limitation is the difficulty to take into account the effects of PRD. The second theoretical approach is the semi-classical one, which provides the advantage of including the effects of PRD by means of redistribution matrices (Stenflo, 1994, hereafter S94). Using this "redistribution matrix" approach, our understanding of the physics of resonance scattering has improved greatly and the effects of PRD have been studied extensively. The limitation of this theory is that using it we can deal with only two-level and two-term atoms with unpolarized, infinitely sharp lower levels.

The many anomalous spectral structures in the SSS (Stenflo & Keller, 1997; Stenflo et al., 2000) casts doubt on the general assumption made in the standard theoretical formulation that, the anisotropic illumination of atoms in the solar atmosphere induces population imbalances only in the upper level and the lower level is assumed to be unpolarized. Except for the case when the total angular momentum* of the lower level is $J_a = 0$ or $1/2$, the assumption of unpolarized lower level is questionable particularly when the lower level is different from the ground state. Trujillo Bueno & Landi Degl'Innocenti (1997) studied the influence of lower level atomic polarization on the scattering line polarization for the case of a two-level atom with $J_a = 1$ and $J_b = 0$. This is an example where the resulting polarization is completely due to the population imbalances in the sublevels of the lower atomic level. They used the density matrix approach and solved simultaneously the statistical equilibrium equations (SEEs) neglecting stimulated emission and the transfer equation under CRD. Later this theory was applied to explain many spectral features in the SSS. Landi degl'Innocenti (1998) attempted to explain the peaks in the linearly polarized profiles of both the Na I D_1 and D_2 lines by accounting for the optical depopulation

*J_a and J_b represent total angular momentum quantum numbers of the lower and upper levels respectively.

pumping of the split lower levels. Trujillo Bueno (1999) showed the importance of LLP in the case of Mg I b_2 line. Also he pointed out the importance of the depolarizing elastic collisions and their role in decreasing the alignment of the atomic levels (see also Casini et al., 2002). Trujillo Bueno et al. (2002) demonstrated the operation of the ground-level Hanle effect and importance of the selective absorption from the ground level to the generation of the polarization in the He I triplet system. Also the importance of atomic polarization of the metastable lower level of the Ca II infrared triplet was presented by Manso Sainz & Trujillo Bueno (2003b, 2010). However in all the above mentioned studies the effects of the PRD were neglected. In Nagendra (2003) the effects of PRD on linear polarization profiles have been reviewed and the limitations of CRD approximation are pointed out (see also Nagendra, 2014, 2015). It is well know that CRD approximation is sufficient in describing the line core polarization, whereas the PRD effects are important in the wings of strong resonance lines.

Formulation of a general self consistent theory for radiative transfer problem including the effects of PRD and LLP is a complex theoretical problem. Landi degl'Innocenti et al. (1997) has formulated a theory for coherent scattering which takes into account the LLP. This theory is based on the concept of 'metalevels'. Based on this theory, Belluzzi et al. (2015) have recently derived the collisionless redistribution matrix for a two term atom with hyperfine structure splitting in the non-magnetic regime by including the polarizability of the lower hyperfine levels (F levels). They have applied this theory to the problem of Na I D lines. In their studies they have treated the LLP factor as a free parameter. Note that in the present chapter we treat this factor self consistently but for a two-level atom. Also Casini et al. (2014) have presented a new quantum scattering theory with which they have derived a generalized redistribution function for a polarized two-term atom with hyperfine structure splitting. As an alternative attempt, in the present chapter, we try to formulate a general theory for a two-level atom by combining the redistribution matrix approach and the density matrix approach. Using the redistribution matrix approach we derive the collisionless PRD matrix (the so called type II redistribution matrix in the nomenclature of Hummer, 1962) including the effects of LLP. In the process the density matrix elements of the lower level are appropriately incorporated in to the PRD matrix derived starting from the Kramers-Heisenberg scattering formulation. We remark that only the population imbalances among the sublevels of the lower level are taken into account, while the coherences among them are ignored. This is consistent with the assumption of infinitely sharp lower level. The lower level density matrix elements are obtained by solving the SEEs that are derived using the density matrix approach. The type II redistribution matrix so derived is then included in the radiative transfer equation. To this end we use the quantum

field theory approach given by S94 to obtain the transfer equation for the problem at hand. We further apply this theoretical formulation to the cases of $1\rightarrow0\rightarrow1$ and $1\rightarrow1\rightarrow1$ transitions in the non-magnetic regime.

In Section 6.2 we derive the collisionless redistribution matrix for a two-level atom with PRD and LLP mechanisms properly taken into account. In Section 6.3 the radiative transfer equation for solving the concerned problem is formulated. Section 6.4 concerns a discussion on the influence of LLP on the polarized line profiles formed under PRD. In Section 6.5 we propose a simple alternative approach to solve the same problem. The conclusions are presented in Section 6.6. In Appendix A the collisionless non-magnetic redistribution matrix is presented. Appendix B is dedicated to a verification of the expressions for the absorption matrix elements derived from the quantum field theory approach of S94. The two-stage numerical procedure used to solve the transfer equation and SEEs is described in Appendix C.

6.2 Redistribution matrix with partial frequency redistribution and lower-level polarization

6.2.1 Type-II redistribution matrix in the atomic frame

As a first step in our theoretical approach we derive the redistribution matrix including the effects of PRD and LLP. We consider a general case of $J_a \rightarrow J_b \rightarrow J_a$ scattering transition. We follow the Kramers-Heisenberg approach as given in Stenflo (1998) but include the contribution from the lower level density matrix elements. In Stenflo (1998) these elements were assumed to be the same for different magnetic sublevels of the lower level. We relax this assumption here and thereby take into account the population imbalances among the lower level. We start from Equations (7) and (8) of Stenflo (1998) which are given by

$$\mathbf{M} = \mathbf{T}\mathbf{W}\mathbf{T}^{-1}, \tag{6.1}$$

$$\mathbf{W} = \sum_{\mu_a} \rho_{\mu_a\mu_a} \sum_{\mu_f} w(\mu_f\mu_a) \otimes w^*(\mu_f\mu_a), \tag{6.2}$$

where $\mathbf{M}$ is the Mueller scattering matrix and $\mathbf{W}$ is the coherency matrix. They basically give scattering cross-sections for polarized scattering. In the above equations μ's denote the magnetic substates of a given J-state. The relative populations of the initial magnetic substates μ_a are denoted by $\rho_{\mu_a\mu_a}$. They can be obtained by solving the polarized SEEs as given in Equations (10.1) and (10.2) of Landi Degl'Innocenti & Landolfi (2004, hereafter LL04). SEEs given in LL04 take into account both popu-

lation imbalances and coherences while the coherency matrix given above takes into account only the population imbalances. When LLP is included the coherency matrix **W** not only depends on the bilinear product of the transition amplitudes $(w \otimes w^*)$ but also on the $\rho_{\mu_a\mu_a}$. The expression for transition amplitude is given by

$$w_{\alpha\beta}(\mu_f\mu_a) \sim \sum_{\mu_b}(-1)^{q-q'}(-1)^{2r_{ab}} f_{ab}(2J_a+1) \times \begin{pmatrix} J_b & J_a & 1 \\ -\mu_b & \mu_a & -q' \end{pmatrix} \begin{pmatrix} J_b & J_a & 1 \\ -\mu_b & \mu_f & -q \end{pmatrix} \Phi_{\mu_b\mu_f} \varepsilon_q^{\alpha *}\, \varepsilon_{q'}^{\beta}. \tag{6.3}$$

The above expression is obtained from Kramers-Heisenberg formula (see Equation (3) in Stenflo, 1998) for the scattering from a given initial magnetic substate with quantum numbers J_a and μ_a to a final magnetic substate with quantum numbers J_a and μ_f via all the possible intermediate magnetic substates μ_b of the upper level J_b (see also Equation (1) in Sampoorna, 2011a). In the above expression $\varepsilon_q^{\alpha *}$ and $\varepsilon_{q'}^{\beta}$ are the geometrical factors for the outgoing and incoming radiation respectively. f_{ab} denotes the absorption oscillator strength and r_{ab} its sign (see S94, pp. 192 and 199). The area-normalized profile function $\Phi_{\mu_b\mu_f}$ is given in Equation (3) of Sampoorna (2011a), where it is denoted as $\Phi_\gamma(\nu_{\mu_b\mu_f} - \xi)$. In order to derive the expression for redistribution matrix in terms of irreducible spherical tensors $T^K_Q(i,\mathbf{n})^\dagger$ of LL04 now including the effects of LLP we follow the same procedure as given in Appendices A and B of Sampoorna et al. (2007b). After an elaborate algebra we obtain the expression for the type II redistribution matrix with LLP in the atomic frame as

$$\begin{aligned} \mathbf{R}^{\rm II}_{ij}(\xi,\mathbf{n},\xi',\mathbf{n}',\mathbf{B}) &= \frac{2}{3}(2J_a+1)^2 \sum_{\mu_a\mu_f\mu_b\mu_b' qq'q''q'''} \sum_{K'K''Q} (-1)^{q''-q'}(-1)^Q \\ &\times \sqrt{(2K'+1)(2K''+1)}\frac{\Gamma_R}{\Gamma_R+\Gamma_I+{\rm i}Qg_b\omega_L}\rho_{\mu_a\mu_a} \begin{pmatrix} 1 & 1 & K'' \\ q & -q'' & Q \end{pmatrix} \\ &\times \begin{pmatrix} 1 & 1 & K' \\ q' & -q''' & Q \end{pmatrix} \begin{pmatrix} J_b & J_a & 1 \\ -\mu_b & \mu_a & -q' \end{pmatrix} \begin{pmatrix} J_b & J_a & 1 \\ -\mu_b & \mu_f & -q \end{pmatrix} \begin{pmatrix} J_b & J_a & 1 \\ -\mu_b' & \mu_a & -q''' \end{pmatrix} \\ &\times \begin{pmatrix} J_b & J_a & 1 \\ -\mu_b' & \mu_f & -q'' \end{pmatrix} \delta(\xi-\xi'-\nu_{af})\frac{1}{2}[\phi(\nu_{J_b\mu_b',J_a\mu_a}-\xi') + \phi^*(\nu_{J_b\mu_b,J_a\mu_a}-\xi')] \\ &\times (-1)^Q T^{K''}_Q(i,\mathbf{n}) T^{K'}_{-Q}(j,\mathbf{n}'). \end{aligned} \tag{6.4}$$

All the different symbols appearing in the above equation are the same as Sampoorna (2011a) and therefore we do not elaborate on them. The profile function $\phi(\nu_{J_b\mu_b,J_a\mu_a}-\xi)$ is defined in Equation (40) of Sampoorna (2011a). Note that Equa-

†Here $i = 0,1,2,3$ are the indices of Stokes parameters I, Q, U, V respectively, the multipolar index $K = 0,1,2$ with $Q \in [-K,+K]$, and $\mathbf{n}$ denotes the ray direction with respect to the atmospheric normal.

tion (6.4) is the same as Equation (47) of Sampoorna (2011a) except for the absence of elastic collisions (because we are dealing with collisionless redistribution) and for the presence of the new term $\rho_{\mu_a\mu_a}$ which arises due to the contribution from the LLP. Now writing $\rho_{\mu_a\mu_a}$ in terms of its multipolar components using Equation (3.99) of LL04 we get

$$
\begin{aligned}
\mathbf{R}^{\rm II}_{ij}(\xi,\mathbf{n},\xi',\mathbf{n}',\mathbf{B}) &= \frac{2}{3}(2J_a+1)^2 \sum_{\mu_a\mu_f\mu_b\mu_b' qq'q''q'''} \sum_{K'K''Q} \sqrt{(2K'+1)(2K''+1)} \\
&\times \sum_{K_LQ_L} \sqrt{(2K_L+1)}(-1)^{q''-q'}(-1)^{J_a-\mu_a}(-1)^{Q}\frac{\Gamma_R}{\Gamma_R+\Gamma_I+{\rm i}Qg_b\omega_L}\rho^{K_L}_{Q_L} \\
&\times \begin{pmatrix} J_a & J_a & K_L \\ \mu_a & -\mu_a & -Q_L \end{pmatrix} \begin{pmatrix} J_b & J_a & 1 \\ -\mu_b & \mu_a & -q' \end{pmatrix} \begin{pmatrix} J_b & J_a & 1 \\ -\mu_b & \mu_f & -q \end{pmatrix} \begin{pmatrix} J_b & J_a & 1 \\ -\mu_b' & \mu_a & -q''' \end{pmatrix} \\
&\times \begin{pmatrix} J_b & J_a & 1 \\ -\mu_b' & \mu_f & -q'' \end{pmatrix} \begin{pmatrix} 1 & 1 & K'' \\ q & -q'' & Q \end{pmatrix} \begin{pmatrix} 1 & 1 & K' \\ q' & -q''' & Q \end{pmatrix} \delta(\xi-\xi'-\nu_{af}) \\
&\times \frac{1}{2}[\phi(\nu_{J_b\mu_b',J_a\mu_a}-\xi')+\phi^*(\nu_{J_b\mu_b,J_a\mu_a}-\xi')](-1)^Q T^{K''}_{Q}(i,\mathbf{n})T^{K'}_{-Q}(j,\mathbf{n}'). \qquad (6.5)
\end{aligned}
$$

The above expression gives the $\boldsymbol{R}^{\rm II}$ redistribution matrix in the atomic frame for a general $J_a \rightarrow J_b \rightarrow J_a$ transition including the effects of LLP. The multipolar index $K_L = 0, 2, 4, ...2J_a$ with $Q_L \in [-K_L, +K_L]$ is associated with the lower level having total angular momentum J_a. We notice that the first $3j$ symbol which arises due to the inclusion of LLP restricts the value of Q_L to 0. Clearly the LLP is taken into account through population imbalances while the coherences in the lower level are neglected. The $\boldsymbol{R}^{\rm II}$ given in Equation (6.5) is unnormalized. Its normalization is discussed in the next section.

6.2.2 Normalization of the type-II redistribution matrix

In astrophysics one always requires normalized redistribution matrices. The normalization condition for the $\boldsymbol{R}^{\rm II}$ matrix (cf. Equation (6.5)) is given by

$$
\int \frac{d\Omega}{4\pi}\int\frac{d\Omega'}{4\pi}\int d\xi \int d\xi' R^{\rm II}_{00}(\xi,\mathbf{n},\xi',\mathbf{n}',\mathbf{B}) = 1. \qquad (6.6)
$$

After some algebra using the properties of $3j$ and $6j$ symbols we get the normalization constant ($N.C.$) as

$$
\begin{aligned}
N.C. &= \frac{2}{9}\frac{(2J_a+1)^2}{(2J_b+1)} \sum_{\mu_a\mu_b}\sum_{K_LQ_L} \sqrt{(2K_L+1)}(-1)^{J_a+\mu_a}\rho^{K_L}_{Q_L} \\
&\times \begin{pmatrix} J_a & J_a & K_L \\ \mu_a & -\mu_a & -Q_L \end{pmatrix} \begin{pmatrix} J_b & J_a & 1 \\ -\mu_b & \mu_a & -q' \end{pmatrix}^2 . \qquad (6.7)
\end{aligned}
$$

The above equation can be written in a simpler form in terms of $\rho_{\mu_a\mu_a}$ (using Equation (3.99) of LL04) as

$$N.C. = \frac{2}{9}\frac{(2J_a+1)^2}{(2J_b+1)}\sum_{\mu_a\mu_b}\rho_{\mu_a\mu_a}\begin{pmatrix} J_b & J_a & 1 \\ -\mu_b & \mu_a & -q' \end{pmatrix}^2. \tag{6.8}$$

It is easy to verify that when we set $\rho_{\mu_a\mu_a} = 1$ in Equation (6.8), the normalization constant for a general $J_a \to J_b \to J_a$ transition with unpolarized lower level reduces to $2(2J_a+1)^2/9(2J_b+1)$ which is expected as in (see Sampoorna, 2011a).

6.2.3 Type-II redistribution matrix in the laboratory frame

We now transform the atomic frame $\boldsymbol{R}^{\rm II}$ matrix (Equation (6.5)) to the laboratory reference system. Following Section 4 of Sampoorna (2011a) we obtain the elements of the normalized type II redistribution matrix in the laboratory frame as

$$\begin{aligned}
\mathbf{R}^{\rm II}_{ij}(x,\mathbf{n},x',\mathbf{n}',\mathbf{B}) &= \frac{1}{N.C.}\frac{2}{3}(2J_a+1)^2 \sum_{\mu_a\mu_f\mu_b\mu_b'qq'q''q'''}\sum_{K'K''Q}\sum_{K_LQ_L} \\
&\times\sqrt{(2K'+1)(2K''+1)(2K_L+1)}(-1)^{q''-q'}(-1)^{J_a-\mu_a}(-1)^{Q}\rho^{K_L}_{Q_L} \\
&\times\frac{\Gamma_R}{\Gamma_R+\Gamma_I+\mathrm{i}Qg_b\omega_L}\begin{pmatrix} J_a & J_a & K_L \\ \mu_a & -\mu_a & -Q_L \end{pmatrix}\begin{pmatrix} J_b & J_a & 1 \\ -\mu_b & \mu_a & -q' \end{pmatrix}\begin{pmatrix} J_b & J_a & 1 \\ -\mu_b & \mu_f & -q \end{pmatrix} \\
&\times\begin{pmatrix} J_b & J_a & 1 \\ -\mu_b' & \mu_a & -q''' \end{pmatrix}\begin{pmatrix} J_b & J_a & 1 \\ -\mu_b' & \mu_f & -q'' \end{pmatrix}\begin{pmatrix} 1 & 1 & K'' \\ q & -q'' & Q \end{pmatrix}\begin{pmatrix} 1 & 1 & K' \\ q' & -q''' & Q \end{pmatrix} \\
&\times[h^{\rm II}_{\mu_b\mu_b'}(\mu_f\mu_a)+\mathrm{i}f^{\rm II}_{\mu_b\mu_b'}(\mu_f\mu_a)](-1)^{Q}T^{K''}_{Q}(i,\mathbf{n})T^{K'}_{-Q}(j,\mathbf{n}'),
\end{aligned} \tag{6.9}$$

where $h^{\rm II}$ and $f^{\rm II}$ are the auxiliary functions which are defined in Equations (22) and (23) of Sampoorna (2011a). The above expression takes a particularly simple form in the absence of magnetic field (see Appendix A). In the next section we include the type II redistribution matrix derived above for a two-level atom with LLP, into the radiative transfer equation.

6.3 Radiative transfer equation for a two-level atom with lower-level polarization

We remark that in the density matrix approach of LL04 the transfer equation is written in terms of emission and absorption coefficients. These emission and absorption coefficients depend on the density matrix elements of the upper and lower levels respectively. On the other hand in the redistribution matrix approach the transfer equation for a two-level atom without LLP is written in terms of a source vector that

depends on the scattering integral. The scattering integral basically contains the redistribution matrix for the problem at hand. However the transfer equation of LL04 (which can handle two-level atom with LLP) cannot be used for our purposes because the emission vector is not written in terms of the scattering integral involving the redistribution matrices. Therefore we need to extend the transfer equation in the redistribution matrix approach to include the effects of LLP.

In order to derive the radiative transfer equation for a two-level atom with LLP we follow the quantum field theory approach of S94 (see his Chapters 7 and 8). In this section we first recall the necessary equations from S94 which are originally written in coherency matrix formalism. We then present the transformation of this radiative transfer equation from coherency matrix formalism to Stokes vector formalism. The notations have the same meaning as in S94 unless specified. From Equation (8.15) of S94 the radiative transfer equation can be written as

$$\frac{dD_{\alpha\alpha'}}{ds} = -\sum_{\beta}\{(g_{\alpha\beta} - f_{\alpha\beta})D_{\beta\alpha'} + D_{\alpha\beta}(g^{\dagger}_{\beta\alpha'} - f^{\dagger}_{\beta\alpha'})\} + \frac{h\nu^3}{c^2}(f_{\alpha\alpha'} + f^{\dagger}_{\alpha\alpha'}). \tag{6.10}$$

The components of the $\boldsymbol{g}$ and $\boldsymbol{f}$ matrices are given by Equations (8.94) and (8.95) of S94 respectively which are

$$g_{\alpha\alpha'} = \frac{3}{2}\frac{h\nu}{4\pi}N\sum_{J_aJ_b}(2J_a+1)B_{J_aJ_b}\sum_{\mu_a\mu'_a\mu_b}\begin{pmatrix} J_b & J_a & 1\\ -\mu_b & \mu_a & \mu_b-\mu_a\end{pmatrix} \times \begin{pmatrix} J_b & J_a & 1\\ -\mu_b & \mu'_a & \mu_b-\mu'_a\end{pmatrix}\varepsilon^{\alpha'*}_{\mu_b\mu_a}\,\varepsilon^{\alpha}_{\mu_b\mu'_a}\,\rho_{\mu_a\mu'_a}\,\Phi_{\mu_b\mu_a}, \tag{6.11}$$

and

$$f_{\alpha\alpha'} = \frac{3}{2}\frac{h\nu}{4\pi}N\sum_{J_aJ_b}(2J_b+1)B_{J_bJ_a}\sum_{\mu_a\mu_b\mu'_b}(-1)^{\mu_b-\mu'_b}\begin{pmatrix} J_b & J_a & 1\\ -\mu_b & \mu_a & \mu_b-\mu_a\end{pmatrix} \times \begin{pmatrix} J_b & J_a & 1\\ -\mu'_b & \mu_a & \mu'_b-\mu_a\end{pmatrix}\varepsilon^{\alpha'*}_{\mu'_b\mu_a}\,\varepsilon^{\alpha}_{\mu_b\mu_a}\,\rho_{\mu_b\mu'_b}\,\Phi_{\mu'_b\mu_a}. \tag{6.12}$$

In S94 the total angular momentum quantum numbers of the lower and upper levels are denoted by J_μ and J_m respectively. However to be consistent with the notations used in the present chapter, we denote them by J_a and J_b. Further, the magnetic quantum numbers μ, μ', m and m' of S94 respectively are replaced by μ_a, μ'_a, μ_b and μ'_b. Also the subscripts of the geometrical factors ε are denoted by $\mu_b\mu_a$ instead of $(\mu_b-\mu_a)$. The above stated Equations (6.10) - (6.12) are derived in S94 for a general transition in a multi-level system. In Section 6.2 we derived the redistribution matrix for a two-level atomic system with LLP under the following assumptions: (1) We

neglect the off-diagonal terms of the lower level density matrix. This means that we consider only the populations imbalances in the lower level and neglect the coherences between the magnetic substates. In other words only $\rho_{\mu_a\mu_a}$ terms contribute to the transfer equation; (2) We consider the case of Rayleigh scattering i.e., $J_a = J_f$. With these assumptions Equations (6.11) and (6.12) can be re-written as

$$g_{\alpha\alpha'} = \frac{3}{2}\frac{h\nu}{4\pi}N(2J_a+1)B_{J_aJ_b}\sum_{\mu_a\mu_b}\begin{pmatrix} J_b & J_a & 1 \\ -\mu_b & \mu_a & \mu_b-\mu_a\end{pmatrix}^2 \varepsilon^{\alpha'*}_{\mu_b\mu_a}\,\varepsilon^{\alpha}_{\mu_b\mu_a}\,\rho_{\mu_a\mu_a}\,\Phi_{\mu_b\mu_a}, \tag{6.13}$$

and

$$f_{\alpha\alpha'} = \frac{3}{2}\frac{h\nu}{4\pi}N(2J_b+1)B_{J_bJ_a}\sum_{\mu_a\mu_b\mu'_b}(-1)^{\mu_b-\mu'_b}\begin{pmatrix} J_b & J_a & 1 \\ -\mu_b & \mu_a & \mu_b-\mu_a\end{pmatrix} \times\begin{pmatrix} J_b & J_a & 1 \\ -\mu'_b & \mu_a & \mu'_b-\mu_a\end{pmatrix}\varepsilon^{\alpha'*}_{\mu'_b\mu_a}\,\varepsilon^{\alpha}_{\mu_b\mu_a}\,\rho_{\mu_b\mu'_b}\,\Phi_{\mu'_b\mu_a}. \tag{6.14}$$

The elements of the $\boldsymbol{g}$ matrix in the first two terms of the RHS of Equation (6.10) represent radiative absorption. The $\boldsymbol{f}$ matrix elements in the first and second term represent the stimulated emission and those in the last term represent the spontaneous emission. The spontaneous emission term is simplified in Section 8.10 of S94 in terms of scattering amplitude. Considering all the assumptions made so far, the expression for the spontaneous emission term for a two level system turns out to be (see Equation 8.112 of S94)

$$\frac{h\nu^3}{c^2}(f_{\alpha\alpha'}+f^{\dagger}_{\alpha\alpha'}) = \frac{1}{c}\sum_{\mu_a}\rho_{\mu_a\mu_a}\sum_{\mu_f}\sum_{\beta\beta'\boldsymbol{k}}w_{\alpha\beta}w^*_{\alpha'\beta'}D_{\beta\beta'}. \tag{6.15}$$

If we transform the sum over $\boldsymbol{k}$ into integrals using Equation (7.44) of S94, we get

$$\frac{h\nu^3}{c^2}(f_{\alpha\alpha'}+f^{\dagger}_{\alpha\alpha'}) \sim \int\frac{d\Omega'}{4\pi}\int dx'\sum_{\mu_a}\rho_{\mu_a\mu_a}\sum_{\mu_f}\sum_{\beta\beta'}w_{\alpha\beta}\,w^*_{\alpha'\beta'}\,D_{\beta\beta'}. \tag{6.16}$$

From Equations (8.113) and (8.114) of S94 and the explanation that follows we see that the terms inside the summation in Equation (6.16) can be written as Mueller matrix $\mathbf{M} = \mathbf{TWT}^{-1}$ for the scattering of the Stokes vector $\boldsymbol{S}_k$. In this manner the spontaneous emission term can be transformed from the coherency matrix formalism to the Stokes vector formalism. This transformation has to be applied also to the absorption and stimulated emission terms in the radiative transfer equation (6.10). The procedure followed for achieving this is described below.

6.3.1 The absorption and stimulated emission matrices

We can rewrite Equation (6.10) as

$$\frac{dD_{\alpha\alpha'}}{ds} = -\sum_{\beta}[(g_{\alpha\beta}\, D_{\beta\alpha'} + D_{\alpha\beta}\, g^{\dagger}_{\beta\alpha'}) - (f_{\alpha\beta}\, D_{\beta\alpha'} + D_{\alpha\beta}\, f^{\dagger}_{\beta\alpha'})] + F_c, \quad (6.17)$$

where F_c represents the spontaneous emission term in the coherency matrix formalism. Before we proceed with the transformation of radiative absorption and stimulated emission terms we recall the necessary equations from chapter 2 of S94 which are used for the simplification. According to Equation (2.43) of S94 the relation between Stokes parameters S_k (k = 0, 1, 2, 3) and the coherency matrix is given by

$$S_k = \mathrm{Tr}\,(\boldsymbol{\sigma_k D}) = \sum_{\alpha\alpha'} (\boldsymbol{\sigma_k})_{\alpha'\alpha}\, D_{\alpha\alpha'}, \quad (6.18)$$

where σ_k's are the Pauli spin matrices given by (cf. Equation (C12) of Sampoorna et al., 2007b)

$$\sigma_0 = \begin{pmatrix} 1 & 0 \\ 0 & 1 \end{pmatrix}, \qquad \sigma_1 = \begin{pmatrix} 0 & -1 \\ -1 & 0 \end{pmatrix},$$
$$\sigma_2 = \begin{pmatrix} 0 & i \\ -i & 0 \end{pmatrix}, \qquad \sigma_3 = \begin{pmatrix} -1 & 0 \\ 0 & 1 \end{pmatrix}. \quad (6.19)$$

The inverse of Equation (6.18) in the component form can be written as (see Equation (2.46) of S94)

$$D_{\alpha\alpha'} = \frac{1}{2}\sum_{k} S_k\, (\boldsymbol{\sigma}_k)_{\alpha\alpha'}. \quad (6.20)$$

From Equations (6.17) and (6.18) we get

$$\frac{dS_k}{ds} = \sum_{\alpha\alpha'} (\boldsymbol{\sigma}_k)_{\alpha'\alpha} \{-\sum_{\beta}[(g_{\alpha\beta}\, D_{\beta\alpha'} + D_{\alpha\beta}\, g^{\dagger}_{\beta\alpha'}) - (f_{\alpha\beta}\, D_{\beta\alpha'} + D_{\alpha\beta}\, f^{\dagger}_{\beta\alpha'})] + F_c\}. \quad (6.21)$$

Substituting from Equation (6.20) in the above equation and using the conjugation relation $(\boldsymbol{\sigma}_k)^{*}_{\alpha\alpha'} = (\boldsymbol{\sigma}_k)_{\alpha'\alpha}$ and the cyclic properties of trace, we get

$$\frac{dS_k}{ds} = -\sum_{j}\{\mathrm{Re}\,[\mathrm{Tr}\,(\boldsymbol{\sigma}_j\, \boldsymbol{\sigma}_k\, \boldsymbol{g})]\, S_j \; - \mathrm{Re}\,[\mathrm{Tr}\,(\boldsymbol{\sigma}_j\, \boldsymbol{\sigma}_k\, \boldsymbol{f})]\, S_j\} \; + \; F_{S_k}, \quad (6.22)$$

where the components of the matrices $\boldsymbol{g}$ and $\boldsymbol{f}$ are given by Equations (6.13) and (6.14) respectively. F_{S_k} is the spontaneous emission coefficient in Stokes vector formalism which in turn can be written in terms of the scattering integral. The co-

efficient of S_j in the first term of RHS of Equation (6.22) represents the radiative absorption term in the Stokes vector formalism whose elements can be explicitly derived. Let us denote $\mathrm{Re}\left[\mathrm{Tr}\left(\boldsymbol{\sigma}_j\,\boldsymbol{\sigma}_k\,\boldsymbol{g}\right)\right] = A_{kj}$, which are the elements of the radiative absorption matrix $\boldsymbol{\eta}^A$. The matrix $\boldsymbol{\eta}^A$ is given by

$$\boldsymbol{\eta}^A = \begin{pmatrix} \eta_I^A & \eta_Q^A & \eta_U^A & \eta_V^A \\ \eta_Q^A & \eta_I^A & \rho_V^A & -\rho_U^A \\ \eta_U & -\rho_V^A & \eta_I & \rho_Q^A \\ \eta_V & \rho_U^A & -\rho_Q^A & \eta_I \end{pmatrix}, \tag{6.23}$$

where

$$\begin{aligned} \eta_I^A &= A_{00} = A_{11} = A_{22} = A_{33} = \mathrm{Re}\,(g_{11} + g_{22}), \\ \eta_Q^A &= A_{01} = A_{10} = -\mathrm{Re}\,(g_{12} + g_{21}), \\ \eta_U^A &= A_{02} = A_{20} = \mathrm{Im}\,(g_{12} - g_{21}), \\ \eta_V^A &= A_{03} = A_{30} = \mathrm{Re}\,(g_{22} - g_{11}), \\ \rho_Q^A &= A_{23} = -A_{32} = \mathrm{Im}\,(g_{12} + g_{21}), \\ \rho_U^A &= A_{31} = -A_{13} = -\mathrm{Re}\,(g_{21} - g_{12}), \\ \rho_V^A &= A_{12} = -A_{21} = \mathrm{Im}\,(g_{11} - g_{22}). \end{aligned} \tag{6.24}$$

Similarly we can obtain the expression of stimulated emission matrix using the relation $\mathrm{Re}\left[\mathrm{Tr}\left(\boldsymbol{\sigma}_j\,\boldsymbol{\sigma}_k\,\boldsymbol{f}\right)\right] = A_{kj}^S$. The elements of the stimulated emission matrix $\boldsymbol{\eta}^S$ have the same expressions as those for $\boldsymbol{\eta}^A$ but for $g_{\alpha\beta}$ replaced by $f_{\alpha\beta}$.

The absorption matrix derived above has a form similar to that derived in LL04 (see Section 6.7, p.271). However, the elements of the matrix appear to be different from those given in LL04. This is because the Pauli spin matrices (which in turn depend on the choice of the linear polarization unit vectors) involved in the transformation from the coherency matrix formalism to Stokes formalism are different in the present chapter and LL04. The Pauli spin matrices used here differ by a complex conjugate from the corresponding matrices given in LL04 and we see the similar difference in the absorption matrix elements. However we expect the final expression of the absorption matrix elements to be the same in both the cases when simplified for any given transition with corresponding eigen vectors. This verification is described in Appendix B.

Thus the radiative transfer equation in Stokes vector basis can now be written as

$$\frac{dS_k}{ds} = -\sum_{j=0}^{3} A_{kj}\,S_j + \sum_{j=0}^{3} A_{kj}^S\,S_j + \frac{h\nu}{4\pi} N_{J_a} B_{J_a J_b} \int \frac{d\Omega'}{4\pi} \int dx' \sum_{j=0}^{3} M_{kj} S_j, \tag{6.25}$$

where M_{kj} are the elements of the Mueller scattering matrix. For the problem at hand namely, a two-level atom with LLP this matrix is simply the type II redistribution matrix given in Equation (6.9).

6.3.2 Contribution from thermal emission

The transfer equation (6.25) derived in Section 6.3.1 does not take into account the contribution from the thermal emission. Thus the transfer equation obtained in Equation (6.25) represents only pure scattering. For practical applications however, we need to take into account the contribution from the thermal emission. For this purpose we follow the procedure given in Section 6.9 of S94 to calculate the contribution from thermal emission.

Thermal emission is nothing but a limiting case in which the scattering atom has completely lost its memory about how it was excited (see Stenflo, 1998). Hereafter we neglect the contribution from the stimulated emission (the second term on the right hand side of Equation (6.25)). The radiative transfer equation including the contribution from thermal emission ($\boldsymbol{j}_k^{thermal}$) can be written as

$$\frac{dS_k}{ds} = -\sum_{j=0}^{3} A_{kj}\, S_j \; + \frac{h\nu}{4\pi} N_{J_a} B_{J_a J_b} \int \frac{d\Omega'}{4\pi} \int dx' \sum_{j=0}^{3} R_{kj}^{\mathrm{II}} S_j + \boldsymbol{j}_k^{thermal}. \quad (6.26)$$

Generally the thermal emission is given by the absorption matrix times the Planck function (B_{ν_o}). However for the problem at hand it is necessary to distinguish the processes of absorption and thermal emission. While the LLP is relevant for radiative absorption it is irrelevant for the thermal emission. Therefore to distinguish these two processes we define the emission profile matrix as $\boldsymbol{\Phi}^{emi}$ and absorption profile matrix as $\boldsymbol{\Phi}^{abs}$. The absorption profile matrix is related to the absorption matrix $\boldsymbol{\eta}^A$ derived starting from quantum field theory of S94 through

$$\boldsymbol{\eta}^A = k_L \boldsymbol{\Phi}^{abs}, \quad (6.27)$$

where k_L is the line averaged absorption coefficient (for the case when stimulated emission is neglected) defined as

$$k_L = \frac{h\nu}{4\pi} N_{J_a} B_{J_a J_b}. \quad (6.28)$$

The expression of the absorption profile matrix $\boldsymbol{\Phi}^{abs}$ in the atmospheric reference frame is the same as the expression under the summation K, Q, K_l, Q_l of Equation (7.15a) of LL04. In the line of sight reference frame this matrix is the same as

Equation (6.59) of S94 which is given by

$$\mathbf{\Phi}^{abs} = \begin{pmatrix} \phi_I^{abs} & \phi_Q^{abs} & \phi_U^{abs} & \phi_V^{abs} \\ \phi_Q^{abs} & \phi_I^{abs} & \psi_V^{abs} & -\psi_U^{abs} \\ \phi_U^{abs} & -\psi_V^{abs} & \phi_I^{abs} & \psi_Q^{abs} \\ \phi_V^{abs} & \psi_U^{abs} & -\psi_Q^{abs} & \phi_I^{abs} \end{pmatrix}, \tag{6.29}$$

where

$$\begin{aligned} \phi_I^{abs} &= \phi_\Delta^{abs} \sin^2\gamma + \frac{1}{2}(\phi_+^{abs} + \phi_-^{abs}), \\ \phi_Q^{abs} &= \phi_\Delta^{abs} \sin^2\gamma \cos 2\chi, \\ \phi_U^{abs} &= \phi_\Delta^{abs} \sin^2\gamma \sin 2\chi, \\ \phi_V^{abs} &= \frac{1}{2}(\phi_+^{abs} - \phi_-^{abs}) \cos\gamma, \\ \phi_\Delta^{abs} &= \frac{1}{2}[\phi_0^{abs} - \frac{1}{2}(\phi_+^{abs} + \phi_-^{abs})], \end{aligned} \tag{6.30}$$

with corresponding expressions for $\psi_{Q,U,V}^{abs}$ where ϕ_q is replaced by ψ_q, the anomalous dispersion profile. In the above expressions γ and χ denote the inclination and azimuth of the magnetic field with respect to the line of sight. Since the transfer equation is solved in the frame where the z-axis is along the atmospheric normal we need to convert the angles γ and χ in the line of sight frame to the atmospheric reference frame. This can be done following Appendix B of Anusha et al. (2011). The expression for ϕ_q^{abs} is given by (see Equation (6.52) of S94)

$$\phi_q^{abs} = \frac{N(2J_a+1)}{N_{J_a}\sqrt{\pi}\Delta\nu_D} \sum_{\mu_a\mu_b} \rho_{\mu_a\mu_a} S_q(\mu_a,\mu_b) H_q. \tag{6.31}$$

In Equation (6.31) the contribution from the population imbalances in the lower level to the absorption processes is included via $\rho_{\mu_a\mu_a}$. The transition strength $S_q(\mu_a,\mu_b)$ is given by (see Equation (6.33) of S94)

$$S_q(\mu_a,\mu_b) = 3 \begin{pmatrix} J_a & J_b & 1 \\ -\mu_a & \mu_b & q \end{pmatrix}^2. \tag{6.32}$$

In the case of thermal emission, the emission processes are independent of the absorption. Therefore, we define a separate profile matrix ($\mathbf{\Phi}^{emi}$) to account for the emission processes. The matrix elements of the $\mathbf{\Phi}^{emi}$ matrix are now independent of the population imbalances in the lower level. The expression for ϕ_q^{emi} is given by

(see Equation (6.37) of S94)

$$\phi_q^{emi} = \frac{1}{\sqrt{\pi}\Delta\nu_D} \sum_{\mu_a \mu_b} S_q(\mu_a, \mu_b) H_q. \tag{6.33}$$

The form of the emission profile matrix $\mathbf{\Phi}^{emi}$ is same as the absorption profile matrix $\mathbf{\Phi}^{abs}$ with the elements $\phi^{abs}_{I,Q,U,V,\Delta}$ replaced by $\phi^{emi}_{I,Q,U,V,\Delta}$. The thermal emission consists of contributions from incoherent scattering $\boldsymbol{j}_{ic}$ (for which the phases of the upper level magnetic sublevels are scrambled by collisions) and the non-scattering emission processes $\boldsymbol{j}_{ns}$. The expressions for $\boldsymbol{j}_{ic}$ and $\boldsymbol{j}_{ns}$ are derived in Sections 5.17 and 6.9 of S94. For the problem at hand the total thermal emission term is

$$\begin{aligned} \boldsymbol{j}_{thermal} &= \boldsymbol{j}_{ns} + \boldsymbol{j}_{ic} \\ &= k_L \Big[1 - \alpha + \frac{(1-k_c)\alpha e}{\int \phi_x J_x dx} \Big] S_{ba}\, \mathbf{\Phi}^{emi}\, \mathbf{1}, \end{aligned} \tag{6.34}$$

where $\mathbf{1} = (1,\, 0,\, 0,\, 0\,)^{\mathrm{T}}$ and ϕ_x is the area normalized profile function and is equal to ϕ_q^{emi} when q=0. In the above equation the coherent scattering fraction k_c is given by $k_c = A_{ba}/(A_{ba} + C_{ba})$ and α is the fraction of the scattering process given by

$$\alpha = \frac{N_{J_a} B_{J_a J_b} \int \phi_x J_x dx}{N_{J_a} B_{J_a J_b} \int \phi_x J_x dx + N_{J_a} C_{J_a J_b}}. \tag{6.35}$$

The quantity e is given by

$$e = \frac{1}{2} \int d\mu' \int dx' \, [\phi_I^{abs} I(x', \mu') + \phi_Q^{abs} Q(x', \mu') + \phi_U^{abs} U(x', \mu') + \phi_V^{abs} V(x', \mu')]. \tag{6.36}$$

The line source function S_{ba} takes the following simple form when stimulated emission is neglected :

$$S_{ba} = \frac{N_{J_b} A_{J_b J_a}}{N_{J_a} B_{J_a J_b}}. \tag{6.37}$$

By defining $d\tau = -k_L ds$ we can rewrite the transfer equation (6.26) including the unpolarized continuum as

$$\begin{aligned} \frac{d\boldsymbol{I}}{d\tau} &= (\mathbf{\Phi}^{abs} + r\boldsymbol{E})\boldsymbol{I} - (r B_{\nu_0} \mathbf{1} + \boldsymbol{S}_{scatt}) \\ &- [1 - \alpha + (1-k_c)\alpha e / \int \phi_x J_x dx]\, S_{ba}\, \mathbf{\Phi}^{emi}\, \mathbf{1}, \end{aligned} \tag{6.38}$$

where $\boldsymbol{I} = [S_0, S_1, S_2, S_3]^{\mathrm{T}} = [I, Q, U, V]^{\mathrm{T}}$, r is the ratio of continuum to line averaged opacity, and $\boldsymbol{E}$ is a 4×4 unit matrix. The scattering source vector $\boldsymbol{S}_{scatt}$ is

given by

$$\boldsymbol{S}_{scatt} = \int \frac{d\Omega'}{4\pi} \int dx' \boldsymbol{R}^{\rm II}(x, \mathbf{n}, x', \mathbf{n}', \mathbf{B}) \boldsymbol{I}(x', \mathbf{n}'). \tag{6.39}$$

The above equations take a simpler form in the absence of magnetic fields. These equations are given in the next section.

6.3.3 The non-magnetic case

To numerically solve the problem of polarized radiative transfer including the effects of LLP we restrict our attention to the non-magnetic case. For this particular case the Stokes V is zero and for the planar geometry Stokes U is zero. Therefore the dimension of the problem reduces from 4×4 to 2×2. The emission profile matrix $\boldsymbol{\Phi}^{emi}$ which contributes to the thermal emission can be simplified further for this case. In the absence of magnetic field, Equation (6.33) reduces to

$$\phi_q^{emi} = \frac{H}{\sqrt{\pi}\Delta\nu_D} = \phi_x. \tag{6.40}$$

Therefore $\phi_\Delta^{emi} = 0$ (cf. Equation (6.30)). Thus ϕ_I^{emi} is the only non-zero term in the emission profile matrix $\boldsymbol{\Phi}^{emi}$, which takes the form

$$\boldsymbol{\Phi}^{emi} = \begin{pmatrix} \phi_I^{emi} & 0 \\ 0 & \phi_I^{emi} \end{pmatrix}. \tag{6.41}$$

From Equations (6.34) and (6.41) we see that the thermal emission contributes only to the Stokes I. Equation (6.38) can thus be re-written as

$$\frac{d\boldsymbol{I}}{d\tau} = \boldsymbol{K}\boldsymbol{I} - [rB_{\nu_0}\mathbf{1} + \boldsymbol{S}_l], \tag{6.42}$$

where $\boldsymbol{K} = \boldsymbol{\Phi}^{abs} + r\boldsymbol{E}$. The elements of the line source vector $\boldsymbol{S}_l = (S_{I,l} S_{Q,l})^{\rm T}$ can be written as

$$\begin{aligned} S_{I,l} &= \frac{1}{2} \int d\mu' \int dx' [R_{00}^{\rm II}(x, \mu, x', \mu') I(x', \mu') + R_{01}^{\rm II}(x, \mu, x', \mu') Q(x', \mu')] \\ &\quad + [1 - \alpha + (1 - k_c)\alpha e / \int \phi_x J_x dx] \, S_{ba} \, \phi_I^{emi}, \\ S_{Q,l} &= \frac{1}{2} \int d\mu' \int dx' [R_{10}^{\rm II}(x, \mu, x', \mu') I(x', \mu') + R_{11}^{\rm II}(x, \mu, x', \mu') Q(x', \mu')]. \end{aligned} \tag{6.43}$$

To solve the problem of polarized line formation including PRD and LLP we follow a two stage approach. In the first stage we solve the SEEs and the transfer equation simultaneously for given J_a and J_b taking into account the effects of the polarization

of the lower level but in the limit of CRD. The density matrix elements obtained as an output from the first stage is used as an input to compute the redistribution matrix that enters the second stage (cf. Equation (6.43)). In the second stage we solve the radiative transfer equation (see Equation (6.42)) including the effects of PRD and LLP. Further details on the numerical method adopted are described in Appendix C. In this two stage approach, the density matrix elements are computed neglecting the effects of PRD and they are kept fixed when computing the polarized PRD line profiles. Such an approach is valid since the density matrix elements represent a property of the atom (acquired through the process of optical pumping), and has nothing to do with the frequency of the photons that are being scattered on that atom. The photon scattering process is not responsible for any optical pumping, the pumping has been done before. Hence ρ's are the same regardless of whether the scattering takes place in the limit of CRD or PRD.

6.4 Polarized line profiles with partial frequency redistribution and lower-level polarization in the absence of magnetic fields

For our studies we consider two cases namely J_a = 1, J_b = 0 and J_a = J_b =1 to illustrate the effects of LLP on the polarized line formation. The governing equations and the concerned numerical method of solution are described for the J_a = J_b =1 case in Appendix C. A similar procedure can be followed for deriving corresponding expressions for the J_a = 1, J_b = 0 case (see also Trujillo Bueno & Landi Degl'Innocenti, 1997). For our computations we have considered a plane parallel isothermal atmospheric slab with effective temperature of 6000 K with no incident radiation at the boundaries. Background continuum opacity is assumed to be zero. For all the results presented in this chapter we consider a thick slab of total optical thickness $T = 10^{12}$. The effect of depolarizing elastic collisions is neglected and k_c is set to 1.

6.4.1 The case of 1→0→1 transition

We consider a two-level atom with $J_a = 1$ and $J_b = 0$. The concerned SEEs and the transfer equations are given in Trujillo Bueno & Landi Degl'Innocenti (1997). Because of the cylindrical symmetry of the problem, only three density-matrix elements are needed to fully specify the excitation state of the atoms, namely, $\rho^0_0(a)$, $\rho^0_0(b)$ and $\rho^2_0(a)$. For this particular case we consider the example of a hypothetical line at 5000 Å whose Einstein coefficient for spontaneous emission is $A_{ba} = 10^8 s^{-1}$

and downward inelastic collisional rate is $C_{ba} = 10^4 s^{-1}$. Figure 6.1 shows the emer-

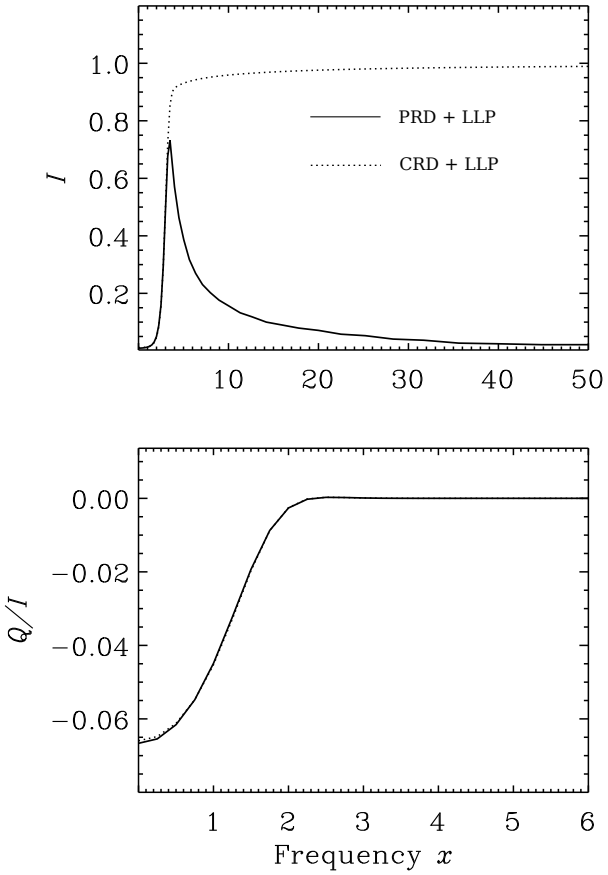

Figure 6.1: Emergent intensity and polarization for $\mu = 0.11$ computed using the two stage approach. The case of 1→0→1 transition is considered with the effects of LLP. Solid line represents the case of PRD and the dotted line that of CRD. Other input parameters are $A_{J_b J_a} = 10^8 s^{-1}$; $C_{J_b J_a} = 10^4 s^{-1}$. No background continuum opacity is used.

gent (I, Q/I) at $\mu = 0.11$ for 1→0→1 transition. Here we compare the results obtained under the limits of PRD and CRD when LLP is taken into account. We see that the intensity profiles show the typical signatures of PRD and CRD mechanisms. The Q/I profiles are identical for the PRD and CRD limits. This is because, for this particular transition in the non-magnetic regime only the elements $R^{\rm II}_{00}$ and $R^{\rm II}_{01}$ of the redistribution matrix are non-zero and all the other elements are zero (see Equation (A.2)). Hence the line source vector corresponding to the polarization ($S_{Q,l}$) is always zero (see Equation (6.43)). This implies that the contribution to the emitted polarization for this case does not come from the redistribution processes but only from the dichroic absorption (see Trujillo Bueno & Landi Degl'Innocenti, 1997). In order to understand the combined effects of PRD and LLP in a better way we consider another case study with J_a = J_b = 1.

6.4.2 The case of 1→1→1 transition

For the case when J_a = J_b = 1, even in the absence of LLP, since the upper level is polarized a finite amount of emergent polarization is generated unlike the case of J_a = 1, J_b = 0. For all the computations of this particular transition ($J_a = J_b = 1$) we again consider the hypothetical case like that described for J_a = 1, J_b = 0. In this case there are four density matrix elements to be determined namely, $\rho^0_0(a)$, $\rho^2_0(a)$, $\rho^0_0(b)$ and $\rho^2_0(b)$ when polarizability of both the levels are taken into account. Figure 6.2 shows the emergent (I, Q/I) at $\mu = 0.11$ for the 1→1→1 transition.

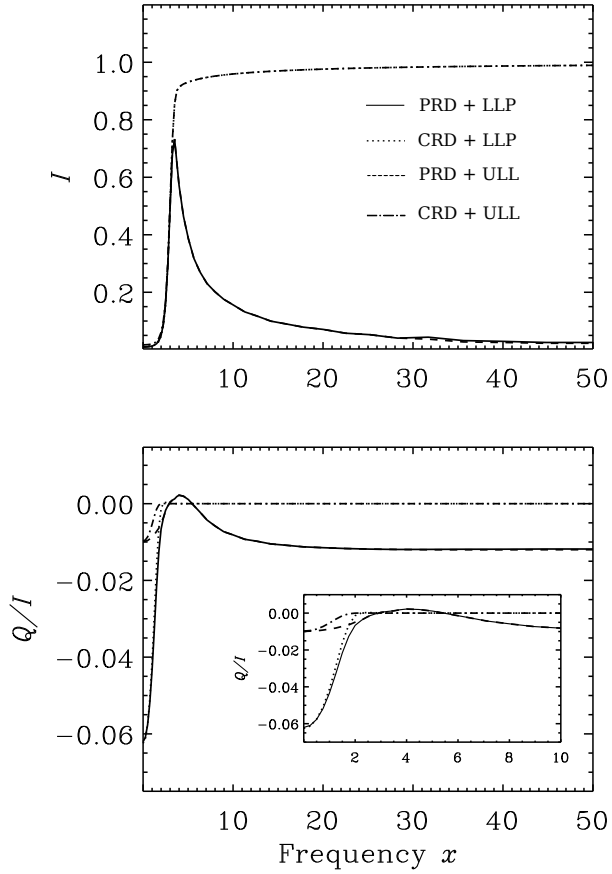

Figure 6.2: Emergent intensity and polarization for $\mu = 0.11$ computed using the two stage approach for 1→1→1 case. The different line types correspond to: solid line - PRD + LLP, dotted line - CRD + LLP, dashed line - PRD + ULL, and the dot-dashed line - CRD + ULL. The abbreviation ULL stands for unpolarized lower level. Other input parameters are $A_{J_b J_a} = 10^8 s^{-1}$; $C_{J_b J_a} = 10^4 s^{-1}$. No background continuum opacity is used. The inset in Q/I panel shows the Q/I profiles for a shorter frequency bandwidth for the sake of clarity.

Solid line in Figure 6.2 represents the emergent profiles obtained when both the effects of PRD and LLP are considered. In order to see the importance of both the effects we have over-plotted the (I, Q/I) profiles obtained – when only the effects of PRD are considered with unpolarized lower level (ULL - dashed line); when the effects of LLP is considered in the limit of CRD (dotted line); and the case where only the CRD effects are considered with ULL (dot-dashed line). Figure 6.2 clearly

shows that the LLP effects appear only in the emergent polarization and the intensity profiles remain unchanged whether LLP is taken into account or not. We see that the LLP effects in the emergent Q/I are significant mainly in the core (up to ~ 2 Doppler widths, see inset in the lower panel of Figure 6.2) and in the wings the effects of PRD are dominant (compare solid and dashed lines). The enhancement in the emergent polarization at the line center when LLP is included is around 5%. Such large enhancements are noticed only when the elastic collisions are not taken into account namely, $D^{(2)}_{J_a} = D^{(2)}_{J_b} = 0$. However when elastic collisions are included, they reduce the alignment of the atomic levels, which in turn leads to depolarization (see Trujillo Bueno, 1999), and hence a smaller enhancement.

The absence of the LLP effects in the line wings has perhaps to do with the following reason. We know that all the transition rates that enter into the SEEs are frequency-integrated quantities. Therefore all the redistribution effects are integrated away. The contributions to the frequency-integrated scattering probability come almost entirely from the Doppler core. In optically thin media, the damping wings do not play any role. It is only in situations when we have significant optical thickness in the wings (leading also to core saturation) that we need to pay attention to the wings, and then PRD effects are important, because they govern what happens in the wings. This is however a radiative transfer effect. In contrast, in SEEs we compare the individual transition rates for a given radiation field. For each individual transition the contributions of the wing photons are insignificant as compared with the core photons. Since it is only the core photons that are relevant to SEEs, the effects of LLP only show up in the core but are absent in the wings.

6.5 An alternative approach to include the effects of lower-level polarization in lines formed under partial frequency redistribution

The conclusion that LLP effects are only significant in the line core allows us to use an alternative approach to solve the problem at hand. We refer to this approach as the correction method. In this method we compute the line profiles taking account of PRD neglecting LLP (in the standard 2-level approach) and later apply to it the corrections due to the effects of LLP computed using the density matrix approach with CRD. The actual procedure is described below.

(i) We solve the SEEs and the transfer equation simultaneously for a given J_a and J_b taking into account the effects of polarized lower level in the limit of CRD. For this purpose we use the relevant equations derived from the density matrix approach. Also we neglect the stimulated emission. The Stokes Q parameter obtained through

a simultaneous solution of SEEs and the polarized transfer equation is denoted by $Q_{\rm CRD}^{\rm LLP}$. For the numerical solution of this problem we use the Rybicki and Hummer method (see Rybicki & Hummer, 1991) appropriately generalized to handle polarized lower level. The governing equations and the details of the numerical procedure followed are described in Appendix C.1.

(ii) We solve the same problem as above, but now neglecting the effects of LLP. The resulting Stokes Q parameter is denoted by $Q_{\rm CRD}^{\rm ULL}$.

(iii) The difference between the solutions obtained with and without the effects of LLP is

$$\Delta Q_{\rm CRD} = Q_{\rm CRD}^{\rm LLP} - Q_{CRD}^{\rm ULL}. \tag{6.44}$$

We refer to $\Delta Q_{\rm CRD}$ as the correction term.

(iv) We now solve the transfer equation for the atomic system under consideration using the standard 2-level atom approach including PRD. For this purpose we use a polarized approximate lambda iteration (PALI) method (Nagendra et al., 1999). The polarization thus obtained is referred to as $Q_{\rm PRD}^{\rm ULL}$.

(v) It is well known that the effects of PRD are noticeable mainly in the line wings. Our studies show that the effects of polarized lower level of an atomic system are confined to the line core region (see Figure 6.2). To a good approximation a solution including the effects of PRD and also the LLP can be obtained from

$$Q_{\rm PRD}^{\rm LLP} = Q_{\rm PRD}^{\rm ULL} + \Delta Q_{\rm CRD}. \tag{6.45}$$

In Figure 6.3 we compare the Q/I profiles obtained using the simple correction

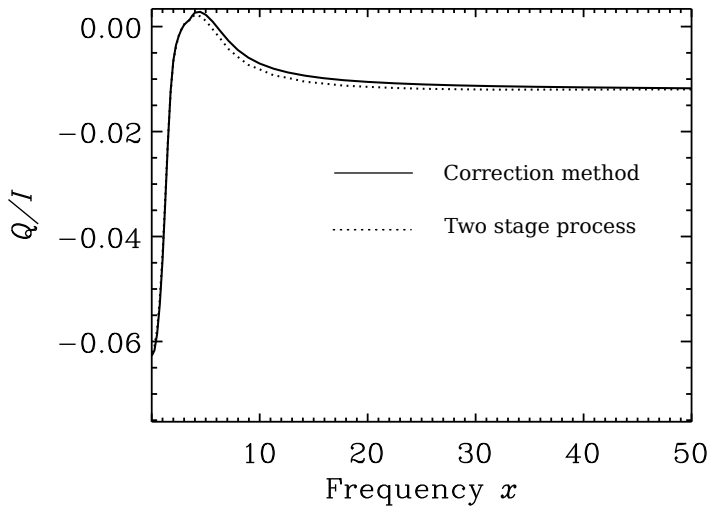

Figure 6.3: Emergent polarization for $\mu = 0.11$ computed using the correction method (solid line) and the two stage approach (dotted line). Other parameters are the same as in Figure 6.2.

method described above and the elaborate two stage approach proposed in this chapter (see Appendix C). We see that the results from both the methods match closely. Thus in order to simplify the computational efforts one can use the simple correction method instead of the two stage approach.

6.6 Conclusions

In this chapter we attempted to develop a theoretical approach to solve the polarized radiative transfer problem including the effects of PRD and LLP in the general case of magnetic media. We have derived the general collisionless redistribution matrix in the atomic frame including the effects of LLP for a two-level atomic system. For this we have used the Kramers-Heisenberg approach as given in Stenflo (1998), now including the contributions from the polarizability of the lower level. The collisionless redistribution matrix thus obtained is transformed to the laboratory frame which is now dependent on the density matrix elements of the lower atomic level. In order to include this redistribution matrix in the transfer equation we formulated the transfer equation including both the LLP and PRD. For this purpose we followed the quantum field theory approach of S94. Subsequently the absorption matrix for this problem is also derived.

A two stage approach is proposed to solve the polarized radiative transfer problem including the effects of PRD and LLP in the non-magnetic regime. In the first stage we solve the SEEs and the transfer equation simultaneously under flat spectrum approximation using the density matrix formalism developed by Landi Degl'Innocenti (1983). The density matrix elements thus obtained from the first stage are used as inputs to the second stage to compute the collisionless redistribution matrix elements. In the second stage we use the DELOPAR method to obtain the formal solution. Furthermore we use the frequency-angle-by-frequency-angle method to compute the source vector corrections. To demonstrate the effects of PRD and LLP we consider two examples namely, $1\rightarrow0\rightarrow1$ transition and $1\rightarrow1\rightarrow1$ transition. The case of $1\rightarrow0\rightarrow1$ transition does not show any signatures of PRD in the emergent polarization profile. This is because in this particular case, in the non-magnetic regime, the contribution to the emergent linear polarization does not come from the scattering processes but only from the dichroic absorption from the lower level. However in the $1\rightarrow1\rightarrow1$ transition the PRD signatures in the emergent polarization profile can be clearly seen in the line wings. Our studies indicate that the LLP effects are confined mostly to the line core region. The reason behind this might be that the SEEs are solved under the flat spectrum approximation, which makes the concerned transition rates frequency integrated quantities. This leads us to a computationally simpler numerical approach called the "correction method" to study the

effects of PRD and LLP on polarized line formation. We have verified that for all practical purposes this computationally simpler correction method represents a sufficiently good approximation and is therefore useful in practical model calculations.

Chapter 7

Summary and future work

7.1 Summary

The aim of the present thesis is to understand in a better way the Second Solar Spectrum (SSS), which is the linearly polarized spectrum of the Sun formed due to the coherent scattering process. In this regard, in Part I of the thesis we observe and model the center-limb-variation (CLV) of the Stokes profiles of the Ca I 4227 Å line and in Parts II and III we explore the properties of the fundamental tool of the scattering polarization, the redistribution matrix by conducting a series of theoretical studies.

In the recent years, with the availability of advanced polarimeters, the efforts in understanding the SSS have increased and have lead to the development of sophisticated theories of polarized radiative transfer. One of the methods adopted to understand the solar atmosphere is to model the CLV of the Stokes profiles. The variation of the Sun's spectrum from center-to-limb is governed by the underlying temperature density structure. Thus by modeling the CLV of the Stokes profiles we can infer further on the height dependence of various physical quantities in the solar atmosphere like the magnetic field. Though there are many efforts in the literature to model the limb observations of the linear polarization profiles of different lines, there have been very few attempts to understand and model the CLV of the Stokes profiles. This is because of the complexity involved in finding a single solar model atmosphere which can provide a simultaneous fit to the CLV of the (I, Q/I) profiles. In Chapter 2 we have attempted to model the CLV of the Stokes profiles of the famous Ca I 4227 Å line. This line is of particular interest as it exhibits largest scattering polarization of all the lines in the visible spectrum of the Sun. The CLV observations of the Ca I 4227 Å line were obtained from the Zurich Imaging Polarimeter-3 at Istituto Ricerche Solari Locarno in Switzerland. All the solar one-dimensional (1D) models attempted by us and also an appropriate combination of

them failed to provide a simultaneous fit to the (I, Q/I) profiles of the CLV of the Ca I 4227 Å line. However this doesn't limit the use of the Ca I 4227 Å line as a diagnostic tool to map the depth dependence of magnetic field. This is demonstrated in Chapter 2. These studies point towards the necessity to use multi-dimensional modeling to overcome the limitations of 1D modeling approach.

In the theoretical studies undertaken in the Chapters 3 - 6 of the thesis the efforts are towards understanding the partial frequency redistribution (PRD) matrix which contains all the physics of a scattering event. In Chapters 3 - 5 we study the effects of using angle-dependent PRD on emergent Stokes profiles by comparing them with the profiles obtained when angle-averaged PRD functions are used. We consider different examples in each of the chapters to highlight the importance of considering or not considering the angle-dependent PRD effects. In Chapter 3 we study the effects of electron scattering on atomic line polarization in non-magnetic regime. We have considered angle-dependent redistribution functions for both electron and atomic scattering. In Chapter 4 we consider the two-term and two-level atomic system, respectively, with quantum interference between the fine structure states and hyperfine structure states individually in the non-magnetic regime. We use the angle-dependent PRD functions to compute the emergent Stokes profiles. The studies conducted in Chapters 3 and 4 indicate that the effects of the angle-dependent PRD functions in the non-magnetic regime is dependent on the thickness of the optical slab considered for radiative transfer computations. The angle-dependent effects are important only when optically thin slabs are considered and hence computationally simpler angle-averaged PRD functions can be safely used for all realistic computations. In Chapter 5 we study the effects of angle-dependent PRD in weak magnetic field regime. We consider different cases of vertical and turbulent magnetic fields to highlight the importance of using angle-dependent PRD especially to study the Stokes U profiles. The angle-averaged approximation is often made to reduce the computational complexities. For each of the problem we have considered in Chapter 3 - 5 we have developed efficient numerical techniques to handle the problem at hand.

Finally in Chapter 6 another important theoretical improvement necessary to understand different lines in the SSS, namely the polarization of the lower-level of the atom involved in the transition is addressed. The theoretical frame work to handle the lower-level polarization and PRD in a magnetic regime is developed. This theory is applied to different atomic systems in the non-magnetic regime and the effects of polarization of the lower atomic level is studied along with the effects of PRD. It is noticed that the lower-level polarization affects only the line center while the PRD effects are seen in the line wings. This conclusion also leads us to propose a new simpler numerical method to solve the problem of polarized radiative transfer including the effects of lower-level polarization and PRD.

Thus the thesis addresses the challenges involved in both the observations and modeling of the SSS (Part I) and in the theoretical formulation in deriving and using the redistribution matrix for the radiative transfer problem (Parts II and III). These studies guide us towards the further improvements necessary in both theoretical formulation and modeling efforts of the SSS using the polarized radiative transfer.

7.2 Future work

The studies undertaken in the present thesis clearly point towards necessity to carry-out further studies in order to understand the SSS. The conclusion from the part I of the thesis i.e., 1D modeling of the center-to-limb observations of the Ca I 4227 Å line clearly show that we need to go beyond 1D modeling efforts like multi-dimensional modeling in order to obtain a simultaneous fit to the (I, Q/I) profiles of the Ca I 4227 Å line. However multi-dimensional modeling is computationally expensive. A further step in 1D modeling efforts will be to impose additional constraints on the 1D solar model atmospheres. In Stenflo (2015a, see also, Ramelli et al. 2015) a new spectra has been introduced called the third solar spectrum (SS3) which is the ratio of limb to disk-center intensity. This new spectrum can be used as an observational constraint to test and improve the structure of the existing solar atmospheric models. Also in Stenflo (2015a) an analytical model is proposed to model different lines formed under local thermodynamic equilibrium (LTE) conditions in the SS3. Along with this a full radiative transfer modeling of different LTE lines using the available solar model atmosphere can be attempted, and checked for deviations of the analytical model results, if any, from the radiative transfer model results. This can be further used to constrain the temperature modifications of the 1D solar model atmosphere. Also modeling of the SS3 using the 1D solar models will help to eliminate or justify the 1D modeling approach.

The theoretical studies presented in the Part III of the thesis opens up a new window to further study the effects of the polarization of the lower-level of the atom involved in the scattering event. The theory presented in the thesis is for a collisionless redistribution matrix for a two-level atom in the magnetic regime. The next logical step would be to examine what will be the effects of elastic collisions on the polarization contribution from the lower-level? The studies done in literature under the complete frequency redistribution limit indicates that the collisions destroy the atomic alignment in the lower-level and hence destroying the polarization generated by the lower level (see Trujillo Bueno, 1999; Casini et al., 2002). It will be interesting to study the effects of elastic collisions on lower-level polarization together with the effects of PRD by formulating an appropriate theory starting from the Kramers-Heisenberg scattering formulation. Also the numerical results presented in the part

III of the thesis is for the non-magnetic regime. It will be interesting to conduct similar studies in the presence of magnetic fields. But these studies are numerically expensive hence an appropriate numerical method should be devised to conduct such studies. Further the non-magnetic numerical results presented in the thesis are for an hypothetical atomic system with $J_a = 1$, $J_b = 0$ and $J_a = J_b = 1$, where J_a and J_b represent the total angular momentum quantum numbers of the lower and upper states respectively. As a next step we can consider a suitable solar line in SSS with these transitions and carry out radiative transfer modeling with realistic solar model atmospheres. This will further highlight the importance of accounting for polarization of the lower atomic level and PRD. The theoretical formulation presented in Chapter 6 can also be extended from the case of a simple two-level atomic system (the one described in the present thesis) to the complex system of two-term atom with quantum interference effects. Though there are efforts in the literature in this regard, they are still in early stages of development. This problem can be attempted using the Kramers-Heisenberg scattering theory presented in this thesis. This kind of studies may help us to account for many unexplained features in the SSS.

Appendix A

Collisionless redistribution matrix with lower-level polarization for the non-magnetic case

In the absence of magnetic field ($\mathbf{B} = 0$), the redistribution matrix expression given in Equation (6.9) which accounts for the contribution from the lower-level can be further simplified. The auxiliary functions become independent of the magnetic sub-states and reduce to well known type II redistribution function represented by $R_{\rm II}(x, x', \Theta)$. The contraction property of $3j$ symbols can be used to simplify Equation (6.9) further and we get

$$\mathbf{R}^{\rm II}_{ij}(x,\mathbf{n},x',\mathbf{n}') = \frac{1}{N.C.}\frac{2}{3}(2J_a+1)^2 \sum_{\mu_a\mu_b\mu_b'}\sum_{K'K''Q}\sum_{K_LQ_L}(-1)^Q\rho^{K_L}_{Q_L}\frac{\Gamma_R}{\Gamma_R+\Gamma_I+\Gamma_E}$$
$$\times\sqrt{(2K'+1)(2K''+1)(2K_L+1)}\begin{pmatrix}J_a & J_a & K_L\\ \mu_a & -\mu_a & -Q_L\end{pmatrix}\begin{pmatrix}J_a & 1 & J_b\\ -\mu_a & q' & \mu_b\end{pmatrix}$$
$$\times\begin{pmatrix}J_a & 1 & J_b\\ -\mu_a & q''' & \mu_b'\end{pmatrix}\begin{pmatrix}1 & 1 & K'\\ q' & -q''' & Q\end{pmatrix}\begin{pmatrix}J_b & J_b & K''\\ \mu_b' & -\mu_b & Q\end{pmatrix}\begin{Bmatrix}J_b & J_b & K''\\ 1 & 1 & J_a\end{Bmatrix}$$
$$\times R_{\rm II}(x,x',\Theta)(-1)^Q T^{K''}_{Q}(i,\mathbf{n})T^{K'}_{-Q}(j,\mathbf{n}'). \tag{A.1}$$

Of particular interest is the case of $J_a = 1$ and $J_b = 0$. This is because for this transition the scattering polarization can be generated only through the population imbalances in the lower level. For this case the non-magnetic $\boldsymbol{R}^{\rm II}$ matrix simplifies to

$$\mathbf{R}^{\rm II}_{0j}(x,\mathbf{n},x',\mathbf{n}') = \frac{3}{\rho^0_0}\frac{\Gamma_R}{\Gamma_R+\Gamma_I+\Gamma_E}[\rho^0_0 T^0_0(j,\mathbf{n}') + \rho^2_0 T^2_0(j,\mathbf{n}')]R_{\rm II}(x,x',\Theta). \tag{A.2}$$

We note that only the elements R_{00}^{II} and R_{01}^{II} are non-zero and all the other elements go to zero for this particular case. For this reason the line source vector for the Stokes Q parameter $S_{Q,l}$ is zero.

Appendix B

Validation of the absorption matrix elements derived from the quantum field theory approach

As explained in Section 6.3.1, here we check the consistency of the radiative absorption matrix elements (A_{kj}) derived in the Chapter 6 by comparing with the expressions given in the literature for certain specific cases.

B.1 J_a = 1 and J_b = 0

In Trujillo Bueno & Landi Degl'Innocenti (1997) we find the expressions for the radiative absorption coefficients η_I and η_Q (which correspond to η_I^A and η_Q^A respectively in our notation) for J_a = 1 and J_b = 0 as

$$\eta_I = \sqrt{3}\,\frac{h\nu}{4\pi}\,B_{ab}\,N\,\phi_x[\rho^0_0(a) + \frac{1}{2\sqrt{2}}(3\mu^2-1)\rho^2_0(a)],$$
$$\eta_Q = \sqrt{3}\,\frac{h\nu}{4\pi}\,B_{ab}\,N\,\phi_x\frac{3}{2\sqrt{2}}(\mu^2-1)\rho^2_0(a). \tag{B.1}$$

Substituting in Equation (6.13) for J_a and J_b and taking into account that $\Phi_{\mu_b\mu_a}$ is independent of magnetic quantum numbers in the non-magnetic case we get

$$g_{\alpha\alpha'} = \frac{3}{2}\frac{h\nu}{4\pi}NB_{J_aJ_b}\sum_{\mu_a}\varepsilon^{\alpha'*}_{0\mu_a}\varepsilon^{\alpha}_{0\mu_a}\rho_{\mu_a\mu_a}\Phi. \tag{B.2}$$

The geometrical factors are given by (see Equation (27) of Stenflo, 1998)

$$\varepsilon^1_0 = -\sin\theta, \qquad \varepsilon^2_0 = 0,$$

$$\varepsilon^1_{\pm} = \mp\mu\frac{e^{\pm i\phi}}{\sqrt{2}}, \qquad \varepsilon^2_{\pm} = -i\frac{e^{\pm i\phi}}{\sqrt{2}}. \tag{B.3}$$

The multipolar components of the density matrix elements $\rho_{\mu_a\mu_a}$ are given by (see Equation (3.99) of Landi Degl'Innocenti & Landolfi, 2004)

$$\rho_{\mu_a\mu_a} = \sum_{K_L}(-1)^{J_a-\mu_a}\sqrt{2K_L+1}\begin{pmatrix} J_a & J_a & K_L \\ \mu_a & -\mu_a & 0\end{pmatrix}\rho_0^{K_L}. \tag{B.4}$$

Simplifying Equation (B.2) using Equations (B.3) and (B.4) and substituting in Equation (6.24) results in the expression for η_I^A and η_Q^A as

$$\begin{aligned}\eta_I^A &= \sqrt{3}\,\frac{h\nu}{4\pi}\,B_{J_aJ_b}\,N\,\phi_x\left[\rho_0^0(a) + \frac{1}{2\sqrt{2}}(3\mu^2-1)\rho_0^2(a)\right],\\ \eta_Q^A &= \sqrt{3}\,\frac{h\nu}{4\pi}\,B_{J_aJ_b}\,N\,\phi_x\frac{3}{2\sqrt{2}}(\mu^2-1)\rho_0^2(a).\end{aligned} \tag{B.5}$$

Clearly, the expressions for η_I^A and η_Q^A match with η_I and η_Q for the particular case of $J_a = 1$ and $J_b = 0$ as given in Trujillo Bueno & Landi Degl'Innocenti (1997) in the non-magnetic regime.

B.2 $J_a = 1$ and $J_b = 1$

We follow the same kind of testing as described in the previous section but for the case of $J_a = 1$ and $J_b = 1$. The expressions for the radiative absorption coefficients η_I and η_Q for this particular case are (simplified starting from Equations (9) and (10) of Trujillo Bueno, 1999)

$$\begin{aligned}\eta_I &= \sqrt{3}\,\frac{h\nu}{4\pi}\,B_{ab}\,N\left[\rho_0^0(a) - \frac{1}{4\sqrt{2}}(3\mu^2-1)\rho_0^2(a)\right]\phi_x,\\ \eta_Q &= -\sqrt{3}\,\frac{h\nu}{4\pi}\,B_{ab}\,N\left[\frac{3}{4\sqrt{2}}(\mu^2-1)\rho_0^2(a)\right]\phi_x.\end{aligned} \tag{B.6}$$

Simplification of Equation (6.13) for $J_a = 1$ and $J_b = 1$ gives

$$g_{\alpha\alpha'} = \frac{3}{2}\frac{h\nu}{4\pi}NB_{J_aJ_b}\sum_{\mu_b\mu_a}\begin{pmatrix}1 & 1 & 1\\ -\mu_b & \mu_a & \mu_b-\mu_a\end{pmatrix}^2\varepsilon^{\alpha'*}_{\mu_b\mu_a}\,\varepsilon^{\alpha}_{\mu_b\mu_a}\,\rho_{\mu_a\mu_a}\,\Phi. \tag{B.7}$$

Using again Equations (B.3) and (B.4), the above equation can be simplified and substituted in Equation (6.24) to obtain η_I^A and η_Q^A as

$$\eta_I^A = \sqrt{3}\,\frac{h\nu}{4\pi}\,B_{J_aJ_b}\,N\left[\rho_0^0(a) - \frac{1}{4\sqrt{2}}(3\mu^2-1)\rho_0^2(a)\right]\phi_x,$$

$$\eta_Q^A = -\sqrt{3}\,\frac{h\nu}{4\pi}\,B_{J_a J_b}\,N\left[\frac{3}{4\sqrt{2}}(\mu^2-1)\rho_0^2(a)\right]\phi_x. \tag{B.8}$$

The expressions for η_I^A and η_Q^A match with η_I and η_Q for the case of J_a = 1 and J_b = 1 in the non-magnetic regime.

Appendix C

Numerical method: two stage approach

In this section we describe the two stage approach to solve the problem of polarized line formation including lower-level polarization (LLP) and partial frequency redistribution (PRD) for the non-magnetic case. In the first stage we solve the statistical equilibrium equations (SEEs) and transfer equation simultaneously in the limit of complete frequency redistribution (CRD). For the numerical solution of this problem we use the Rybicki and Hummer method (see Rybicki & Hummer, 1991) appropriately generalized to handle polarized lower level (see also Trujillo Bueno, 2003). In the second stage we solve the polarized radiative transfer equation including the effects of LLP (through the density matrix elements derived in the first stage) and PRD.

C.1 Stage 1 of the two stage approach

The governing equations and concerned numerical method for the simultaneous solution of the SEEs and transfer equation in the limit of CRD is illustrated here for the $1\rightarrow1\rightarrow1$ transition. For this particular transition the SEEs and transfer equations are given in Trujillo Bueno (1999). For clarity we recall those equations here. For this particular case there are four density matrix elements to be determined namely, $\rho^0_0(a)$, $\rho^2_0(a)$, $\rho^0_0(b)$ and $\rho^2_0(b)$ when polarizability of both the levels are taken into account. The SEEs to be solved correspond to the $K = 0$ and 2 components of the upper level, $K = 2$ component of the lower level density matrix and the number conservation equation. These equations can be derived starting from the general equations (10.4) given in Landi Degl'Innocenti & Landolfi (2004) and they are

$$B_{J_a J_b} J^0_0 \rho^0_0(a) - \frac{1}{2} B_{J_a J_b} J^2_0 \rho^2_0(a) - A_{J_b J_a} \rho^0_0(b) + C_{J_a J_b} \rho^0_0(a) - C_{J_b J_a} \rho^0_0(b) = 0,$$

$$
\begin{aligned}
&-\frac{B_{J_aJ_b}}{2}J_0^2\rho_0^0(a)-\frac{B_{J_aJ_b}}{2}J_0^0\rho_0^2(a)-\frac{B_{J_aJ_b}}{\sqrt{2}}J_0^2\rho_0^2(a)-A_{J_bJ_a}\rho_0^2(b)\\
&+C^{(2)}_{J_aJ_b}\rho_0^2(a)-\left[C_{J_bJ_a}+D^{(2)}_{J_b}\right]\rho_0^2(b)=0,\\
&-A_{J_bJ_a}\rho_0^2(b)+B_{J_aJ_b}J_0^2\rho_0^0(a)-2B_{J_aJ_b}J_0^0\rho_0^2(a)-\frac{B_{J_aJ_b}}{\sqrt{2}}J_0^2\rho_0^2(a)+2C^{(2)}_{J_bJ_a}\rho_0^2(b)\\
&-2\left[C_{J_aJ_b}+D^{(2)}_{J_a}\right]\rho_0^2(a)=0,\\
&\sqrt{3}\rho_0^0(a)+\rho_0^0(b)=1.
\end{aligned}
\tag{C.1}
$$

Here $A_{J_bJ_a}$ and $B_{J_aJ_b}$ are the Einstein coefficients for the spontaneous emission and absorption respectively, $C_{J_aJ_b}$ and $C_{J_bJ_a}$ are the upward and downward inelastic collisional rates, and $D^{(2)}_{J_b}$ and $D^{(2)}_{J_a}$ are the upper and lower level depolarizing elastic collision rates. In the present case there is a contribution from the $K=2$ multipole component of the inelastic collision rates namely, $C^{(2)}_{J_aJ_b}$ and $C^{(2)}_{J_bJ_a}$. The relation between the K^{th} multipole component and zeroth component of different collision rates is given in Appendix 4 of Landi Degl'Innocenti & Landolfi (2004). Using that relation we get $C^{(2)}_{J_aJ_b}=-C_{J_aJ_b}/2$ and $C^{(2)}_{J_bJ_a}=-C_{J_bJ_a}/2$ for 1→1→1 transition (we have taken $\widetilde{K}=1$). There are two quantities related to the radiation field that enter the SEEs. They are

$$
\begin{aligned}
J_0^0&=\frac{1}{2}\int dx\;\phi_x\int_{-1}^{1}d\mu\;I(x,\mu),\\
J_0^2&=\frac{1}{4\sqrt{2}}\int dx\;\phi_x\int_{-1}^{1}d\mu\;\left[(3\mu^2-1)\,I(x,\mu)+3(\mu^2-1)\,Q(x,\mu)\right],
\end{aligned}
\tag{C.2}
$$

where I and Q are the Stokes parameters which are obtained by solving the transfer equations

$$dI/ds=\epsilon_I-\eta_I^AI-\eta_Q^AQ, \tag{C.3}$$

$$dQ/ds=\epsilon_Q-\eta_Q^AI-\eta_I^AQ. \tag{C.4}$$

Here s is the geometrical distance along the ray. In the preceding equations, ϵ_I and ϵ_Q are the emission coefficients which are given by

$$
\begin{aligned}
\epsilon_I&=\frac{h\nu}{4\pi}N\sqrt{3}A_{J_bJ_a}\left[\rho_0^0(b)-\frac{1}{4\sqrt{2}}(3\mu^2-1)\rho_0^2(b)\right]\phi_x,\\
\epsilon_Q&=-\frac{h\nu}{4\pi}N\sqrt{3}A_{J_bJ_a}\left[\frac{3}{4\sqrt{2}}(\mu^2-1)\rho_0^2(b)\right]\phi_x.
\end{aligned}
\tag{C.5}
$$

The expressions for the absorption coefficients η_I^A and η_Q^A are given by Equation (B.6). Here N is the total number of atoms per unit volume. We note that $\epsilon_Q\neq 0$ whereas it is equal to 0 in the case of $1\rightarrow 0\rightarrow 1$ transition as the upper level with $J_b=0$

cannot lead to the emission of polarized radiation.

From Equations (C.5) and (B.6) we see that ϵ_I, ϵ_Q, η_I^A and η_Q^A depend on the atomic density matrix elements, which in turn depend on the Stokes I and Q parameters (see Equations C.1 and C.2). Thus the problem becomes both nonlinear and nonlocal. This is referred to as the non-local thermodynamic equilibrium (NLTE) problem of the second kind (see Landi Degl'Innocenti & Landolfi, 2004). To solve this problem, we use an iterative technique based on the approximate lambda iteration (ALI) method.

From Equation (B.6) we see that when the lower level polarization is neglected (i.e., $\rho_0^2(a) = 0$), the coefficient $\eta_Q^A = 0$. The transfer equations in this case get decoupled and hence the numerical method of solution becomes simple. The details of the Λ-iteration method to solve this NLTE resonance line transfer problem can be found in Trujillo Bueno & Manso Sainz (1999). However when the effects of polarization of the lower atomic level are considered, $\eta_Q^A \neq 0$ and thus the transfer equations are coupled (see Equation C.4). These coupled transfer equations can be decoupled by working with $I_+ = I + Q$ and $I_- = I - Q$ (see Trujillo Bueno, 2003). The decoupled transfer equations can be written as

$$\frac{dI_+}{ds} = \epsilon_+ - \eta_+ I_+, \tag{C.6}$$

$$\frac{dI_-}{ds} = \epsilon_- - \eta_- I_-, \tag{C.7}$$

where $\epsilon_+ = \epsilon_I + \epsilon_Q$; $\epsilon_- = \epsilon_I - \epsilon_Q$; $\eta_+ = \eta_I + \eta_Q$ and $\eta_- = \eta_I - \eta_Q$. Thus we can write the source functions S_+ and S_- as

$$S_+ = \frac{\epsilon_+}{\eta_+} = \frac{2h\nu^3}{c^2} \frac{\rho_0^0(b) - \frac{1}{4\sqrt{2}}\left[(3\mu^2-1) + 3(\mu^2-1)\right]\rho_0^2(b)}{\rho_0^0(a) - \frac{1}{4\sqrt{2}}\left[(3\mu^2-1) + 3(\mu^2-1)\right]\rho_0^2(a)}, \tag{C.8}$$

$$S_- = \frac{\epsilon_-}{\eta_-} = \frac{2h\nu^3}{c^2} \frac{\rho_0^0(b) - \frac{1}{4\sqrt{2}}\left[(3\mu^2-1) - 3(\mu^2-1)\right]\rho_0^2(b)}{\rho_0^0(a) - \frac{1}{4\sqrt{2}}\left[(3\mu^2-1) - 3(\mu^2-1)\right]\rho_0^2(a)}. \tag{C.9}$$

The formal solution of the transfer equations (C.6) and (C.7) can be written as

$$I_+ = \Lambda_+[S_+], \tag{C.10}$$

$$I_- = \Lambda_-[S_-], \tag{C.11}$$

where Λ_+ and Λ_- are the operators which depend on the optical distances between the grid points. We use the short characteristics method (Olson & Kunasz, 1987) to find the formal solution of the transfer equations (C.6) and (C.7).

Now, in order to linearize the SEEs (C.1), we introduce the approximate operator

via the ALI approximation

$$I_+ \simeq \Lambda_+[S_+] + (\Lambda_+ - \Lambda^*_+)[S^\dagger_+],$$
$$I_- \simeq \Lambda_-[S_-] + (\Lambda_- - \Lambda^*_-)[S^\dagger_-], \tag{C.12}$$

where the '†' represent the quantities known from the previous iteration. Following Olson et al. (1986), the approximate operators Λ^*_+ and Λ^*_- are chosen to be the diagonals of the respective actual lambda operators. Using Equations (C.12) in Equation (C.2) we obtain

$$J^0_0 = J^{0,\,eff}_0 + (\Lambda^{*0}_0 + \Lambda^{*0}_2)\frac{\rho^0_0(b)}{\rho^0_0(a)}, \tag{C.13}$$

$$J^2_0 = J^{2,\,eff}_0 + (\Lambda^{*2}_0 + \Lambda^{*2}_2)\frac{\rho^0_0(b)}{\rho^0_0(a)}, \tag{C.14}$$

where $J^{0,\,eff}_0$ and $J^{2,\,eff}_0$ are given by

$$J^{0,\,eff}_0 = \frac{1}{2}\int dx\ \phi_x \int_{-1}^{1} d\mu\ \frac{1}{2}\left[(\Lambda_+ - \Lambda^*_+)[S^\dagger_+] + (\Lambda_- - \Lambda^*_-)[S^\dagger_-]\right], \tag{C.15}$$

$$J^{2,\,eff}_0 = \frac{1}{4\sqrt{2}}\int dx\ \phi_x \int_{-1}^{1} d\mu\ \frac{1}{2}[((3\mu^2-1) + 3(\mu^2-1))\,(\Lambda_+ - \Lambda^*_+)[S^\dagger_+] +$$
$$((3\mu^2-1) - 3(\mu^2-1))\,(\Lambda_- - \Lambda^*_-)[S^\dagger_-]]. \tag{C.16}$$

The components of the Λ^* operator are given by

$$\Lambda^{*0}_0 = \frac{1}{2}\int dx\ \phi_x \int_{-1}^{1} d\mu\ \frac{1}{2}\frac{2h\nu^3}{c^2}\,\Lambda^*_+ \frac{1 - \frac{1}{4\sqrt{2}}\left[(3\mu^2-1) + 3(\mu^2-1)\right]\left[\rho^2_0(b)/\rho^0_0(b)\right]}{1 - \frac{1}{4\sqrt{2}}\left[(3\mu^2-1) + 3(\mu^2-1)\right]\left[\rho^2_0(a)/\rho^0_0(a)\right]},$$

$$\Lambda^{*0}_2 = \frac{1}{2}\int dx\ \phi_x \int_{-1}^{1} d\mu\ \frac{1}{2}\frac{2h\nu^3}{c^2}\,\Lambda^*_- \frac{1 - \frac{1}{4\sqrt{2}}\left[(3\mu^2-1) - 3(\mu^2-1)\right]\left[\rho^2_0(b)/\rho^0_0(b)\right]}{1 - \frac{1}{4\sqrt{2}}\left[(3\mu^2-1) - 3(\mu^2-1)\right]\left[\rho^2_0(a)/\rho^0_0(a)\right]},$$

$$\Lambda^{*2}_0 = \frac{1}{4\sqrt{2}}\int dx\ \phi_x \int_{-1}^{1} d\mu\ \frac{1}{2}\frac{2h\nu^3}{c^2}\,\Lambda^*_+\left[(3\mu^2-1) + 3(\mu^2-1)\right]$$
$$\times\frac{1 - \frac{1}{4\sqrt{2}}\left[(3\mu^2-1) + 3(\mu^2-1)\right]\left[\rho^2_0(b)/\rho^0_0(b)\right]}{1 - \frac{1}{4\sqrt{2}}\left[(3\mu^2-1) + 3(\mu^2-1)\right]\left[\rho^2_0(a)/\rho^0_0(a)\right]},$$

$$\Lambda^{*2}_2 = \frac{1}{4\sqrt{2}}\int dx\ \phi_x \int_{-1}^{1} d\mu\ \frac{1}{2}\frac{2h\nu^3}{c^2}\,\Lambda^*_-\left[(3\mu^2-1) - 3(\mu^2-1)\right]$$
$$\times\frac{1 - \frac{1}{4\sqrt{2}}\left[(3\mu^2-1) - 3(\mu^2-1)\right]\left[\rho^2_0(b)/\rho^0_0(b)\right]}{1 - \frac{1}{4\sqrt{2}}\left[(3\mu^2-1) - 3(\mu^2-1)\right]\left[\rho^2_0(a)/\rho^0_0(a)\right]}. \tag{C.17}$$

In the computation of S_+ and S_- in the first iteration, we need the values of $\rho^0_0(a)$, $\rho^0_0(b)$, $\rho^2_0(a)$, and $\rho^2_0(b)$. These are obtained by assuming the local thermodynamic equilibrium populations. First we compute the number densities of the lower level

(N_{J_a}), upper level (N_{J_b}) and the total density ($N = N_{J_a} + N_{J_b}$). From this, we compute $\rho^0_0(a) = \frac{1}{\sqrt{3}}\frac{N_{J_a}}{N}$ and $\rho^0_0(b) = \frac{1}{\sqrt{3}}\frac{N_{J_b}}{N}$. We assume $\rho^2_0(a) = \rho^2_0(b) = 0$ in the first iteration. Substituting Equations (C.13) and (C.14) in Equations (C.1), and preconditioning the quantity $\rho^0_0(b)/\rho^0_0(a)$ we can linearize these SEEs to obtain the corresponding set of linearized equations

$$\left[B_{J_aJ_b}J_0^{0,\,eff} + C_{J_aJ_b}\right]\rho^0_0(a) + \left[B_{J_aJ_b}({\Lambda^*}_0^0 + {\Lambda^*}_2^0) - A_{J_bJ_a} - C_{J_bJ_a}\right]\rho^0_0(b) - \left[\frac{1}{2}B_{J_aJ_b}J_0^{2,\,eff} + \frac{1}{2}B_{J_aJ_b}({\Lambda^*}_0^2 + {\Lambda^*}_2^2)\left(\frac{\rho^0_0(b)}{\rho^0_0(a)}\right)^{\dagger}\right]\rho^2_0(a) = 0, \tag{C.18a}$$

$$\left[-\frac{B_{J_aJ_b}}{2}J_0^{2,\,eff}\right]\rho^0_0(a) - \left[\frac{B_{J_aJ_b}}{2}({\Lambda^*}_0^2 + {\Lambda^*}_2^2)\right]\rho^0_0(b) + \Big[C^{(2)}_{J_aJ_b} - \frac{B_{J_aJ_b}}{2}J_0^{0,\,eff} - \frac{B_{J_aJ_b}}{2}({\Lambda^*}_0^0 + {\Lambda^*}_2^0)\left(\frac{\rho^0_0(b)}{\rho^0_0(a)}\right)^{\dagger} - \frac{B_{J_aJ_b}}{\sqrt{2}}J_0^{2,\,eff} - \frac{B_{J_aJ_b}}{\sqrt{2}}({\Lambda^*}_0^2 + {\Lambda^*}_2^2) \times \left(\frac{\rho^0_0(b)}{\rho^0_0(a)}\right)^{\dagger}\Big]\rho^2_0(a) + \left[C_{J_bJ_a} + D^{(2)}_{J_b} - A_{J_bJ_a}\right]\rho^2_0(b) = 0, \tag{C.18b}$$

$$\left[B_{J_aJ_b}J_0^{2,\,eff}\right]\rho^0_0(a) + \left[B_{J_aJ_b}({\Lambda^*}_0^2 + {\Lambda^*}_2^2)\right]\rho^0_0(b) - \Big[2B_{J_aJ_b}J_0^{0,\,eff} + 2B_{J_aJ_b}({\Lambda^*}_0^0 + {\Lambda^*}_2^0)\left(\frac{\rho^0_0(b)}{\rho^0_0(a)}\right)^{\dagger} + \frac{B_{J_aJ_b}}{\sqrt{2}}({\Lambda^*}_0^2 + {\Lambda^*}_2^2)\left(\frac{\rho^0_0(b)}{\rho^0_0(a)}\right)^{\dagger} + 2C_{J_aJ_b} + 2D^{(2)}_{J_a}\Big]\rho^2_0(a) + \left[2C^{(2)}_{J_bJ_a} - A_{J_bJ_a}\right]\rho^2_0(b) = 0. \tag{C.18c}$$

These equations are then solved for the density matrix elements $\rho^0_0(a)$, $\rho^0_0(b)$, $\rho^2_0(a)$, and $\rho^2_0(b)$. In the subsequent iterations the source functions and the quantities J^0_0 and J^2_0 are updated. The iteration sequence is continued until the convergence is obtained over the density matrix elements. In this way we solve the SEEs and the transfer equations simultaneously using the ALI method. The limit of unpolarized lower-level is recovered by setting $\rho^2_0(a)$ to zero in the above equations. It has to be noted that the time evolution equation of the lower level will then be given by $\rho^K_Q(a) = \delta_{K0}\delta_{Q0}\rho^0_0(a)$, and therefore, the equation (C.18c) will vanish. The rest of the iteration procedure remains the same, which then involves solving the SEEs for the three unknowns namely, $\rho^2_0(b)$, $\rho^0_0(b)$, and $\rho^0_0(a)$. A similar procedure can also be followed for the case of $J_a = 1$ and $J_b = 0$ which is simpler compared to $J_a = J_b = 1$ case, with only three density matrix elements to be determined. The SEEs and the transfer equation for this case (J_a = 1 and J_b = 0) in the non-magnetic regime, is given in Trujillo Bueno & Landi Degl'Innocenti (1997).

C.2 Stage 2 of the two stage approach

The density matrix elements obtained from the first stage described above are used to compute the elements of the redistribution matrix $\mathbf{R}^{\mathrm{II}}_{ij}(x, \mu, x', \mu')$ which is needed in the the second stage. In this stage we solve the polarized transfer equation given in Equation (6.42). By defining total optical depth $d\tau_{tot} = (\phi_I^{abs} + r)d\tau$ we can simplify Equation (6.42) as

$$\frac{d\boldsymbol{I}}{d\tau_{tot}} = \boldsymbol{I} - \boldsymbol{S}_{eff}. \tag{C.19}$$

Here, the effective source vector is

$$\boldsymbol{S}_{eff} = \boldsymbol{S}_{tot} - \boldsymbol{K}'\boldsymbol{I}, \tag{C.20}$$

where we have redefined the total absorption matrix as

$$\boldsymbol{K}' = \frac{\boldsymbol{K}}{\phi_I^{abs} + r} - \boldsymbol{E}. \tag{C.21}$$

The total source vector is defined as

$$\boldsymbol{S}_{tot} = \frac{1}{\phi_I^{abs} + r}[rB_{\nu_0}\mathbf{1} + \boldsymbol{S}_l]. \tag{C.22}$$

With these expressions we can apply the same steps as in Equations (19) - (26) of Sampoorna et al. (2008c) to obtain the formal solution of the transfer equation using DELOPAR method (see also Trujillo Bueno, 2003). The transfer equation (C.19) is solved iteratively using an ALI method. To compute the source vector corrections we use the so called frequency-angle by frequency-angle (FABFA) method, similar to that given in Sampoorna et al. (2011).

However in the present case the thermal emission term (see Equation (6.34)) is not a constant factor unlike in Sampoorna et al. (2011). Therefore we apply ALI for the thermal term also and hence the corrections are computed over the total source vector. Hereon the dependencies over x and μ appear as subscripts. The formal solution of the transfer equation (C.19) can be written as

$$\boldsymbol{I}_{x\mu} = \boldsymbol{\Lambda}_{x\mu}[\boldsymbol{S}_{tot,x\mu}]. \tag{C.23}$$

$\boldsymbol{\Lambda}_{x\mu}$ is frequency and angle dependent integral operator which can be split as

$$\boldsymbol{\Lambda}_{x\mu} = \boldsymbol{\Lambda}^*_{x\mu} + (\boldsymbol{\Lambda}_{x\mu} - \boldsymbol{\Lambda}^*_{x\mu}), \tag{C.24}$$

where $\boldsymbol{\Lambda}^*_{x\mu}$ represents the diagonal approximate operator. Now we can write the total source vector as

$$\boldsymbol{S}^{n+1}_{tot,x\mu} = \boldsymbol{S}^{n}_{tot,x\mu} + \delta\boldsymbol{S}^{n}_{tot,x\mu}. \tag{C.25}$$

Here n represents the iteration index. Using Equations (C.22), (C.24), (C.25), and (6.43) we obtain

$$\begin{aligned}
&\delta\boldsymbol{S}^{n}_{tot,x\mu} - p_{x\mu}\frac{1}{2}\int d\mu' \int dx' \frac{\boldsymbol{R}^{\rm II}_{x\mu,x'\mu'}}{\phi_x}\boldsymbol{\Lambda}^*_{x'\mu'}[\delta\boldsymbol{S}^{n}_{tot,x'\mu'}] - p_{x\mu}\frac{(1-k_c)\alpha S_{ba}}{\int \phi_x J_x dx}\\
&\times\frac{1}{2}\int d\mu' \int dx' \boldsymbol{X}_{x'\mu'}\boldsymbol{\Lambda}^*_{x'\mu'}[\delta\boldsymbol{S}^{n}_{tot,x'\mu'}] = p_{x\mu}\overline{\boldsymbol{J}}^{n}_{x\mu}\\
&+p_{x\mu}\left[\mathbf{1} - \alpha\mathbf{1} + \frac{(1-k_c)\alpha\boldsymbol{e}^n}{\int \phi_x J_x dx}\right] S_{ba} + p^c_{x\mu}B_{\nu_0}\mathbf{1} - \boldsymbol{S}^{n}_{tot,x\mu},
\end{aligned} \tag{C.26}$$

where $p_{x\mu} = \phi_x/(\phi^{abs}_I + r)$ and $p^c_{x\mu} = r/(\phi^{abs}_I + r)$. The mean intensity is given by

$$\overline{\boldsymbol{J}}^{n}_{x\mu} = \frac{1}{2}\int d\mu' \int dx' \frac{\boldsymbol{R}^{\rm II}_{x\mu,x'\mu'}}{\phi_x}\boldsymbol{I}_{x'\mu'}. \tag{C.27}$$

In order to apply the ALI to the thermal emission term, we need to define matrix

$$\boldsymbol{X} = \begin{pmatrix} \phi^{abs}_I & \phi^{abs}_Q \\ 0 & 0 \end{pmatrix}, \tag{C.28}$$

so that the scalar quantity e defined in Equation (6.36) can be rewritten as

$$\boldsymbol{e} = \frac{1}{2}\int d\mu' \int dx' \boldsymbol{X}_{x'\mu'}\boldsymbol{I}_{x'\mu'}. \tag{C.29}$$

Substituting Equations (C.23) and (C.24) in Equation (C.29) we obtain $\boldsymbol{e}$ for the $(n+1)^{th}$ iterate as

$$\boldsymbol{e}^{n+1} = \boldsymbol{e}^{n} + \frac{1}{2}\int d\mu' \int dx' \boldsymbol{X}_{x'\mu'}\boldsymbol{\Lambda}^*_{x'\mu'}[\delta\boldsymbol{S}^{n}_{tot,x'\mu'}]. \tag{C.30}$$

The standard steps of FABFA as given in Sampoorna et al. (2011) can now be applied to solve the system of linear equation (C.26) to obtain the corrections to the total source vector ($\delta\boldsymbol{S}_{tot,x\mu}$) in the iteration process. In this way we solve using the ALI method, the transfer equation which now includes the effects of PRD and LLP.

Bibliography

Anusha, L. S., & Nagendra, K. N. 2011a, ApJ, 738, 116

—. 2011b, ApJ, 739, 40

—. 2012, ApJ, 746, 84

—. 2013, ApJ, 767, 108

Anusha, L. S., & Nagendra, K. N. 2014, in Astronomical Society of the Pacific Conference Series, Vol. 489, Solar Polarization 7, ed. K. N. Nagendra, J. O. Stenflo, Q. Qu, & M. Samooprna, 225

Anusha, L. S., Nagendra, K. N., Stenflo, J. O., Bianda, M., Sampoorna, M., Frisch, H., Holzreuter, R., & Ramelli, R. 2010, ApJ, 718, 988

Anusha, L. S., Nagendra, K. N., Bianda, M., Stenflo, J. O., Holzreuter, R., Sampoorna, M., Frisch, H., Ramelli, R., & Smitha, H. N. 2011, ApJ, 737, 95

Auer, L. H., & Mihalas, D. 1968, ApJ, 153, 245

Auer, L. H., Rees, D. E., & Stenflo, J. O. 1980, Astron. Astrophys., 88, 302

Auer, L. H., & van Blerkom, D. 1972, ApJ, 178, 175

Avrett, E. H. 1995, in Infrared tools for solar astrophysics: What's next?, ed. J. R. Kuhn & M. J. Penn, 303

Avrett, E. H., Kurucz, R. L., & Loeser, R. 1984, in Bulletin of the American Astronomical Society, Vol. 16, Bulletin of the American Astronomical Society, 450

Barklem, P. S., & O'Mara, B. J. 1997, Mon. Not. Roy. Astron. Soc., 290, 102

Belluzzi, L., Trujillo Bueno, J., & Landi Degl'Innocenti, E. 2015, ApJ, 814, 116

Berdyugina, S. V., Stenflo, J. O., & Gandorfer, A. 2002, Astron. Astrophys., 388, 1062

Bernat, A. P., & Lambert, D. L. 1978, Pub. Astron. Soc. Pac., 90, 520

Bianda, M., Solanki, S. K., & Stenflo, J. O. 1998, Astron. Astrophys., 331, 760

Bianda, M., Stenflo, J. O., Gandorfer, A., & Gisler, D. 2003, in Astronomical Society of the Pacific Conference Series, Vol. 286, Current Theoretical Models and Future High Resolution Solar Observations: Preparing for ATST, ed. A. A. Pevtsov & H. Uitenbroek, 61

Bianda, M., Stenflo, J. O., & Solanki, S. K. 1999, Astron. Astrophys., 350, 1060

Bianda, M., Ramelli, R., Anusha, L. S., Stenflo, J. O., Nagendra, K. N., Holzreuter, R., Sampoorna, M., Frisch, H., & Smitha, H. N. 2011, Astron. Astrophys., 530, L13

Bommier, V. 1980, Astron. Astrophys., 87, 109

—. 1997a, Astron. Astrophys., 328, 706

—. 1997b, Astron. Astrophys., 328, 726

Bommier, V. 1999, in Astrophysics and Space Science Library, Vol. 243, Polarization, ed. K. N. Nagendra & J. O. Stenflo, 43–59

Bommier, V. 2003, in Astronomical Society of the Pacific Conference Series, Vol. 307, Solar Polarization, ed. J. Trujillo-Bueno & J. Sanchez Almeida, 213

Bommier, V., & Sahal-Brechot, S. 1978, Astron. Astrophys., 69, 57

Bommier, V., & Stenflo, J. O. 1999, Astron. Astrophys., 350, 327

Brückner, G. 1963, Zeitschrift für Astrophysik, 58, 73

Casini, R., Landi Degl'Innocenti, E., Landolfi, M., & Trujillo Bueno, J. 2002, ApJ, 573, 864

Casini, R., Landi Degl'Innocenti, M., Manso Sainz, R., Landi Degl'Innocenti, E., & Landolfi, M. 2014, ApJ, 791, 94

Castor, J. I., Smith, L. F., & van Blerkom, D. 1970, ApJ, 159, 1119

Chandrasekhar, S. 1950, Radiative transfer.

Chugai, N. N. 2001, Mon. Not. Roy. Astron. Soc., 326, 1448

Collett, E., ed. 1993, Polarized Light - Fundamentals and Applications (Marcel Dekker, Inc., New York/Basel/ Hong Kong)

Dirac, P. A. M. 1925, Mon. Not. Roy. Astron. Soc., 85, 825

Domke, H., & Hubeny, I. 1988, ApJ, 334, 527

Dumont, S., Pecker, J.-C., & Omont, A. 1973, Solar Phys., 28, 271

Dumont, S., Pecker, J. C., Omont, A., & Rees, D. 1977, Astron. Astrophys., 54, 675

Faurobert, M. 1987, Astron. Astrophys., 178, 269

—. 1988, Astron. Astrophys., 194, 268

Faurobert, M. 2000, in Astronomical Society of the Pacific Conference Series, Vol. 205, Last Total Solar Eclipse of the Millennium, ed. W. Livingston & A. Özgüç, 156

Faurobert, M. 2003, in EAS Publications Series, Vol. 9, EAS Publications Series, ed. J. Arnaud & N. Meunier, 77

—. 2012, IAU Special Session, 6, E3.01

Faurobert-Scholl, M. 1991, Astron. Astrophys., 246, 469

—. 1992, Astron. Astrophys., 258, 521

—. 1993, Astron. Astrophys., 268, 765

—. 1994, Astron. Astrophys., 285, 655

—. 1996, Solar Phys., 164, 79

Faurobert-Scholl, M., Feautrier, N., Machefert, F., Petrovay, K., & Spielfiedel, A. 1995, Astron. Astrophys., 298, 289

Faurobert-Scholl, M., Frisch, H., & Nagendra, K. N. 1997, Astron. Astrophys., 322, 896

Faurobert-Scholl, M., Paletou, F., & Bommier, V. 1999, in Astrophysics and Space Science Library, Vol. 243, Polarization, ed. K. N. Nagendra & J. O. Stenflo, 115–125

Fluri, D. M., Nagendra, K. N., & Frisch, H. 2003, Astron. Astrophys., 400, 303

Fontenla, J. M., Avrett, E., Thuillier, G., & Harder, J. 2006, ApJ, 639, 441

Fontenla, J. M., Avrett, E. H., & Loeser, R. 1990, ApJ, 355, 700

—. 1991, ApJ, 377, 712

—. 1993, ApJ, 406, 319

Fontenla, J. M., Balasubramaniam, K. S., & Harder, J. 2007, ApJ, 667, 1243

Fontenla, J. M., Curdt, W., Haberreiter, M., Harder, J., & Tian, H. 2009, ApJ, 707, 482

Frisch, H. 1988, in Saas-Fee Advanced Course 18: Radiation in Moving Gaseous Media, ed. Y. Chmielewski & T. Lanz, 339

Frisch, H. 1996, Solar Phys., 164, 49

—. 2007, Astron. Astrophys., 476, 665

Frisch, H. 2009, in Astronomical Society of the Pacific Conference Series, Vol. 405, Solar Polarization 5: In Honor of Jan Stenflo, ed. S. V. Berdyugina, K. N. Nagendra, & R. Ramelli, 87

—. 2010, Astron. Astrophys., 522, A41

Frisch, H., Anusha, L. S., Sampoorna, M., & Nagendra, K. N. 2009, Astron. Astrophys., 501, 335

Frisch, H., Faurobert, M., & Nagendra, K. N. 2001, in Astronomical Society of the Pacific Conference Series, Vol. 236, Advanced Solar Polarimetry – Theory, Observation, and Instrumentation, ed. M. Sigwarth, 197

Gandorfer, A. 2000, The Second Solar Spectrum: A high spectral resolution polarimetric survey of scattering polarization at the solar limb in graphical representation. Volume I: 4625 Å to 6995 Å

—. 2002, The Second Solar Spectrum: A high spectral resolution polarimetric survey of scattering polarization at the solar limb in graphical representation. Volume II: 3910 Å to 4630 Å

—. 2005, The Second Solar Spectrum: A high spectral resolution polarimetric survey of scattering polarization at the solar limb in graphical representation. Volume III: 3160 Å to 3915 Å

Hale, G. E. 1908, ApJ, 28, 315

Hanle, W. 1924, Zeitschrift fur Physik, 30, 93

Heinzel, P. 1981, J. Quant. Spectrosc. Radiat. Transfer, 25, 483

Hillier, D. J. 1991, Astron. Astrophys., 247, 455

Holzreuter, R., Fluri, D. M., & Stenflo, J. O. 2005, Astron. Astrophys., 434, 713

Holzreuter, R., & Stenflo, J. O. 2007a, Astron. Astrophys., 467, 695

—. 2007b, Astron. Astrophys., 472, 919

Howard, R., & Stenflo, J. O. 1972, Solar Phys., 22, 402

Hubeny, I. 1985, in NATO Advanced Science Institutes (ASI) Series C, Vol. 152, NATO Advanced Science Institutes (ASI) Series C, ed. J. E. Beckman & L. Crivellari, 27–58

Hubeny, I. 1992, in Lecture Notes in Physics, Berlin Springer Verlag, Vol. 401, The Atmospheres of Early-Type Stars, ed. U. Heber & C. S. Jeffery, 377

Hubeny, I., & Cooper, J. 1986, ApJ, 305, 852

Hubeny, I., & Lites, B. W. 1995, ApJ, 455, 376

Hubeny, I., & Mihalas, D. 2014, Theory of Stellar Atmospheres

Hubený, I., Oxenius, J., & Simonneau, E. 1983, J. Quant. Spectrosc. Radiat. Transfer, 29, 495

Hummer, D. G. 1962, Mon. Not. Roy. Astron. Soc., 125, 21

Hummer, D. G., & Mihalas, D. 1967, Astrophys. J. Lett., 150, L57

Ivanov, V. V. 1991, in NATO Advanced Science Institutes (ASI) Series C, Vol. 341, NATO Advanced Science Institutes (ASI) Series C, ed. L. Crivellari, I. Hubeny, & D. G. Hummer, 81

Ivanov, V. V., Grachev, S. I., & Loskutov, V. M. 1997, Astron. Astrophys., 321, 968

Jäger, F. W. 1954, Zeitschrift für Astrophysik, 34, 237

Kurucz, R. 1969, in Theory and Observation of Normal Stellar Atmospheres, ed. O. Gingerich, 375

Kurucz, R. L. 1973, PhD thesis, HARVARD UNIVERSITY.

—. 1979, Astrophysical Journal Supplement Series, 40, 1

Kurucz, R. L. 1990, in 3rd International Collogium of the Royal Netherlands Academy of Arts and Sciences, ed. J. E. Hansen, 20

Kurucz, R. L., Furenlid, I., Brault, J., & Testerman, L. 1984, Solar flux atlas from 296 to 1300 nm (Aura)

Küveler, G., Dao, V. D., & Ramelli, R. 2011, Astronomische Nachrichten, 332, 502

Landi Degl'Innocenti, E. 1982, Solar Phys., 79, 291

—. 1983, Solar Phys., 85, 3

—. 1984, Solar Phys., 91, 1

—. 1996, Solar Phys., 164, 21

Landi degl'Innocenti, E. 1998, Nature, 392, 256

Landi degl'Innocenti, E., Landi degl'Innocenti, M., & Landolfi, M. 1997, in in Proc. Forum THEMIS, ed. N. Mein & S. Sahal Bŕechot, Paris: Obs. Paris-Meudon (Paris: Obs. Paris-Meudon), 59

Landi Degl'Innocenti, E., & Landolfi, M., eds. 2004, Astrophysics and Space Science Library, Vol. 307, Polarization in Spectral Lines (LL04)

Leroy, J. L., Ratier, G., & Bommier, V. 1977, Astron. Astrophys., 54, 811

Machado, M. E., Avrett, E. H., Vernazza, J. E., & Noyes, R. W. 1980, ApJ, 242, 336

Maltby, P., Avrett, E. H., Carlsson, M., Kjeldseth-Moe, O., Kurucz, R. L., & Loeser, R. 1986, ApJ, 306, 284

Manso Sainz, R., & Trujillo-Bueno, J. 1999, in Astrophysics and Space Science Library, Vol. 243, Polarization, ed. K. N. Nagendra & J. O. Stenflo, 143–156

Manso Sainz, R., & Trujillo Bueno, J. 2003a, in Astronomical Society of the Pacific Conference Series, Vol. 307, Solar Polarization, ed. J. Trujillo-Bueno & J. Sanchez Almeida, 251

Manso Sainz, R., & Trujillo Bueno, J. 2003b, Physical Review Letters, 91, 111102

Manso Sainz, R., & Trujillo Bueno, J. 2007, in Astronomical Society of the Pacific Conference Series, Vol. 368, The Physics of Chromospheric Plasmas, ed. P. Heinzel, I. Dorotovič, & R. J. Rutten, Heinzel

—. 2010, ApJ, 722, 1416

Marlborough, J. M. 1969, ApJ, 156, 135

McKenna, S. J. 1984, Astrophysics and Space Science, 106, 283

—. 1985, Astrophysics and Space Science, 108, 31

Mihalas, D. 1978, Stellar atmospheres /2nd edition/

Moruzzi, G., & Strumia, F., eds. 1991, The Hanle Effect and Level-Crossing Spectroscopy

Münch, G. 1948, ApJ, 108, 116

Nagendra, K. N. 1988, ApJ, 335, 269

—. 1989, Astrophysics and Space Science, 154, 119

—. 1994, ApJ, 432, 274

—. 1995, Mon. Not. Roy. Astron. Soc., 274, 523

Nagendra, K. N. 2003, in Astronomical Society of the Pacific Conference Series, Vol. 288, Stellar Atmosphere Modeling, ed. I. Hubeny, D. Mihalas, & K. Werner, 583

Nagendra, K. N. 2014, in Astronomical Society of the Pacific Conference Series, Vol. 489, Solar Polarization 7, ed. K. N. Nagendra, J. O. Stenflo, Z. Q. Qu, & M. Sampoorna, 179

Nagendra, K. N. 2015, in IAU Symposium, Vol. 305, IAU Symposium, ed. K. N. Nagendra, S. Bagnulo, R. Centeno, & M. Jesús Martínez González, 351–359

Nagendra, K. N., Frisch, H., Faurobeet-Scholl, M., & Paletou, F. 2000, Journal of Astrophysics and Astronomy, 21, 255

Nagendra, K. N., Frisch, H., & Faurobert, M. 2002, Astron. Astrophys., 395, 305

Nagendra, K. N., Frisch, H., & Faurobert-Scholl, M. 1998, Astron. Astrophys., 332, 610

Nagendra, K. N., Frisch, H., & Fluri, D. M. 2003, in Astronomical Society of the Pacific Conference Series, Vol. 307, Solar Polarization, ed. J. Trujillo-Bueno & J. Sanchez Almeida, 227

Nagendra, K. N., Paletou, F., Frisch, H., & Faurobert-Scholl, M. 1999, in Astrophysics and Space Science Library, Vol. 243, Polarization, ed. K. N. Nagendra & J. O. Stenflo, 127

Nagendra, K. N., Rangarajan, K. E., & Rao, D. M. 1993, Mon. Not. Roy. Astron. Soc., 262, 855

Nagendra, K. N., & Sampoorna, M. 2009, in Astronomical Society of the Pacific Conference Series, Vol. 405, Solar Polarization 5: In Honor of Jan Stenflo, ed. S. V. Berdyugina, K. N. Nagendra, & R. Ramelli, 261

Nagendra, K. N., & Sampoorna, M. 2011, Astron. Astrophys., 535, A88 (NS11)

—. 2012, ApJ, 757, 33

Neckel, H., & Labs, D. 1994, Solar Phys., 153, 91

Öhman, Y. 1929, Mon. Not. Roy. Astron. Soc., 89, 479

Olson, G. L., Auer, L. H., & Buchler, J. R. 1986, J. Quant. Spectrosc. Radiat. Transfer, 35, 431

Olson, G. L., & Kunasz, P. B. 1987, J. Quant. Spectrosc. Radiat. Transfer, 38, 325

Omont, A., Smith, E. W., & Cooper, J. 1972, ApJ, 175, 185

—. 1973, ApJ, 182, 283

Oxenius, J. 1965, J. Quant. Spectrosc. Radiat. Transfer, 5, 771

Paletou, F., & Faurobert-Scholl, M. 1997, Astron. Astrophys., 328, 343

Povel, H.-P. 1995, Optical Engineering, 34, doi:10.1117/12.200596

Querfeld, C. W., Smartt, R. N., Bommier, V., Landi Degl'Innocenti, E., & House, L. L. 1985, Solar Phys., 96, 277

Ramelli, R., Setzer, M., Engelhard, M., Bianda, M., Stenflo, J. O., Küveler, G., & Plewe, R. 2015, IAU General Assembly, 22, 2256989

Ramelli, R., Balemi, S., Bianda, M., Defilippis, I., Gamma, L., Hagenbuch, S., Rogantini, M., Steiner, P., & Stenflo, J. O. 2010, in Society of Photo-Optical Instrumentation Engineers (SPIE) Conference Series, Vol. 7735, Society of Photo-Optical Instrumentation Engineers (SPIE) Conference Series, 1

Rangarajan, K. E. 1999, Mon. Not. Roy. Astron. Soc., 308, 1053

Rangarajan, K. E., Mohan Rao, D., & Peraiah, A. 1991, Mon. Not. Roy. Astron. Soc., 250, 633

Redman, R. O. 1941, Mon. Not. Roy. Astron. Soc., 101, 266

Rees, D. E., & Saliba, G. J. 1982, Astron. Astrophys., 115, 1

Rybicki, G. B., & Hummer, D. G. 1991, Astron. Astrophys., 245, 171

Sahal-Brechot, S. 1977, ApJ, 213, 887

Saliba, G. J. 1985, Solar Phys., 98, 1

Sampoorna, M. 2008, PhD thesis, Indian Institute of Science.

—. 2011a, ApJ, 731, 114

—. 2011b, Astron. Astrophys., 532, A52

Sampoorna, M. 2014, in Astronomical Society of the Pacific Conference Series, Vol. 489, Solar Polarization 7, ed. K. N. Nagendra, J. O. Stenflo, Q. Qu, & M. Samooprna, 197

Sampoorna, M., Nagendra, K. N., & Frisch, H. 2008a, J. Quant. Spectrosc. Radiat. Transfer, 109, 2349

—. 2008b, J. Quant. Spectrosc. Radiat. Transfer, 109, 2349

—. 2011, Astron. Astrophys., 527, A89

Sampoorna, M., Nagendra, K. N., & Stenflo, J. O. 2007a, ApJ, 663, 625

—. 2007b, ApJ, 670, 1485

—. 2008c, ApJ, 679, 889

—. 2013, ApJ, 770, 92

Sampoorna, M., Stenflo, J. O., Nagendra, K. N., Bianda, M., Ramelli, R., & Anusha, L. S. 2009, ApJ, 699, 1650

Sampoorna, M., & Trujillo Bueno, J. 2010, ApJ, 712, 1331

Sampoorna, M., Trujillo Bueno, J., & Landi Degl'Innocenti, E. 2010, ApJ, 722, 1269

Shapiro, A. I., Fluri, D. M., Berdyugina, S. V., Bianda, M., & Ramelli, R. 2011, Astron. Astrophys., 529, A139

Smitha, H. N., Nagendra, K. N., Sampoorna, M., & Stenflo, J. O. 2011a, Astron. Astrophys., 535, A35

—. 2013a, J. Quant. Spectrosc. Radiat. Transfer, 115, 46

Smitha, H. N., Nagendra, K. N., Stenflo, J. O., Bianda, M., & Ramelli, R. 2014, ApJ, 794, 30

Smitha, H. N., Nagendra, K. N., Stenflo, J. O., Bianda, M., Sampoorna, M., Ramelli, R., & Anusha, L. S. 2012a, Astron. Astrophys., 541, A24

Smitha, H. N., Nagendra, K. N., Stenflo, J. O., & Sampoorna, M. 2013b, ApJ, 768, 163

Smitha, H. N., Sampoorna, M., Nagendra, K. N., & Stenflo, J. O. 2011b, ApJ, 733, 4

Smitha, H. N., Sowmya, K., Nagendra, K. N., Sampoorna, M., & Stenflo, J. O. 2012b, ApJ, 758, 112

Sowmya, K., Nagendra, K. N., & Sampoorna, M. 2012, Mon. Not. Roy. Astron. Soc., 423, 2949

Sowmya, K., Nagendra, K. N., Sampoorna, M., & Stenflo, J. O. 2014a, ApJ, 793, 71

—. 2015, ApJ, 814, 127

Sowmya, K., Nagendra, K. N., Stenflo, J. O., & Sampoorna, M. 2014b, ApJ, 786, 150

Stenflo, J., ed. 1994, Astrophysics and Space Science Library, Vol. 189, Solar Magnetic Fields: Polarized Radiation Diagnostics (S94)

Stenflo, J. O. 1973, Solar Phys., 32, 41

—. 1974, Solar Phys., 37, 31

—. 1980, Astron. Astrophys., 84, 68

—. 1982, Solar Phys., 80, 209

—. 1984, Appl. Opt., 23, 1267

Stenflo, J. O. 1985, in Solar Physics and Interplanetary Travelling Phenomena, ed. C. de Jager & B. Chen, 1275

—. 1996a, Nature, 382, 588

—. 1996b, Solar Phys., 164, 1

—. 1997, Astron. Astrophys., 324, 344

—. 1998, Astron. Astrophys., 338, 301

Stenflo, J. O. 2002, in Astrophysical Spectropolarimetry, ed. J. Trujillo-Bueno, F. Moreno-Insertis, & F. Sánchez, 55–100

—. 2005, Astron. Astrophys., 429, 713

—. 2013, Astron. Astrophys. Rev., 21, 66

—. 2015a, Astron. Astrophys., 573, A74

—. 2015b, Space Science Reviews, arXiv:1508.03312

Stenflo, J. O., Baur, T. G., & Elmore, D. F. 1980, Astron. Astrophys., 84, 60

Stenflo, J. O., Bianda, M., Keller, C. U., & Solanki, S. K. 1997, Astron. Astrophys., 322, 985

Stenflo, J. O., & Keller, C. U. 1997, Astron. Astrophys., 321, 927

Stenflo, J. O., Keller, C. U., & Gandorfer, A. 1998, Astron. Astrophys., 329, 319

—. 2000, Astron. Astrophys., 355, 789

Stenflo, J. O., & Povel, H. 1985, Appl. Opt., 24, 3893

Stenflo, J. O., Solanki, S., Harvey, J. W., & Brault, J. W. 1984, Astron. Astrophys., 131, 333

Stenflo, J. O., & Stenholm, L. 1976, Astron. Astrophys., 46, 69

Stenflo, J. O., Twerenbold, D., & Harvey, J. W. 1983a, Astronomy and Astrophysics Supplement Series, 52, 161

Stenflo, J. O., Twerenbold, D., Harvey, J. W., & Brault, J. W. 1983b, Astronomy and Astrophysics Supplement Series, 54, 505

Supriya, H. D., Nagendra, K. N., Ravindra, B., & Sampoorna, M. 2014a, in Astronomical Society of the Pacific Conference Series, Vol. 489, Solar Polarization 7, ed. K. N. Nagendra, J. O. Stenflo, Q. Qu, & M. Samooprna, 117

Supriya, H. D., Nagendra, K. N., Sampoorna, M., & Ravindra, B. 2012, Mon. Not. Roy. Astron. Soc., 425, 527

Supriya, H. D., Samooprna, M., Nagendra, K. N., Stenflo, J. O., & Ravindra, B. 2016, ApJ, under review

Supriya, H. D., Sampoorna, M., Nagendra, K. N., Ravindra, B., & Anusha, L. S. 2013a, J. Quant. Spectrosc. Radiat. Transfer, 119, 67

Supriya, H. D., Smitha, H. N., Nagendra, K. N., Ravindra, B., & Sampoorna, M. 2013b, Mon. Not. Roy. Astron. Soc., 429, 275

Supriya, H. D., Smitha, H. N., Nagendra, K. N., Stenflo, J. O., Bianda, M., Ramelli, R., Ravindra, B., & Anusha, L. S. 2014b, ApJ, 793, 42

Supriya, H. D., Smitha, H. N., Nagendra, K. N., Stenflo, J. O., Bianda, M., Ravindra, B., Ramelli, R., & Anusha, L. S. 2015, in IAU Symposium, Vol. 305, Polarimetry, ed. K. N. Nagendra, S. Bagnulo, R. Centeno, & M. Jesús Martínez González, 381–386

Trujillo Bueno, J. 1999, in Astrophysics and Space Science Library, Vol. 243, Polarization, ed. K. N. Nagendra & J. O. Stenflo, 73–96

Trujillo Bueno, J. 2001, in Astronomical Society of the Pacific Conference Series, Vol. 236, Advanced Solar Polarimetry – Theory, Observation, and Instrumentation, ed. M. Sigwarth, 161

Trujillo Bueno, J. 2003, in Astronomical Society of the Pacific Conference Series, Vol. 288, Stellar Atmosphere Modeling, ed. I. Hubeny, D. Mihalas, & K. Werner, 551

Trujillo Bueno, J., & Landi Degl'Innocenti, E. 1996, Solar Phys., 164, 135

—. 1997, Astrophys. J. Lett., 482, L183

Trujillo Bueno, J., Landi Degl'Innocenti, E., Collados, M., Merenda, L., & Manso Sainz, R. 2002, Nature, 415, 403

Trujillo Bueno, J., & Manso Sainz, R. 1999, ApJ, 516, 436

Uitenbroek, H. 2001, ApJ, 557, 389

Vernazza, J. E., Avrett, E. H., & Loeser, R. 1973, ApJ, 184, 605

—. 1976, Astrophysical Journal Supplement Series, 30, 1

—. 1981, Astrophysical Journal Supplement Series, 45, 635

Wiehr, E. 1975, Astron. Astrophys., 38, 303

Zanstra, H. 1941, Mon. Not. Roy. Astron. Soc., 101, 250

Zeeman, P. 1897, ApJ, 5, 332